Dynamics of a Small Tidal Estuarine Plume

by

Mark Pritchard B.Sc. (Joint Hons.)

A thesis submitted to the University of Plymouth in partial fulfilment for the degree of

Doctor of Philosophy

Institute of Marine Studies
Faculty of Science

October 2000

90 0451423 1

UNIVERSITY OF PLYMOUTH

Item No. 900 451423 1

Date 22 NOV 2000 S

Class No. T 556.4609 PRI

Contl. No. X704163208

LIBRARY SERVICES

REFERENCE ONLY

LIBRARY STORE

Abstract

Small-scale estuarine plume discharges into adjacent seas are common inshore features responsible for the transportation and dispersion of brackish water in the coastal zone. However, the physics that govern small-scale mixing in the frontal regions of river plumes are still poorly understood. The current study quantified and compared the observed hydrodynamic properties present inside a radially spreading river plume discharge from the River Teign, Teignmouth, Devon, UK, to those predicted by a generic plume model. Numerical simulations designed to replicate time dependent radial plume spreading from a constant source predicted the development of an internal interfacial bore that lagged the surface plume front through radial distance and time from initial plume release. The model was scaled from time lapse X-band radar imagery that recorded several plume discharge events. Scaled model output predicted the internal bore to form approximately 180 m behind the leading surface front. Subsequent field studies employed instrumentation capable of recording high-resolution measurements of temperature, salinity and velocity, spatially and vertically throughout the plume's buoyant layer over two ebb tidal cycles. Results suggested the plume advanced at a rate dependent on a super-critical interfacial Froude number of $O(1.3)$ and was a region of intense mixing and downward mass entrainment. Temperature contours recorded through the stratified plume gave no indication of an internal bore in its predicted position but did show an abrupt shallowing of the interfacial region some 40 to 60 m behind the surface plume front. Super-critical interfacial Froude and critical Gradient Richardson numbers present in this region of the plume implied that this was the position of the predicted bore. The form of the bore often appeared as an ensemble of undular internal hydraulic jumps rather than a singular discontinuity as predicted by the model. Bulk mixing analysis inside the leading front based on established gravity current theory suggested that the extent of turbulent exchange in the model frontal boundary condition β, was underestimated by about a factor of 2. With the required increase in β, model simulations showed a decrease in the lag distance of internal bore formation to one where critical Froude numbers were detected inside the actual plume. Throughout both surveys, the gravity head remained a reasonably constant size due to any increase in across frontal velocity over the ebb tidal cycle being matched by an increase in entrainment and mixing. The subsequent conclusions from the study show the outflow and mixing dynamics are controlled by the estuary's tidal modulation of estuarine brackish water outflow / plume inflow rate behind the leading plume frontal discontinuity.

List of Contents

Chapter 1: Introduction

Chapter 2: A Literature Review

Chapter 3: Preliminary Fieldwork & Numerical Modelling

Chapter 4: Results: Plume Hydrodynamics

Chapter 5: Results: Frontal Mixing & Circulation

Chapter 6: Results: Model-Data Comparison

Chapter 7: Discussion & Conclusions

Appendix:

List of Tables & Figures

Figures

Tables

Plates

List of Symbols

(Variations in symbolism or other symbols are stated in the text next to derivation)

B_f	Buoyancy flux
C	Non-dimensional model phase velocity
C^2	Coherence squared
C_D	Drag coefficient
$\mathrm{C_f}$	Non-dimensional model phase speed behind the front
c	Model phase velocity
c_i	Interfacial wave phase velocity
c_g	Interfacial wave group velocity
D_E	Ekman layer depth
D	Non-dimensional model depth
D	Depth of interface
$\overline{D}$	Tidal energy dissipation
$\overline{D}_T$	Total tidal energy dissipation
$\overline{D}_f$	Total frontal energy dissipation
d	Depth
$\tilde{\mathrm{d}}$	Ratio of model interfacial friction and entrainment coefficients
E	Entrainment coefficient
F	Model Froude number
$\mathrm{F_{a1}}$	Model Froude number based on $\mathrm{Q_a}$ and $\mathrm{C_f}$
Fr_i	Interfacial Froude number
f	Coriolis parameter
g	Gravitational acceleration
g'	Reduced gravitational acceleration
H_k	Gain
h	Depth
i	Imaginary operator
K	Kelvin number
K_z	Vertical eddy diffusivity
k	Wave number
L	Length scale
L_u	Upwelling distance
L_f	Length of the front
N^2	Brunt-Väisälä frequency
Ny	Nyquest frequency
P	Position
$\overline{P}_{vm}$	Energy requirement for vertical mixing
$\overline{P}_{vmT}$	Total energy requirement for vertical mixing
p	Pressure
$\mathrm{Q_a}$	Modelled speed of front relative to ambient water
Q	Non-dimensional model fluid velocity
$\mathrm{Q_f}$	Non-dimensional model fluid velocity behind the front
q	Model fluid velocity
q_e	Entrainment velocity
q_m	Non-dimensional mixing coefficent

R'	Internal baroclinic Rossby radius
Ri_g	Gradient Richardson number
Ri_b	Bulk Richardson number
r	Model radius
$\mathrm{S_e}$	Model direction of entrainment
T	Model non-dimensional time
T	Period
t	Time
U_t	RMS value of tidal current velocity
U_w	Average wind speed
$\overline{u}$	Depth mean velocity
u	Cartesian longitudinal velocity
u_*	Surface friction velocity
$\overline{u}_a$	Velocity of front relative to ambient water
$\overline{u}_b$	Height mean velocity in bottom boundary layer
u_{av}	Depth averaged current velocity
$\overline{u}_d$	Ship's drift velocity
$\overline{u}$	Mean along frontal velocity
v	Cartesian lateral velocity
$\overline{v}$	Mean across frontal velocity
$\overline{W}$	Wind energy dissipation
$\overline{W}_T$	Total wind energy dissipation
W_{10}	Wind drag coefficient
w	Cartesian vertical velocity
X_k	Fourier coefficient
x	Cartesian longitudinal direction
y	Cartesian lateral direction
z	Cartesian vertical direction
ρ	Density
$\Delta\rho$	Density anomaly
Ω	Angular frequency
α	Thermal constant of proportionality
β	Model decay scale of mass and entrainment (mixing coefficient)
ϕ_{xxk}	Power spectral density
ϕ_{xyk}	Power cross spectral density
γ	Efficiency factor
η	Sea surface relative to tidal elevation
λ	Wave length
λ_i	Interfacial wave length
θ	Angle
σ_t	Density anomaly of seawater
τ_w	Wind stress
ω_i^2	Interfacial wave dispersion
δ	Efficiency factor
ζ	Tidal elevation
ϕ	Frontal bulk energy dissipation
κ	Frontal bulk energy dissipation per unit mass, depth and width

Acknowledgements

I'll be sensible, start at the beginning as tradition has it, and express my extreme gratitude for the excellent guidance and supervision of Professor David Huntley, my principle supervisor. His vision and patience made the whole project possible as well as causing the odd headache. Thanks David (not for the headaches).

A big thank you also goes to Dr Tim O'Hare, my 2nd supervisor who made time to help out with the modelling and discuss problems as and when they arose.

'Mucho gracious' to Pete Ganderton, IMS's resident electronics and field technician who developed, serviced and stopped me kicking all the shinny gadgets that sometimes go wrong when they touch seawater. In addition, a thank you to Greg Allen the skipper of 'Grey Dawn' and the survivor of several 'stomach' mutinies instigated by the research staff due to a combination of sea conditions, donuts and bacon sandwiches.

Formal thanks must go to PERC and IMS for the scholarship, departmental resources, the desk and the airfare to New Orleans. I'm indebted to Professor Keith Dyer, Professor Rich Garvine, Dr Mike Fennessy, The Environmental Agency, South West Water, Plymouth Marine Laboratory, MAFF, Southampton Oceanographic Centre and HR Wallingford for contributions to this study.

Now, the next acknowledgements goes to my many colleagues and friends (past and present) who aided fieldwork, my brain, both, or by just going to the pub to ensure sobriety (sometimes they failed!) and hear me complain. These individuals are members of the exclusive (elusive ?) 'Help Club' and too numerous to mention. However, if they ever pick up this thesis and stumble across this page they'll know who they are. Cheers Mates!

Lastly but by no means least I must mention my family. Thanks for Leila's unconditional love and her understanding of where Dad's been these last few years, you're the best. Thanks to Isobel, my sister for proof reading and being there. I conclude by thanking my parents for their undying support and encouragement throughout the college years. Mum and Dad, you made sacrifices to give Isobel and I opportunities that you both couldn't have. I'll never forget that!

Author's Declaration

At no time during the registration for the degree of Doctor of Philosophy has the author been registered for any other University award.

Relevant scientific seminars and conferences were regularly attended at which work was often presented and several papers prepared for publication.

Publications

Pritchard, M., Huntley, D.A. & O'Hare, T.J., 1998. The Teign Plume: Measurement & Modelling. Abstract. Challenger Society for Marine Science - UK Oceanography 98, September 1998, University of Southampton, UK.

Pritchard, M. & Huntley, D.A. & O'Hare, T.J., 2000. Mixing in a Small Tidal Estuarine Plume. In: Estuarine and Coastal Modelling: Proceedings of the Sixth International Conference. November 3rd-5th 1999, New Orleans, Louisiana., USA / edited by Malcolm L. Spaulding, H. Lee Butler. ISBN 0-7844-0504-2

Presentations and Conferences Attended

LOIS Annual Meeting, University of Hull, UK, 1997.
UK Oceanography 98, University of Southampton, UK, 1998. Oral presentation.
6th International Conference on Estuarine and Coastal Modelling, November 1999, New Orleans, L.A., USA. Oral Presentation.
Oceanology International 2000, March 2000, Brighton, UK.
Two oral presentations in the Institute of Marine Studies, University of Plymouth, Research Seminar Series 1996-1999.

Signed....M Pritchard....
Date......3\10\00.............

Dynamics of a Small Tidal Estuarine Plume

by

Mark Pritchard B.Sc. (Joint Hons.)

Chapter 1

Introduction

1.1 Why Study River Plumes ?

The potential of river plumes to transfer pollutants and deposit terriginous sediment in the coast zone is unparalleled. Vast deposits of sediment that accumulates dissolved and particulate matter from rivers and streams end up in the coastal zone via estuarine outflows. The flux of these materials is subject to natural variations in the quality and timing of freshwater inflows, tides and meteorological conditions. The vicinity of many of the larger scale freshwater discharges tends to be highly productive and may support major commercial fisheries.

The geographical regions of freshwater inflows into the coastal zone are also amongst those most densely populated by humans due to fertile flood plains and access to shipping. Thus, human impact on the local environment in these regions which includes eutrophication due to fertiliser and sewage inputs into coastal waters is of a major concern in the management of these regions.

Consequently, estuarine plumes have received considerable attention in the scientific press over the last three decades and studies have encompassed large to small-scale physical processes active in their presence and dispersion.

Garvine & Munk (1974) made the first detailed physical observations of smaller scale plume discharges in the early 1970's. Their comprehensive study of a plume's small-scale structure and motion field in the Connecticut River discharge led the way to numerical simulation of the physical processes active at plume fronts and the waters contained within them (Garvine, 1974a). The concepts introduced by Garvine (1974a, 1981) have since been adopted and improved to explore various different aspects of river plumes and plume front hydrodynamics at the coast and in the shelf seas.

However, until recently few of these models have been applied to real outflows and authenticated by observations. With the recent advances in technology Marmorino & Trump (1996), O'Donnell (1997) and Brubaker & Simpson (1999) have shown with 'state of the art' instrumentation there is now the ability to collect the high-resolution and accurately positioned data sets required for the validation of the numerical hypothesises on mixing and propagation. This instigated the current project, as only a few studies have focused on the smaller scale physics of plume outflows from the many UK estuaries.

1.2 Specific Aims of the Present Study

The approach adopted for this research was to consider the smaller scale features and boundaries of a plume outflow. This was entirely motivated through the knowledge that dynamically, the smaller scale features provide some of the most physically active and philosophically challenging regions of spreading freshwater plumes in the coastal zone. A study providing a good physical description of processes that drive mixing and provide quantitative estimates of initial and transient conditions can be incorporated or used to perfect model schemes. Resulting applications include improvements in water quality control and forecast capabilities of coastal outflow models.

The Teign estuary, Teignmouth, Devon, UK was chosen for the current study as it exemplified some of the hallmark features described in the literature. From a logistical perspective, the Teign plume was also a manageable size to survey from a small research vessel.

1.3 Outline of the Thesis Structure

Chapter 2 presents a literature review that includes general and specific concepts dealt with in this thesis and is intended to make the reader aware of the importance and shortcomings of past studies in this area of oceanographic science. It also provides a benchmark for the current project. Chapter 3 introduces the study site and gives a full description of preliminary work that helped develop hypothesises. This is followed by a detailed description of the tidal hydrodynamics and geostropic influence in the study area. This is principally to inform the reader of processes influential in plume formation and the fate of river derived outflow. Sections on model development and scaling for the Teign plume is ensued by details of the instrumentation used to collect the high-resolution data used in the field study. Chapter 4 describes and discusses the larger scale hydrodynamics observed during the fieldwork. The first section describes the field conditions during plume surveys followed by an account of the measures taken to correct and remove all the superfluous signals from the high resolution data that was required to resolve internal features present inside the plume. The rest of the chapter describes and quantifies the bulk dynamics using the tidal and survey data and a simple model of estuarine outflow. Chapter 5 is a continuation of Chapter 4 but focuses on the frontal regions of the plume. Mixing processes are investigated using various quantifying parameters and the results compared with an analytical model of gravity current mixing. Results from this chapter are then used in model validation discussed in Chapter 6. The chapter concludes with a energy budget that investigates the extent and influence of tidal, wind and plume frontal mixing in the region of the outflow. Although Chapter 6 is brief, it examines the effect of reintroducing field derived mixing parameters into the model and looks at the sensitivity of the model to the alterations of the boundary and initial start conditions. The conclusions from the study are drawn together in Chapter 7 and provide the reader with a summary of the project. Recommendations for future projects interested in plume and frontal dynamics that may help resolve outstanding questions are discussed in this final section of the thesis.

Chapter 2

A Literature Review

2.1 Foreword

Although the current study was focused on a small estuarine discharge into a semi-enclosed sea, the processes under review are generally accepted as being driven by the same physical principles as the larger scale outflows on to the continental shelf. Hence, this chapter contains a brief literature review applicable to both scenarios, but mainly focuses on the specific topics and hypothesises currently under investigation. Aquatinted with this information, the reader can then proceed onto later chapters being aware of the well established and 'state of the art' theory and the supportive evidence from other observational, laboratory and modelling studies.

2.2 Introduction

Buoyant freshwater or thermal (power plant) discharge surface plumes are commonly observed features in coastal waters (Garvine, 1982; Masse & Murthy, 1990). Often they remain connected to their discharge source while continually spreading out as a stratified layer into receiving coastal waters. The frontal zones, shear flow instabilities and internal waves accompanying or present in these outflows may enhance mixing and dispersion of the source water during the plume's movement. Knowledge of any spatial and temporal variability in freshwater discharge into the coastal zone is particularly interesting to the marine scientist. For example, thin surface layers of buoyant freshwater can dominate local physical-biological processes. The presence of plume discharges into the coastal zone can significantly contribute to the transport and mixing of larvae, sediments, sewage, pollutants and provide a primary source of nutrients into adjacent seas (Nittrouer *et.al.*, 1991; Masse & Murthy, 1992; Morris *et.al.* 1995).

2.3 Plume Dynamics

As this thesis is centred on the study of a surface advected estuarine plume, only low salinity gravity currents driven by tidal forcing and longitudinal density gradients into a higher salinity coastal sea or ocean are considered. Oceanographic literature contains a multitude of references to plume outflows and their respective physical constraints and control. Therefore, the following section aims to provide the reader with not only an introduction to the basic concepts by example of plume dynamics, but also the variability in their form due to a variety of physical forcing mechanisms.

The main driving force of plume expansion is analogous to a breaking dam and bore formation described in Stoker (1957) where the quantity of freshwater input influences the initial buoyant expansion of the plume. A plume then forms from the balance between inertia and gravity (buoyancy) forces with a sharp discontinuity between the free surface of the spreading plume and the ambient water. Additional forcing may also be provided by barotropic tidal currents and wind stress. This discharge often forms a 'jet' at the mouth of the estuary (Lukitina & Imberger, 1987). Masse & Murthy (1992) and Munchow & Garvine (1993b) suggest plume dynamics are complex and include a number of different dynamical regimes between the source and downstream coastal currents. The complexity of these flows is due to their dependence on the magnitude of the river discharge, rotational effects and the importance of the non-linear terms. These determine the extent of offshore and alongshore spreading.

Smaller scale plumes are unaffected by the Earth's rotation and retain non-linear dynamics resulting from the outflow velocity and volume of freshwater discharge (Jaeger, 2000). However, larger scale outflows that exceed the internal Rossby radius of deformation, R' are forced to turn or rotate due to the Coriolis force (right in the Northern Hemisphere).

$$R' = (g'h_1)^{1/2}/f \qquad [2.1]$$

R' = Internal Rossby Radius (m)
g' = Reduced gravitational acceleration
= $\Delta\rho/\rho\, g$ (ms^{-2})
h_1 = Plume layer depth (m)

f = Coriolis parameter $= 2\Omega \sin\theta$ (s^{-1})
Ω = Angular frequency
θ = Latitude

In large scale plume discharges where the width of the current is $O(R')$, instabilities or meanders form along the frontal regions. These instabilities scale on the width of the flow due to barotropic instability where eddy energy is drawn from the kinetic energy of the mean flow of the coastal attached current (Griffiths & Linden, 1982; Hill, 1998).

$$Fr_i = u / c_i \qquad [2.2]$$

Fr_i = Froude number
u = Alongshore velocity of the upper buoyant layer (ms^{-1})
$c_i = \sqrt{g'h_1}$ = Interfacial wave speed (ms^{-1})

The plume first bulges and flow is super-critical and distinguishable by interfacial Froude numbers (Fr_i) exceeding unity, where Fr_i represents the ratio between flow velocity u and interfacial wave speed 'c_i' in a 2-layer fluid (Yankovsky & Chapman, 1997). The observed reduction from $Fr_i > 1$ in the near field (non-linear phase) to $Fr_i < 1$ in the far field (linear phase) suggests the presence of internal bores (McClimans, 1988). The presence of such internal features was predicted through computer simulations of non-linear plume spreading by Garvine (1984) and O'Donnell (1988, 1990) but remains unobserved in the field. These implications of the predicted non-linearities in the near field of plume discharges are addressed later in this review.

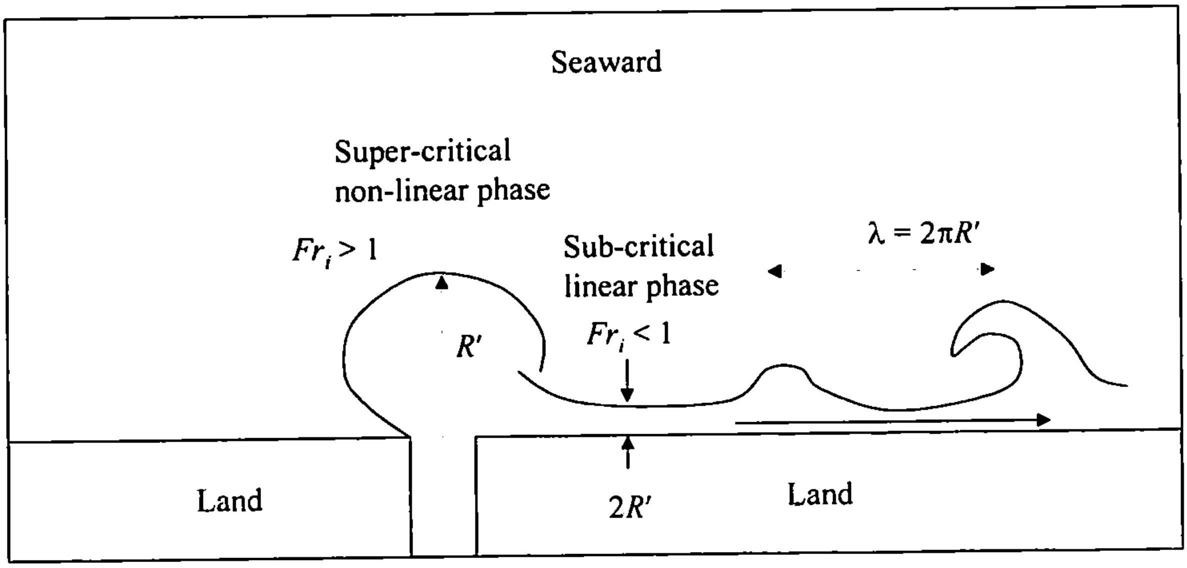

Fig 2.1: Schematic diagram of non-linear and linear phase of plume discharge currents and eventual formation of a coastal current in the Northern Hemisphere.

After further expansion and spreading, the plume turns at the limit of the internal Rossby radius, the flow then returns to sub-critical levels and consequently attaches to the coastline forming an alongshore current at approximately 2 R'. The plume now displays a linear mode of motion following the direction of Kelvin wave propagation (Davies & Xing, 1999). The scales of these parameters are shown schematically in Fig 2.1. Examples of outflows influenced by Coriolis force are found in the Shannon and Delaware estuaries (Huang *et.al.*, 1993; Wiseman & Garvine, 1995). Hill (1998) gives a complete review of such buoyancy discharges into coastal waters.

2.4 Tidal Current & Plume Interaction

Larger scale plumes require a continuous freshwater river discharge that is often subject to some tidal and seasonal modulation and Chao's (1990) model showed that tides may play an important role in the spreading of offshore plumes from an estuary.

Plume outflows in the presence of strong alongshore tidal currents can undergo significant changes over the ebb and flood cycle. Observations made in the Tees plume by Lewis (1984) showed the formation of a plume at low water that moved northwards. At half flood the plume was 'cut-off' from the estuary mouth by a NW current forming a pool of brackish water disconnected from the river source. Then, towards high water, reversing tidal currents transferred a diluted salinity tongue to the southeast of the estuary mouth. Subsequently, the cycle was then repeated and a new plume was formed on the ebb tide. As shown through this example, tidally 'cut' discharges cause a pulsated (at dominant tidal frequencies) release of freshwater which forms isolated patches of buoyant freshwater disconnected from the estuary during the flood phase (Hickey, 2000).

Smaller estuaries affected by a strong tidal influence can 'cut-off' any discharge due to tidal intrusion. Flood currents cause the free surface slope (barotropic pressure gradient) to reverse which, in most instances, causes the plume front to disperse (Bowman & Iverson, 1978). An extreme example of excessive tidal forcing can lead to the formation of 'tidal intrusion' fronts actually inside the estuary mouth as, for example, in The Seiont estuary in North Wales (Simpson & Nunes, 1981). Alternatively, a *quasi*-stationary plume front may form outside the estuary during the tidal flood phase where the interaction of bathymetry and tidal currents restricts further plume spreading (Huzzey, 1982).

Further modification of plume outflows may arise from the spring-neaps cycle and diurnal inequalities resulting in temporal variation of tidal amplitudes and currents. This can affect the level of mixing, dispersion and frontogenesis in estuarine plume coastal discharges. Linden & Simpson (1989) illustrated this through simple experimentation by modulating mixing in a stratified gravity flow inside a tank by using an air bubble curtain. This effectively mimicked stirring and mixing over a tidal cycle. As stirring is increased due to the air supply being switched on in analogy to tidal mixing, the freshwater gravity current is dispersed. Whereas at slack water or in context of these experimental conditions, the air supply being switched off, frontal formation in front of the gravity current resulted through the lack of any turbulent mixing. In reality, the tidal contribution to plume formation, movement and mixing could be highly significant but not the dominant factor. Additional work has looked at Regions of Fresh Water Influence (ROFI) that develop from fresh water input over several tidal cycles and respond to seasonal changes in river flow. Their similar hydrodynamics were found to be governed by density stratification, spring-neap tidal cycles, tidal straining by vertical shear and the Earth's rotation, combined with more random processes due to surface wind stress and surface wave activity (Simpson *et.al.*, 1993, Souza & Simpson, 1997).

2.5 Wind Forcing

Wind driven circulation and dispersion of buoyant plumes is clearly an important factor to consider, especially on the continental shelf. The prevailing wind is responsible for the majority of alongshore transport that affects the direction of plume propagation and spatial structure. Prevailing onshore winds that cause upwelling can also influence the offshore movement of surface plumes and can separate them entirely from the coast (Hickey, 2000). The opposite occurs in the presence of downwelling where the plumes tend to move onshore, deepen and make bottom contact near to the coast.

Kourafalou *et.al.* (1996a, 1996b) and Chao (1988a) showed through modelling studies that plumes are very sensitive to local wind changes that cause perturbation in surface Ekman layer flow. Csanady (1982) suggests that under steady state conditions away from the coast with wind stress as the only driving force, friction and Coriolis force balance to form an Ekman layer, D_E. Under these circumstances for a homogenous water column, a layer of zero velocity is found at great depth. However, in a stratified water column the level of zero flow becomes the depth of the pycnocline, h_1. This stratified model of surface layer wind transport is dependent on the ratio, h_1 / D_E.

$$D_E = 0.4u_*/f = \sqrt{2K_z/f} \qquad [2.3]$$

D_E = Ekman layer depth (m)
$u_* = \sqrt{\tau_w/\rho}$ =Surface friction velocity (ms^{-1})
f = Coriolis parameter (s^{-1})
ρ = Density of upper layer (kgm^{-3})
K_z = Eddy viscosity (m^2s^{-1})

τ_w= Wind stress = $\rho_a W_{10} U_w^2$ ($kgm^{-1}s^{-2}$)
ρ_a = Density of air (kgm^{-3})
W_{10} = Drag coefficient
U_w = Wind speed (ms^{-1})

For large h_1 / D_E the solution is the classical Ekman spiral but for the stratified case ($h_1 << D_E$), the model predicts the surface transport in a perpendicular direction to the wind. Therefore, stratification decreases D_E and increases surface transport. Stumpf *et.al.* (1993) showed their estimates of wind induced surface transport (6 to 11 % of measured wind velocity) increased as the depth of the surface layer decreased and was 50 % greater than previous research suggested (Huang, 1979). They argue that a strong pycnocline would reduce vertical transfer of horizontal momentum and lead to a near frictionless movement of the plume, thus increasing surface velocities. However, the stratified model predictions on surface transport being directed at 90° to the right of the wind were inconsistent with the observations as flow was in the same direction as the prevailing wind. The discrepancy in the observed and predicted direction of the surface layer was attributed to the model assuming an equilibrium state where the effects of any inertial period are ignored.

2.6 Plume Models

Plume model development over the last two decades has provided a good qualitative framework within which plume processes can be addressed. Numerical simulations have included dominant processes thought to control the observed behaviour of a given type of river plume in coastal waters and the continental shelf. Solutions to the modelled dynamics have considered the effects of river discharge alone (Chao & Boicourt, 1986; Weaver & Hseih, 1987, Chao, 1988b), Coriolis force (Garvine, 1987, 1996), tidal forcing (Chao, 1990; Wheless & Valle-Levinson, 1996), wind stress on an existing plume (Chao, 1988a; Kourafalou *et.al.*, 1996a, 1996b), ambient coastal flow (Zhang *et.al.*, 1987; O'Donnell, 1990) and river discharge angle (Garvine, 1987).

Numerical output from many of these models appear to produce 'believable' results for salinity distribution and alongshore or alongshelf flow (Hickey, 2000). However, attempts to apply models to transverse circulation patterns still show considerable variability where the majority of the variance in observational data is unexplained by the modelled processes (Munchow & Garvine, 1993b). Therefore, the model-data comparison provided recently by O'Donnell *et.al.* (1998) was welcome and more studies of the same calibre are required to alleviate pertinent questions on whether there is sufficient theory based on actual observational data for accurate model development and improvement.

Studying plume evolution and estimating frontal position, spreading rates, total area of dispersion and the scale of instabilities present on convergent frontal regions has proved difficult to resolve from observations at sea. The few 'high-resolution' observational studies to date have employed 'state of the art instrumentation' using either static sampling equipment (Lukitina & Imberger, 1989) or as in Marmorino & Trump (1996), O'Donnell (1997) and Brubaker & Simpson (1999) utilising high frequency data in a Lagrangian reference frame that is corrected through DGPS (Differential Global Positioning Systems). The remote sensing of larger scale plume features using airborne and coastal remote sensing platforms for various types of instrumentation has also proven useful. These include, coastal X-band radar (M. Tenorio, SOC, *pers.comm.*), Ocean Surface Current Radar, OSCR (Gmitrowicz & Brown, 1993), airborne radar (Marmorino *et.al.*, 2000) and airborne passive microwave instrumentation for remotely sensing salinity (M.L. Heron, James Cook University, *pers.comm.*). In later chapters of this thesis, an applied example of using one such remote sensing technique to a plume discharge is presented and discussed.

2.7 Frontal Dynamics

With few exceptions (see Munchow & Garvine, 1993a), the offshore spreading of a fresher water layer, usually no more than a few metres deep, results in the free surface slope gradient terminating in a region where a plume front is formed.

Largier (1993) and Simpson & James (1986) generally describe frontal zones as having an anomalous local maximum horizontal gradient in both scalar and vector properties such as temperature, salinity and velocity. These steep gradients in water column properties are also often present in the vertical co-ordinate of a frontal region. The temporal and spatial scale of fronts varies from tidal periods to months and from the length of a tidal excursion to thousands of kilometres respectively. The following review of frontal properties now focuses on plume fronts but the author refers the reader to O'Donnell (1993) for a full description of other frontal categories.

Plume frontal formation results from the juxtaposition of the two dissimilar water types where it is assumed that the direction of movement is aligned in the direction of ambient flow (O'Donnell, 1993; Lewis, 1997). A schematic of a plume front is presented in Fig 2.2 showing various general physical properties.

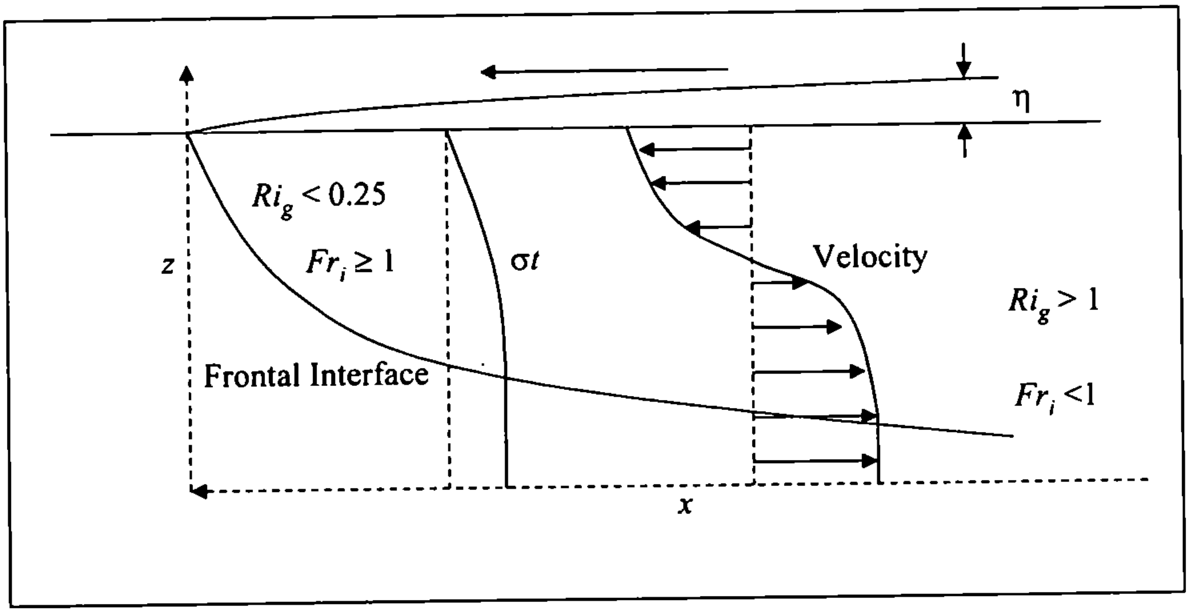

Fig 2.2: Schematic diagram of frontal properties in a frame of reference moving with the front. The diagram illustrates the general observed trends in the velocity and density distribution and regions of mixing and stability.

From inviscid theory, the propagation velocity of the front into ambient water is dependent on $c_i = (g'h_1)^{1/2}$, the phase speed of a long interfacial wave. If the plume is propagating into deep ($h_1 << h_2$) or shallow ($h_1 \approx h_2 / 2$) water, frontal speed then approximates to c_i multiplied by a factor of $2^{1/2}$ or $2^{-1/2}$ respectively (Benjamin, 1968, Simpson, 1982). Frontogenesis in a plume outflow only occurs when the pressure gradient established by the free surface slope and the opposing baroclinic force produced by the interfacial slope with the underlying ambient water are convergent and maintain a strong density gradient. This results in a vertically varying cross frontal pressure gradient that opposes the outflow (Garvine & Munk, 1974; Bowman & Iverson, 1978). Observational studies by Garvine & Munk (1974) and O'Donnell *et.al.* (1998) showed a strong horizontal frontal convergence due to this variation in the pressure gradient.

Numerous field and laboratory studies (see for example: Garvine & Munk, 1974; Stronach, 1981; Huzzey, 1982; Pelegri, 1988; O'Donnell, 1997; Benjamin, 1968; Simpson, 1982) have shown the plume front's dynamical signature marked explicitly by super-critical flow conditions with bore like characteristics and mixing. Through hydraulic theory, the criterion for super-critical flow is then expressed through the densimetric interfacial Froude number. Fr_i gives an indication of stability in a 2-layer flow and in essence represents the balance between inertia and gravity or buoyancy forces (McClimans, 1988). Super-critical flow conditions are characterised by the presence of mixing and energy loss at the front as the 'head wave' breaks and a consequential deepening of the interfacial region follows. Kinematics then dictates a downwelling of fresher and saline water into the water column and an accumulation of flotsam and foam, due to converging water masses, visibly marks the position of the front. Friction on the interfacial region entrains water down at the frontal convergence and into the layer of brackish water (Garvine, 1974a; O'Donnell *et.al.*, 1998). In a plume where the surface layer depth is much less than total depth, the frontal region is dominated by turbulence generated in the buoyant layer's interior. The turbulent kinetic energy (T.K.E.) required for mixing arises through interfacial shear instabilities produced by friction between the overlying and lower layers (O'Donnell, 1993). If this interfacial friction was absent the lack of any entrainment and mixing with the underlying water would cause a plume to spread indefinitely seaward as an infinitely thinning sheet of lower density water (Bowman & Iverson, 1978; Bowman, 1988).

Curiously, mixing in the frontal regions of plume outflows has still only received meagre attention by researchers in comparison to the other more orderly or easier quantified impact of wind stress and tidal mixing and/or straining on buoyant plumes outflows. This is probably due to the difficulty in measuring these comparatively narrow transient features. However, to ignore or assume levels of frontal mixing leaves a deficit in the dispersion budget and makes any boundary condition in a numerical model used to describe observed spreading phenomena subjective and, therefore, uncertain.

2.8 Mixing in Plume Fronts

The physics of river plumes hinge critically on mixing processes, yet few studies have focused on the actual mechanisms that result in the progressive dilution of freshwater in saltwater. Mixing processes in river plumes are thought to be the same as for those occurring in coastal regions where buoyant forcing is absent. For example, these include baroclinic and barotropic instabilities in coastal currents, tides, surface waves and wind mixing (Hickey, 2000). These processes affect the amount of vertical or lateral entrainment (transport of seawater into the plume) and detrainment (transport of brackish water out of the plume). In contrast to open oceanic regions, lateral and vertical regions of the plume boundary are marked by extremely sharp density contrasts forming the frontal convergence from a predominantly gravity driven flow.

Through both observations and modelling, Gavine & Munk (1974), Garvine (1974a, 1981) and O'Donnell *et.al.* (1998) have shown that the frontal convergence is dominated by downwelling activity. Both fresh and saltwater is forced down into the water column and subjected to intense shear that causes exchange and mixing of water types. The vertical mass flux is balanced by a horizontal flux of fresh-brackish water from the inshore side of the plume. The governing equations of motion stipulate that a three dimensional effect must take place in the upper layers of a frontal convergence. Flow towards the front in the upper layers is not entirely entrained down or swept away by the return flow perpendicular to the frontal edge. A significant proportion of the converging flow on reaching the interfacial region is diverted parallel to the front. Sinuosity observed by Garvine (1974b) in frontal boundaries in the Connecticut River outflow is thought to be a product of the parallel shear present at the frontal region (Huzzey, 1982).

The intensity of mixing in the frontal region can be quantified through the interfacial Froude number (Fr_i). Alternatively, a more refined method to express the effect of vertical velocity shear to overcome stability and cause mixing at the front or in stratified flow may be represented by the Gradient Richardson number (Ri_g).

$$Ri_g = -\frac{g}{\rho}\frac{\partial \rho}{\partial z}\left(\frac{\partial u}{\partial z}\right)^{-2} \qquad [2.4]$$

g = Gravitational acceleration (ms^{-2})
ρ = Density of surface layer ($kg\ m^{-3}$)
z = Depth (m)
u = Horizontal velocity (ms^{-1})

This ratio is specific to a stratified water column and can be quantified relatively easily through field observations. Laboratory observations by Miles (1961), Linden (1979), Thompson (1980) and Dyer (1988) suggest that for $Ri_g < 0.25$ shear is sufficient to overcome the effects of stratification, flow becomes unstable and this leads to mixing.

Reduction of the Ri_g number can be produced by the action of internal interfacial waves. Long wavelength interfacial waves cause a stretching of the interface and enhance velocity shear at the crests and troughs of the waveforms and are likely to be produced by turbulent instabilities in frontal regions and/or the interaction of flow with bottom topography (Dyer, 1988). Internal waves have been observed in estuarine studies by Maxworthy (1979), Chereskin (1983), New *et.al.* (1986) and New & Dyer (1988). More recently, and of specific interest to this study, a plume front has been observed with a turbulent 'rotor' at the foremost region of the front followed by a packet of internal soliton waves (Johnson & Weidemann, 1998).

The instabilities within the interfacial waves may grow and can form regular oscillations or Kelvin-Helmholtz (K-H) instabilities in the form of vortices that in the absence of turbulence either collapse or spread (Dyer, 1988). Instability due to the difference in density of the two layers leads to mixing or intense local shear in the vortex producing turbulence. Turbulence in one of the layers may interact with breaking waves causing a preferential transfer of water from a turbulent layer to a less turbulent layer. Averaged over time this process appears to be discrete but is, however, continuous and known as entrainment. It may be deduced that an interface can be eroded away by a turbulent layer at a vertical velocity equivalent to the rate at which dense water is injected into the upper layer.

The actual flux of turbulent momentum and passive scalar properties, or Reynold's fluxes, are represented by the terms, eddy viscosity (N_z) and eddy diffusivity (K_z) respectively.

These two quantities can be related to mean gradient properties of velocity and salinity or temperature and are useful in the description of turbulent mixing. However, to resolve these quantities in frontal regions that give a good representation of turbulent fluxes presents problems due to their continual fluctuation over both time and spatial locality. Several authors have managed to provide good estimates of turbulent properties when examining mixing processes in stratified flows and in plumes (Osbourne & Cox, 1972; Gregg, 1987; Wu *et.al.*, 1994).

The best theoretical solutions to date that have quantified mixing in and behind the front lie in the results and analytical solutions arrived at by Britter & Simpson (1978), Simpson & Britter (1979) and summarised in Simpson (1982). From experiments with physical models of gravity currents they arrived at a complex analytical solution to what they describe as a gravity head followed by shear generated K-H instabilities that are quantified through a critical Richardson number criterion proposed by Thorpe (1973). They established from laboratory results that the basic structure of a gravity current is not strongly affected by turbulent mixing and friction. Their observations of gravity currents, with tentative agreement from field studies by Pelegri (1988) and Lukitina & Imberger (1987), suggest that frontal velocity relative to the ambient fluid depends on the relative depth of the upper buoyant layer and the volume of flux entrained out of the gravity head. Gravity currents in the Britter & Simpson (1978) and Simpson & Britter (1979) experiments were typically composed of a small-scale head wave where density changed rapidly and a larger tail where density changes were subtler. The flux of water between the layers due to entrainment was established to be a weak function of the relative layer depth. Lukitina & Imberger (1987) suggested the presence of a turbulent core in the gravity head behind the plume front. This overturning of water acted as a ‘rotor’ which created a mixing layer. This layer extends some distance back upstream of the front and is thought to be a site of rigorous entrainment possibly dominated by overturning due to K-H instabilities (McClimans, 1988). Lukitina & Imberger (1989) report the best fine scale quantification of turbulence levels present in a plume front to date. Their studies showed through turbulence activity diagrams that energy bearing turbulent eddies were isotropic in the frontal nose and not affected by stratification due to intense velocity shear. In contrast, some distance inside the plume, behind the turbulent rotor, buoyancy effects became dominant and turbulent eddies were shown to become increasing anisotropic and of negligible energy.

Various other theoretical approaches to solving frontal dynamics were proposed by Garvine (1981, 1982, 1984) through a series of papers dealing with small-scale frontal processes. Garvine (1981) firstly developed a set of integral relationships that describe the change in flow properties across an internal hydraulic jump. The predominant method of obtaining solutions to the small-scale non-linear mechanisms was to employ the method of characteristics in the numerical integration of the governing equations. This avoided using complex primitive equations and excessive computational time. Boundary conditions for the frontal regions of these numerical investigations assumed a critical Froude number criterion, vertical entrainment, interfacial friction and a presumption of a 2-layer inviscid flow. The actual jump condition specified a relationship between ambient and plume flow velocities. Ambient water could modify the pressure and velocity field and layer thickness through convergence at the front. The model featured a partitioning of the upper flow field into two domains. The first is a frontal domain where the dissipative effects are concentrated and horizontal gradients are very high, and secondly, there is an internal wave domain where these effects are low. The jump conditions derived for the layer model accounted for the conservation of mass and momentum in the direction locally normal to the front. The author refers the reader to O'Donnell (1993) for a clear and uncomplicated explanation of his own and Garvine's various investigations into buoyant plume spreading by exploiting these methods.

Previous sections have hinted that the frontal region of river plumes has inherent non-linear dynamics and, therefore, forms complex internal features generated by internal-interfacial wave regimes. Internal features, as predicted in models used to simulate small-scale plume discharges, suggest the semblance of an internal bore(s) following the main frontal discontinuity. Garvine (1984) analysed the effect of constant radial fluid release from an estuary where there was no local mechanism (cross-flow) to arrest the discharge so that flow remained unsteady. Therefore, as in Garvine (1982), the longwave equations were hyperbolic and were solved through the method of characteristics. Assuming appropriate boundary conditions, an abrupt shallowing of the plume interface behind the gravity head and supercritical flow conditions suggested the formation of an interior hydraulic jump or bore on the plume interface behind the leading front. Fig 2.3 shows a schematic diagram of the predicted internal bore and its proposed mechanism of formation due to interfacial wave coalescence. Chapter 3 of this thesis gives a full explanation of the

Garvine (1984) model later used in the present study and the scale of the predicted internal feature.

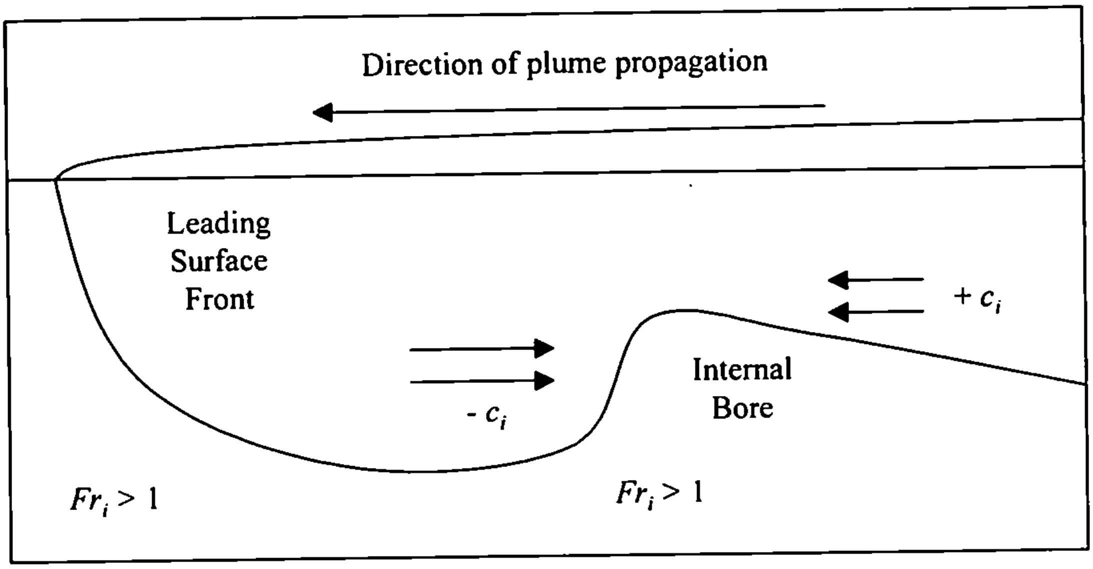

Fig 2.3: A schematic diagram of the predicted internal interfacial bore as predicted by the Garvine (1984) model.

O'Donnell (1988) extended Garvine's (1984) investigation through a radial release of buoyant fluid into a steady cross-flow. On this occasion, radial spreading was maintained in the early stages of development but an asymmetrical internal jump formed on the upstream side of the cross-flow. On the downstream side of the cross-flow, the plume continually thinned away from the source. Later experiments showed lower cross flow velocities allowed more radial spreading in the interior with a faster but thinner spreading layer inside the plume (O'Donnell, 1990).

The importance of establishing whether these internal features exist is crucial for modelling studies, as they govern the spatial and temporal extent of grid and time step resolution respectively that is required to simulate mixing processes in the frontal regions of plume discharges. As O'Donnell (1993) comments, "*The answer to this question is an adequate description of turbulence generation, transport and dissipation in the neighbourhood of the front*".

2.9 Summary

The physics inside plume fronts determine the rate and extent of a spreading plume and the structure of the water column within small-scale plumes or near field regions of larger scale estuarine plume discharges. Frontal mixing processes that control the rate of vertical mixing within a confined area of the plume appear to singularly provide the most intense mechanism in plume discharges for the dispersion of the freshwater in the coastal zone.

However, this literature review has highlighted the fact that few field investigations have examined the form and effects of mixing and friction in the frontal regions of estuarine discharges. Hence, the aim of the current project is to provide a qualitative and quantitative study into frontal mixing through both observational work and numerical simulations of a radially spreading plume. Hopefully, by using the results collected from instrumentation capable of resolving the smaller scale hydrodynamics and mixing processes present in a plume, a combined modelling-observational study should help clarify some of the outstanding questions on small-scale plume frontal mixing dynamics and lead to a better understanding of their larger scale counterparts.

Chapter 3

Preliminary Fieldwork & Numerical Modelling

3.1 Introduction to Field Site

The current study examines the dynamics of a small estuarine outflow plume from the River Teign at Teignmouth, Devon, in the UK. Freshwater input into the Teign Estuary drains from the upland region of Dartmoor. The catchment area of the Teign basin is approximately 380 km^2 with additional inputs from the River Lemon and River Bovey. Fresh water flow rates into the estuary are highly variable being dependent on seasonal rainfall. Environmental Resources Ltd (1990) quote freshwater inflow rates varying from 2 to 200 m^3s^{-1} for drought and extreme storm conditions respectively. The estuary discharges freshwater into Lyme Bay, a region of the English Channel via a small tidal basin where a large central sandbank known as 'The Salty' interrupts the free flow of water to the mouth. The tidal regime at Teignmouth is semi-diurnal with mean spring and neap tidal ranges of 4.2 m and 1.7 m respectively at the mouth of the estuary. An overall progression of tidal distortion is observed further up the estuary. The narrow mouth of the estuary or the 'Point' obstructs and funnels the outflow causing a departure from coastal tidal curves inside the estuary and abrupt changes in phase from ebb to flood tide. Currents at the mouth of the estuary off the Point are typically in order of 2 ms^{-1}, 0.3 m above the bed at mid-ebb and mid-flood (Robinson, 1975). Outside the estuary mouth, a complex shifting sand bar continually changes bottom topography. This area of the inlet channel is in need of frequent dredging to maintain an open shipping lane.

3.2 Motivation of Study

The most distinguishing physical feature of this freshwater outflow is the formation of an almost radially symmetrical plume that is discharged on the estuary's ebb tide. Plate 3.1 shows the brackish water plume spreading offshore, bound by a strong frontal convergence. The plume remains attached to the source mouth throughout the estuary's ebb cycle.

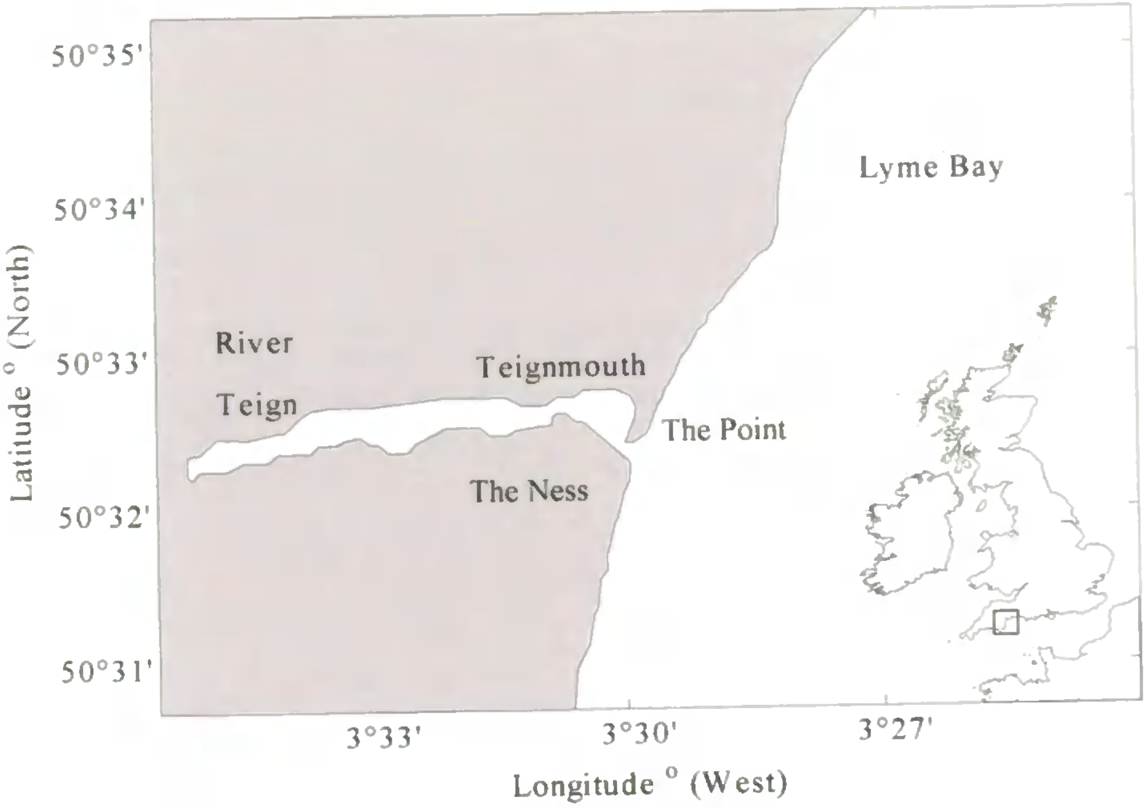

Fig 3.1: Geographical location of the study area with respect to the UK mainland.

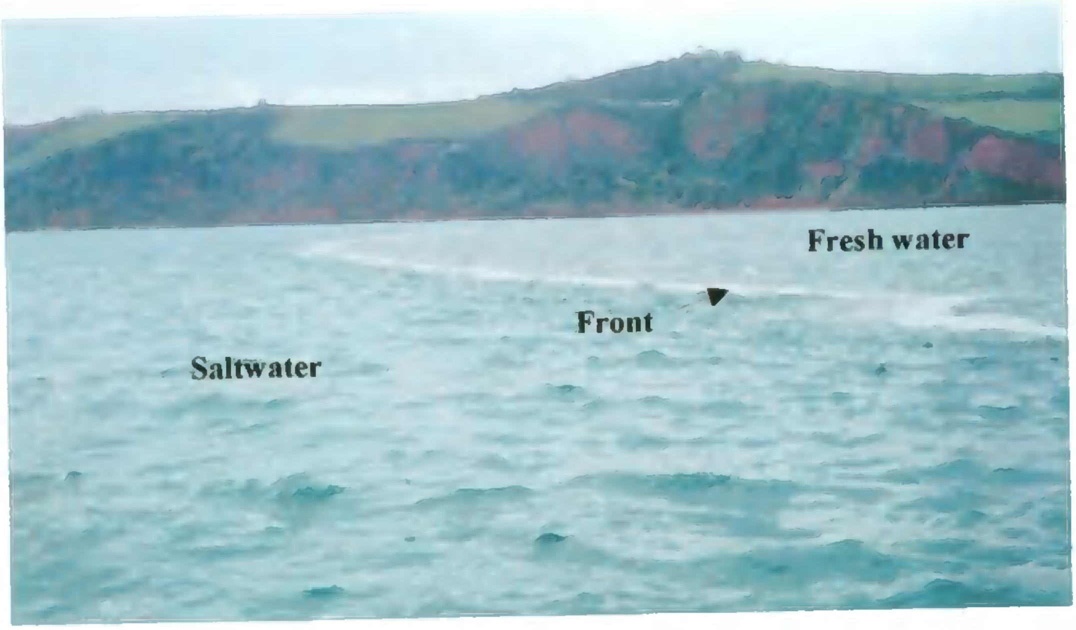

Plate 3.1: Photograph of the convergent foam line and spreading plume outflow from the Teign estuary on the 25th November 1998.

The formation of a radial plume and its colour contrast with surrounding Lyme Bay water are strongly correlated with runoff rate, sediment load and sea state. The effect of tidal currents on the spreading and dispersion of the fresh water in the locality of the bay are considered in later Chapters.

3.3 Preliminary Experiments

The first specific scientific studies of the Teign River Plume were carried out in 1993 and 1994 by Matthews (1997) and by staff from the Institute of Marine Studies, University of Plymouth (IMS) in March 1995. The latter study was a multidisciplinary approach that looked at the basic plume structure and dynamics and the optical properties of the water column as well as at sea surface films in the plume outflow. These experiments included a significant contribution from Southampton Oceanography Centre (SOC) who provided the X-band radar imagery of the plume outflow discussed in a later section of this Chapter.

Although this author was not involved with the 1993, 1994 and 1995 surveys, this section provides a brief recap and general description of the previous work. The survey results of 1993 and 1994 are described in Matthews (1997). Surprisingly, the best-defined plume fronts were observed on a flood tide, a feature that is counter intuitive to expectations of a gravity driven flow on the ebb tide. The formation of outflow fronts on the flood phase is not thought to be a regular event by this author. Judging by the paucity of Matthews (1997) data due to problems with instrumentation, low runoff conditions and an over ambitious sampling protocol, a full spreading cycle was never properly surveyed. Her observations could suggest that residues from the previous ebb tide outflow were observed on this occasion. The depth of the frontal zone was recorded as greater than 3.5 m which contravened expectations of a much shallower feature. This was probably produced by the flood current strengthening the definition of the front by restricting gravitational spreading. Local knowledge and subsequent surveys suggest that the plume outflows dominate on the ebb tide and only tentative conclusions can be drawn from Matthews' (1997) study of the plume.

The observations made in March 1995 provided excellent data on plume spreading rates and plume spatial development. However, the vertical structure of the plume was again difficult to confidently resolve due to instrument problems and a limited data set. A brief account of the instrumentation and experimental protocol follows.

3.3.1 1995 X-band Radar & Survey Results

The main use of marine radar is to detect obstacles at sea, aiding the safe navigation of shipping. Targets are displayed on a Plane Position Indicator (PPI) as a microwave backscatter return or a sequence of pulses from a rotating antenna. Once a target is detected, range and azimuth angle can be calculated. The signal below a threshold level is considered noise and, in the case of the sea surface signals, called sea clutter. Sea clutter has been studied extensively by engineers so that filters could be designed to eliminate this unwanted signal from the PPI. The physical processes that cause sea surface clutter are still not fully understood but are generally accepted as a product of Bragg resonant scattering produced by sea surface roughness. Ripples on the sea surface cause constructive interference with electro-magnetic waves when wavelength $\lambda = 2L\cos\theta$, where L = wavelength of surface water wave and θ = incident angle of the water wave with the transmitted wave. For ground waves where electro-magnetic waves strike the sea surface at grazing incidence the Bragg resonance condition is $\lambda_{sea} = \lambda_{radar} / 2$. The importance of the Bragg scattering mechanism is that when properly adjusted, radar can be used to study a particular selected wavelength component of a chaotic pattern of waves on the sea surface. The major disadvantage of this technique is use of the PPI 2-bit resolution (M.Tenorio, SOC, *pers.comm.*). However, the WAVEX operating system used by workers at SOC effectively digitises the raw signal of the radar into 8-bit resolution. This enhancement in resolution greatly increases the potential of the X-band radar to detect sea surface features that relate to physical processes where apparent changes in sea surface roughness are present. The immediate application of X-band radar in the study of river plume dynamics was to map changes in sea surface roughness in frontal zones due to water mass convergence, wave-current interaction and wave breaking (Lyzenga, 1991, Johannesen *et.al.*, 1991, 1996; Nilsson & Tildesly, 1995; Marmorino *et.al.*, 2000). As the range on the instrument is known precisely, images can easily be scaled and co-ordinates transferred to map references. This made it possible to assemble a spatial and temporal record of plume development over various ebb tidal cycles when the X-band was deployed at Teignmouth in 1994 and 1995.

Plate 3.2 presents an example of a time series of X-band radar captures of the ebb plume recorded on the 7th March 1995 where local HW was at 09:28 GMT. All images were produced by averaging 64 raw capture images, where one raw image was acquired for every (2.4 s) rotation of the radar and total capture time lasted (64 × 2.4 s) 2.5 minutes. Image averaging reduced the wave speckle and enhanced the plume edge signature. The X-band radar was sited approximately 1 km north of the river mouth at 50°32.94′ North, 3°29.34′ West, 80 m away from the beach on a 20 m high platform. The maximum range of the radar was set at 3750 m on the 19th November 1994 and 3810 m on the 3rd and 7th March 1995. With azimuth coverage of 180°, it was possible to map the entire plume through the majority of each spreading cycle. The best captures of the developing plume were recorded from 09:45 GMT to 12:15 GMT on the 19th November 1994 and 11:38 GMT to 13:54 GMT on 7th March 1995.

Plate 3.2: Time series of X-band radar images recording plume development on 7th March 1995. Imagery was made available courtesy of M. Tenorio and N. Ward, SOC. Images are corrected to UK OSGB National Grid.

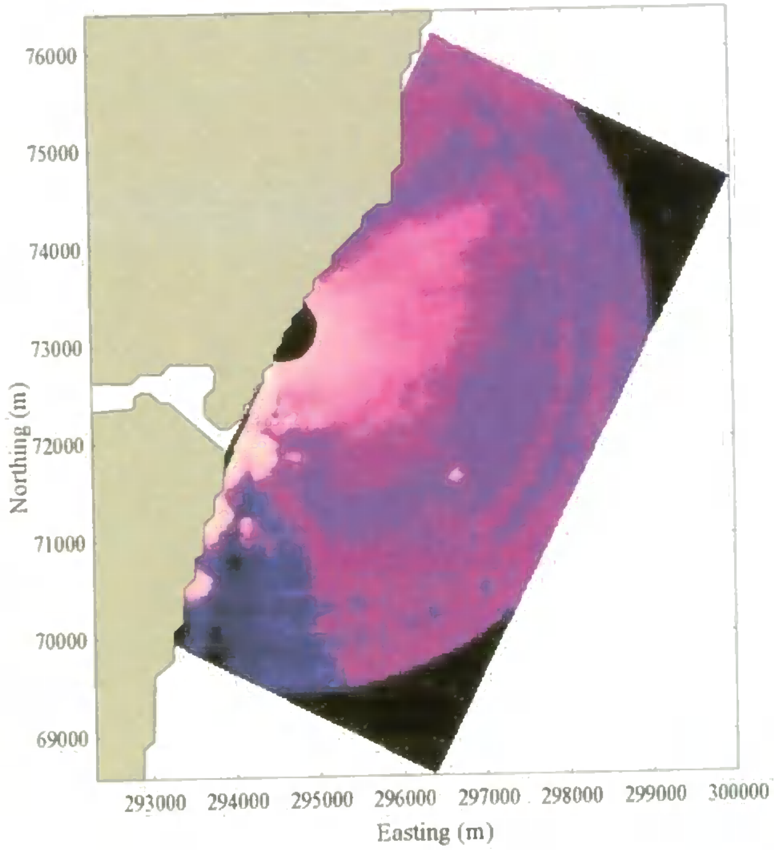
11:38 GMT (HW + 2:10 hours)

12:26 GMT (HW + 2:58 hours)

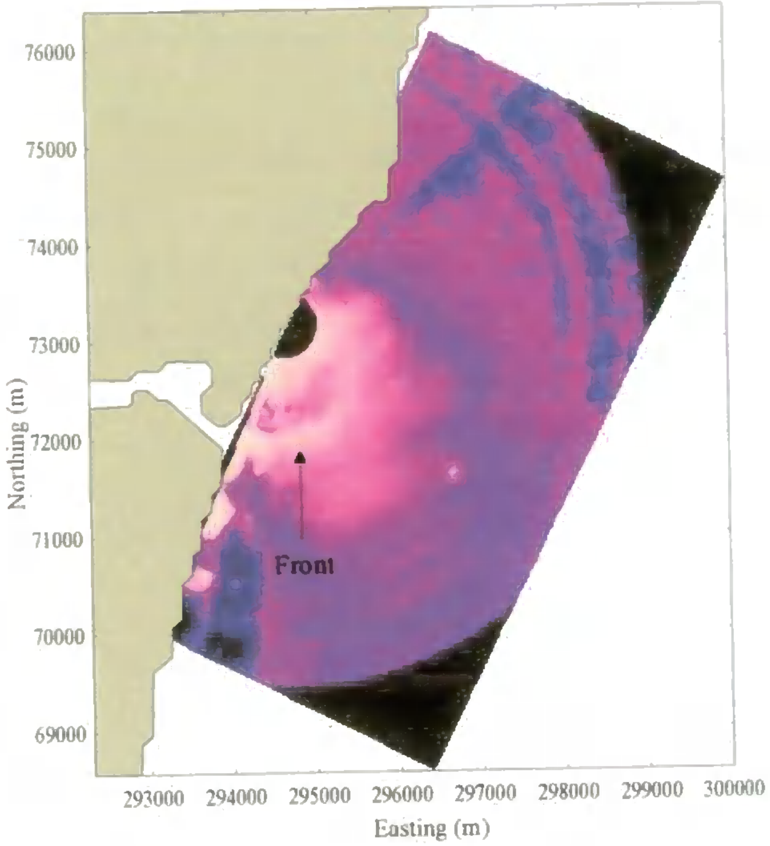

12:36 GMT (HW + 3:08 hours)

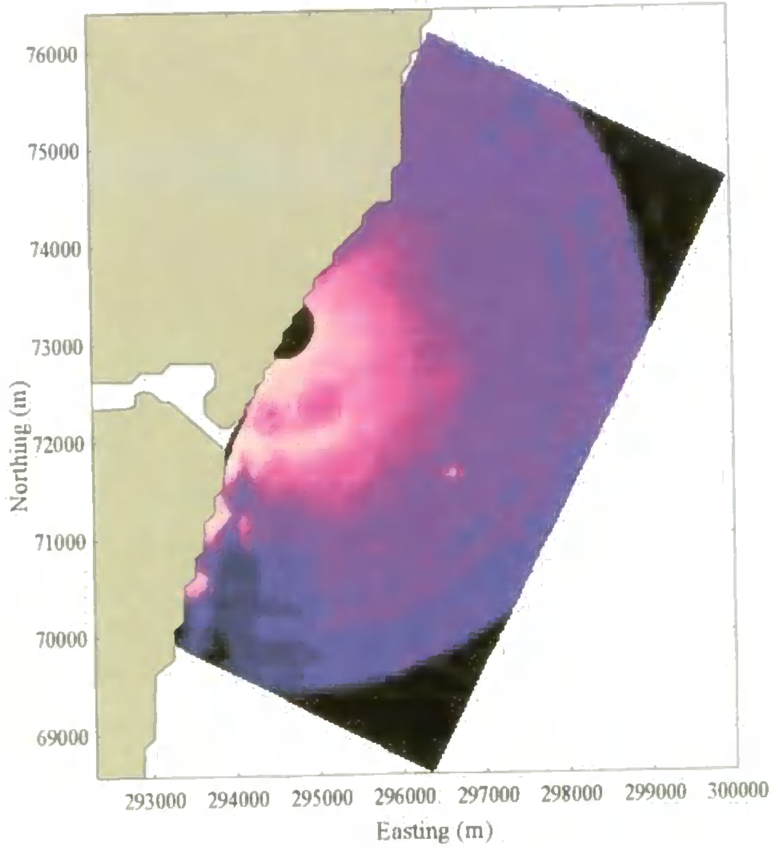

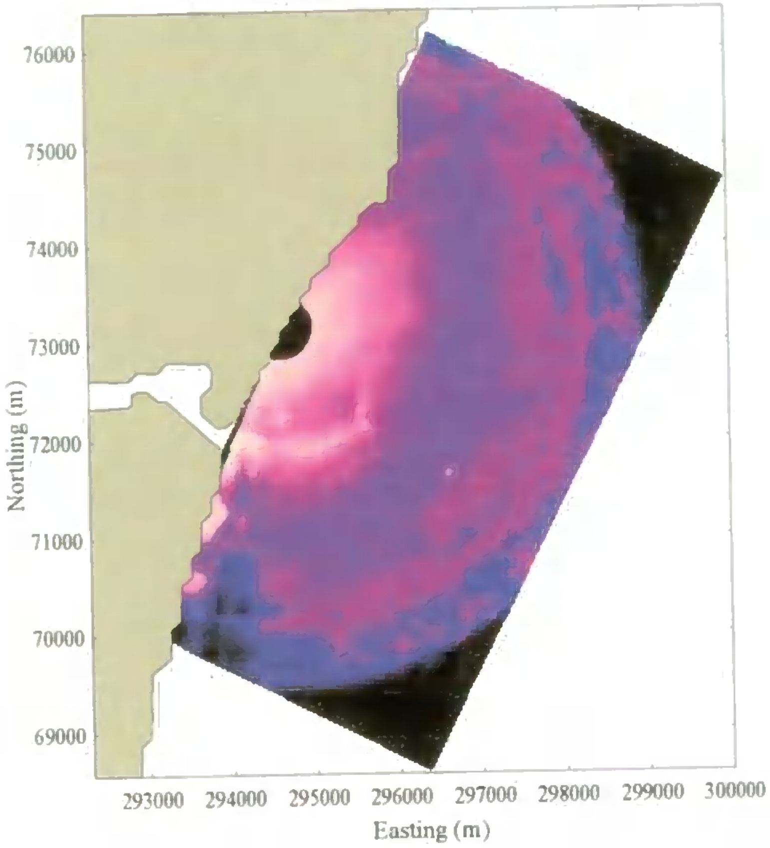
12:46 GMT (HW + 3:18 hours)

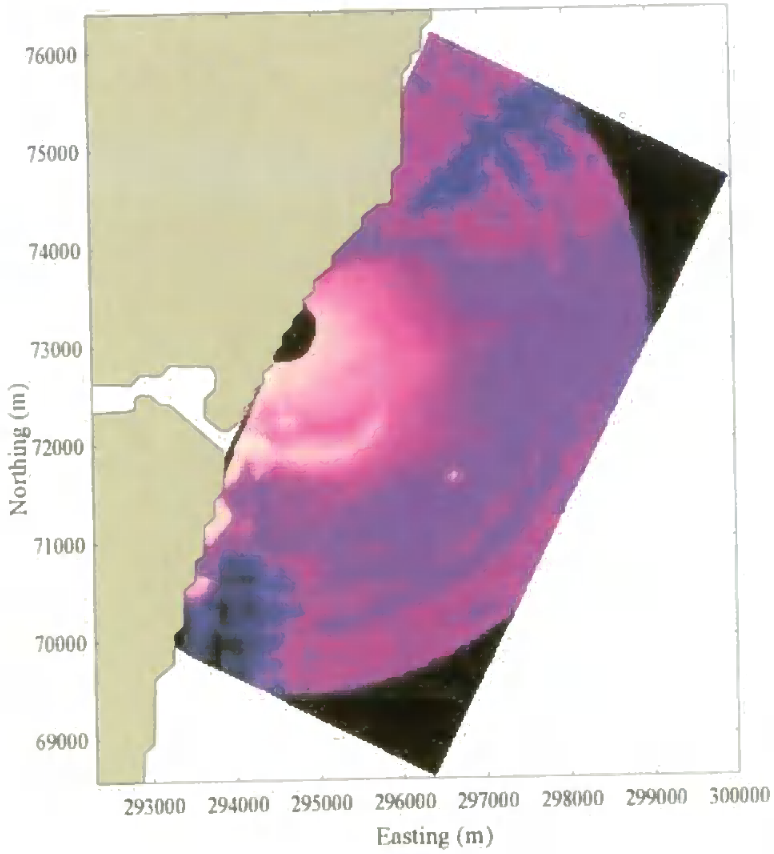
12:56 GMT (HW + 3:28 hours)

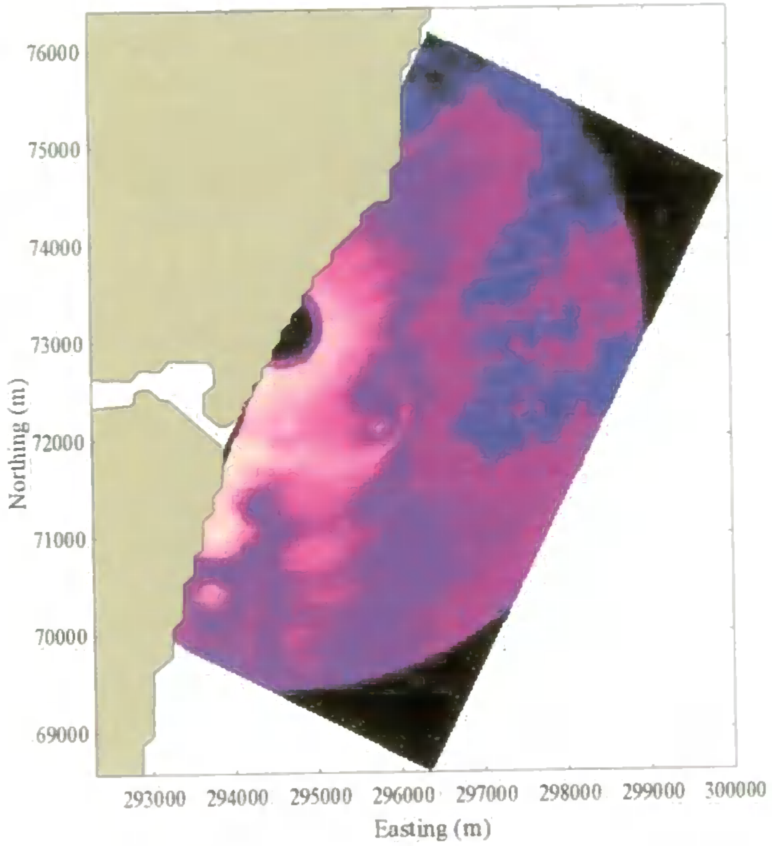
13:05 GMT (HW + 3:37 hours)

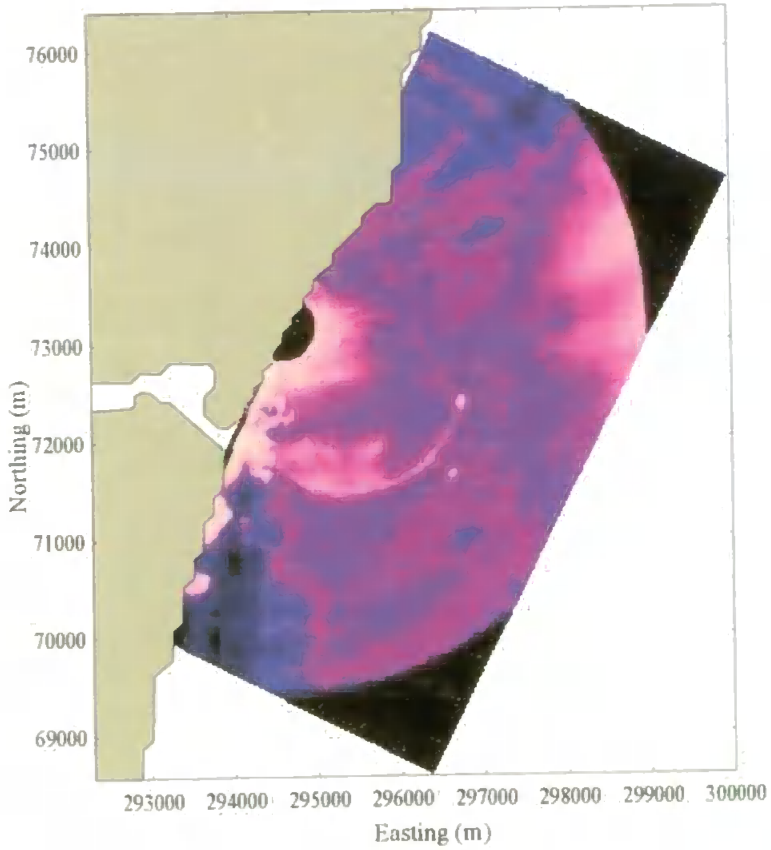
13:15 GMT (HW + 3:47 hours)

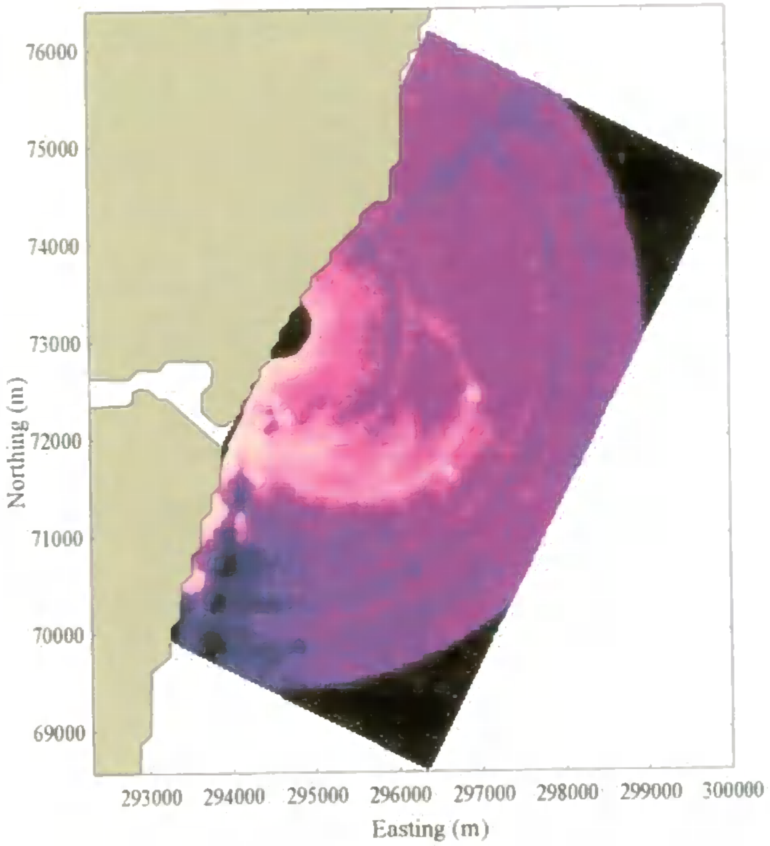

13:25 GMT (HW + 3:57 hours)

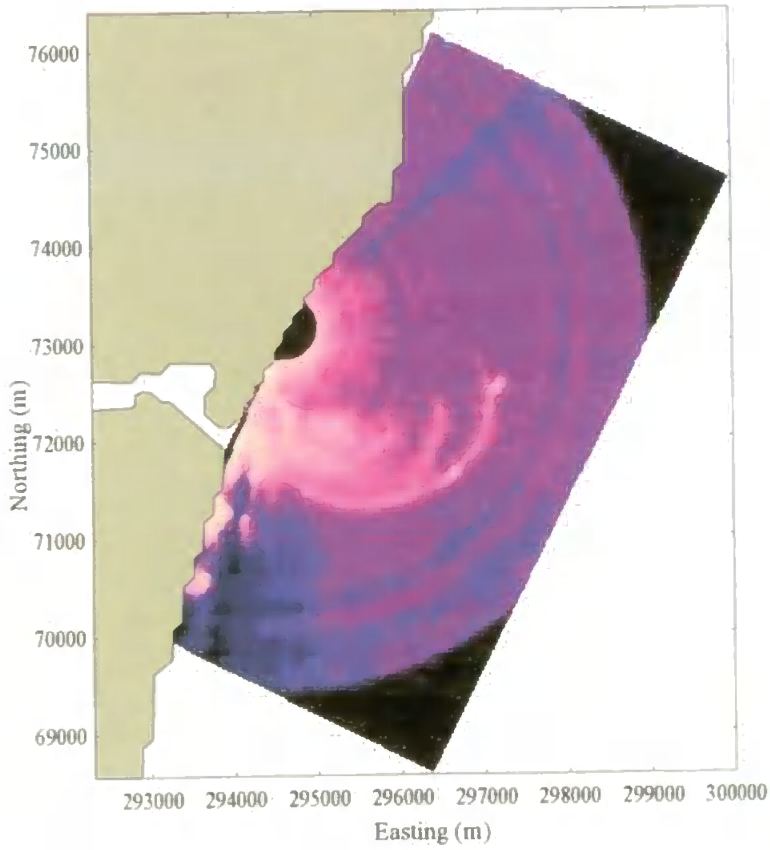

13:34 GMT (HW + 4:06 hours)

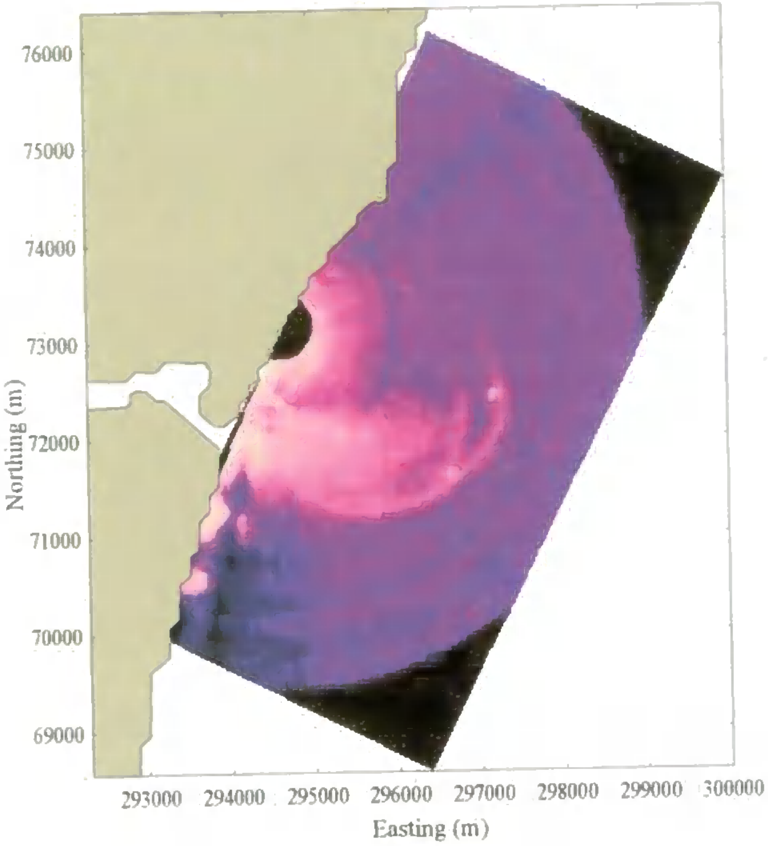

13:44 GMT (HW + 4:16 hours)

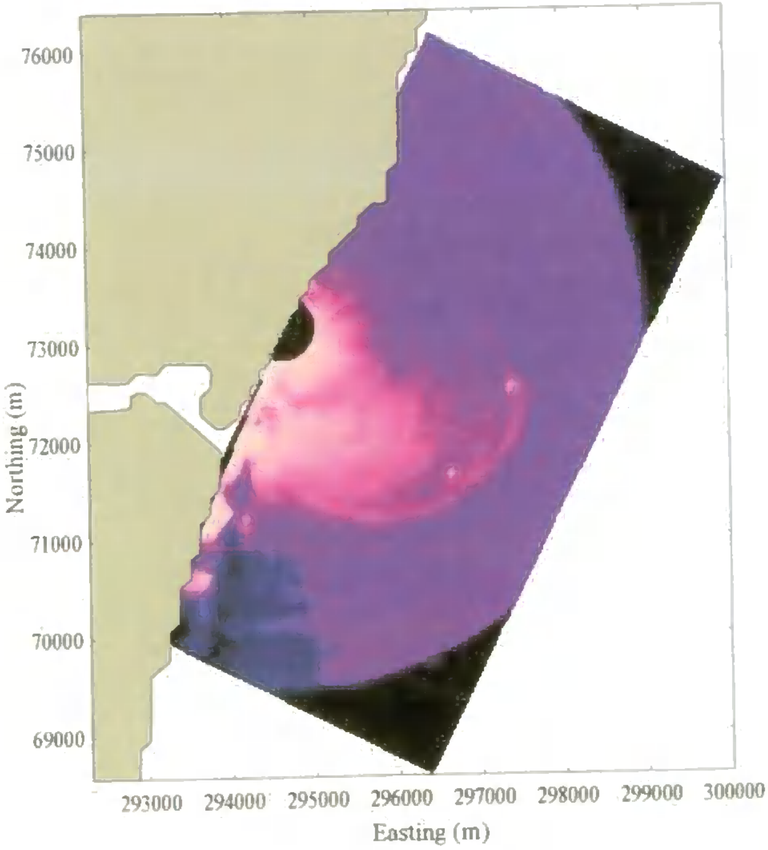

13:54 GMT (HW + 4:26 hours)

The frontal perimeter of the spreading plume first appears in the captures at 12:26 GMT (HW + 2:58 hours) as a white semi-circular line (labelled on the plate). This line in the imagery effectively represents the boundary or frontal region of the spreading plume that encompassed the brackish water lens being discharged from the estuary on the ebb tide. In addition, the permanent feature in each image to the south of the estuary is 'The Ness' headland and also the research vessel making measurements on the plume edge becomes visible on the third image to the east of the estuary mouth. The X-band time series illustrates the gradual expanse of the plume and the retention of its radial symmetry about the source through the estuary's ebb tidal cycle.

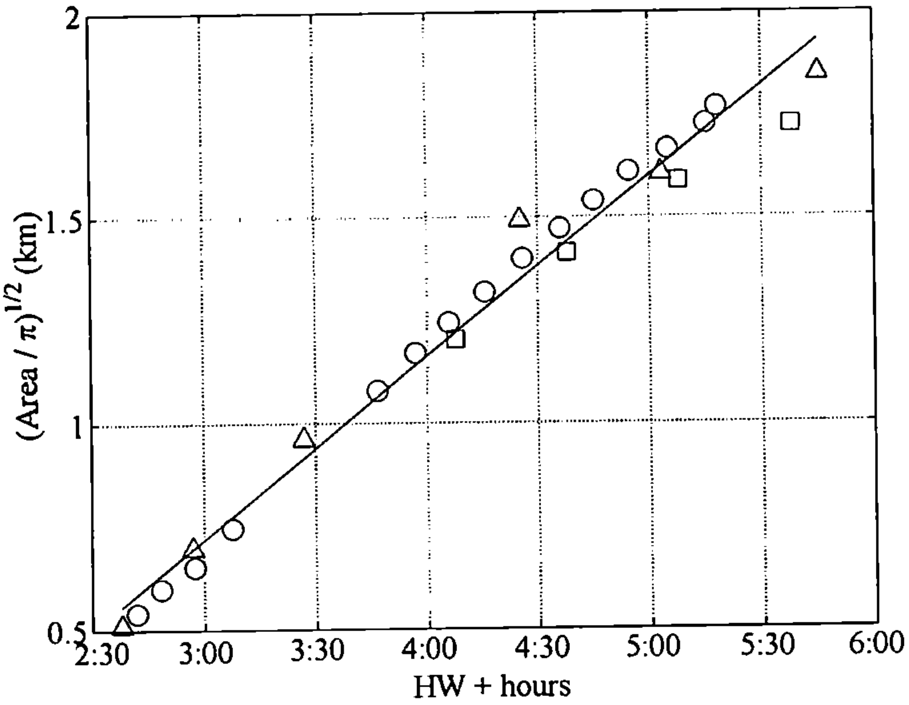

Fig 3.2: Plume effective spreading radius (km) vs. time (local HW + hours) as calculated from the area development captured in X-band radar imagery. □ = 19th November 1994; Δ = 3rd March 1995; O = 7th March 1995.

The rates of radial spreading were calculated from the X-band radar images by scaling each image by the radar range limit and the time intervals between captures of the frontal boundary. The area of the developing plume was then computed for each individual image capture for each three sets of images by calculating the area encompassed by the plume front. Fig 3.2 illustrates the subsequent results from the analysis of the three sets of images, where time is with respect to local HW. The effective radius of the plume was computed by (Area / π)$^{1/2}$. Fig 3.2 illustrates a good agreement between the rate of radial spreading for the separate outflow events. Simple linear regression analyses of radial distance (km) on time (hours) estimates the linear spreading rate as 0.45 kmh^{-1} or 0.13 ms^{-1} ($R^2 = 0.98$). A similar spreading rate of 0.12 ms^{-1} was also observed in the plume discharge from the Tees estuary by R. Lewis (Brixton Environmental Laboratory, Zenica Ltd., Devon, UK, *pers.comm.*).

Due to anomalous noise present in the CTD data collected on 3rd March 1995, the spatial and vertical physical structure of the plume could not be confidently resolved, despite using various methods and numerous attempts to solve the instrument noise problem. Thus, the simultaneous velocity measurements made with NBA current meters were alone insufficient to quantify mixing and stability inside the plume in terms of the Richardson and Froude numbers. However, sparse but more successful *in situ* observations were made on the 7th March 1995. CTD and NBA current meter casts recorded vertical salinity, temperature and velocity profiles from a survey vessel at three-fixed anchor stations during the plume outflow period. A summary of station position and time is presented in Table 3.1.

Fig 3.3 shows the position of each sampling station with respect to the estuary mouth. Spatial position and the extent of plume spreading as calculated from the X-band radar imagery is also projected on to Fig 3.3. Station 1 was situated in a water depth ranging from 5.2 to 4 m during the ebb and a series of CTD casts recorded the passage of the plume. The same protocol was applied at Station 2 at a depth of 11.5 m. Only a single CTD cast and velocity profile was made in the plume at Station 3 in a water depth of 17.6 m.

Station	Position	Distance offshore (m)	Start time (GMT)	End Time (GMT)	HW + hours
1	50°32.25′ N – 3°29.44′ W	658	11:01	12:01	1:33-2:33
2	50°32.26′ N – 3°28.51′ W	1759	12:19	12:54	2:53-3:26
3	50°32.42′ N – 3°27.19′ W	3314	13:42	13:46	4:14-4:18

Table 3.1: Summary of station positions and time (local HW: 09:28 GMT).

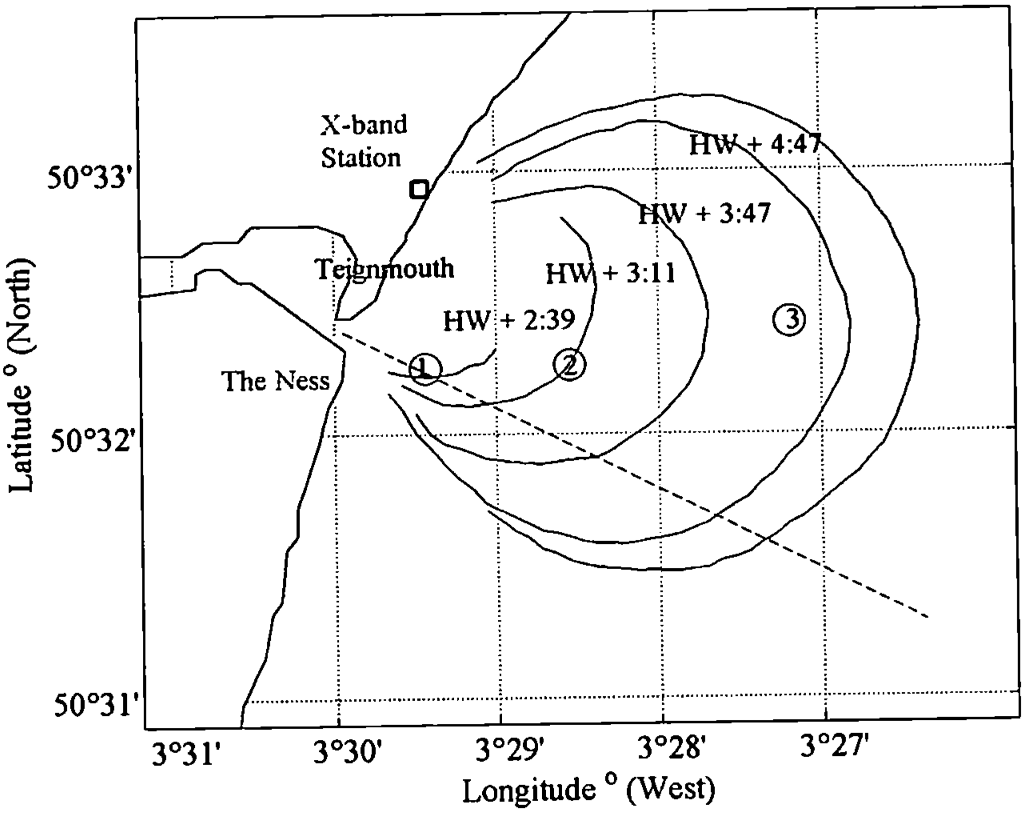

Fig 3.3: Map of study area including projections of plume development as estimated from X-band radar imagery and position and time (see Table 3.1) of survey Stations 1-3 on the 7th March 1995.

Fig 3.4a presents a time series of the densimetric interfacial Froude (Fr_i) numbers estimated from the X-band radar radial spreading speed, surface layer depth (h_1) averaged NBA current meter readings and CTD casts recorded on the 7th March. In addition, the parameters c_i, g' and h_1 computed for each cast are also shown in Fig 3.4a and Fig 3.4b. CTD casts recorded the presence of homogenous coastal water at the start of sampling at Station 1 (HW + 1:33 hours) and are, therefore, not shown in the figures. The time series shows how Fr_i increased to super-critical levels on passage of the plume front. The high Fr_i values of > 3 computed at HW + 2:10 hours are due to a low interfacial wave speed c_i due to a small density anomaly shown through g' and shallow interface h_1. Through examination of the X-band radar captures, the author is cautious in the interpretation of these results and is not entirely convinced that the CTD was profiling inside the plume front proper when these recording were made.

Fr_i number calculated at HW + 2:30 hours from the X-band radar of $O(1.3)$ are far more reasonable, yet the Fr_i estimate from the NBA layer averaged current is again high. This trend is displayed throughout all the calculations and is probably caused by erroneous velocity data due to movements in the survey vessel and insufficient averaging (settling down) periods when profiling. Fr_i numbers computed from the X-band radar showing super-critical flow $O(1.3)$ on passage of the front and sub-critical values inside the plume after the front's passage inside a stable 2-layer flow.

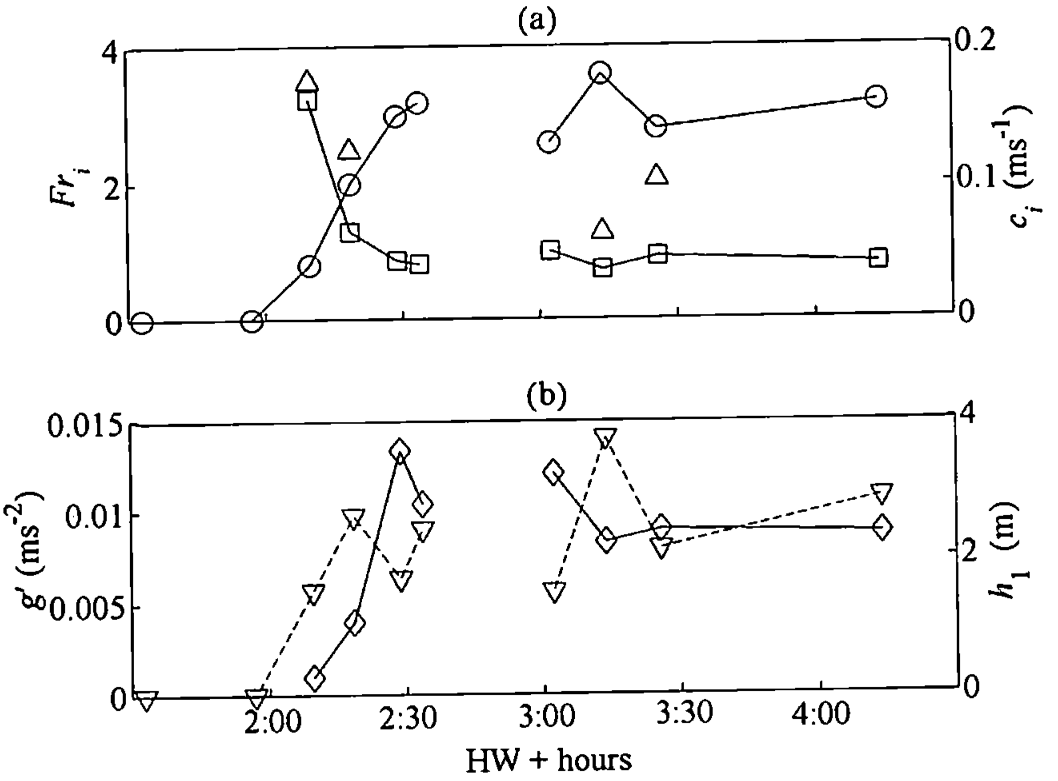

Fig 3.4: Time series (HW (09:28) + hours) of (a) Fr_i values estimated from both X-band radar spreading speed and in-situ current meter profiles and c_i on the 7th March 1995 (b)The parameters g' and $h_1$and used in the Fr_i computations. □ = Fr_i from X-band radar spreading velocities; Δ = Fr_i from velocity profiles; O = Interfacial wave speed, c_i (ms^{-1}); ∇ = Reduced gravity, g' (ms^{-2}); ◇= Interface depth, h_1 (m).

3.4 Summary of Preliminary Results

At Station 2 homogenous water is again present at the start of sampling outside the plume. On passage of the front an $O(1)$ Fr_i number suggests critical flow at HW + 3:03 hours as the front propagates through the Station. At HW + 3:14 hours, sub-critical Fr_i values again signified a stable 2-layer flow. Fig 3.4b illustrates how the interface deepens as the front passes through the station front and then shallows as Fr_i numbers go sub-critical, possibly indicating the passage of a gravity head (Britter & Simpson, 1978). Only one CTD cast was made at Station 3 inside the plume. Water column structure appeared stable and continuously stratified with an interfacial depth of 2.86 m.

The current study was motivated by the findings of the earlier work conducted on the Teign river plume dynamics. Imagery from the X-band radar clearly indicated the frontal boundaries, mapping the entire form of the ebb plume discharge from the estuary on the 7th March 1995. The image time series illustrates the formation of a radial shaped spreading plume that remains nearly symmetrical around the source discharge. A linear radial spreading rate of 0.13 ms^{-1} was estimated by scaling images from each set of captures and calculating the equivalent radius from the area of dispersion.

The slight perturbations and increase in observed spreading rates after the initial formation probably concur with increases in g' and h_1 used in the determination of $2^{-1/2}\sqrt{g'h_1}$ the propagation speed of the front in shallow water (where $h_1 < z / 2$).

A wider aspect of these results is that it verifies the potential of radar as a viable remote sensing instrument for the detection of discharge plumes with strongly defined frontal boundaries (see Vogelznag *et.al.*, 1997). X-band radar is presently under continued development at the Proudman Oceanographic Laboratories (POL) and being used to study currents and tidal streams in the coastal zone (P. Bell, POL, *pers.comm.*).

Unfortunately, due to the lack of *in situ* CTD casts and uncertainty in current meter data, few conclusions on mixing dynamics can be drawn from this data. However, the Fr_i numbers calculated from the survey on the 7th March 1995 indicate the presence of an internal structure typical of a spreading plume as observed by Garvine & Munk (1974). Critical Fr_i numbers in the frontal region of the plume are followed by a deepening of the interface and a relatively quiescent sub-critical surface layer of brackish water from the outflow.

Results from these preliminary studies now allowed the development of hypotheses on the Teign plume dynamics and mixing through both numerical modelling and further observational work.

3.5 Larger Scale Dynamics of the Teign Plume

The data analysis of earlier observational work on plume spreading dynamics and the suggestion of an ebb tide dominated process prompted an investigation into local tidal phenomena and geostropic forcing in the region of the discharge. All tidal analysis preceded the development of hypotheses on plume dynamics and numerical simulations of radial plume spreading.

The subsequent sections on tidal hydrodynamics in the Teignmouth region aim to provide the reader with a synopsis of the larger scale tidal influence in the study region during November 1998, when current fieldwork was planned. This analysis is further refined and integrated into the present studies results during Chapter 4's discussion on plume front dynamics.

3.5.1 Estuarine Tidal Effects

A buoyant surface layer of brackish water arrives at the mouth of the estuary due to upstream freshwater input from the river(s). The water is then released into Lyme Bay via a narrow constricted mouth some 100 m wide, 500 m long and with a tidal mean depth of approximately 2 m between the Point at Teignmouth and the Ness at Shaldon (see Fig 3.1). On the flood tide, freshwater outflow is halted and a plume fails to form due to the tidal excursion into the estuary. It should be mentioned that no tidal intrusion front as described by Simpson & Nunes (1981) was observed inside the estuary. The absence of an intrusion front in the estuary implies either that the estuary is vertically mixed or any 2-layer stratified flow is sub-critical ($Fr_i < 1$). Wimpol (now Fugro Geos Ltd, 1989) recorded temperature, salinity and current speed from stations near the estuary mouth to 7.2 km upstream. Flood tidal intrusion was measured up to 6.8 km upstream and was found to be subject to spring-neap modulation, where spring tides penetrated the furthest upstream. Further downstream the water column appeared well mixed with some stratification occurring at local HW. Mean water levels were found to increase in the upper estuary due to the increase of river influence and, at times of high freshwater input, water level became significantly elevated with respect to the level downstream. Local knowledge (G.Allen, *pers.comm.*) also suggests a 'Freshet' of brackish water can be seen after high rainfall, due to sediment load being passively transported downstream towards the estuary mouth on the ebb tide.

Gill (1977) suggests that a subsequent narrowing of the outlet channel, as is the case at the 'The Point', Teignmouth, can cause a transition in the 2-layer outflow from sub-critical to super-critical flow ($Fr_i > 1$) in terms of the across-channel averaged hydrodynamic properties. This forms a typical control section for an hydraulic jump (Garvine, 1987). As the channel widens into Lyme Bay the surface layer depth decreases and the flow generates even higher super-critical speeds which allows the plume front to form outside the estuary. The duration of the lag period from local HW until the plume front forms depends on the volume of freshwater input and tidal asymmetry. Thus, the lag period remains variable, as both river runoff and the tides are susceptible to variability due to rainfall and local tidal forcing.

3.5.2 Tidal Hydrodynamics in the English Channel

The tidal regime in the English Channel is driven by a Kelvin wave propagating in from the Celtic Sea. In simple terms, the English Channel Basin responds as a half-wave length resonator with a nodal line between The Isle of Wight and Cherbourg (Huntley, 1980; Pugh, 1987). This produces maximum amplitudes in opposite phase at the two ends of the virtual basin which is bound by the Dover straits and the shelf edge respectively. However, Coriolis force and friction are important and the response of the basin tidal circulation may be described as a damped progressive Kelvin wave travelling north-easterly up the English Channel (Bowden, 1983). Large tidal amplitudes on the French coast are due to the Kelvin wave dynamics. Frictional dissipation and a leakage of energy into the southern North Sea make the reflected tidal wave much weaker than the in going wave. The superposition of the two waves reduces the notional nodal line to a degenerate amphidrome located some 25 km inland of the English coast (George & Buxton, 1983; Bowden, 1983; George, 1997). Generally, the tides in the southerly inshore regions of Lyme Bay are associated with moderately high tidal amplitudes and weak tidal currents.

The next section of the thesis analyses tidal data collected from two different sets of observations and uses the results to discuss the magnitude of tidal streams and the tidal circulation local to the Teign river plume discharge into Lyme Bay.

3.5.3 Local Tidal Analysis

In 1988, South West Water (SWW) commissioned an environmental impact analysis to access the effects of a sewage outflow approximately 1 Nm offshore from the mouth of the Teign estuary. Wimpol (now Fugro Geos Ltd.) collected tidal data for the EIA by deploying three Aanderaa Recording Current Meters (Aanderaa model RCM 3) in Lyme bay and two NBA DNT8 tide gauges, one inside the mouth of the Teign Estuary (TG1) and the other offshore (TG0) over a coinciding period during August- September 1988. Each RCM logged current magnitude and direction at a frequency of 0.17 Hz. The tide gauges recorded tidal height corrected to Ordinance Datum Newlyn (OND) at frequencies of 0.13 Hz. Wimpol provided the relevant tidal constituents for each respective mooring from least squares harmonic tidal analysis of the observational data.

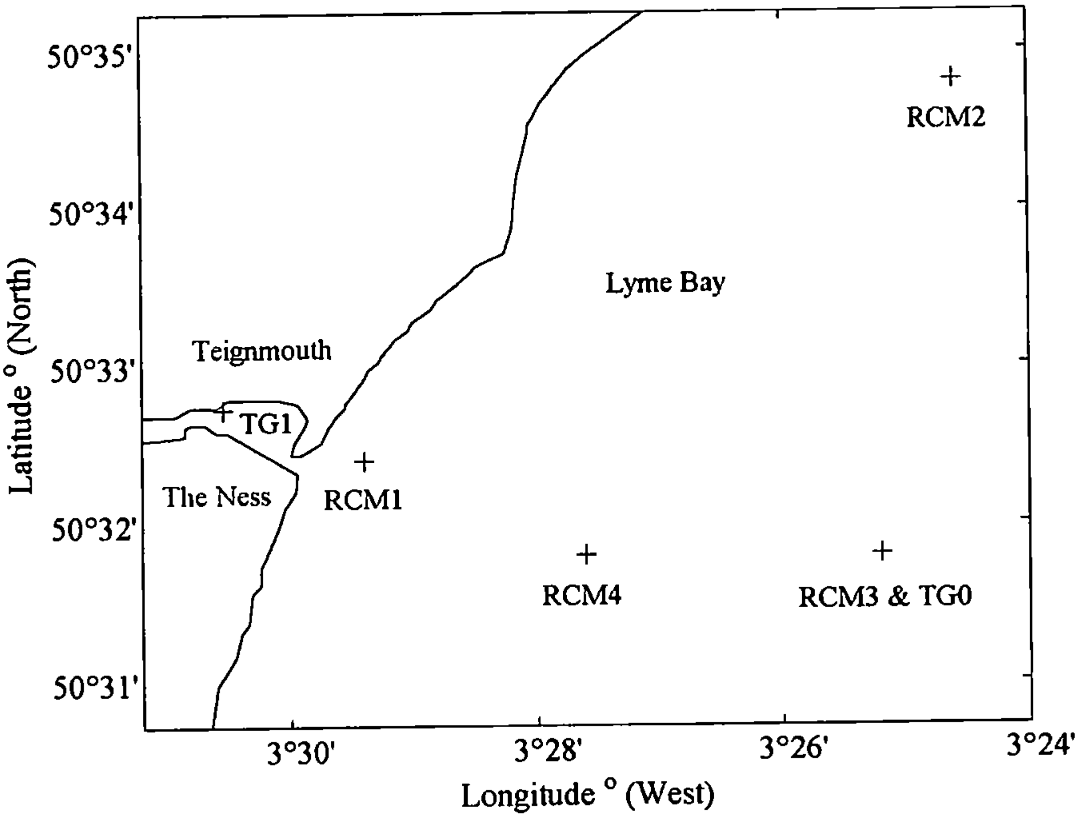

Fig 3.5: Geographical location of RCM current meter and tide gauge moorings.

The present author collected additional tidal current meter data using an Aanderaa RCM 7 Recording Current Meter moored in Lyme Bay during October 1997. This sampled the magnitude and direction of tidal currents at a frequency of 0.17 Hz. Directional data was corrected for true north and the vector current speed split into its *u* and *v* components. The harmonic constants for the 1997 deployment were calculated using TIRA, an in house least squares fitting package developed at NERC (Courtesy of Colin Griffiths, Plymouth Marine Laboratory). A summary of all mooring details and the geographical location of each current meter and tide gauge moorings are shown in Appendix 1 and Fig 3.5 respectively.

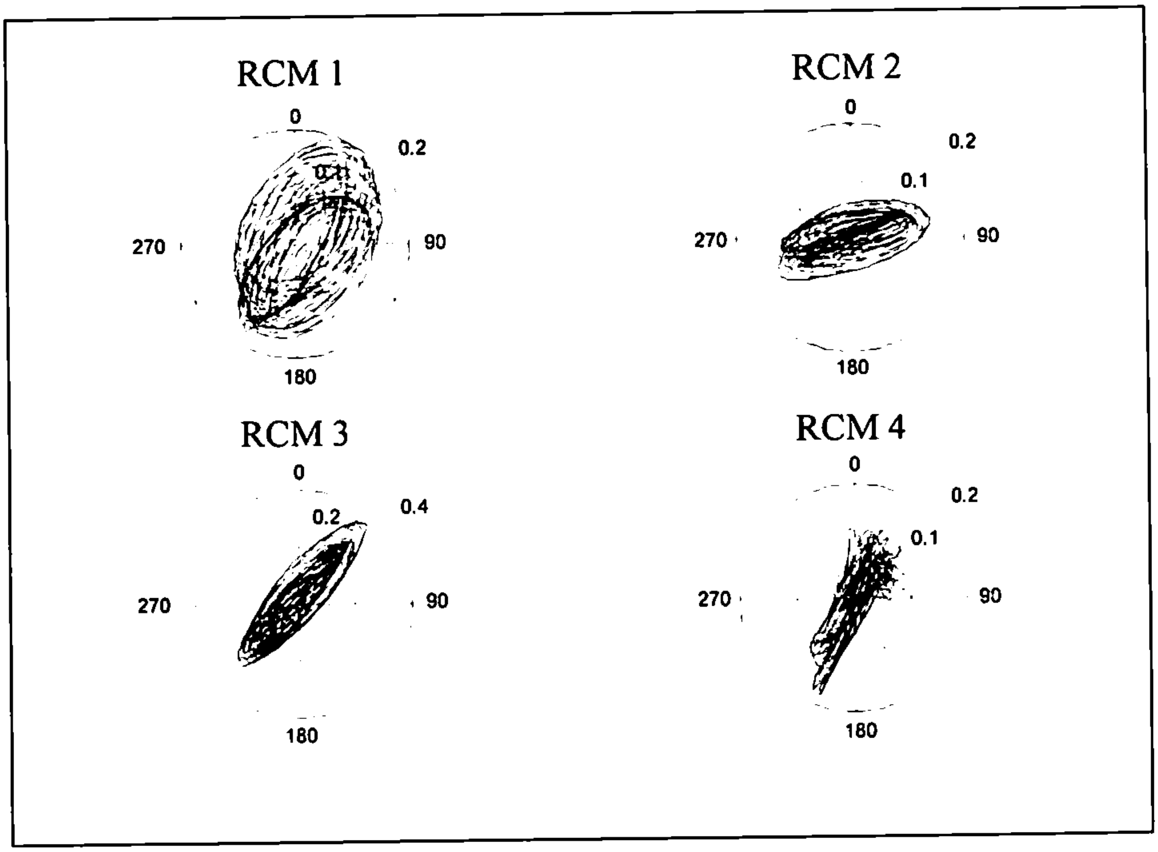

Fig 3.6: The predicted tidal current ellipses, *u* (ms^{-1}) vs. *v* (ms^{-1}) from the 1st November 1998 to 30th November 1998 at the sites of four RCM tidal current meter data moorings in Lyme Bay.

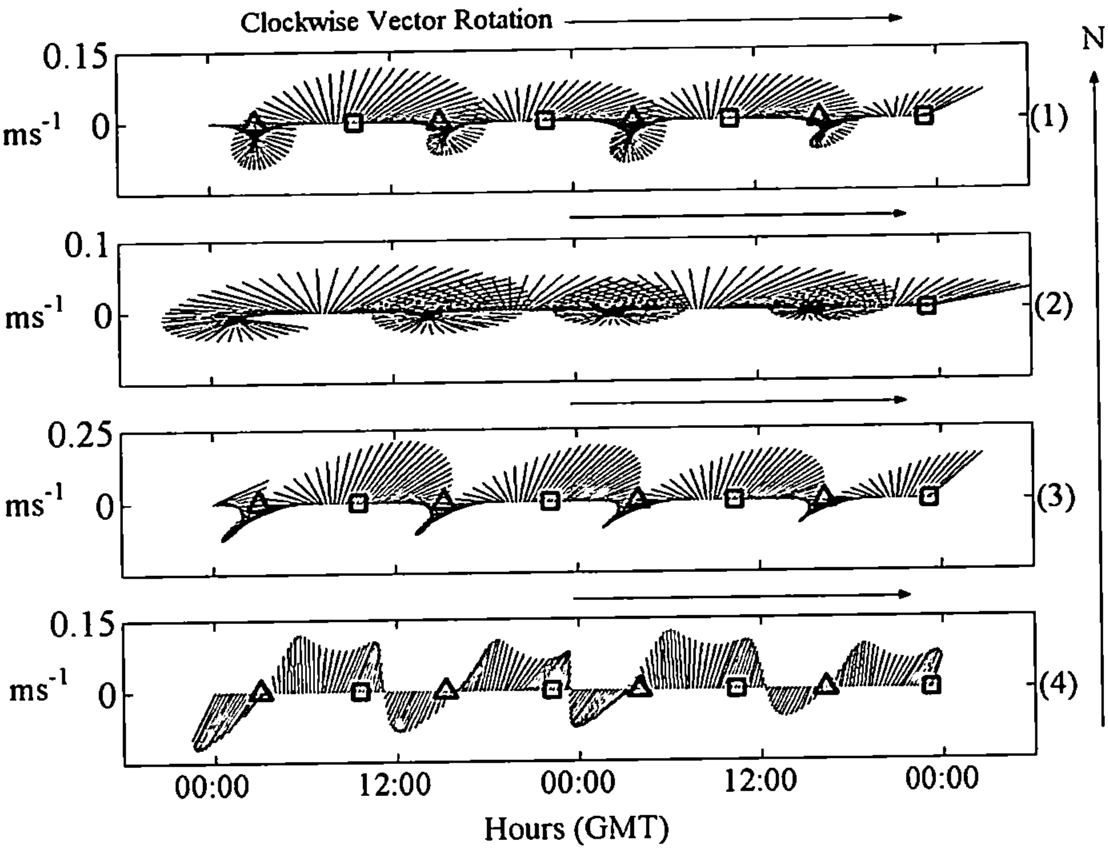

Fig 3.7: Predicted vector stick plots (ms^{-1}) vs. time (GMT) computed for moorings RCM 1-RCM 4 for the 25th and 26th November 1998. Δ = LW; □ = HW.

Fig 3.6 illustrates the four predicted tidal ellipses for tidal currents (ms^{-1}) computed from the harmonic constants for each respective current meter mooring from 00:00 GMT 1st November 1998 to 23:59 GMT 30th November 1998. Each prediction was calculated from an epoch time corresponding to the start of the least squares fitting procedure of the data (see Appendix 1). The precision of this procedure was considered acceptable as all the future tidal predictions were computed with double precision accuracy using MATLAB software (M. Fennessey, *pers.comm.*). The greater variability present in the RCM 4 ellipse (also reflected in Fig 3.7) is attributed to the processing techniques as the author is lead to believe that the 1988 Wimpol data underwent smoothing during processing before harmonic analysis (M. Fennessey, *pers.comm.*) whereas the 1997 data was processed in its original form.

The next stage of the analysis examined the consequences of siting the RCM moorings near the bottom boundary layer. Soulsby (1997) proposed a 1/7-power law vertical velocity profile to describe the effects of bottom stresses on boundary layer flows, where the depth averaged current u_{av} occurs at 0.32 times total water depth h. Through Soulsby's empirical relationship shown in Equation 3.1, it was possible to determine whether the difference in the measured current velocity and the depth-averaged current velocity was acceptably small ($\overline{u}_b \approx u_{av}$) or would require correcting. Transposition of Equation 3.1 and using the mooring details (mooring and total depth) shown in Appendix 1 suggested only RCM 4 would require correction. This correction was subsequently applied in order to obtain a better estimate of the true depth-averaged current and surface flow at this particular geographical location.

$$\overline{u}_b = \left(\frac{z}{0.32h}\right)^{1/7} u_{av} \qquad [3.1]$$

$\overline{u}_b$ = Mean velocity in the boundary layer (ms^{-1}) at height z (m)

z = Height of mooring above the seabed (m)

u_{av} = Depth averaged current (ms^{-1})

h = Total mean depth (m)

The orientation of the predicted tidal ellipses shown in Fig 3.6 clearly illustrates the rectilinear tidal streams at moorings RCM 2, RCM 3 and RCM 4. RCM 1, located just outside the mouth of the estuary, shows a rotation of the semi-major axis of the tidal ellipse from NNE to NE over the spring-neaps period and a generally greater eccentricity about the semi-minor axis. As anticipated, the magnitude of currents predicted at the positions of all moorings were small and rarely exceeded 0.25 ms^{-1} and 0.12 ms^{-1} over a spring-neaps cycle respectively. The rotational sense of the predicted currents over the flood-ebb cycle is better illustrated in Fig 3.7 as a series of vector stick plots. Predictions were made over a 48 hour period for the 25th and 26th November 1998 (dates coinciding with the present surveys and discussed in later chapters) for the geographical positions of each mooring. Results suggest the general trend of a weak, alongshore ebb tidal stream approximately 1 Nm offshore from the estuary that meanders in an easterly direction at the site of RCM 2. The stream is initially directed towards the NE on the 1st quarter of the ebb tide phase. During the 2nd quarter of the ebb, flow is directed due east offshore with currents being directed to the south of the bay during the latter half of the 3rd quarter and all of the 4th quarter. During the flood cycle easterly onshore flow above Teignmouth is directed alongshore towards the SW and rotates clockwise to form an onshore flow at approximately HW - 2 hours. The inshore mooring RCM 1, sited outside the estuary, was more susceptible to the influence of tidal discharge from the estuary and shallow water effects. The increase in eccentricity of the tidal currents around the semi-minor and semi-major axis is a reflection of estuarine outflow influence as noted by Wimpol (1989).

To examine the phase relationship between the tidal currents and sea surface elevation, the power spectra of the *u* and *v* components of current plus the spectrum of tidal elevation (ς) recorded at mooring RCM 4 were computed and are displayed in Fig 3.8. Peaks in the power spectra at frequencies (cycles d^{-1}) that coincide with M_2 and S_2 periods illustrate the semi-diurnal domination of the tide. Calculation of the co-spectrum and coherence show how the tidal currents are phase locked with sea surface elevation, with a phase near 0°. This phase relationship confirms the progressive nature of the tidal wave in the locality of the plume discharge. Despite semi-diurnal domination of tidal forcing, higher harmonics present in the power spectrums at higher frequencies are suggestive of the shallow water effects on tidal modulation in this region of Lyme Bay.

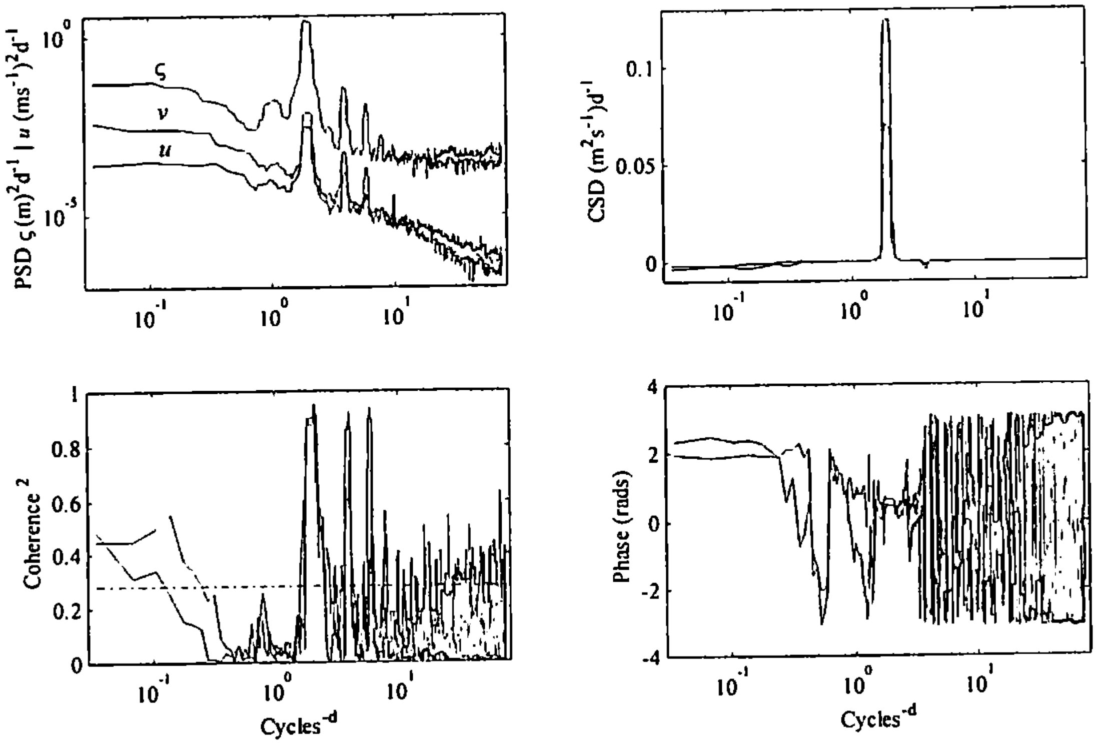

Fig 3.8: Summary of frequency domain analysis of Mooring 4 RCM velocity and tidal elevation data (see Section 4.2 for spectral analysis methods). PSD = Power Spectral Density; CSD = Cross Spectral Density.

No current meter records were available for the inside the mouth of the estuary where the plume originates. G. Allen (*pers.comm.*) suggests currents through the narrows could be in the order of 3 to 4 ms^{-1} on the ebb cycle of high tides. To estimate the magnitude of longitudinal flow through the mouth, a simple dynamical model based on barotropic forcing and bottom friction was applied to the outlet. The model, based on the work of Campbell *et.al.* (1998), assumes that the frictional effects of a narrow rectangular channel balance the flow driven by the pressure gradient force (PGF) due to the difference in sea surface elevation (ζ). Fig 3.9 shows a schematic diagram of the proposed model and the corresponding derivation of the governing equations.

Continuity can be expressed as: $A_b \frac{\partial \zeta}{\partial t} = \hat{u}bh$ for a rectangular channel [3.2]

By integrating the linearised equation of motion from the seabed to the surface and expressing the bottom stress through a quadratic drag law the simplified force balance for the channel is:

$$\frac{\partial \hat{u}}{\partial t} = -g\frac{\partial \zeta}{\partial x} - \frac{C_D|\hat{u}|\hat{u}}{h} \approx 0 \qquad [3.3]$$

$$\frac{\Delta u}{\Delta t} = -g\frac{\Delta \zeta}{\Delta L} - \frac{C_D|\hat{u}|u}{h} \approx 0 \qquad [3.4]$$

Assuming ΔL is the length of the channel and $\Delta\zeta$ is the difference in sea surface elevation between the estuary basin and the open sea it follows that:

$$\hat{u}|\hat{u}| = \frac{-gh}{C_D L}(\zeta_0 - \zeta) \qquad [3.5]$$

The velocity, $\hat{u}$ through the channel can be then calculated from Equation 3.6:

$$\hat{u} = \left(\frac{gh}{C_D L}|\zeta_0 - \zeta|\right)^{\frac{1}{2}} SGN(\zeta_0 - \zeta) \qquad [3.6]$$

A_b = Area of basin (m^2)
b = Breath (m)
$\hat{u}$ = Velocity (ms^{-1})
C_D = Drag coefficient (0.0025)
L = 500 m (length of channel)

ζ_0 = Tidal elevation outside of basin (m)
ζ = Tidal elevation inside basin (m)
t = Time (hrs)
$h = h_0 + ½(\zeta_0 - \zeta)$ (m)
h_0 = 2 m (mean inter-tidal depth)

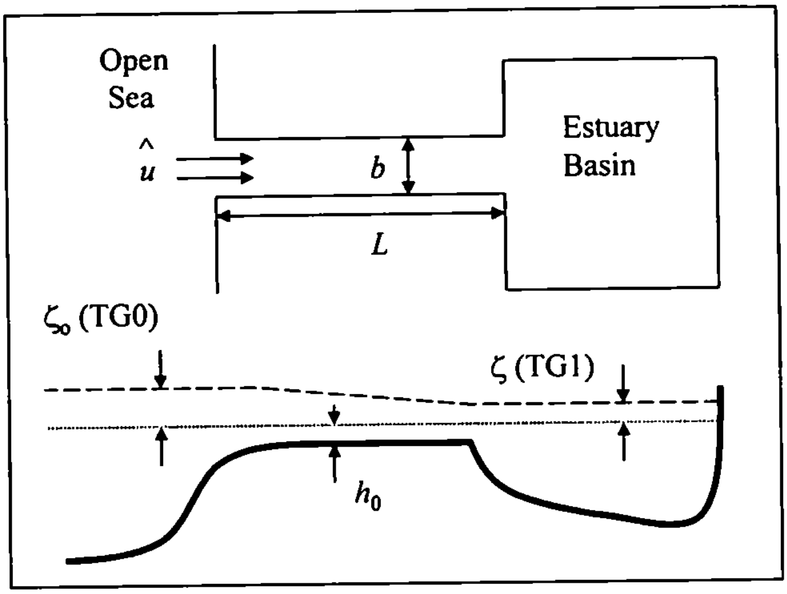

Fig 3.9: Schematic and derivation of equations for a simple model based on Helmoltz tidal pumping from a choked estuarine outflow.

The tidal elevation input into the model was estimated from the tidal range predictions from the sites of tide gauges, TG0 and TG1 using their respective harmonic constants. Predictions from the model for the 25th November estimated outflow started through the mouth of the estuary at approximately local HW + 1 hour, the phase lag being induced by the effects of tidal asymmetry, funnelling and friction in the channel. Fig 3.10a illustrates how the channel flow is phase locked with the PGF created by the difference in the estuary and offshore tidal elevation. The abrupt turning of the tidal flow is best shown in Fig 3.10b as a time series of the modelled acceleration ($\partial\hat{u}/\partial t$) of flow through the connecting channel from the estuary to the open sea. A sudden surge in the ebb tidal current from the estuary is initiated by the change in sea surface elevation and the limited effect of bottom friction to penetrate up into the initially deeper water column of the channel on the early stages of the ebb tide.

The modelled longitudinal flow speeds in the channel approach nearly 4 ms^{-1} on the flood and 3.5 ms^{-1} on the ebb. The duration of slack water inside the estuary is minimal and the tide current abruptly turns on both the ebb and flood phase. According to Robinson (1975), a residual velocity must be present to account for the observed sedimentation in the estuary. Model predictions for a 48 hour period estimates an asymmetry in the peak flood and ebb current of 0.36 ms^{-1} into the estuary that seems to add support to the findings of Robinson (1975).

This analysis shows that the funnelled outflow from the estuary decelerates when entering Lyme Bay as maximum current speeds predicted at mooring RCM 1 were *O*(14) less than the values modelled through the mouth on the ebb tide. Flow outside the mouth is probably channelled to the NE through the inner and outer pole of the bar. As tidal elevation drops, the decelerating outflow is directed offshore by the Ness through the series of now exposed bars. Then, according to Robinson (1975), on approach to local LW the estuary outflow converges with the turning bay tidal currents and for a short period forms a gyre by the Ness until the estuary again begins to flood.

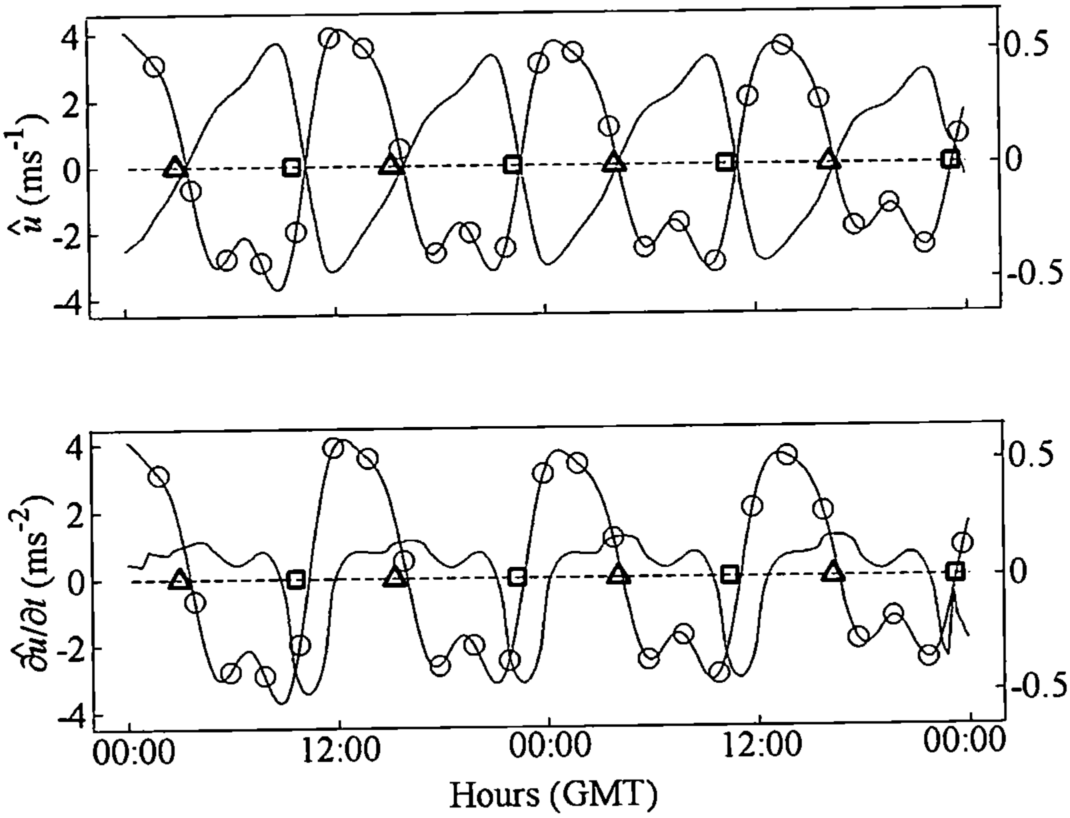

Fig 3.10: (a) Predicted outflow velocity and (b) the acceleration that corresponds to the predicted offshore and inshore tidal elevations through the outflow channel from the Teign estuary for the 25th & 26th November 1998. — = $\hat{u}$ flow velocity (ms^{-1}); O = $\Delta\zeta$ difference in sea surface elevation TG1 – TG0 (m); Δ = Time of local LW; □ = Time of local HW.

3.5.4 Summary of Tidal Analysis

The analysis described in this section on the local tidal regime predicts the magnitude and direction of tidal flows during a plume outflow event.

Shortly after local HW, outflow from inside the estuary accelerates due to barotropic gravity forcing and the limited effects of bottom friction in the connecting channel. During the early ebb phase, flow was in the order of 3.5 ms^{-1} through the mouth of the estuary. The currents then quickly decelerated and is then steered through the spit and outer bars outside estuary before aligning with the north-easterly Lyme Bay ebb tidal flow. As the ebb phase progresses, the estuary's outflow is then directed offshore by the turning coastal tide and the effect of funnelling. This results in the outflow being restrained and steered by the increasingly exposed outer bar region of the estuary.

X-band radar images that show the formation of a plume front outside the Ness Head is consistent with the 2nd quarter of the ebb phase when tidal currents are turning from NE to ENE (offshore) flow. Initially, the barotropic ebb current from the estuary converges with the north-easterly coastal tide. The converging currents limit plume outflow spreading to the south, and hence, the plume spreads offshore with a strongly defined front that remains parallel and attached to the estuary mouth. Further progression of the ebb cycle into the 3rd and 4th quarter sees the appearance of the radial shaped plume. The plume spreads in both the cross-shore and alongshore axis directions although the direction of surface wind waves and swell propagation can inhibit plume spreading where outflow and sea surface direction converge. At local low water, outflow from the estuary abruptly turns and past observations have suggested the plume is effectively cut-off from the estuary source.

Residual tidal flows in the location of all the current meter moorings were extremely small, in the order of 0.005 ms^{-1} towards the NE-ENE, and would appear insignificant in their overall contribution to the plume spreading dynamics.

Past observations (M. Fennessey, *pers.comm.*) which suggested variability in the time of plume frontogenesis after local HW would seem more dependent on runoff conditions than the state of the ebb tide currents. For example, in the instance of low runoff conditions, the smaller volume of freshwater entering the estuary is more easily constricted by the penetrating flood tide. The phase lag of the flood intrusion current initially counteracts the baroclinic gravitational outflow of freshwater. As tidal levels begin to fall on the ebb tide, the combined effect of the barotropic and baroclinic PGF then allow freshwater to flow downstream. Under low river runoff conditions, the baroclinic component of the PGF is significantly reduced. However, higher tidal ranges and larger barotropic currents combined with high river runoff enhance the outflow velocity and could add a significantly greater barotropic component to the spreading velocity of the plume.

3.5.5 Earth Rotation

As discussed in Chapter 2, the effect of the Earth's rotation is to transform an estuarine plume into a coastal current. This is accompanied by a transition from non-linear to the linear dynamics and is an important consideration in the formulation of a force balance. Gill (1982) explains that the acceleration term in the equations of motion becomes important when the term representing the Earth's rotation (*fu*, *v*) is dominant over the pressure gradient term. This is equivalent to a distance in a 2-layer flow of the internal baroclinic Rossby radius of deformation, *R′* as discussed in Chapter 2. Estimates of *R′* computed from the CTD casts taken on the 7th March 1995 were in order of 2 km. However, the results from the X-band radar imagery suggested the retention of radial symmetry of the Teign plume with strong frontal boundaries over a complete tidal ebb cycle with no apparent effect from the Coriolis parameter. This apparent discrepancy can be explained as follows.

$$\frac{\partial u}{\partial t} + u\frac{\partial u}{\partial x} + v\frac{\partial u}{\partial y} + w\frac{\partial u}{\partial z} = -\frac{1}{\rho_\infty}\frac{\partial p}{\partial x} - g\frac{\partial \eta_{BT}}{\partial x} + F_x + fv \qquad [3.7]$$

Temporal + Advective = Baroclinic & barotropic pressure + Effects from tides, friction, wind + Coriolis

u, v, w = Velocity (ms^{-1})
x, y, z = Cartesian Co-ordinate (m)
t = Time (s)
g = Gravitational acceleration (ms^{-2})
ρ_∞ = Density of seawater (kgm^{-3})
p = Pressure ($kgm^{-1}s^{-2}$)
η_{BT} = Sea surface elevation (m)
f = Coriolis parameter (s^{-1})

Equation 3.7 represents the general form of the equation of motion to maintain momentum balance in the longitudinal direction of flow in the Northern Hemisphere. Analogous equations can be developed for the lateral and vertical directions. Terms that provide the greatest interest for a first order estimate of a local force balance are from the contribution of the pressure gradient and Coriolis force term on the right hand side of the equation. The non-linear longitudinal and vertical terms as discussed in Chapter 2 are important in plume dynamics but are initially ignored in this simple analysis. The pressure gradient term incorporates the force from the longitudinal pressure gradient due to density differences (baroclinic force) and the contribution of the free sea surface slope (barotropic force) that will be modulated by the tidal contribution to the equation. It is assumed for ebb conditions a maximum across shore extent of plume spreading $\partial x \approx 4000$ m as captured in X-band radar imagery, across shore difference in sea surface elevation during tidal ebb conditions $\partial\eta_{BT} \approx 0.1$ m (see Section 3.5.3), mean ambient seawater density $\rho_\infty \approx 1026.9$ kgm^{-3}, mean density difference between plume and ambient seawater $\Delta\rho \approx 1.26$ kgm^{-3}, surface layer depth $h_1 \approx 2.5$ m, velocity $u = v \approx 0.13$ ms^{-1} and $f \approx 10^{-4}$ s^{-1}. For a shallow plume it is then assumed that the plume has a uniform density and the Boussinesq approximation applies.

The Boussinesq approximation assumes that the density of a fluid is constant when computing rates of change in momentum from accelerations, but takes full account of the density variations when they give rise to buoyancy forces. For example, when using a multiplying factor of g in the vertical component of the momentum equations (Gill, 1982).

Term		Acceleration (ms^{-2})
$\frac{1}{\rho_\infty}\frac{\partial p}{\partial x}$	Baroclinic pressure gradient	7.52×10^{-6}
$g\frac{\partial\eta_{BT}}{\partial x}$	Barotropic pressure gradient	245.0×10^{-6}
fv	Coriolis force	13×10^{-6}

Table 3.2: Estimated order of magnitude for each acceleration term per unit mass investigated in the longitudinal momentum equation.

Because the plume is shallow, the pressure field is isostatic and the free surface elevation due to the density anomaly between plume and ambient water is given by $\eta_{BC} = (\Delta\rho/\rho)\, h_1$ (Garvine, 1987), thus, $\partial p/\partial x \equiv \partial\eta_{BC}/\partial x$. The magnitude of each component term investigated is shown in Table 3.2.

Clearly, the most important term to emerge from the scaling argument is the tidal contribution to the barotropic slope in the pressure gradient term $O(10^{-3})$. The sum of the two components of the pressure gradient term are in order of 20 times greater than fv, illustrating the dominance of slope driven currents from the estuary that arise due to relatively large tidal ranges and phase differences between the inshore and offshore sea surface elevation. Other contributions to the balance from funnelling at the estuary mouth and the non-linear terms such as outflow velocity and volume of freshwater discharge would further decrease the effects of the Earth's rotation on the flow. Thus, to try to classify this tidally modulated plume into a non-geostophic (K<<1) or geostrophic (K>>1) case through Equation 3.8, the Kelvin number K criterion as proposed by Garvine (1994) or alternatively by the method discussed in Chapter 2 (Hill, 1998) is inappropriate in this instance.

$$K = \frac{\gamma L}{\sqrt{g' h_1} / f} \qquad [3.8]$$

K = Kelvin number
f = Coriolis parameter (s^{-1})
L = Width of discharge (m)

γ = Slenderness (length / width) of discharge
g' = Reduced gravity (ms^{-2})
h_1 = depth of surface layer (m)

For the scalar and vector values used in the prior force balance analysis at Teignmouth, K returns a value of 2.5 suggesting a geostropically modified outflow which is clearly incorrect in context of the scaling argument. However, Garvine (1994) does acknowledge this method of classification is limited to plumes with temporal scales of one week or more where tidal and meteorological variability is averaged over a considerable period of time. As the preliminary analysis showed, tidal modulation of discharge from the estuary at semi-diurnal frequencies and the barotropic pressure gradient is a major contributor to the dynamics of the Teign outflow. Therefore, based on the observational evidence and the scaling arguments for the Teignmouth study site, it was assumed that the Earth's rotational effects on flow modification were negligible. This allowed Coriolis force to be ignored in a numerical model of the radially spreading plume from the Teign estuary.

3.6 Model Development

Numerical solutions to explain the radial spreading of a buoyant surface plume from a radially symmetrical discharge were proposed by Garvine (1984). Due to the difficulties in deriving solutions to primitive equations to explain the apparent non-linear mechanisms present in the frontal boundary, Garvine (1981) took an intermediate approach (O'Donnell, 1993). The plume front is set to obey certain bulk or integral relationships and is treated as a free moving boundary whose solution is part of the problem. This is analogous to shock fitting techniques used in the study of compressible gas dynamics. The interior or body of the plume is assumed to be a thin layer and governed by the non-linear long-wave equations. The frontal boundary conditions first described by Garvine (1981) require a relationship between the ambient water, plume flow velocities and the depth of the layer at the front. The flow of ambient water then modifies the pressure and the velocity fields in an otherwise inviscid plume by convergence at the front and consequently influences the layer thickness of the plume.

Garvine's (1984) model assumes a radially symmetric source that discharges fresh-water into a stationary ambient fluid. As the flow of interest is on scales less than the internal baroclinic Rossby radius R', rotational effects due to Coriolis force are assumed negligible. Outflow from the estuary starts at time zero ($t = 0$) and remains constant thereafter. The lack of any mechanism to arrest the plume front results in an inherently unsteady flow. Therefore, the long-wave equations explaining the flow have real characteristics. This feature can be exploited to produce numerical results.

The model assumes local depth of the plume is everywhere small compared to local water depth and the density of the ambient seawater is uniform (ρ) and the plume is also uniform with a density ρ-$\Delta\rho$. Thus, the vertical momentum balance is assumed to be hydrostatic. Because $\Delta\rho$ is small, the Boussinesq approximation (as described in Section 3.5.5) applies and therefore, the plume floats in isostatic balance on top of the ambient seawater. Hence, the free surface elevation inside the plume is then simply $\eta= (\Delta\rho/\rho)d$ + constant, where d

is the surface layer depth. Assuming $\Delta\rho$ is constant and r is the radius of the plume, the horizontal pressure gradient force (PGF) is simply expressed as $\rho g' \partial d / \partial r$. These assumptions allow the PGF to be considered vertically uniform and as only inviscid processes inside the plume are considered the fluid velocity, q is also vertically uniform.

Mass continuity that is mathematically represented by Equation 3.9 describes the time dependent change in the surface layer i.e. the interfacial wave phase velocity squared, $c^2 \equiv$ depth and the additional term, (rc^2q) is the measure of flux into the surface buoyant layer per unit radius of the plumes expansion. The momentum inside the radial plume (Equation 3.10) is simply stated as the time derivative of flow velocity plus the change in the pressure gradient force per unit radius as represented through a Bernoulli type equation. The $c^2 \equiv$ depth in the second expression of Equation 3.10 is equivalent to the gravitational potential that produces a pressure gradient force acting outwards into the plume from the radial source.

To summarise the model assumes:

a) Density differences are small and a Boussinesq approximation can be applied.
b) The plume floats in isostatic balance.
c) The pressure gradient force (P.G.F) is vertically uniform in the plume body.
d) Only inviscid processes are considered in the plume body (mixing can take place only at the front).
e) Fluid velocity in the plume is assumed vertically uniform.
f) Only supercritical flow is examined ($Fr_i > 1$) at the front
g) Coriolis Force is assumed negligible (no rotation)
h) Windstress is ignored

Mass continuity and momentum equations of the model can be expressed as:

mass:
$$\frac{\partial c^2}{\partial t} + \frac{1}{r}\frac{\partial}{\partial r}\left(rc^2 q\right) = 0 \qquad [3.9]$$

momentum: $$\frac{\partial q}{\partial t}+\frac{\partial}{\partial r}\left(\frac{q^2}{2}+c^2\right)=0 \qquad [3.10]$$

r = Radial distance from source (m)
t = Time from release (s)
c = Phase velocity of internal wave on the plume interface $=\sqrt{g'h_1}$ ($\mathrm{ms^{-1}}$)
g' = Reduced gravity $(\Delta\rho/\rho)g$ ($\mathrm{ms^{-2}}$)
h_1 = Buoyant layer depth (m)
q = Fluid velocity ($\mathrm{ms^{-1}}$)

The mass continuity and momentum equations (3.9 & 3.10) are hyperbolic with a pair of characteristic lines given locally by:

$$\frac{dr}{dt}=q\pm c \qquad [3.11]$$

where a change in radius with change in time is equal to radial water velocity ± long internal wave speed. The corresponding characteristic equations along the lines given by Equation 3.11 are:

$$dq\pm 2dc=\mp\frac{cq}{r}dt \qquad [3.12]$$

The ± families represent non-linear internal gravity waves that propagate upstream and downstream respectively, at phase speed c relative to the buoyant layer and at an absolute wave speed $q\pm c$ relative to fixed co-ordinates. The model is made non-dimensional by introducing scaled variables using q^*, d_0 and r_0 as a reference velocity, depth and length scale:

$$\mathrm{R}\equiv r/r_0 \qquad \mathrm{T}\equiv q^* t/r_0$$

$$\mathrm{Q}\equiv q/q^* \qquad \mathrm{C}\equiv c/q^*$$

$$\mathrm{D}\equiv d/d_0=\mathrm{C}^2 \qquad \mathrm{F}=\mathrm{Q}/\mathrm{C}$$

The schematic format of the modelled conditions is shown in Fig 3.11. When F the Froude number equals 1, the flow is termed critical and the fluid speed for critical flow is $q^*=c^*$. To find solutions of the finite difference forms of Equation 3.12, incremental marching is done in the R direction rather than the more traditional T space downstream from the constant source boundary at T = 0, R = 1 (Garvine, 1984).

Time interval steps were held constant, but each increment of radial expansion from the source was re-computed for each marching step to limit the Courant value to a maximum value of 0.8 and so maintain numerical stability. At the source boundary, Q_0 and F_0 were held constant for all release times greater than T > 0. Therefore, as only supercritical flow is examined (F > 1) and at R = 1, $C_0 = Q_0 / F_0$, the two dependent variables Q and C (also D and F from scaling argument) can be computed from Equation 3.12.

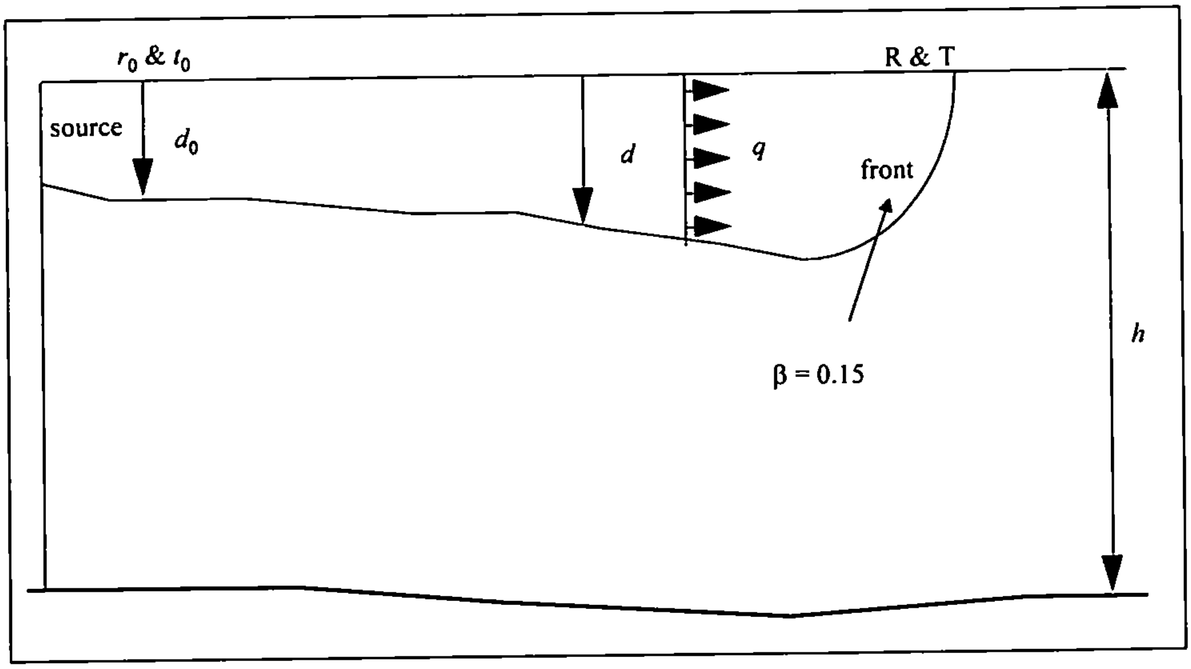

Fig 3.11: A schematic diagram of the radial spreading plume model.

$$Q_a = F_{a1}\, C_f \qquad [3.13]$$

$$Q_f = F_{a1}\, (1 - S_e\beta) C_f \qquad [3.14]$$

Where:

Q_f = Fluid speed behind the front

C_f = Phase speed behind the front

Q_a = The speed of the front relative to the ambient water.

$F_{a1} = [2\beta\,(\tilde{d} + S_e^2\beta\,)]^{-1/2}$ = The Froude number based on Q_a and C_f

β = Positive dimensionless constant that indicates the decay scale or fraction of the front where significant turbulent mass exchange (entrainment) and momentum exchange (interfacial friction and entrainment of momentum) occurs i.e. mixing. (Refer ahead to Section 5.4.1 for a full description of β).

$\tilde{d}$ = Positive constant that specifies the ratio of interfacial friction and entrainment coefficients and computed through $\tilde{d} = -S_e - S_e^2\beta + (2\beta F_{a1}^2)^{-1}$.

S_e = The vertical direction of entrainment in the front i.e. 0 = No entrainment; 1= upward entrainment: -1= downward entrainment.

The frontal boundary conditions were first derived in Garvine (1981) and adapted to force convergence in the characteristics plane of a radially spreading plume. Garvine (1981) derived a set of integral relationships that describe a change in flow properties across an internal hydraulic jump of a thin buoyant surface layer overlying a deeper ambient fluid. The leading edge of the spreading plume is treated as the jump discontinuity where its position at $T = 0$, $R = 1$ is at the source boundary. For the limit of a surface front where the buoyant layer depth tends to zero, the frontal 'jump' boundary conditions for a radially spreading plume are cited as Equation 3.13 and 3.14.

Equations 3.13 and 3.14 are the two jump conditions of Garvine (1981) adapted to describe the mass continuity and horizontal momentum balance in the frontal region of a radially spreading plume. These are combined with the plus family branch of Equation 3.12. This relates Q_f and C_f to the interior flow state Q and C, at the point where the plus or downstream propagating wave of Equation 3.11 passes through the front and intersects the previous R step. The ambient flow is then allowed to modify the pressure and velocity of an otherwise inviscid plume by causing convergence and also influencing the plume layer thickness (O'Donnell, 1993). The Froude number that describes the state of flow behind the front, $F_f = Q_f / C_f = F_{a1} (1-S_e\beta)$ is held constant throughout the computations. Stoker (1957), Garvine (1981, 1984) and O'Donnell (1993) provide full discussions on the derivation of boundary conditions in hydraulic jumps.

3.6.1 Model Results

A series of diagrams in the characteristics plane or R-T space and isometric projections of interfacial depth best represent the numerical solutions that describe the time and spatial dynamics of plume outflow. Results from model runs with only downward entrainment, $S_e = -1$ at the leading front are discussed hereafter, as O'Donnell *et.al.* (1998) and Brubaker & Simpson (1999) convincingly showed through field observations the presence of downwelling at the leading frontal boundary. The mixing parameter $\beta = 0.15$, a value derived from laboratory studies on gravity currents (Simpson, 1982). Fig 3.12 is an isometric projection (D = 0 at the bottom) of the developing plume outflow interface through radial distance and time. For this sample calculation $Q_0 = 1.2$ and $F_{a1} = \sqrt{2}$.

Fig 3.12 has been inverted (D = 0 at the surface) so the predicted internal features can be seen. From T (0) to T = 0.5 the depth of the spreading plume spreads out from the source and is bound by the abrupt frontal discontinuity. At T = 0.6, a ridge in the depth of the spreading layer behind the leading front begins to form and widens as T and R increase. The back edge of this ridge eventually forms an internal 'jump' on the interfacial region of the plume. Fig 3.13 illustrates the model flow field output in characteristics plane (R-T space).

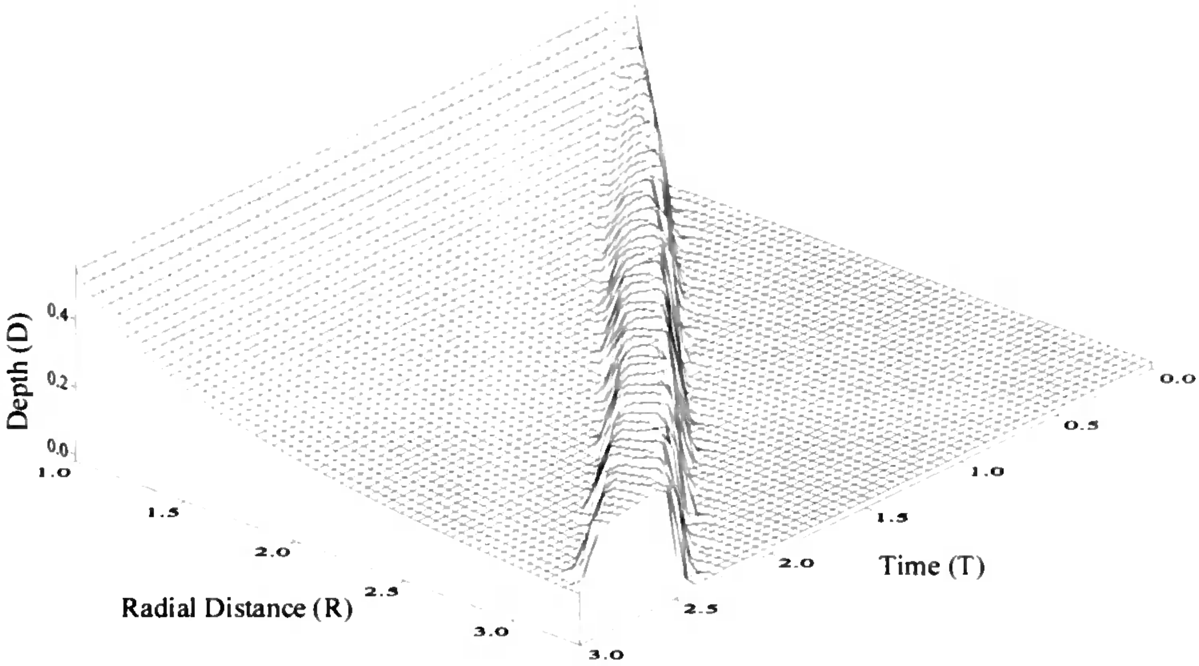

Fig 3.12: Quasi 3-D isometric projection of interfacial depth (D) in radial (R) and time (T).

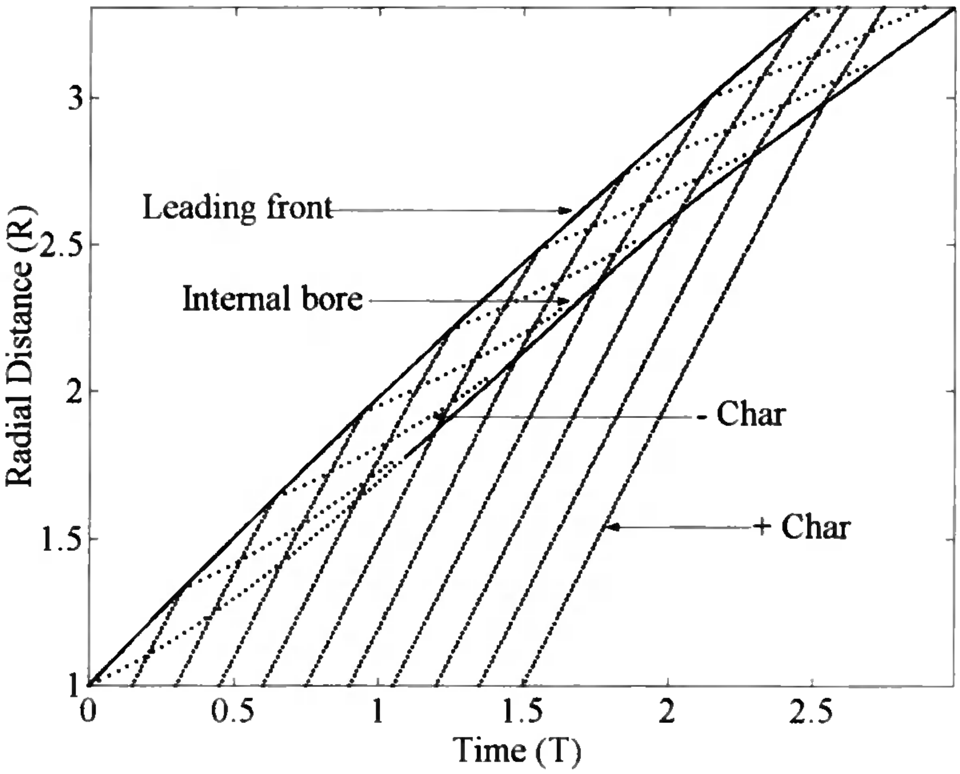

Fig 3.13: Plot of sample calculation of dimensionless characteristics plane in R-T space. Leading surface front and internal bore are shown with respect to R-T space. $\beta = 0.15$; $F_{al} = 2^{1/2} S_e = -1$.

The two different flow regimes are again obvious as the frontal ring and the steady spreading regions. In both regions, the downstream or Q+C characteristics show little variation in their slopes suggesting that flow downstream is essentially invariant. However, examination of upstream Q-C flow illustrates the emergence of different flow patterns for the frontal and spreading regions of the plume. Q-C flow in the steady spreading regime is essentially the same and is represented by the first reflected characteristic off the leading front. As R increases the slopes of these lines increase sharply as Q rises or C falls. The positive curvature of all the Q-C lines is a result of the spreading action. Downstream propagating waves that are reflected off the leading front soon after release have slow initial wave speeds, as C is relatively high near the front. These waves are later overtaken by waves of the same family further upstream near the region of steady flow. This overtaking is in the form of wave coalescence, the necessary condition for the formation of the internal hydraulic jump or bore.

The presence of the internal jump required the fitting of another front or hydraulic jump condition due to the method of characteristics being unable to solve discontinuities in a variable. This trailing front is fitted while change in $C^2 = D$ is weak and represents a jump propagating upstream into the general body of the plume. The motion of ambient water with respect to the internal jump is opposite to that of the leading front i.e. ambient water below the front is swept downstream towards where the leading frontal interface shallows. As T progresses and with a greater R, the reflected waves accumulate within the ring region at the trailing front. This adds to its strength and definition and eventually raises the edge of the trailing ring.

The two distinct flow fields to emerge from the results is a steady-state radial spreading regime preceded by a radial ring where the leading edge forms the front and the trailing edge, an internal hydraulic jump or bore. Garvine (1984) suggests these two prominent features in the model are the main regions of intense mixing and mass loss from a radial outflow plume.

3.6.2 Model Application & Scaling

Model output variables were scaled by choosing the appropriate values of r_0, d_0, q^* and F from the past observational studies. The radial distance r_0 (m) used to convert non-dimensional R from the model output into dimensional space was calculated from the first apparent capture of a radial plume in the X-band radar imagery. It is assumed this capture is representative of the source radial boundary distance where R = 1 and $r_0 = r$. This distance is not arbitrary because the model produces the numerical solutions on the assumption of an immediate constant radial release of fluid from the source. In a real situation, the momentum of fluid from the estuary is subject to the effects of tidal modulation and inertia and time is required to establish the radial source as was shown through the X-band imagery. Hence the chosen r_0 length scale of 541 m at HW + 2:39 hours (12:07 GMT) on the 7th March 1995 was selected from the time and distance of the start of radial spreading as suggested by the set of X-band radar captures. Other initial parameters of $F = \sqrt{2}$ and $q^* = c* = 0.13$ ms^{-1} were based on Garvine (1984) and the radial spreading velocity derived from regression analysis of the X-band radar imagery respectively. Entrainment at the front was set for downward motion ($S_e = -1$) as shown in the study of O'Donnell *et.al.* (1998) and mixing was left at $\beta = 0.15$, the value derived from laboratory results (Simpson, 1982).

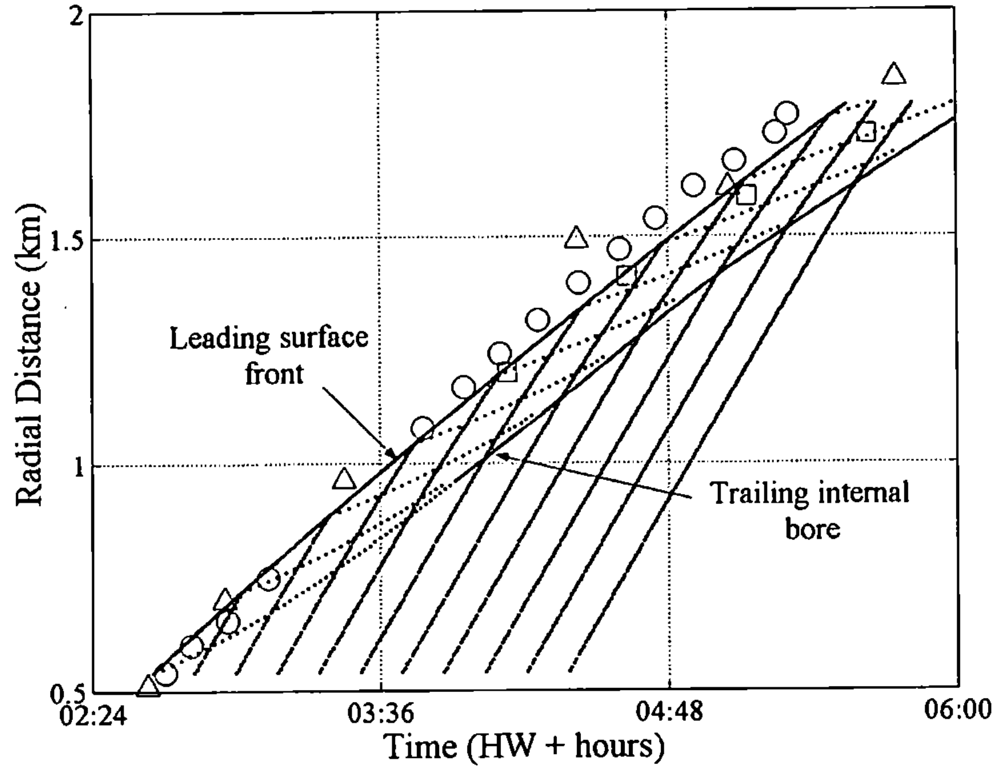

Fig 3.14: A comparison between the scaled characteristics plane of the model and the observed effective radial distance (km) and time (local HW + hours) as calculated from the plume area development captured in X-band radar imagery. □ = 19th November 1994; Δ = 3rd March 1995; O = 7th March 1995.

Results from the simulated outflow and the spreading rates recorded on the 19th November 1994 and the 3rd and 7th March 1995 are illustrated in Fig 3.14. The modelled outflow-spreading rate (T = 0 at the onset of radial formation) showed good agreement with the observations and according to the model predictions for the 19th November 1994 and 3rd and 7th March 1995, the trailing internal hydraulic bore should have formed some 180 m behind the surface front. The predicted form of the interface is illustrated in Fig 3.15 where d_0 was set at 2.5 m, a value estimated from CTD casts. The predicted interfacial depth decrease across the hydraulic jump was 0.7 m over a horizontal distance of 30 m.

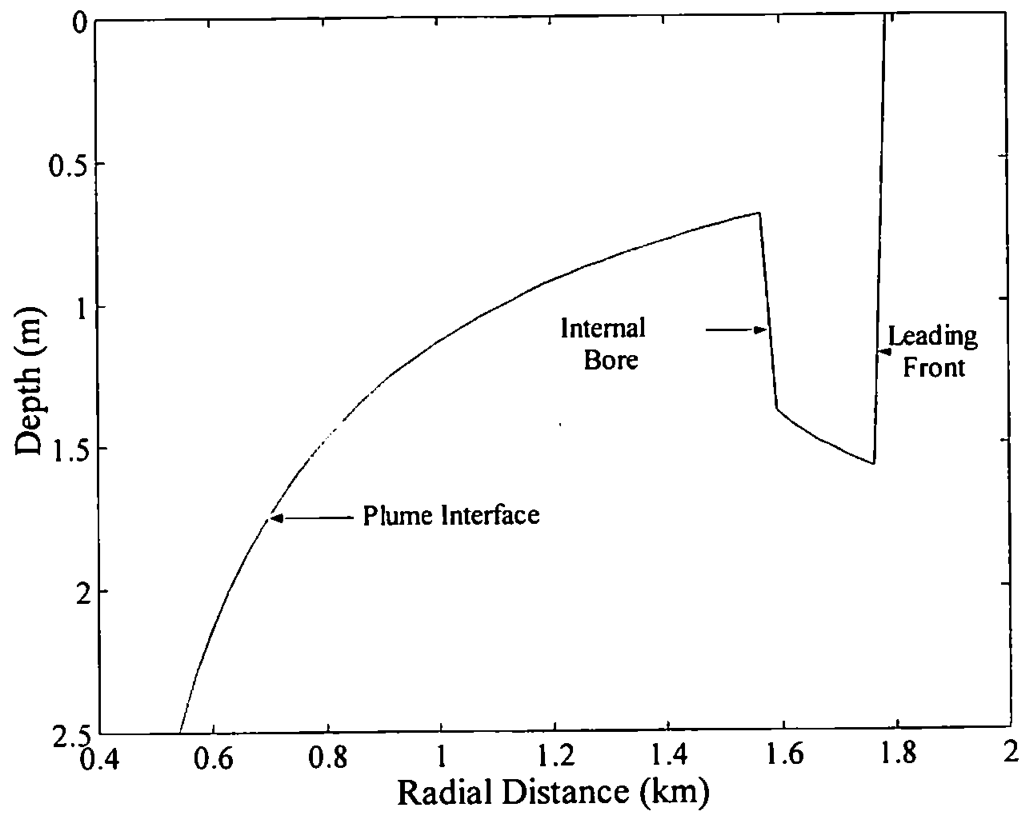

Fig 3.15: Scaled interfacial depth (m) vs. radial distance (m) for model simulation using X-band radar derived spreading rates and depth scale from CTD observations.

3.7 Summary of Modelling

Results from modelling time dependent radial river plume spreading with no rotation and cross flow has suggested there are two specific sites of mixing inside a radial plume. One is the plume front that marks the boundary of the outflow where water was subducted down into the water column. The other site is an internal hydraulic jump that forms some distance behind the leading front due to interfacial wave coalescence. Wave coalescence results from upstream interfacial waves, generated by the disturbances at the leading front, stagnating with downstream interfacial waves travelling from the flow source. These two features form an internal ring-like structure around the perimeter of the radial discharge.

The scaled input parameters used in the model runs to describe radial spreading at Teignmouth were based upon actual observations and the laboratory simulations of gravity currents. In terms of the scaled variables derived from X-band radar imagery, the predicted spatial position of the theoretically predicted internal bore was estimated at some 180 m behind the leading surface front.

To test the model hypothesis and quantify the small-scale internal hydrodynamics and mixing present in the Teignmouth plume would require a highly sensitive, mobile instrument array. It should be designed to resolve small changes in the spatial and vertical physical properties of the water column at length scales better than the scaled model predictions of the surface front and internal bore.

3.8 Field Methodology

The most obvious physical features of estuarine outflows are the salinity and seasonal temperature contrasts between the brackish river water and the receiving coastal waters. Fig 3.16 illustrates past records of the seasonal temperature anomaly between coastal waters and the Teign estuary (Courtesy of MAFF & Environmental Agency). Although the records are not concurrent, this general trend of temperature difference is well documented and considered typical for river outflows in temperate climates. The strongest temperature contrast is in the summer but, unfortunately, lack of runoff reduces outflow and the scale of plume formation is limited. However, in the autumn the river water temperature plummets to below that of the coastal sea with anomalies of up to 4°C. Obviously, some of this temperature signal will be lost by the time the 'Freshet' reaches the coast. However, a discernible temperature anomaly of up to 2°C between plume and ambient seawater is still present in Lyme Bay as shown by Matthews (1997).

This temperature anomaly provides a clear physical trace of plume discharge water as it propagates out of the estuary on the ebb tide. Thus, instrumentation that can measure temperature anomalies with an accuracy of better than 0.1°C will easily detect the plume presence in ambient seawater. Fortunately, the Estuarine Thermistor Spar (ETS), an instrument originally designed for water column structure studies in enclosed estuaries, was available (Sturley & Dyer, 1990). The ETS is a vertical array of thermistors that can accurately detect small changes in temperature and can be deployed from a small research vessel.

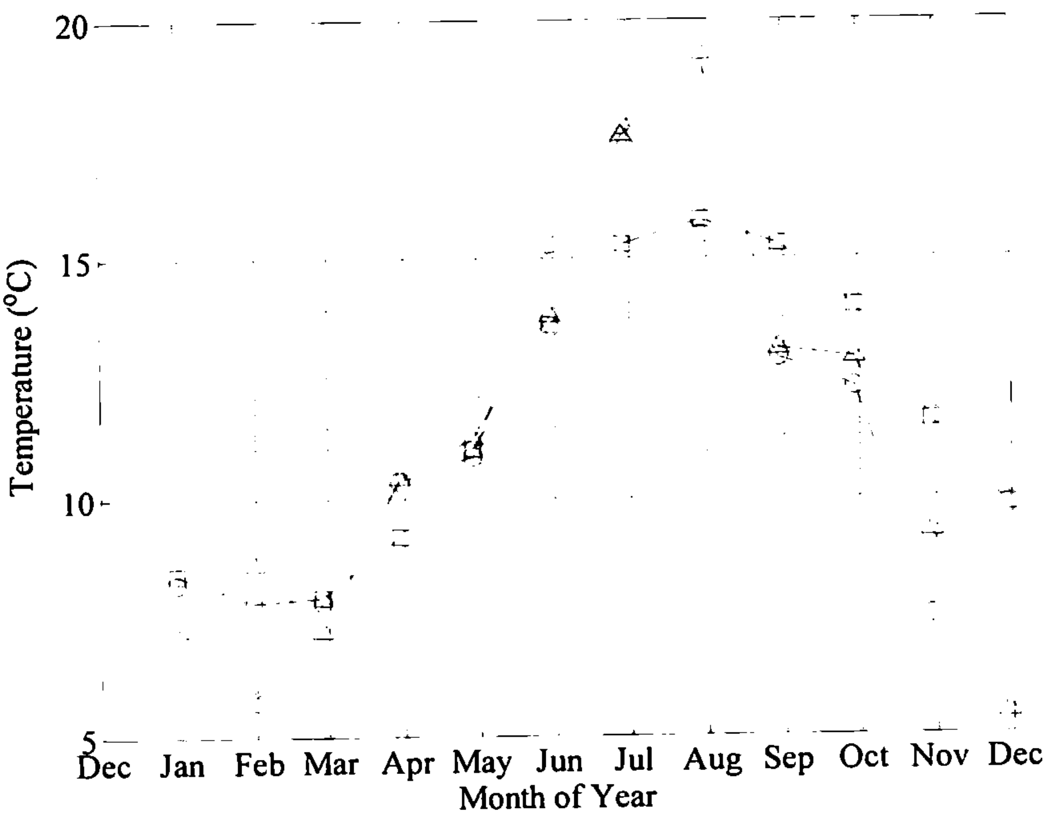

Fig 3.16: Seasonal comparison of sea surface temperature and river water temperature (°C) vs. month. □ = Mean sea surface temperature 1957–1989; Δ = River temperature 1995; O = River temperature 1996.

3.9 Instrumentation

In addition to ETS temperature data, to determine the magnitude of horizontal and vertical flow rates, flow direction and velocity shear inside the plume would require a velocity data set comparable in resolution to that of the ETS. Details on all the instrumentation and data acquisition systems used in the field program are discussed in the following sub-sections.

3.9.1 Estuarine Thermistor Spar (ETS)

The ETS is an instrument developed within IMS and used to determine the vertical temperature structure through a shallow water column (Sturley & Dyer, 1990). It is constructed from a 6 m long alloy tube with 15 thermistors mounted at 0.25 m intervals attached to the lower 4 m. When in operation the ETS is mounted vertically to the bow or side (as long as it is out of the wake) of a survey vessel and the instrument is pushed through the water with the temperature sensors facing forward. This allows vertical temperature profiles of the top 4 m of the water column to be recorded simultaneously at intervals of 0.25 m. Plate 3.3 shows a photograph the ETS.

Plate 3.3: ETS with EMCM's attached before deployment in the field.

Sturley & Dyer (1990) examined the thermistor sensor properties and circuitry in quite extensive detail to obtain the noise levels so to determine the useful resolution of the instrument. In the preliminary tests the resolution proved to be near the least significant bit value of the Analogue to Digital Converter (A-D), i.e. 0.005°C.

The thermistor probes are pairs of glass encapsulated thermistors of high stability. Each thermistor is embedded in a body of Epikote resin, with its body exposed to the environment and connecting leads soldered to male two pin plugs. This configuration gives the sensors an insulation resistance in sea water of 10^9 ohms or higher.

The variation of resistance with temperature is monitored by conditioning circuits before analogue to digital conversion. Each thermistor is arranged in a Wheatstone bridge, with the other resistance chosen so that the bridge is balanced at 0°C with a linear relationship between output voltage and temperature. The bridge output is amplified before A-D conversion and arranged so that the final conditioned signal is in the range 0 to 1 V for the full temperature range 0 to 20°C.

For the current study, 15 new NTC FP14 fastip thermoprobe thermistors were fitted to the ETS. These NTC FP14 thermistors used on the ETS were ideally suited for high-speed measurement of fluid temperature. The manufacturers specification gives a thermal response time from air to water as 16 milliseconds. If a thermistor is already immersed in water one could expect the response time to be considerably less.

Prior to any deployment of the ETS it was necessary to fully calibrate the thermistors. The calibration was performed by firstly immersing all the thermistors in a thermally insulated container holding ice water giving an ambient water temperature of 0°C. The individual output from each circuit board of the signal-conditioning unit was then monitored with a digital voltmeter capable of a five significant figure accuracy. Each circuit output was then tuned as close to 0 ± 0.0005 V as possible by balancing the Wheatstone bridge circuit. Ambient water temperature was then raised to 20°C and the amplifier gain was set to give a circuit output of 1 ± 0.0005 V. The dummy sensor was then fitted to the base of the ETS as channel '0' and consisted of an encapsulated fixed resistance which gave a bridge output voltage of 0 ± 0.0005 V. The dummy channel provided a temperature compensated reference signal for the 15 operational thermistors. Theoretically, this calibration procedure for the ETS should be sufficient to produce the desired range of output voltages to temperature change if all the thermistors have an identical linear response, as was specified by the manufacturers. However, after several trials of this method and continual inconsistencies in the voltage vs. temperature plots, a second stage to the calibration procedure was added.

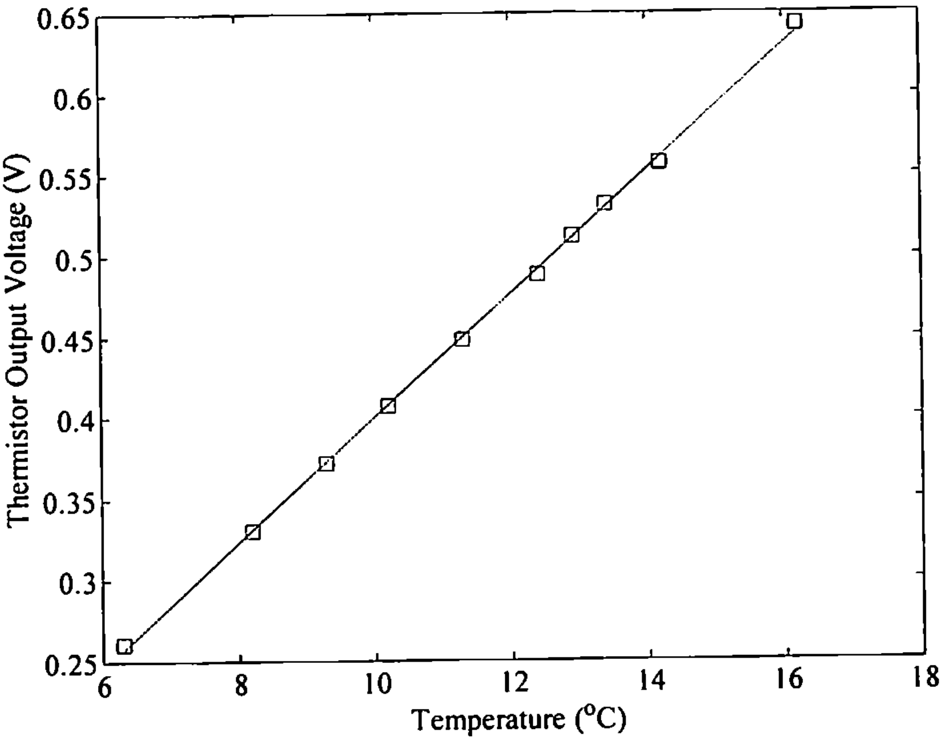

Fig 3.17: An example of thermistor voltage (V) output vs. temperature (°C) calibration for Thermistor 4.

All thermistors were again simultaneously placed in a thermally insulated container. The water in the container was mixed using a stirrer to give an homogenous temperature. Water temperature was then recorded during the calibration using a digital thermometer (0.1°C resolution). Each thermistor output was then recorded at a frequency of 8 Hz via the A-D link for a period of two minutes providing 960 samples per thermistor. This procedure was then repeated at incremental increases in water temperature through the entire expected operational temperature range (0 to 20°C). The mean voltage of each thermistor for each respective temperature increment through the temperature range was linear regressed to obtain a predicted temperature from a given voltage i.e. $y = mx + c$. The standard error from each slope provided the noise level for each thermistor channel. This calibration procedure was carried out before any of the major fieldwork was undertaken to ensure the ETS was operational. An example of a single thermistor calibration is illustrated in Fig 3.17 with the accompanying line of best fit from linear regression analysis. R^2 were consistently better than 0.99 for all thermistor channels with standard errors < 0.003 $°CV^{-1}$. When returning from the field, the instrument was re-calibrated in the same manner. The linear calibration equations for each channel of both calibration procedures were then applied to the field data and by comparing the values from the pre and post calibration provided a measure of instrument reliability and confidence in the results.

During the first stage of calibration, the conditioning circuitry was the worst source of error. In order to reduce this, a highly accurate voltmeter was required with readings expected within 0.1% of any output from the ETS circuitry. The second stage of the procedure involved taking readings from a digital thermometer. Although glass thermometers are considered more accurate, a digital thermometer gives a reading that can be determined absolutely with no human error (reading the LCD scale). Thus, error remains consistent through all calibrations (instrument error only) for all thermistors as human error is eliminated. The accuracy of the digital thermometer was limited to 0.1°C, which was sufficient for this study.

3.9.2 Valeport Marine Scientific Ltd Conductivity-Temperature Probes (CT)

Two Valeport Marine Scientific Ltd Series 600 Mk II temperature and conductivity probes were employed to determine salinity and density field at two different levels in the plume. The CT's were mounted on the ETS at positions that corresponded to a depth of 0.95 m and 2.9 m below the surface. Placement of the CT probes at these specific levels would effectively provide a measurement of temperature and conductivity either side of a horizontal interface, i.e. inside and outside the plume. In conjunction with measurements of velocity, estimates of the densimetric interfacial Froude numbers (Fr_i) could then be calculated. Additional CT data could also help interpret the temperature data from the ETS.

Conductivity is measured by a conductivity sensor consisting of two dual inductive coils. One injects a signal via seawater into the other coil. The seawater acts as a single turn resistive coupling loop and the magnitude of the signal detected in the second coil is proportional to the conductivity of the seawater. The electronic circuitry derives a DC voltage output proportional to the conductivity of the seawater medium linking the two coils.

Temperature is measured via a linearised temperature composite. The temperature sensor gives a high output signal and sufficient linearity and stability for the specification. Conductivity and temperature calibrations were carried out by Valeport Marine Scientific

Ltd and checked by standards prepared from a Guildline Portasal 8410 salinometer in the IMS laboratory. The conversion from conductivity and temperature to salinity is carried out in three stages. The first two stages result in a temperature compensated value of conductivity where the conductivity value is adjusted to its equivalent value at 15°C. The third stage corrects for the inherent non-linearity between conductivity at 15°C and salinity. The final value of salinity closely follows the true salinity over a wide operating range of temperature and conductivity. Density can then be calculated from the salinity and temperature using the International equation of state for seawater (Millero & Poisson, 1981). Valeport quote the accuracy of the CT probes as better than 0.2°C for the temperature sensor. The accuracy of salinity which is derived from measurements of temperature and conductivity is ± 0.4 between a salinity of 0 and 30 at temperatures between 0 to 30°C. This equates to an error in density measurements of ± 0.28 kgm^{-3} at a temperature of 11°C and salinity of 34.

3.9.3 Valeport Marine Scientific Ltd Bi-axial Spherical Electromagnetic Current Meters (EMCM)

Three Valeport series 800 spherical electro-magnetic current meters (EMCM) were used to measure the velocity shear and internal motion field within plume and plume front. The EMCM's were aligned port-starboard, bow-stern on the survey vessel to measure along and cross frontal velocity (x', y') and mounted on the ETS at depths corresponding to 0.9 m, 1.85 m and 2.9 m. In effect, the top EMCM would record in the upper brackish layer and the lower EMCM in ambient seawater. If corrections were applied with respect to the speed of the boat, the velocity field normal and parallel to a plume front could then be resolved.

The EMCM construction comprises a 5.5 cm diameter-sensing head joined to the main body of the instrument by a narrow stem. The four electrodes positioned symmetrically around the head are designed to measure velocity parallel and normal to the sensing head arrangement. The principle of operation is based on Faraday's law where a conductor moving through a magnetic field produces a voltage. Therefore, the magnetic field produced by the sensing head when placed in a conducting medium such as seawater produces a voltage. With appropriate calibration, a 2-D velocity record can be extracted from the instrument voltage output.

Two of the EMCM's were calibrated in Valeport Marine Scientific Ltd's open channel tow tanks. Voltage output was recorded for a range of known speeds and regression coefficients derived. Offsets for each EMCM were adjusted to zero. The bit value calibration can be related to voltage and speed (ms^{-1}) as: - 5 ms^{-1} = - 5 V = - 4096 bits; 0 = 0 V = 0 bits; + 5 ms^{-1} = + 5 V = + 4096 bits. Valeport Ltd supply these EMCM's with a mean zero signal stability of less than 0.005 ms^{-1} and a gain accuracy of better than 1% + 0.005 ms^{-1} of the instrument reading. This suggests that Valeport EMCM's should have a maximum error of 0.015 ms^{-1} in a 1 ms^{-1} flow for averaged readings. This is representative of a 1.5% error. Hence, the magnitude of this error would prove insignificant for the purpose of the current study.

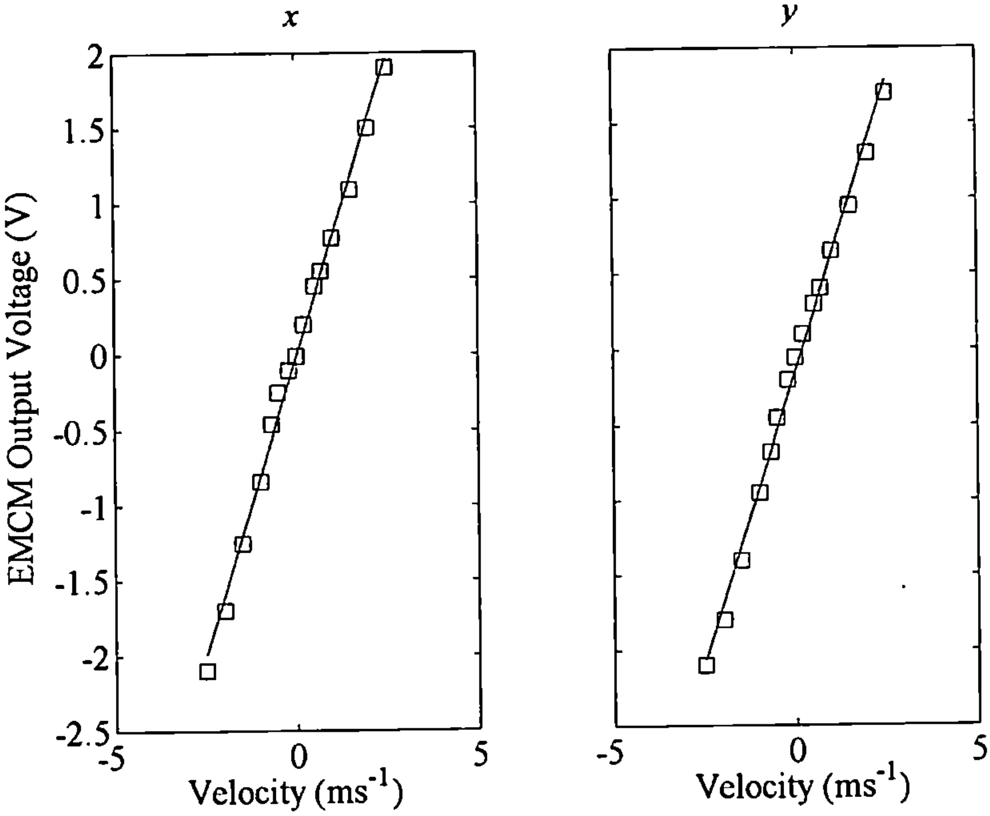

Fig 3.18: An example of linear calibrations of Valeport EMCM voltage output (V) vs. tow velocity (ms^{-1}).

The third EMCM was calibrated for gain in a tow tank at the Royal Naval Engineering College at Manadon, Plymouth, Devon by Miles (1997). The instrument was bolted to a tow truck, the absolute speed which was varied from -2.0 ms^{-1} to 2.0 ms^{-1}, at increments of 0.2 ms^{-1}. The output voltage was recorded through the A-D link onto a PC. Linear regression of the voltage output (V) versus tow truck speed (ms^{-1}) was then used to compute the EMCM gain. R^2 values for both the x and y direction regressions were better than 0.99. The results from this analysis are shown in Fig 3.18.

Cunningham *et.al.* (1979) found an uncertainty in EMCM gain of between 5 and 10%. However, although Huntley and Hanes (1987) found EMCM's to have a generally accepted error of ± 2 - 3 cms^{-1}, they suggest this can be improved upon by recording *in situ* voltage offsets. The EMCM offsets were taken before and after each survey by placing the instruments in a container filled with still water and away from electro-magnetic interference with each other, external electo-magnetic fields and environmental influence. The EMCM's were then allowed to log for two minutes at 8 Hz and the mean of the voltage output was then added or subtracted (depending on a negative or positive offset) to give the absolute output reading.

3.9.4 Druck PTX164 Pressure Transducer (PT)

A major foreseen problem of using the ETS at sea was the effect of surface wave activity and boat movement on all transducer records. To obtain an uncontaminated reading from all the instrumentation it would be necessary to remove this fluctuating component of the signal from all the data. An effective and simplistic way to measure and remove the appropriate level of contamination could be based on the spectral coherence between pressure or depth and a transducer. By calculating the power and cross spectrums between a particular transducer and a pressure sensor, a coherent gain function can be computed. The amplified component of the transducer signal due to changes in pressure or the movement in the sampling platform could then be removed through a filter routine. This is discussed at length in Section 4.3 in a section on data filtering techniques.

Consequently, a Druck PTX164 pressure transducer (PT) was bolted to the bottom of the ETS during the surveys and recorded simultaneously with all other instrumentation. The PT was 2 bar absolute and in normal atmospheric pressure has an operational depth of up to 10 m. The linear relationship between voltage output and pressure on the PT could then be converted to depth.

3.9.5 Seabird Seacat SBE 19-03

The Seabird Seacat SBE 19-03 CTD was used to record vertical profiles of conductivity, temperature and depth though the water column during the surveys. A minimum logging frequency of 4 Hz was used on all casts. Calibrations had been carried out by Sea-Bird Electonics Inc. and checked via standards prepared from the IMS, University of Plymouth Guildline Portasal 8410 salinometer. The author refers the reader to the Seabird Seacat SBE 19-03 operational manual for full specifications.

3.10 Navigation

During the surveys it was imperative to obtain accurate time, position and course so all the measurements recorded from instrumentation could then be related to a latitudinal and longitudinal position relative to the mouth of the estuary. Position fixing would also allow the conversion of time to spatial scales. To obtain geographical position a Trimble 4000 Differential Global Positioning System (DGPS) with local correction was acquired for this purpose. A KVH Europe fluxgate compass provided directional information.

3.10.1 Trimble 4000 DGPS

To obtain real time positioning to an accuracy of ± 5 m from the GPS it must operate in the 'differential mode'. Stand-alone GPS will only produce real time positions to a best accuracy of ± 20 m. This reduces to ± 100 m if the US military Selective Availability (SA) is in operation.

The Trimble 4000 received local correction from a second receiver and transmitter located at The Point where a WGS84 survey point was known (Courtesy of HR Wallingford). This fixed ground station generated Pseudo Range Corrections (PRC) from the satellites in view (SV). These PRC were generated by comparing the observed and calculated ranges for each SV. Corrections were then transmitted to the mobile receiver on the boat and applied to the observed ranges. Only ranges from SV's for which there is a matching PRC can be used to calculate position i.e. SV must be tracked simultaneously by reference and mobile stations. A minimum of four corrected ranges are required to produce a 3-D solution, i.e. latitude, longitude and height. For a 2-D solution, i.e. latitude and longitude when only three corrected SV ranges are available requires the antenna height to be used in the solution as a fourth range. In most instances more than four SV's are continually available for the correction procedure. The Trimble 4000 was interfaced with a laptop PC and data output downloaded at a frequency of 1 Hz on to the hard drive. The obvious advantage of this method of positioning is the ability to calculate the position and speed of the survey vessel to a high degree of accuracy. The actual uncertainty depends on the number of satellites in view and the geometric configurations of the satellites used by the GPS system. The Trimble 4000 system with a local correction from a ground station transmitter /receiver is cited as better than ± 0.25 m (K. Miller, IMS, University of Plymouth, *pers.comm.*).

3.10.2 KVH Europe A/S: C100 Compass Engine

Geographical directional information although available through the DGPS was recorded from a fluxgate compass. Combined with the DGPS output, the compass allowed any deviation from a straight course on the survey to be corrected. Small changes in heading at sea are unavoidable and could have implications on flow velocity measurements and produce anomalous results. In an attempt to reduce this effect, a correctional method was used giving the ability to make subtle rotational corrections to the vector components of the EMCM readings, therefore, compensating for any deviation in the survey vessel. Hence, the output from the C100 compass logged simultaneously with the transducers providing the necessary information for this correctional procedure.

The C100 was a small, accurate, low cost magnetic heading sensor with a linear output where, at a heading of 000° the output switched abruptly from 1.9 V DC to 0.1 V DC when turning clockwise. On turning counter clockwise, the output voltage switched from 0.1 V DC to 1.9 V DC. Manufacturers state the accuracy of the compass to within $\pm 0.5^{\circ}$.

3.11 ETS Instrument Array

The problem initially presented to the author was collecting the high-resolution measurements required to:

1. Quantify the basic hydrodynamic properties present in a temporally and spatially developing freshwater discharge into coastal waters.
2. Identify, quantify and give a precise account of the smaller scale dynamical and mixing properties of the plume frontal region. Eventually this would allow field derived bulk parameters such as Froude numbers and mixing coefficients to be introduced into the numerical model boundary conditions.
3. Explore the hypotheses of the numerical radial spreading plume model. Results from the modelled radial flow problem suggested two specific sites of mixing, one the leading front and the other an internal hydraulic jump. Detection and following these features in time and space would require working in a moving reference frame with respect to a fixed Earth.
4. Produce a complete synoptic description of the Teign plume development, mixing processes and eventual dispersion within Lyme Bay.

Logistically, the hydrodynamic features of a radial plume that were indicated from X-band radar, numerical modelling and previous studies could only be resolved from a moving reference frame. Eulerian measurements inside the plume could not have provided the high-resolution results to test and quantify hypotheses and small-scale dynamics respectively, as a multitude of fixed instrument moorings would be required to study the time and spatial developments in hydrodynamic properties. Also, the inherent variability in the outflow required instrumentation that could be deployed at relatively short notice and located in the precise vicinity of a developing plume front. The ETS instrument array and geographical positioning system discussed in Section 3.10 was specifically designed to be employed for use in a moving reference frame and to provide the high-resolution data set to resolve the four criteria specified above. A full schematic of the instrumentation is shown in Fig 3.19.

The complete instrument array was assembled on site at Teignmouth with the EMCM's, CT probes and PT probes mounted at the appropriate positions on the ETS, as shown in the schematic diagram of Fig 3.20. The survey vessel used to deploy the ETS was a small (26 ft) inshore fishing boat. 'Grey Dawn' was rigged with a scaffold tube bow rig designed to accommodate the ETS as illustrated in Plate 3.4. Once at sea the ETS was mounted vertically in front of the bow as shown in Fig 3.20. The electronic logging equipment, A-D link and PC to simultaneously record all transducer data was housed in the cabin. Subsequently, all data was logged at a frequency of 8 Hz with file lengths of 2^{12} samples. This produced a time series 512 seconds long or allowed a 512 m long transect with a spatial sampling resolution of approximately 0.13 m, assuming the research vessel cruised at 1 ms^{-1} (2 knots). Therefore, files had the potential to record transects over 200 m long and detect if the internal features were present in the plume outflow as predicted by the Garvine (1984) radial spreading plume model. The raw data collected during a survey was down loaded to floppy disk and later de-multiplexed into ASCII format ready for analysis.

3.12 Experimental Protocol

Following the reasoning behind the instrument design and application to the problems of collecting high-resolution data in a moving reference frame, the field experimental protocol was quite simple in concept.

Firstly, ideal-sampling conditions would be under high river runoff and tidal range conditions with a relatively smooth sea state. This would allow properties inside a well-defined plume to be measured without too much external influence from wind wave and swell effects. As explained earlier in Section 3.8, the ethos of the measurement and detection of plume water using the ETS was based on the seasonal temperature anomaly between water types and also a sufficient river runoff rate. This restricted sampling to either early spring or autumn of the seasonal calendar. Logistically, November 1998 was preferable as archived EA runoff levels, weather conditions and availability of the survey vessel suggested this would be an appropriate time to conduct the surveys. In addition, higher than average tidal ranges over the spring-neap cycle would allow slightly more flexibility if weather conditions were unfavourable. The higher than average barotropic forcing from the estuary presented a bonus as alternative survey dates could be chosen if sea conditions on a particular day were 'blown out' or if river runoff rates were low.

Secondly, during sampling only straight transects in and out of the plume would be considered, using the visible frontal foam line as the outer datum, the estuary mouth as the inner reference and the fluxgate compass for navigation. The horizontal length scale of each transect would depend on the distance of the foam line offshore. On early transects inshore bathymetry would limit a transect length due to ETS clearance of the complex inshore sandbar system near to the estuary mouth. Offshore, bottom clearance would not present any problem.

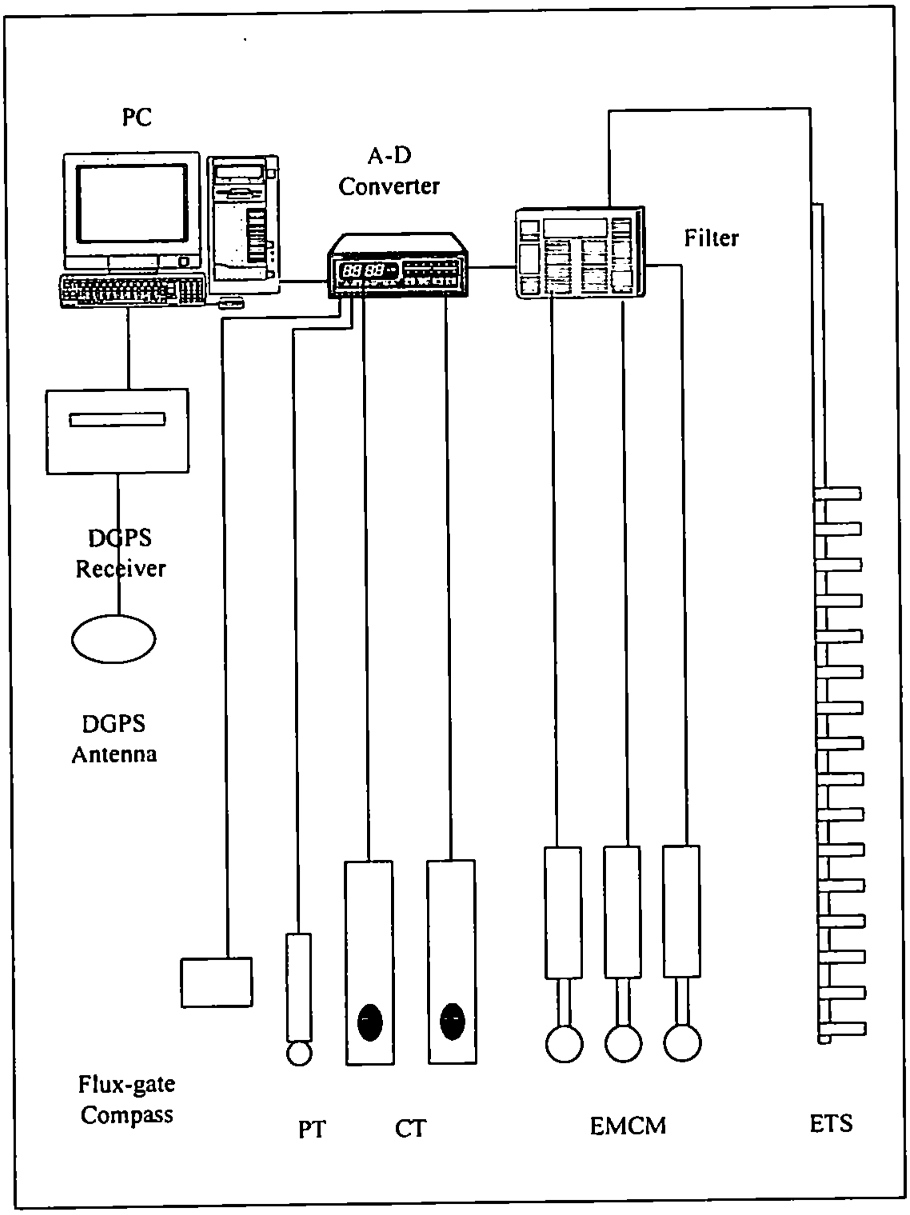

Fig 3.19: Schematic diagram of ETS instrument array.

Plate 3.4: Photograph of ETS boat rig.

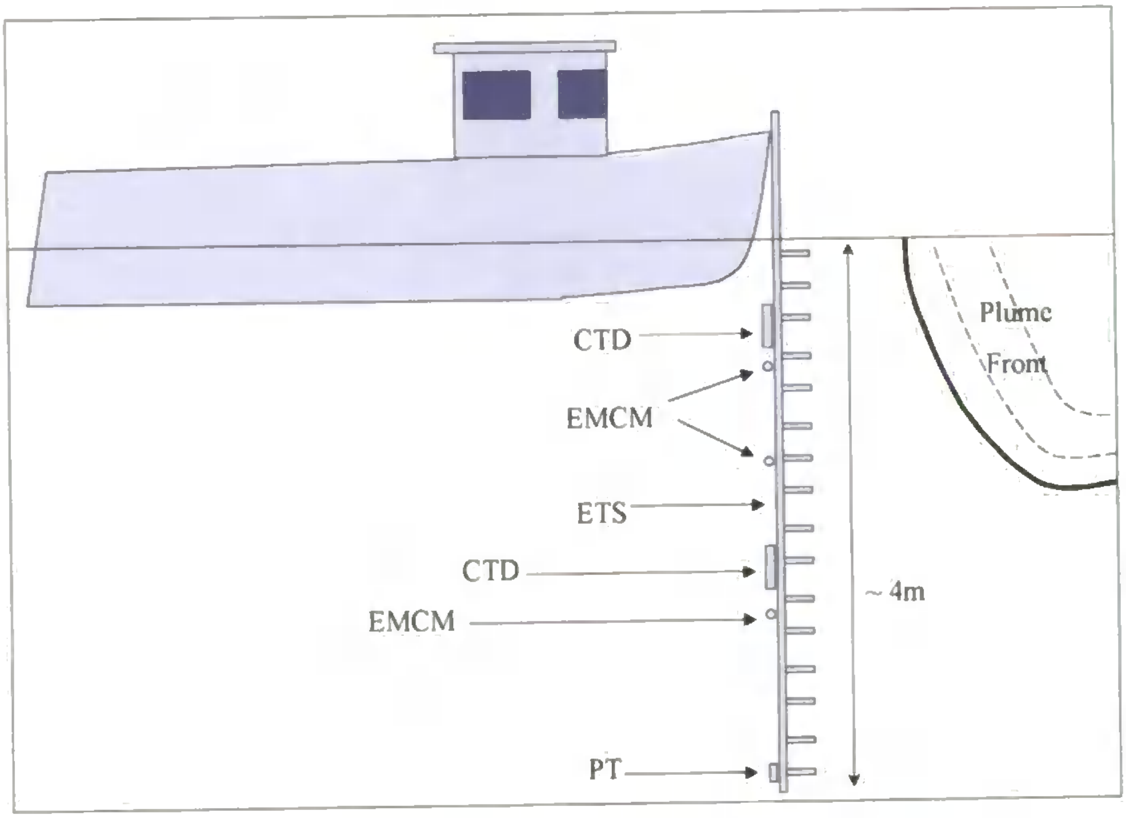

Fig 3.20: Schematic diagram of ETS instrument array during deployment.

Chapter 4

Results: Plume Hydrodynamics

The development of hypotheses through preliminary data analysis and the modelling study led to the design of a sampling protocol that would hopefully resolve the predicted internal features thought responsible for mixing in small-scale river plumes.

Initially, this chapter outlines the environmental conditions while surveying the plume during two plume discharges in November 1998. This is followed by a detailed account of the data correction and filtering procedures necessary for all the subsequent analysis of the plume hydrodynamics. Lastly, a description and quantification of plume dynamics is discussed in context of local tidal flows and interfacial wave packets observed during the surveys.

4.1 Field Conditions

Before observational work was undertaken in November 1998, it was considered a *priori* whether there was a sufficient river runoff rate before any surveys commenced. In November, the seasonal coincidence of rainfall and storm events, large sea-states plus limited times of local HW in daylight hours greatly reduced the size of time windows available for sampling. However, as the response time of river flow to rainfall was relatively short and the ETS instrument array could be mobilised at short notice from the survey vessel, a decision could be made quickly on whether to proceed with a survey following a period of precipitation. Suitable weather conditions and tidal ranges became available on the 25th and 26th November 1998. Fortunately, as mentioned in Sections 3.5 and 3.9 the presence of the higher than average neap tidal ranges in addition to the spate runoff conditions ensured that the gravitational outflow from the estuary was sufficient for plume formation during the two surveys. Table 4.1 summarises the environmental conditions present during the fieldwork.

Both surveys commenced on the estuary's ebb tide when the plume fronts foam line became visible. The actual time of plume front formation on both occasions was approximately local HW + 2:30 to 3:30 hours.

The ETS instrumentation was set to record once at sea when bottom clearance allowed across frontal transects of the developing plume. Once there was sufficient bottom clearance, the survey vessel was held at a constant speed of approximately 1 ms^{-1} and on a straight bearing. Repeated transects were then made perpendicular to a defined front from ambient seawater into the brackish plume or vice versa out of the plume into ambient seawater using the centre of the estuary mouth when possible as the datum (DGPS way point). This sampling procedure continued through the ebb tides as long as weather and sea-state permitted. The positions of each plume survey transect as recorded by the DGPS are shown in Fig 4.1a and Fig 4.1b.

	25.11.98	26.11.98
Time of Local HW (GMT)	0936	1023
Tidal Range (m)	3.3	2.4
River Runoff (m^{3}s^{-1})	13.642	10.942
Stage (m)	0.802	0.709
Sea Surface Temperature (^{0}C)	10.7 - 11.1	10.8 - 11.1
Sea State	2	2
Wind Direction	NW	NW
Swell Direction	SW	SW
Wave Height (m)	0.15	0.15
Wave Period (s)	3.5 – 6.0	2.5 – 6.0
Start of Survey (GMT)	1216	1342
End of Survey (GMT)	1529	1425

Table 4.1: Summary of general environmental conditions during the 1998 Teign Plume surveys.

Water depth restricted the inshore limit of transects in the early stages of the plume discharge cycle due to depth limitation (4 m for the ETS) caused by the complex sand bar and shallow bathymetry by the estuary mouth. This limited the initial start time and the number of observations made earlier on in the plume development and is reflected in the low concentration of measurements near to the estuary. Offshore, conditions were more congenial and transects could be completed in water depths of between 10 and 20 m with no interference from bathymetry. The length of the offshore frontal transects depended on the start position and clear frontal definition, as sometimes the exact position of a front relative to the estuary mouth was difficult to identify from sea level. Thus, on survey runs that were forced to change heading during sampling due to navigational difficulties were terminated early. Furthermore, Fig 4.1a and Fig 4.1b illustrate how the majority of measurements were taken to the south of the estuary. The reason for the 'concerted effort' in this region of the plume was the highly definable frontal foam line. In this region of the discharge, a clearly marked 'frontal line' made it easier to navigate and complete straight transects relative to the front. Interestingly, a 'sharper' front to the south of the estuary is also present in the X-band radar images presented in Section 3 and appears to be related to the convergence of the local tidal streams and the estuary outflow. In addition to the shorter frontal transects, one survey run on the 25th November crossed the entire plume from the NE to the SW and a ETS profile was obtained through a complete interior section of the plume.

Generally, the data collection went quite smoothly and was only disrupted occasionally by local shipping or an increasing sea-state. This either delayed or shortened the survey respectively. Some problems did occur with the ETS, which would unpredictably and indiscriminately log 'noisy' data on certain transects. This noise in the ETS voltage outputs was inexplicable by any physical processes ongoing in the water column. All other instrument outputs appeared normal with respect to the survey vessel's geographical position either inside or outside of the plume. However, the corrupted files accounted for only 11% of the total 28-Mb of raw ASCII data collected during both surveys. These data files were subsequently discarded from any future analysis.

(a) 25th November 1998

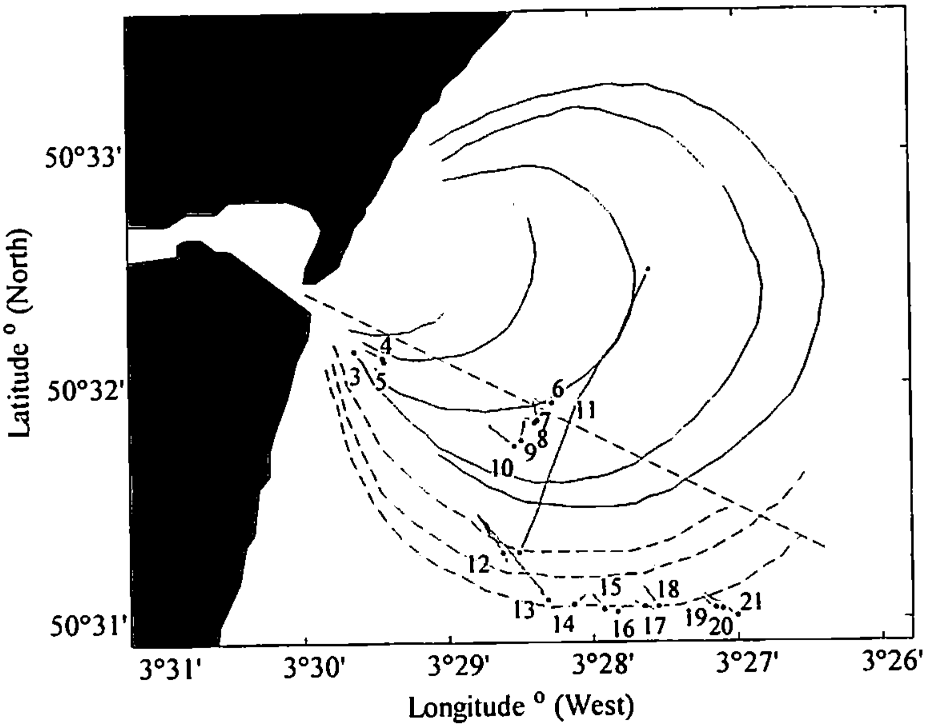

(b) 26th November 1998

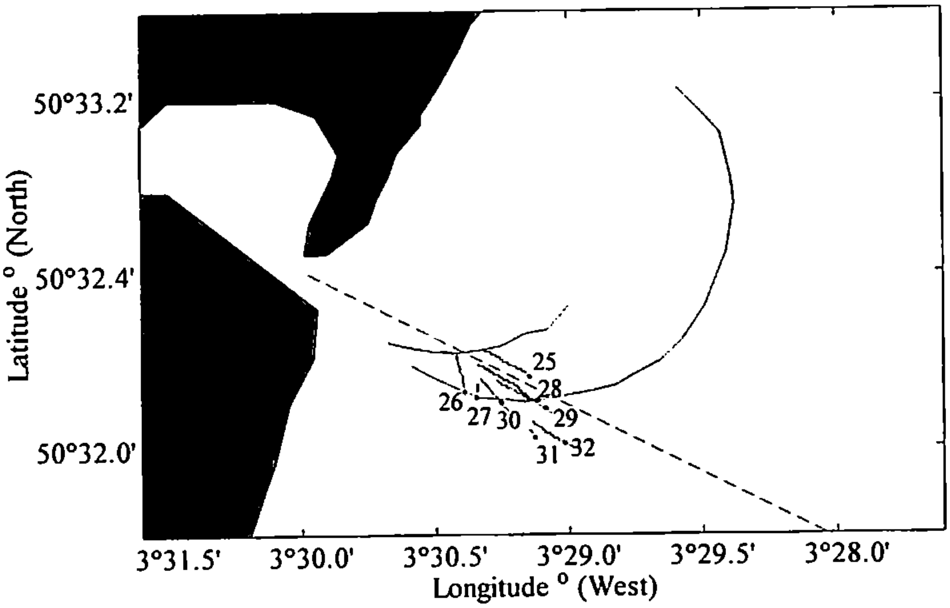

Fig 4.1: Geographical location of plume survey transects conducted during (a) 25th November & (b) 26th November 1998. Projections of the plume boundary through the ebb tidal cycle as estimated from the 1995 X-band radar images are shown in order to give the reader a concept of the plumes area and position during the two surveys.

4.2 Data Processing

All the data from the ETS instrument array was de-multiplexed, downloaded on to a PC and archived. Results from post-survey thermistor calibrations were compared with the pre-survey calibrations. Values from the two sets of calibrations showed no significant drift. A similar procedure was conducted for pre and post-survey EMCM voltage offset values before the appropriate calibrations were used to extract the velocity data from each EMCM. Conductivity, temperature and salinity data recorded by the CT probes, depth fluctuation from the pressure transducer, directional information from the fluxgate compass and salinity and temperature from the profiling CTD were extracted from the voltage records of each instrument through the respective manufacturers' calibration equations or constants. Density from the CT probes and the CTD was calculated through the UNESCO international equation of state for seawater (Millero & Poisson, 1981).

The experimental protocol had previously set a data selection criterion based on survey transects being suitably aligned with the estuary and straight according to the DGPS and fluxgate compass. Under this selection procedure over 84% of the 'noiseless' data collected was included in all or part of the future analysis of plume and plume frontal properties.

4.2.1 Data Filtering & Power Spectral Density

In Section 3.9.4 the importance of removing superfluous noise and possible periodic signals due to survey vessel movement (pitch and roll) that could have contaminated the outputs from the ETS instrument array was emphasised. The obvious consequence of leaving the data in its raw sampled state is to reduce confidence in the results of later detailed analysis that investigated physical processes present inside the plume discharge. To remove unwanted signals, all data was passed through two frequency domain filtration procedures. One was designed to remove the effects of survey vessel movement and attitude due to pitch and roll induced by surface waves and the other would eradicate any high frequency noise.

The principle of the data filtration was based on times series analysis. Fourier (1768-1830) proved that any discrete sampled (i.e. digitised) series, which is repetitive in a time 'T', could be represented exactly by a finite sum of sine and cosine waves of discrete frequency. To estimate the contribution of each relevant frequency, a time series of data is shifted from the time to frequency domain with a Fast Fourier transform (FFT) algorithm (Equation 4.1) as used in the MATLAB signal processing toolbox.

$$X_k = \sum_{m=-N/2+1}^{N/2} x_m e^{-i2\pi km/N} \qquad [4.1]$$

N = Length of series

$k = -N/2 + 1, N/2$

X_k = Fourier Coefficient, at frequency = $\dfrac{2\pi k}{N}$

i = Imaginary component

x_m = Time series

In order to optimise frequency resolution and statistical confidence, a time series that is subjected to an FFT should be as long as possible while retaining stationarity, i.e. the length of the data time series should remain shorter than any detrimental longer period processes. For an efficient calculation, FFT series were conventionally kept to 2^n discrete samples long. With an increase in PC processor speeds and modern FFT algorithms, this is no longer necessary. Before passing a time series through the FFT it must be first detrended to remove any long term 'influence' on the signal. The FFT algorithm can then resolve Fourier coefficients for $N/2$ frequencies between the fundamental ($1/T$) and half the maximum sampling rate or Nyquist frequency (Ny). At each frequency a real and imagery (i) or cosine and sine value can then be found.

4.2.2 Removal of Periodic Sea Surface Motion from the ETS Instrument Array Data Set

An effective way to remove an unwanted signal from data based on the principle of a frequency response to a specific periodic signal is to use an FFT filter. Firstly, the FFT in its 'raw' form is useless for application as a frequency response filter and must be converted into a two-sided power spectrum. The power contained in a unit frequency band, $\Delta f = 1/N\Delta t$ of for example, a PT times series (ϕ_{xxk}) is:

$$\phi_{xxk} = \frac{2X_k^* X_k}{1/N\Delta t}$$ [4.2]

X_k = Fourier Coefficient
X_k*= Complex Conjugate of X_k
ϕ_{xxk} = Power spectral density (units)$^2 f^{-1}$
N = Length of time series
Δt = Sampling interval (s)

The analogous equation expressing the power per unit frequency band for example, a thermistor signal can also be derived in the same manner.

$$\phi_{yyk} = \frac{2Y_k^* Y_k}{1/N\Delta t}$$ [4.3]

Y_k = Fourier Coefficient
Y_k*= Complex Conjugate of Y_k
ϕ_{yyk} = Power spectral density (units)$^2 f^{-1}$
N = Length of time series
Δt = Sampling interval (s)

Equations 4.2 and 4.3 effectively represent the spectral energy contained within each Δf of a PT and thermistor time series. The cross spectrum (a complex quantity) between the two separate Fourier series' is then calculated from:

$$\phi_{xyk} = \frac{2X_k^* Y_k}{1/N\Delta t}$$ [4.4]

X_k*= Complex Conjugate of X_k
Y_k = Fourier Coefficient of series y_m
ϕ_{xyk} = Cross spectral density (units)$^2 f^{-1}$
N = Length of time series
Δt = Sampling interval (s)

Equation 4.4 establishes a relationship through the cross spectrum between the two discrete series and estimates the coherent amplitudes and the relative phase between the two time series at frequency k. In this example, 'coherent' signals in the cross spectrum describe where in the frequency domain fluctuations in depth cause an associated fluctuation in temperature due to vertical movements of the survey vessel. For data filtering, this relationship is very useful as it allows the power fluctuations due to the vertical movements to be computed and ultimately removed form the thermistor signal.

The next second stage is to eliminate and retain the desired Fourier coefficients by means of a selected frequency response function. This 'gain' H_k function (Equation 4.5) between two series can be computed by smoothing ϕ_{xyk} and ϕ_{xxk} over m adjacent estimates about the frequency ϕ_k and then calculated as a ratio of smoothed values (Equation 4.5).

$$H_k = \frac{\langle \phi_{xyk} \rangle}{\langle \phi_{xxk} \rangle} \qquad [4.5]$$

$$\langle \phi_k \rangle = \frac{1}{m} \sum_{j=k-m/2}^{j=k+m/2} \phi_j \qquad [4.6]$$

$$C^2 = \frac{\left| \phi_{xyk} \right|^2}{\phi_{xxk} \phi_{yyk}} \qquad [4.7]$$

H_k = Gain
C^2 = Coherence squared
$\langle \ \rangle$ = Smoothed value over m number of adjacent estimates.

For a significantly coherent signal, $C^2 > 1 - \alpha^{1/m-1}$ where $\alpha = 0.05$ for 95% confidence coherence between the two Fourier series, the predicted Fourier coefficient Y_{kpred} of the y series at frequency k based on significant coherence with series x can then be computed through Equation 4.8.

$$Y_{k\,pred} = H_k X_k \qquad [4.8]$$

(Jenkins & Watts, 1968)

$$y_m = \frac{1}{N} \sum_{k=-N/2+1}^{N-1} Y_{kpred} e^{i2\pi km/N} \qquad [4.9]$$

$m = -N/2 + 1, N/2$

The resultant $Y_{k\,\mathrm{pred}}$ coherent series derived from Equation 4.8 is then IFFTed back to the time domain by Equation 4.9 and subtracted from the original transducer record. This leaves a filtered time series void of any influence from coherent signals from the pressure transducer.

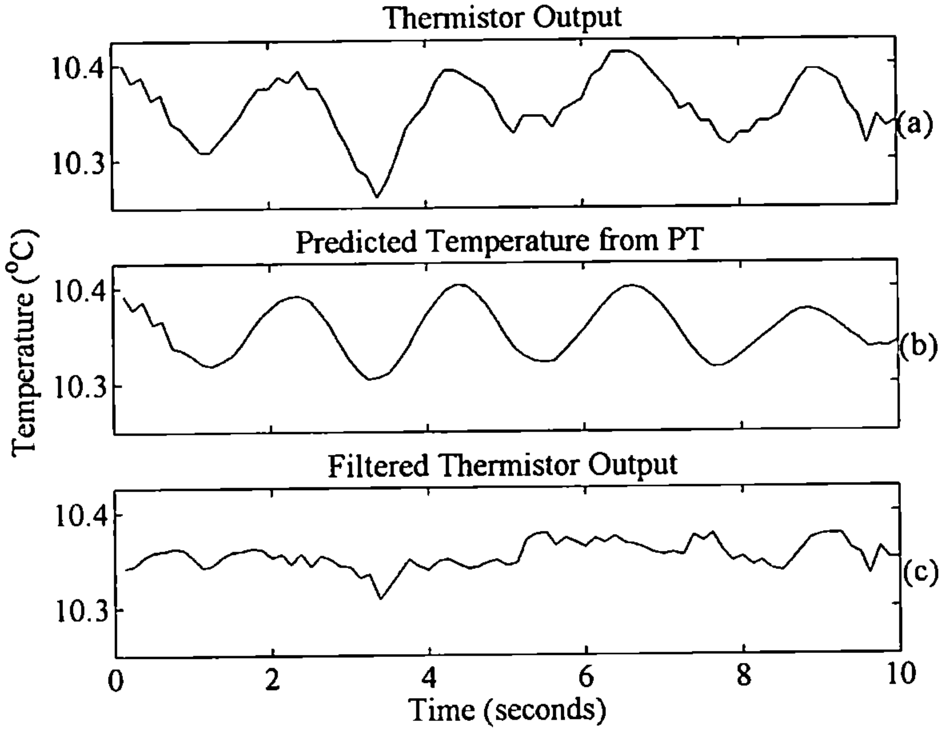

Fig 4.2: Example of pitch and roll spectral filtering procedure showing the three steps of removing contaminated signals from a thermistor output (°C). (a) Raw thermistor output; (b) Predicted temperature from PT transducer; (c) Filtered thermistor output. (see text for more details).

Fig 4.2a to Fig 4.2c illustrates how vertical oscillations in the survey vessel contaminate the temperature measurements made with a thermistor in the time domain. However, once this survey vessel induced oscillatory temperature signal has been removed as shown in Fig 4.2c through Equation 4.8, the real temperature signal appears more stable.

A further example of this successful approach to data filtering is shown through the power spectrum of Fig 4.3. This method of representing the smoothed power spectral density of periodic motion was also presented in Section 3.5 on tidal analysis. Smoothing has the disadvantage of loss of spectral resolution but is advantageous in other respects as it increases the statistical confidence of specific peaks present in the power spectrum. Statistics show that the smoothed spectral power estimate $\langle \phi_k \rangle$ will be chi-squared (χ^2) distributed with 2 *m* degrees of freedom (dof). Using these results, confidence limits can be computed where error bars reduce in size as *m* increases. To obtain the 95% confidence limits ($\alpha = 0.05$) of $\langle \phi_k \rangle$ which is an average value over say $m = 10$ adjacent estimates or 20 dof, then χ^2 tables returns values of $a = 9.59$ and $b = 34.17$. The upper and lower 95% CI can then be estimated for the power spectrum from:

$$\frac{2m\langle \phi_k \rangle}{a} \geq \phi_k \geq \frac{2m\langle \phi_k \rangle}{b} \qquad [4.10]$$

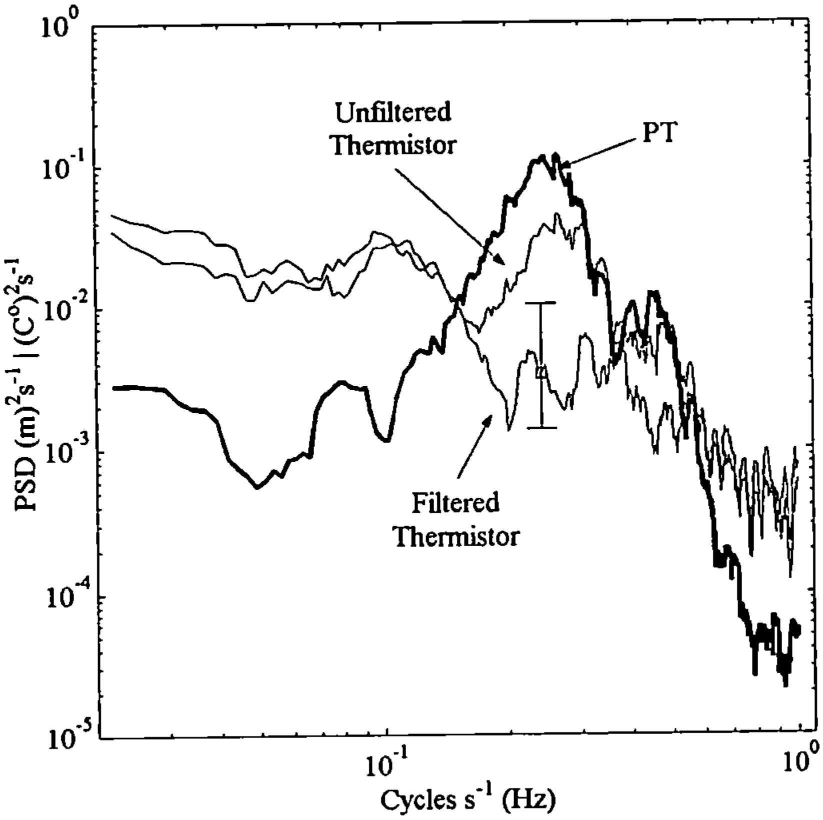

Fig 4.3: Example of the Power Spectral Density (PSD) of PT (m^2s^{-1}), unfiltered and filtered thermistor data ($(^oC)^2s^{-1}$). Error bar on the filtered thermistor spectra is the upper and lower limit of the 95 % CI calculated from Equation 4.10.

4.2.3 Low-Pass Spectral Filtering

The dynamical processes under current investigation were assumed to be present on time scales much slower than the 8 Hz sampling frequency of the instrumentation. So, in order to reduce any excessive 'white' noise due to high frequency signals (f>1 Hz) in the data set, a frequency domain low-pass filter was designed in MATLAB. The filter design comprised of windowing the calibrated time series data with a Hanning type window. The window length consisted of a 5% roll off at each end of the time series. The windowed time series was then de-trended and converted to the frequency domain through an FFT. Low-pass filtering was achieved by multiplying the time series by a gain function (1 - 0) which was then rolled off through half a Hanning type window from 1 to 1.5 Hz. This effectively retained the magnitude of all signals below 1 Hz but removed any high frequency components present in the spectra. The frequency domain series was then IFFTed, de-windowed and converted back to the original time series. Fig 4.4 illustrates how the low-pass filter removed signals above 1 Hz in a test sequence of random numbers generated in MATLAB. The results show there is no detrimental shift in the gain or phase of the post-filtered data.

Due to the proven success of these filtration procedures, all the survey data recorded from the ETS instrument array was filtered using the two described techniques before continuing with any further analysis into plume dynamics and mixing processes.

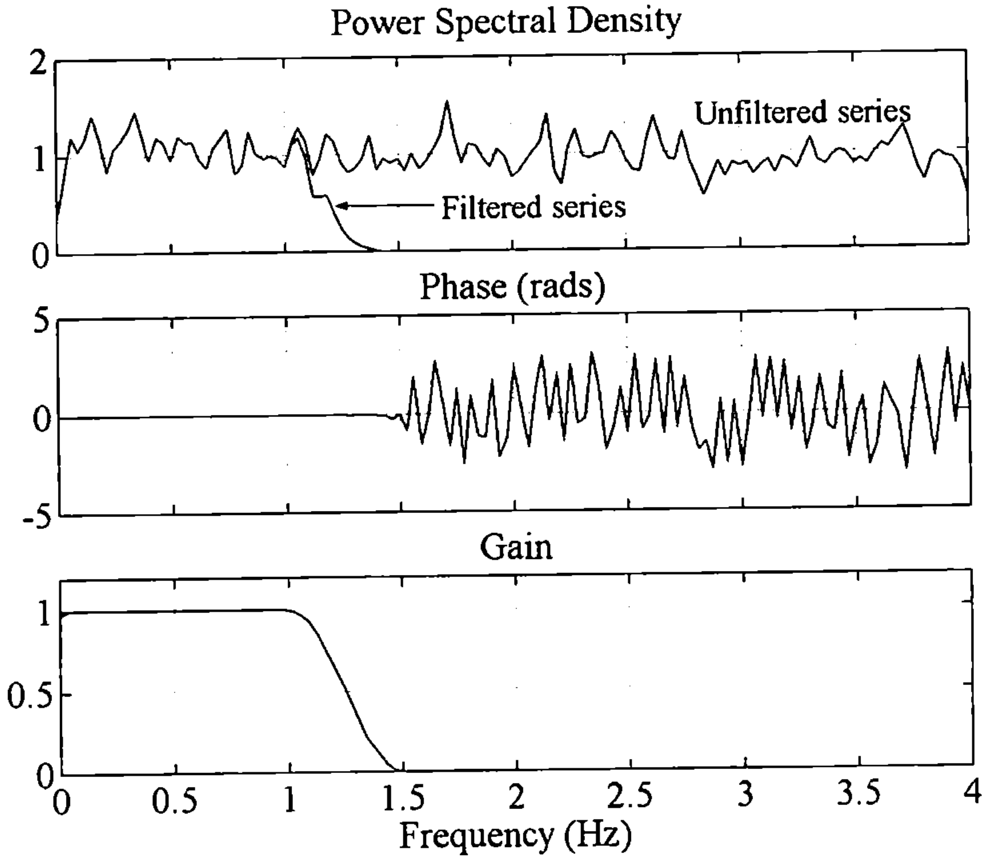

Fig 4.4: Spectral characteristics of the low-pass filter applied to a series of random numbers to demonstrate the filter characteristics.

4.3 Temporal to Spatial Conversion of Data

As the reader is aware, all data acquisition systems during the surveys were logging measurements through time in a Lagrangian, 'moving', Earth reference frame. Therefore, the accurate conversion of temporally logged data into spatial geographical co-ordinates was of paramount importance and laid the keystone for all subsequent analysis.

The conversion from the time domain (s) to spatial distance (m) was a simple process of integrating the distance between consecutive WGS84 positions recorded by the Trimble 4000 DGPS during a transect. Along with the WGS84 position string, the DGPS output also contains a time string (GMT) enabling transects to be precisely aligned through time and space with this information. In addition, differentiation of the distance between consecutive geographical positions with respect to time gave the speed of the survey vessel.

The distance between WGS84 positions was calculated through Robbins formula as given in Bomford (1980). This numerical procedure utilises the WGS84 spheroid, is correct to 1 part in 10^8 at 1600 km and was used for the computation of all transect length scales for the processed survey data. The spatial data resolution of each transect was a simple matter of dividing the total length of each individual transect by the time taken to complete the transect. With instrumentation logging at a rate of 8 Hz it provided measurements through the plume at spatial sampling increments of between 0.1 to 0.25 m ($\bar{x}$ = 0.15 ± 0.02 m) on the 25th November 1998 and 0.1 to 0.23 m ($\bar{x}$ = 0.16 ± 0.04 m) on the 26th November 1998.

To obtain some idea of accuracy of the above methods, a comparison of each transect length derived from DGPS positioning and dead reckoning is shown in Fig 4.5. The slope of the line fitted through the data returns a value of 1, illustrating that all survey transects were relatively straight. Deviation from a dead reckoned course during a transect run was attributed to ship's drift with the exception of when the fluxgate compass showed a deliberate sharp change in course of several degrees. By differentiating the deviated distance from the dead reckoned course for each instance in time, it was possible to estimate the advection velocity or drift speed for all transects.

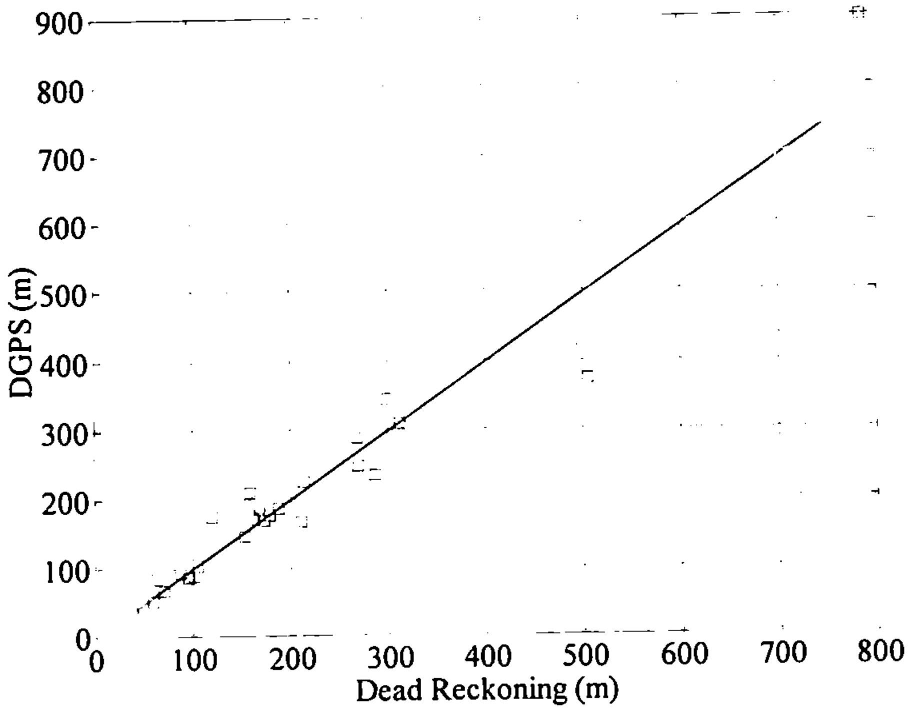

Fig 4.5: Transect length (m) calculated from DGPS vs. dead reckoning (m) for survey transects on the 25th and 26th November 1998.

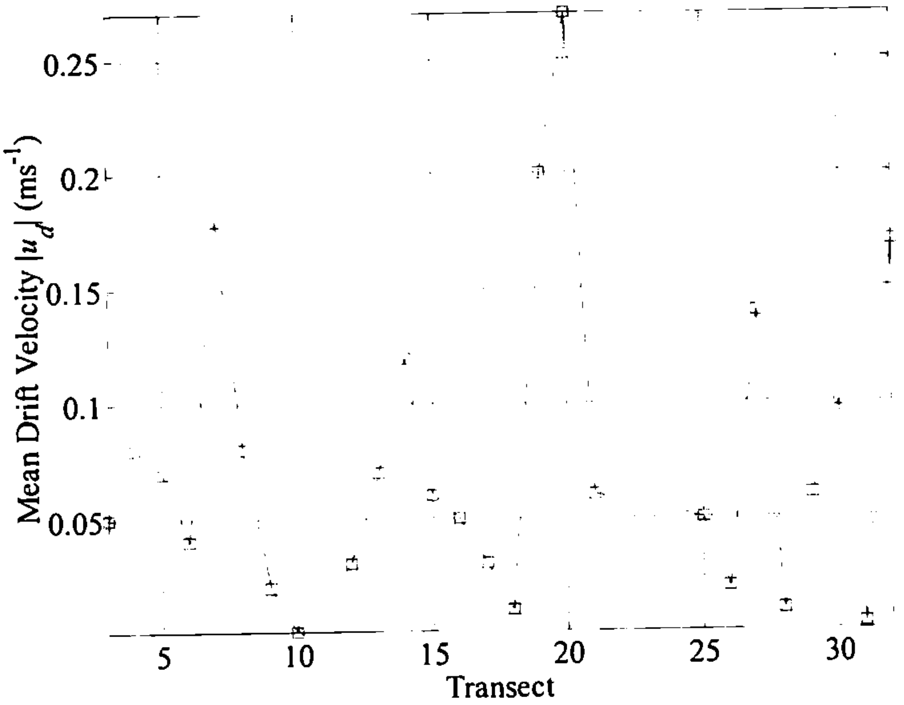

Fig 4.6: Absolute mean ships drift velocity $|\bar{u}_d|$ (ms^{-1}) for each survey transect on the 25th and 26th November 1998.

Fig 4.6 shows the mean absolute drift speeds, $|\bar{u}_d|$ for each respective transect. The majority of $|\bar{u}_d|$ values were below 0.1 ms^{-1} except for Transects 7, 14, 19, 20, 27 and 32 which seemed excessively high. Examination of the fluxgate compass records showed these values were due to sharp alterations in course or corrections made to the survey vessel to get back on a straight course rather than the presence of stronger advective currents. The removal of $\bar{u}_d$ from EMCM records is discussed in a later section of this chapter.

4.3.1 ETS Temperature Data

Fig 4.7 displays an example of filtered temperature traces recorded on plume Transect 4. The traces show the survey vessel entering the plume from left to right, where ambient seawater to the left of the plot has a temperature of approximately 10.8°C. Thermistor 3 at 0.5 m below the surface recorded an abrupt decrease in temperature of approximately 0.5°C on passage through the plume front. The greatest temperature anomalies at the 0.5 m level were measured along a horizontal distance of 4.6 m just inside of the plume front. Further inside of the plume's main body, the temperature then increased to approximately 10.5°C. At a depth of 0.95 m, the top CT probe and Thermistor 5 recorded a similar trend in their respective temperature traces. However, the temperature anomaly between the plume discharge and ambient seawater had apparently decreased with depth. This was a general observation throughout all the data sets and suggested that fresher water from the discharge due to gravitational outflow from the estuary was dominant in the upper few centimetres of the water column and became more diffuse with depth. At lower depths in the water column, the output from Thermistor 15 indicated no evidence of stratification below a depth of 3.5 m. The sharp convergence of the temperature traces in the water column near and at the front infer a region of intense mixing where the two water types converge and are forced down in the water column. The inference and quantification of mixing in this region of the plume is explored later in Chapter 5.

Section 3.8 discussed experimental protocol and put forward an assumption that plume water discharged from the estuary could be detected by the seasonal temperature anomaly. This has been substantiated by the temperature traces presented in Fig 4.7. However, it remained to be seen if salinity and, therefore, density could be related to this temperature signal. A sure way to establish whether this relationship existed was through linear regression of temperature vs. salinity from the profiling CTD cast records made during the surveys. Simple linear regression analysis of the temperature vs. salinity profiles that were simultaneously recorded by CTD casts inside the stratified plume showed the strength of the relationship between to the two scalars through the R^2 values derived from the analysis. Fig 4.8a and Fig 4.8b illustrate the range of R^2 values computed through a plot of the number of occurrences of R^2 values vs. the actual R^2 values computed by the analysis. The majority of R^2 values from this analysis were in excess of 0.95 for the majority of casts made on both surveys and supported the assumptions made earlier in Chapter 3.

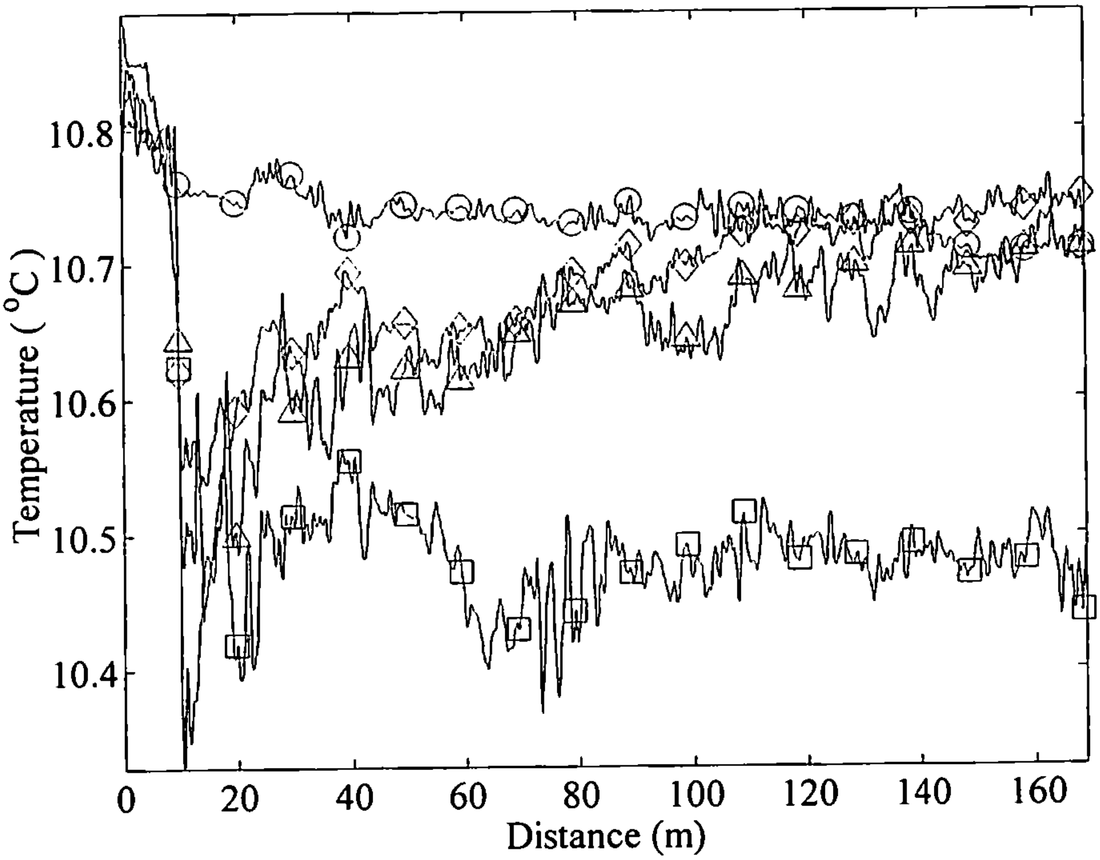

Fig 4.7: An example of a typical temperature trace (°C) from Transect 4 (HW + 2:42 hours) with respect to distance (m) recorded by Thermistors 3, 5 and 15 and the corresponding temperature output (°C) from the upper CT temperature probe. □ = Thermistor 3; Δ = Thermistor 5; O = Thermistor 15; ◇= CT.

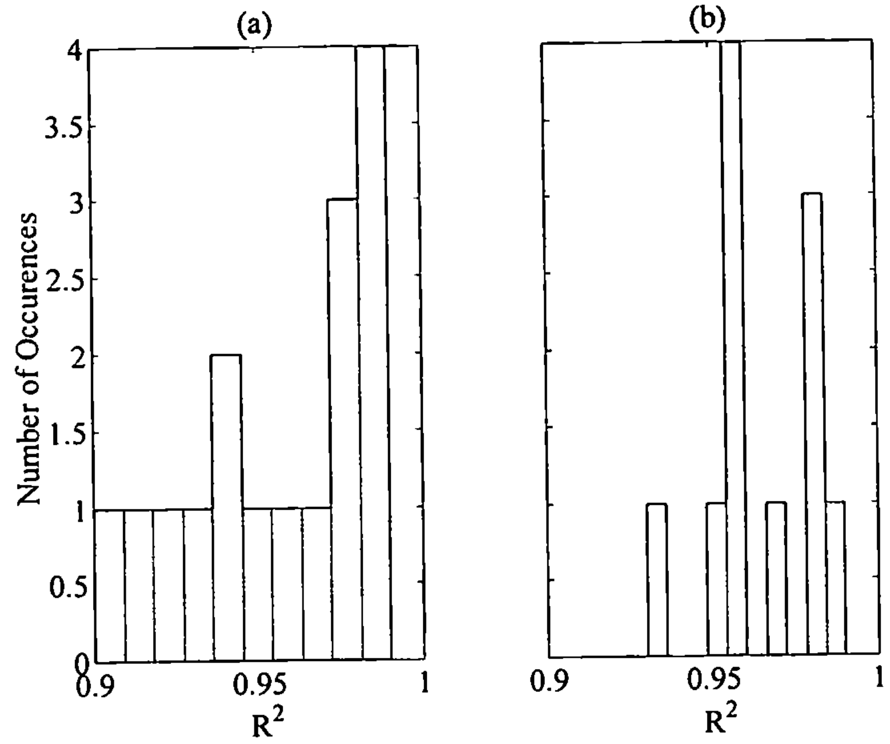

Fig 4.8: Histogram representation of number of occurrences of R^2 values vs. R^2 value for regression analysis of temperature (°C) and salinity data from CTD casts conducted inside the Teign plume. (a) 25th November 1998; (b) 26th November 1998.

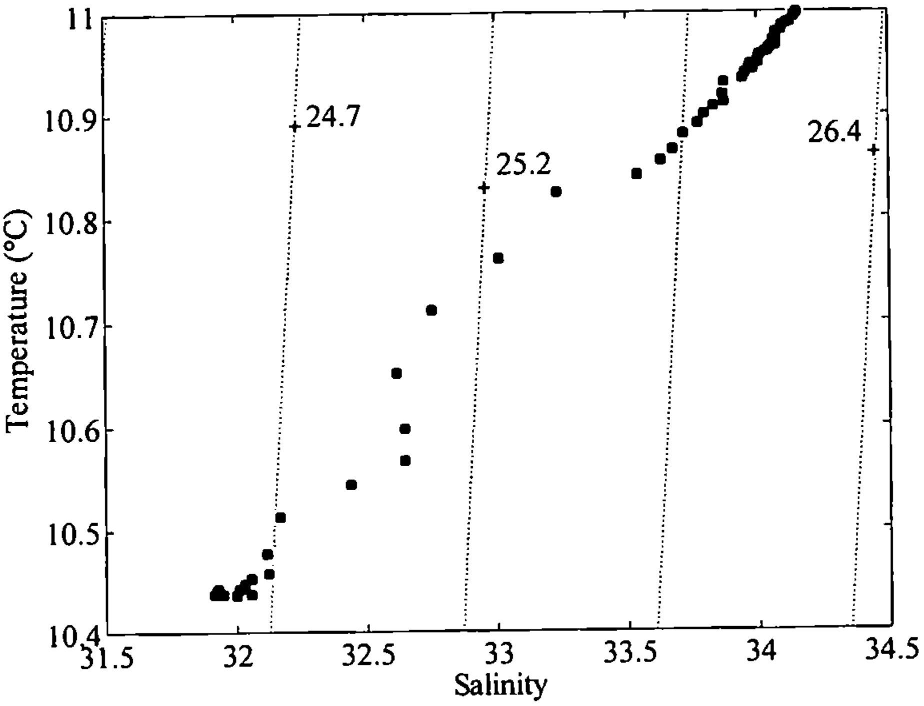

Fig 4.9: T-S diagram of a sample CTD cast illustrating the relationship of temperature (°C) and salinity with σ_t (kg m^{-3}).

Further evidence of the relationship between temperature and salinity inside the plume was seen in T-S diagrams that collate all the scalar properties of the water column. Fig 4.9 illustrates an example of the temperature and salinity data plotted with respect to water density. The concentration of data points at the upper and lower scale of the density (σ_t) contours show the formation of two water types with a region of transition in between. Lower density water present in the upper water column had a characteristic lower order temperature signature whereas higher density bottom water is represented by an accumulation of points in the upper temperature range of the cast.

In order to obtain a better physical and visual description of the longitudinal and vertical thermal structure inside the plume, outputs from all of the 15 thermistors on each transect were reconstructed into contoured isotherms. Before contouring, the filtered ETS thermistor data was smoothed with a running mean function similar to Equation 4.6 over 16 adjacent values. Smoothing effectively reduced any superfluous noise and artificial jumps in the high-resolution data set. Spatially, this corresponded to a smoothing distance of between 1.6 and 4 m as the survey vessel speed was slightly different on each frontal transect. By then passing all the smoothed temperature data through MATLAB contouring software, 2-D contour maps were produced with isotherms levels plotted at 0.1°C increments. Contouring the temperature data would ultimately aid in the analysis of physical processes that cause mixing inside the temporally and spatially developing plume.

It was also a concern that features being mapped were not in a stationary mode. Continual forcing by the estuarine and local tidal dynamics leaves any interruption of the temperature data assuming the water column is in a *quasi*-static mode. In most of the future analysis, presuming static isotherm fields in the context of each individual transect proved a reasonable assumption as the time taken to complete a single transect was relatively brief on most occasions. For example, in a worst case scenario, if it is assumed that radial spreading velocity was in order of 0.20 ms^{-1} then the distance of longitudinal and lateral radial expansion over 512 seconds (or one file) is 102.4 m. In most instances this expansion distance was considerably less as the majority of transects were shorter on both a temporal and, consequently, spatial scale.

Fig 4.10 illustrates an example of the isotherm field produced from the 15 temperature traces of Transect 4. Isotherms clearly indicate the thermal structure of the outflow plume with respect to the ambient water. Temperature outside the plume showed a slight degree of fluctuation and the trend suggested the presence of cooler water at the nearshore. This cooler nearshore water mass was a possible artefact of previous outflow events where brackish estuarine water had not been fully dispersed as outside the Tees estuary (Lewis, 1984).

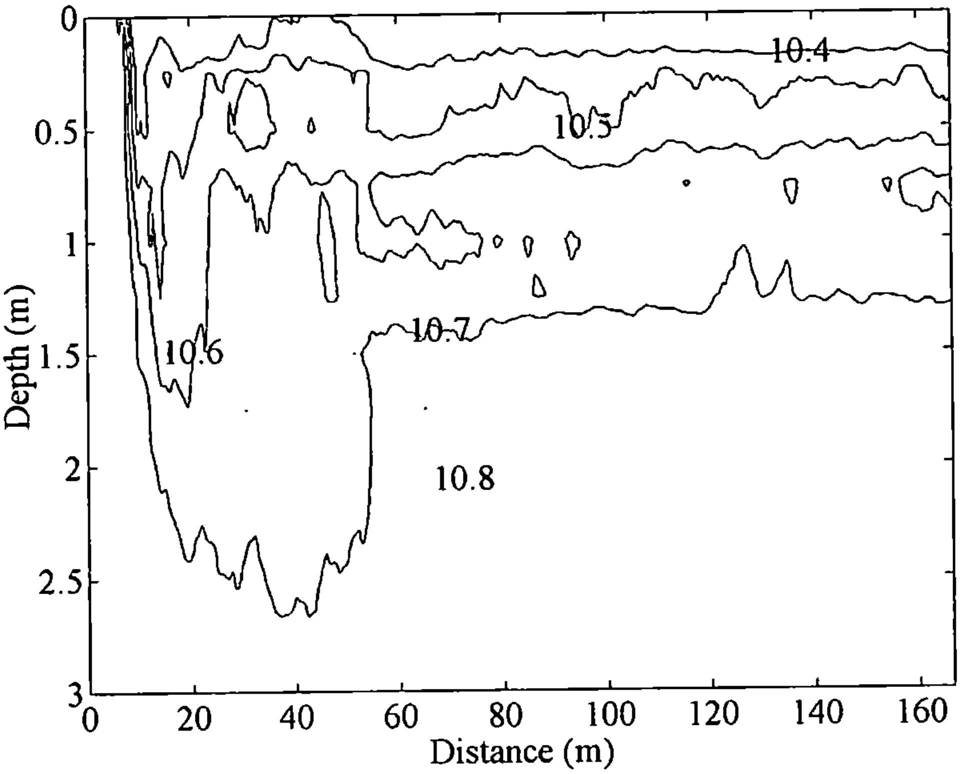

Fig 4.10: Temperature contour plot (°C) of thermal field in Transect 4 (HW + 2:42 hours) vs. distance (m). The plot illustrates the structure of isotherms in the frontal region and body of the spreading plume.

4.3.2 EMCM & Velocity Corrections

This next stage of the correctional procedure proved the most time consuming and thought provoking of all the data processing work. The study conducted by O'Donnell (1997) in the Connecticut river plume had highlighted the necessity to apply correctional measures to bi-axel EMCM's used and positioned in a similar manner as the current project. Following O'Donnell's example, similar techniques were applied to EMCM data from the present data set and the importance of these procedures will become evident to the reader on progression through the next section.

The three EMCM's used on both surveys were mounted on the ETS in a x - y configuration to measure horizontal flow in the along frontal and across frontal direction respectively. After frequency domain filtering, as discussed in Section 4.2, followed by the calibration of the raw velocity data, a problem with the EMCM offsets became apparent. Velocity measurements recorded by the EMCM's in ambient seawater away from any influence of stratification and strong vertical shear showed significant differences in flow speed despite general flow trends being the same. The large deviations in current flow measurements were found as a result of 'wandering' EMCM voltage offsets. Unfortunately, similar problems with voltage offsets have occurred in many previous studies when using EMCM's in the field (D.A. Huntley, *pers.comm.*). After reviewing the present study's objectives and contemplating the problem, it was decided that future analysis could proceed using the EMCM data on the assumption that:

1. Vertical shear in homogenous seawater outside the influence of plume stratification and at depths not exceeding the lower current meter is negligible. This then allows values to be determined for the relative offset values when in ambient seawater.
2. Based on assumption 1, flow is set to zero outside the plume layer.

The spatial position of zero flow for each EMCM record was determined by examining the thermistor outputs from the ETS. The abrupt transition from ambient seawater to plume water was, as shown earlier, marked by a sudden decrease in temperature. The zeroing procedure was thus effected by subtracting the mean velocity reading of each EMCM record in the immediate section of ambient water before entering the plume front from its own respective record. Ideally, this method of correction should not have been necessary. However, in view of the problems encountered with the EMCM offsets, it was now possible to make relative comparisons of flow in a moving reference frame with the front and derive shear profiles within the stratified plume. Therefore, from hereinafter, it must be continually remembered that all velocity measurements were made with respect to ambient water just outside the plume front.

The next stage of the EMCM correctional procedure was to remove the effect of velocity fluctuations due to slight changes in the survey vessel speed. Survey vessel speed was calculated by differentiating the distance between consecutive geographical position fixes (P) from the DGPS with respect to time ($\partial P/\partial t$) and then calculating the u and v components of the survey vessel's vector velocity (u_s, v_s). To complement the EMCM offset correction, the survey vessel's vector velocity components from outside front ($\overline{u}_{so}$ and $\overline{v}_{so}$) were subtracted from the actual survey vessel's vector velocities. Then by subtracting or adding the corrected u_{sc}, v_{sc} (this depended on direction of travel into (+) or out (-) of the plume) to or from each EMCM's u and v components, flow speed relative to ambient water was obtained. This part of the correctional procedure also removed the effects of the survey vessels or 'ships drift' $\overline{u}_d$ which was included in $\overline{u}_{so}$ and $\overline{v}_{so}$. A summary of all these corrections can be expressed as series of terms:

$$u_s - \overline{u}_{so} = u_{sc}$$

$$v_s - \overline{v}_{so} = v_{sc}$$

$$u \pm u_{sc} = u$$

$$v \pm v_{sc} = v$$

4.3.3 Velocity Vector Rotations

All efforts were made during the surveys to remain perpendicular to a front when completing an across frontal transect. However, once navigating a survey vessel at sea this task is by no means straight forward, as no synoptic view of the plume's shape is available on deck whilst surveying. An observer with VHF radio can be advantageous inshore but further offshore this serves no benefit. Therefore, despite accurate navigation equipment, deviations in direction from a presumed across frontal transects appear to be shown in Fig 4.1a and Fig 4.1b. However, in defence, plume fronts meander and are not on scales O(100 m) a constantly straight linear feature. Hence, what is deemed locally as a front normal perpendicular crossing may be seen as off course with respect to the larger scale spreading of an entire plume discharge.

To establish some commonality between all the velocity records a procedure had to be developed which allowed the velocity data to be rotated into a co-ordinate system, $u'(x')$ and $v'(y')$ that was parallel and normal to each local frontal crossing respectively. Resolving each frontal transect into this proposed co-ordinate system would allow later inter-comparisons of velocity records or derivative functions of the velocity data from each individual transect.

To estimate the frontal alignment with respect to north, a method was devised that relied upon both field observations and basic frontal dynamics. From the DGPS data, the distance (L) and the time difference (Δt) between consecutive frontal crossing could be used to estimate the orientation of the front with respect to fixed Earth co-ordinates through Equation 4.11. Equation 4.11 assumes that the frontal Froude number remains at a constant $\sqrt{2}$ (Garvine, 1984) and an interfacial wave speed (c_i) of 0.14 ms^{-1} was derived form CTD casts in the 1995 study. From these two values, frontal speed can be then estimated by $u = Fr_i\ c_i$. The angle θ perpendicular to the local frontal crossing or direction of outward propagation (y') with respect to the position of the prior frontal crossing can be estimated from:

$$\cos\theta = \frac{u\Delta t}{L} \qquad [4.11]$$

$\cos\theta =$ Angle (^{o}) to bearing between frontal positions
u = Speed of frontal propagation (ms^{-1})
Δt = Time between frontal crossings (s)
L = Distance between frontal positions (m)

Therefore, following these assumptions, the predicted along frontal alignment (x') should lie normal to θ as shown schematically in Fig 4.11. Results from Equation 4.11 gave good agreement when compared with the earlier X-band radar captures. This provided a good first order estimate of the rotational angles required to correct velocities through a common local reference frame. Consequently, all flow velocity records (u'', v'') were then rotated to the angle θ into a reference frame $u'(x')$ and $v'(y')$, where y' is locally normal to the frontal.

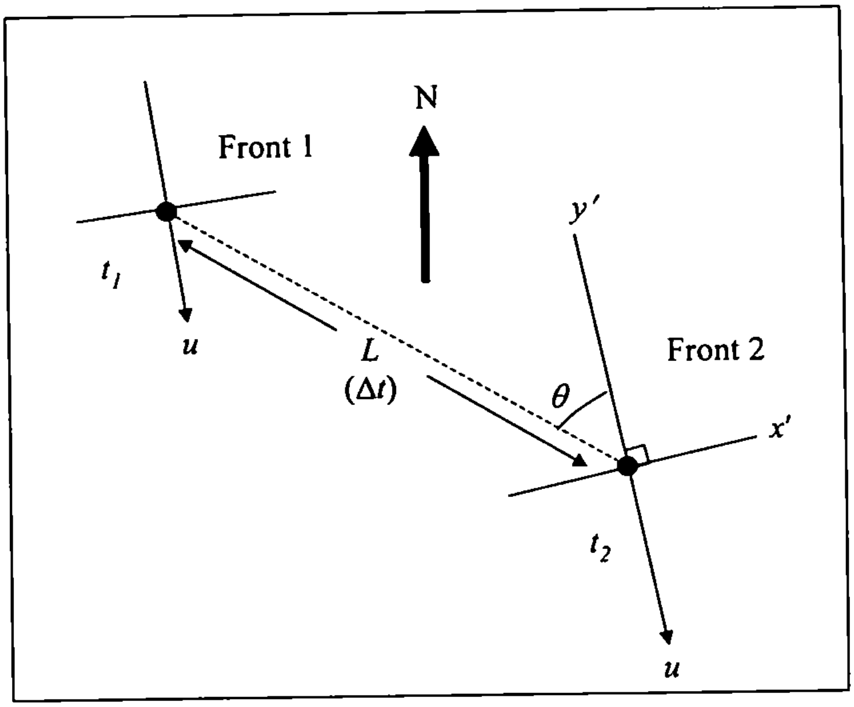

Fig 4.11: Schematic diagram of EMCM rotational method employed to correct flow velocities. Note u is used to represent outward propagation velocity to remain in convention with the derivation of Fr_i.

The exact rotation angle of rotation for each EMCM point sample was determined by the deviation of the fluxgate compass reading from the chosen axis of alignment. Simultaneous compass bearings and EMCM records made these rotations a relatively easy process. The original u'' and v'' components of each EMCM were then converted into a new x', y' co-ordinate system corresponding to velocities, u' and v' through Equations 4.12 and 4.13. The appropriate angles of rotation and axis according to Equation 4.11 are presented in Appendix 1.

$$u' = u''\cos\theta' + v''\sin\theta' \qquad [4.12]$$

$$v' = -u''\sin\theta' + v''\cos\theta' \qquad [4.13]$$

u''= x''-component of flow (ms^{-1})
v'' = y''-component of flow (ms^{-1})
θ' = Angle of rotation (°)

For consistency and uniformity in all future analysis, all three EMCM's were then aligned into a reference frame that would show each transect entering the plume from left to right (ambient water seawater into the plume discharge). Transects conducted from inside the plume to ambient water were rotated to a reciprocal bearing and each EMCM flow sign (+ or -) then reversed. Where necessary, the temperature and CT data was transposed to complement the changes in EMCM data.

4.4 Summary of Data Processing

The procedures described in the previous sections on data processing discuss in detail the methods used to correct instrumentation to estimate the small-scale plume and plume frontal hydrodynamic features in a moving reference frame. The laborious methods used were considered necessary to increase confidence in the high-resolution data sets as averaging was to be kept to a minimum in all-future analysis. The majority of the data recorded by the ETS thermistor and CT probes was of a high quality with the exception of a few corrupted ETS files caused by an intermittent fault in the ETS instrumentation. The offset problems encountered with the EMCM's restricted the present results to velocity readings relative to both ambient seawater and to each other (vertical shear). However, despite this limitation, the EMCM's still provided useful data that was used in further analysis of mixing and flow parameters inside the Teign plume.

4.5 Tidal Influence on Plume Formation

Before committing to an in depth analysis of ETS and EMCM data it was decided to return and look at the effects of tidal hydrodynamics on plume spreading. The main aim of this exercise was to examine the inter-relationship between the tidally-driven discharge from the estuary and the formation of the plume.

On the 25th November 1998 environmental conditions permitted sampling over a full ebb tidal cycle. The positions of each frontal transect of the radially spreading plume is shown in Fig 4.1a. Plume formation started at approximately HW + 2:32 hours (12:08 GMT) where a frontal foam line formed next to 'The Ness'. Frontal regions progressively became more defined as the plume spread offshore and as the radial shape began to manifest. Then, after a period of visible intensification of outflow inside the plume, spreading continued for some hours and eventually lost definition after approximately HW + 6:00 hours. By this time it was estimated the total area of plume dispersion was in the order of 20 km^2.

Recalling the tidal analysis, simple barotropic-friction model of estuary outflow and scaling arguments of Section 3.5, it was suggested that the tidally modulated barotropic contribution to the pressure gradient force was the dominant force in the generalised longitudinal equation of motion. Observations from the current study saw well-defined frontal boundaries throughout plume development. This would suggest that as the area of plume discharge increases, the volume of freshwater or discharge velocity into the coast must also increase to maintain continuity at the sharp frontal boundaries observed on the perimeter of the plume. The next sub-section physically describes the observed spreading phenomena through present observations and archived tidal current meter and tide gauge data.

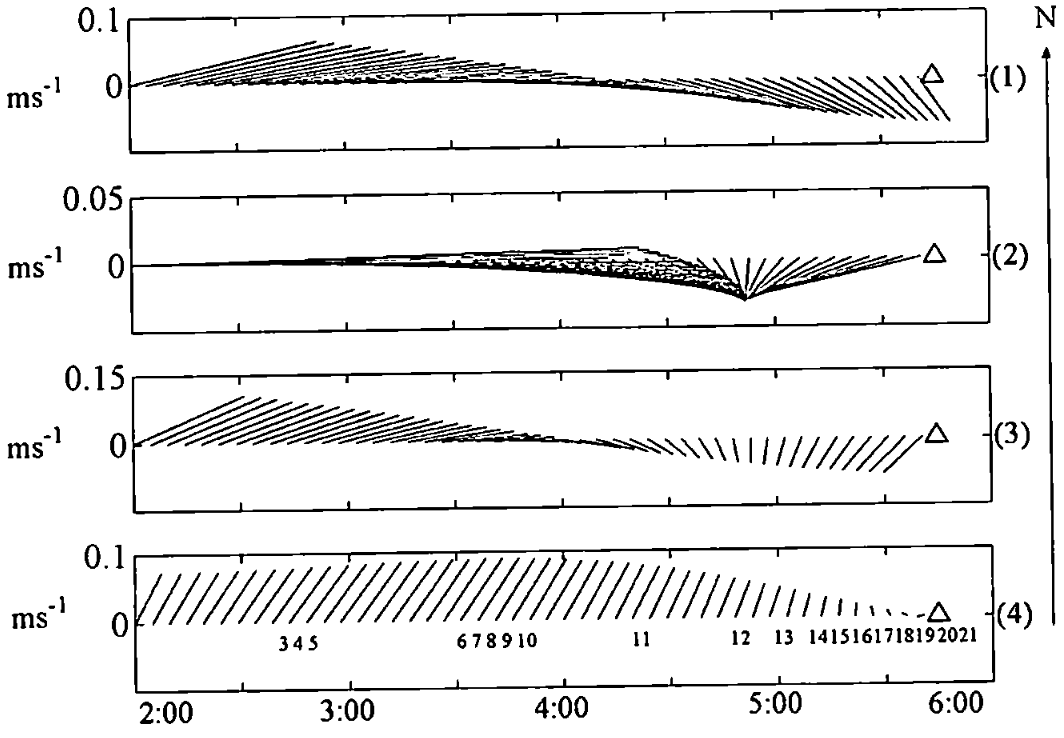

Fig 4.12: Vector stick plots (ms^{-1}) of the predicted tidal currents at moorings RCM 1 to 4 from HW + 2:00 hours to Low water (15:15 GMT) on the 25th November 1998. Δ = LW (15:15 GMT).

Fig 4.12 displays a series of tidal current predictions for the 25th November 1998 corresponding to the geographical locations of the four RCM moorings, as shown in Fig 3.5. The plot is limited in duration to a scale that enhances the resolution during the time of the observed plume formation and spreading. In addition to current speed and direction, transect numbers are also plotted with respect to time to illustrate the magnitude and direction of the coastal tides whilst surveying. The results from these predictions show the inshore tidal currents were directed towards NNE when the plume front was first observed at HW + 2:32 hours (12:08 GMT). The predicted barotropic current directed out of the estuary mouth during the early phase of plume development illustrated in Fig 4.13 shows a corresponding peak in the outflow velocity. The vector representation of the coastal tides shown in Fig 4.12 and the estuarine outflow velocity displayed in Fig 4.13 show how at the time of plume fronts formation there would be a strong flow convergence between the barotropic tidal current from the estuary and the NNE coastal tidal stream at HW + 2:32 hours. These predictions support the field study that observed frontogenesis next to 'The Ness' headland where the two water masses initially converge forming the plume front. Prior to the present study, similar well-defined frontal features were also seen to the south of the estuary in the earlier time series of X-band radar captures recorded in 1995 (see Chapter 3).

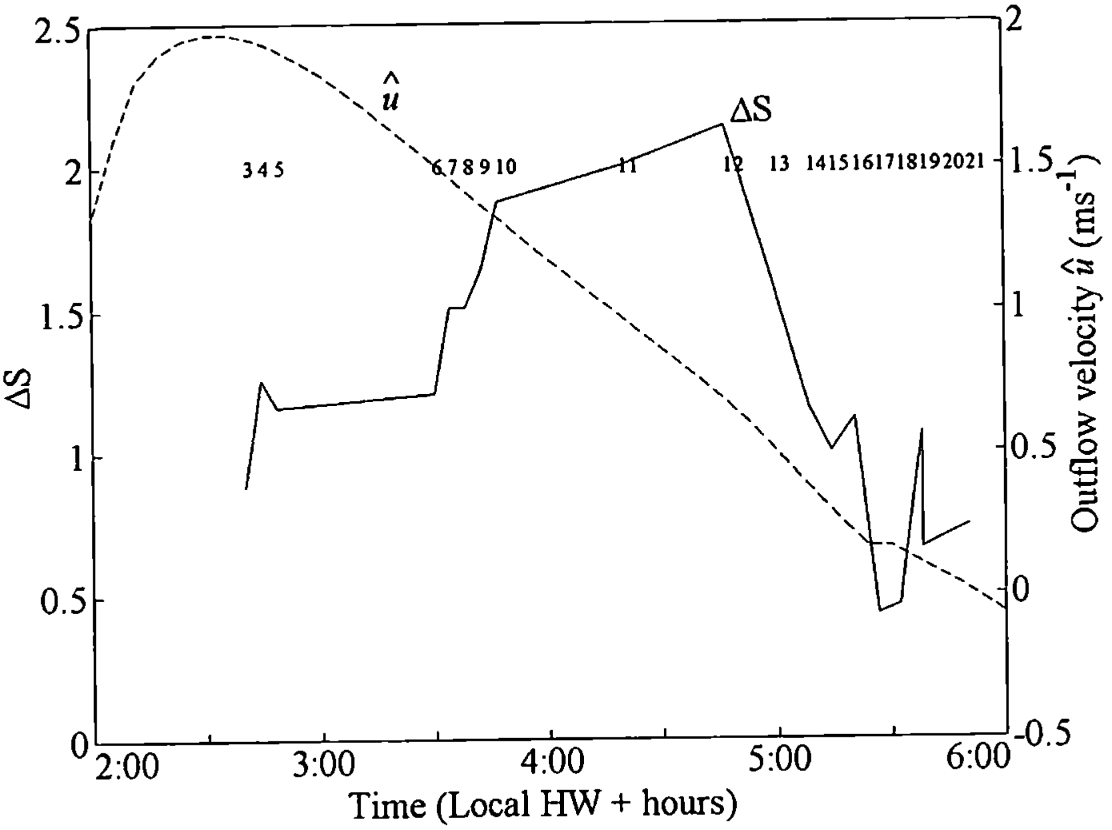

Fig 4.13: Mean salinity anomaly (ΔS) behind the front and modelled channel outflow velocity $\hat{u}$ with respect to time (HW + hours) for the 25th November 1998. — = Salinity; --- = ms^{-1}. Transect numbers are also plotted with respect to time after local HW.

4.5.1 Plume Spreading & Salinity behind the Front

As the ebb tide progressed, coastal tidal current vectors continually decreased in magnitude and were directed easterly offshore (see Fig 4.12 (3)). This was followed by the formation of a clearly defined radial plume that began to form around the estuary mouth. From deck observations it was possible to see a visible intensification of the plume gravity current at HW + 3:12 hours (12:48 GMT). During this time, the plume front appeared elevated on the brackish water side of the frontal convergence zone with respect to the ambient seawater. This period of intensified flow towards the front coincided with an increase in the salinity anomaly (ΔS) between the ambient seawater and the brackish water plume.

Fig 4.13 displays a time series of the mean salinity anomaly in the first 40 m behind the plume front, between the upper and lower CT probes attached to the ETS. The maximum salinity anomalies behind the front had a phase lag of approximately 1:30 hours behind the predicted maximum outflow from the estuary mouth. Hence, the earlier statement that suggested a linear relationship between salinity behind the front and the barotropic outflow velocity from the estuary (i.e. maintenance of continuity at the front) is not entirely justified by solely considering the barotropic flow from the estuary. However, as the scaling argument of Section 3.5 suggests, the establishment of longitudinal density differences between the estuarine source and ambient coastal water adds a substantial baroclinic component to the outward pressure gradient force present in the buoyant layer of the plume discharge. For example, at the time approaching the maximum salinity anomaly (approximately HW + 4 hours or 1:14 hours after frontogenesis), the baroclinic component of gravity flow to momentum across the plume is estimated as 9.14×10^{-5} ms^{-2}. This combined with the momentum due to the across plume barotropic gravity flow of 89.7×10^{-5} ms^{-2} and an offshore coastal tidal stream would effectively increase the flow velocity from the estuary towards the plume front. Thus, the increase in the total flow rate due to baroclinic forcing across the plume provides the additional flux of less saline water towards the front shown in Fig 4.13. This baroclinic flow also maintains continuity in the far field of the plume discharge as the ebb flow velocity through the outlet channel begins to subside.

Towards local LW, surface salinity values began to decrease resulting from the termination of flow from the estuary and the turning coastal tide. Plume spreading then ceased, became diffuse and was difficult to survey due to lack of frontal definition. This marked the end of gravitational spreading from the estuary and led to the eventual 'cut-off ' of the plume from the estuary by the flooding tide as described in Chapter 2.

4.6 Bulk Flow Dynamics & Physical Properties at the Plume Front

After examining the effects of tidal influence on larger scale plume spreading dynamics, attention was then turned to the properties of the observed flow in and near the plume fronts.

Intrigued by the observed intensification of flow inside the plume and the presence of a near surface type bore behind the frontal convergence, it was first decided to examine the development of longitudinal flow dynamics inside the plume. The multiple across frontal transects recorded during the surveys on the 25th and 26th November were conveniently recorded in temporal and spatial steps through plume development that allowed group-time averaging to be applied to the data. The basis of this averaging procedure was to attach some statistical confidence to the observed flow rates.

Velocity measurements recorded along each transect at three levels (0.95 m, 1.85 m, 2.9 m) in the water column were first grouped into chronological order specific to time and spatial locality after local HW. Each individual transect in a group was then spatially aligned with respect to each other through MATLAB rational approximation software. The software derived a fractional value that expressed the actual sampling rate of a transect to the specific group's mean sampling rate. By then multiplying each individual transect's sampling rate by the rational approximated value the data was effectively re-sampled into the same spatial scale as the mean sampling rate of the group. After spatially aligning all the EMCM records at each specific level in the water column, each group was then averaged. Running mean smoothing was then applied to each set of grouped values over a spatial distance that varied between 2 to 3 m according to the mean group-sampling rate. This produced a mean velocity ($\bar{v}$) ± standard deviation (σ_v) for each level in the water column at a group mean distance from the estuary mouth and group mean time after local high water. Negative flow ($-\bar{v}$) represented flow towards the front with respect to ambient seawater (non-plume water). Each specific group is shown in Table 4.2.

Transect Group	Transects	Mean Time (GMT)	HW (09:36) + hours
a	3, 4, 5	12:18	2:42
b	6, 7, 8, 9, 10	13:12	3:36
c	13, 14, 15, 16,17,18	14:48	5:12
d	19, 20, 21	15:18	5:42
e	25, 26	13:46	3:23
f	27, 28, 30	13:50	3:27
g	31, 32	14:22	3:59

Table 4.2: Allotted transect groups for velocity averaging on the 25th and 26th November 1998. Refer to Fig 4.1a and Fig 4.1b for the geographical location of each group.

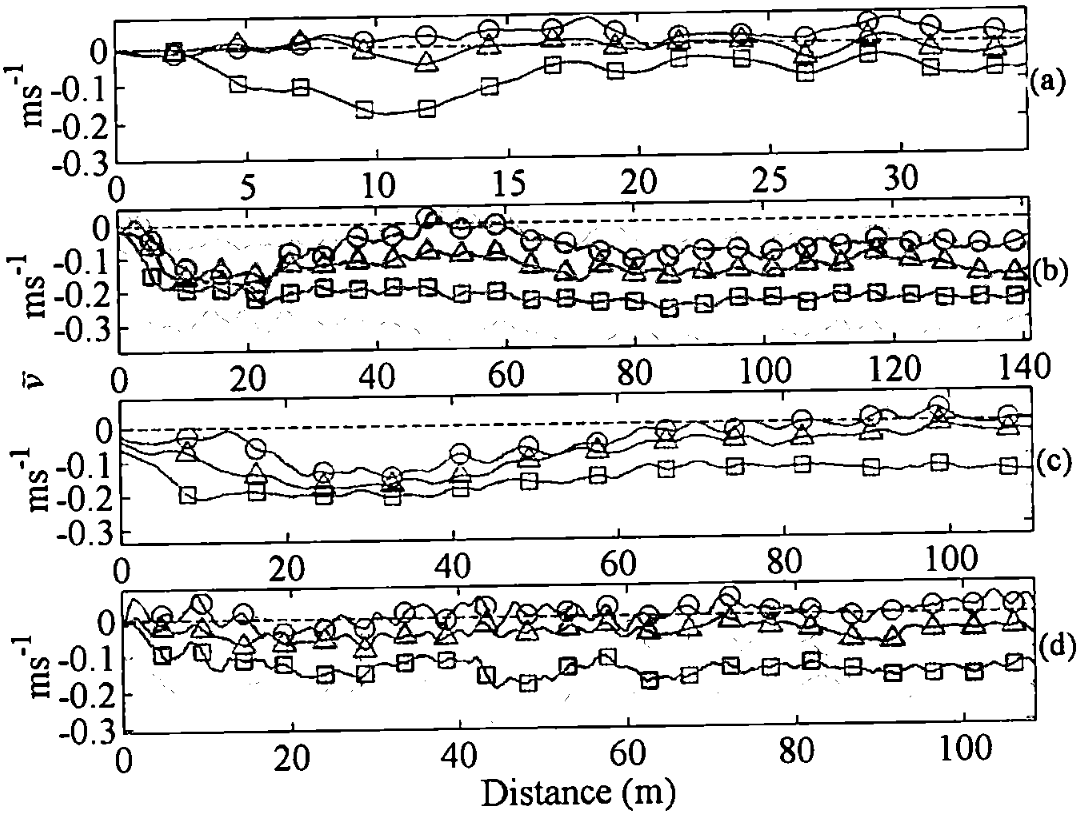

Fig 4.14: Group averaged across frontal velocity profiles, $\bar{v} \pm 2\,\sigma_v$ (ms^{-1}) versus distance (m) on the 25th November 1998. □ = 0.95 m; Δ = 1.85 m; O = 2.9 m entering the plume in the first 5 m on the left-hand side of the diagram. (a) HW + 2:42 hours; (b) HW + 3:36 hours; (c) HW + 5:12 hours; (d) HW + 5:42 hours.

The results from this analysis are illustrated in Fig 4.14 through four sets of mean across frontal velocity profiles recorded on the 25th November 1998. The mean velocity ($\bar{v}$) data showed a significant gravity current flow towards the front in the upper 0.95 m of the water column. The magnitude of the current varied from -0.1 ms^{-1} to -0.25 ms^{-1} through the spreading cycle. At HW + 2:42 hours across frontal flow was predominantly in the upper 0.95 m of the plume as $\bar{v}$ was not significant from zero below this level. Zero flow was representative of ambient water, thus 2-layer shear flow would only extend to depths just beyond the 0.95 m level. This concurred with the temperature contour plot produced from Transect 3 ETS data shown in Fig 4.15. Temperature contours illustrate the shallow extent of stratification during the earlier stages of the gravity driven outflow from the estuary.

As offshore flow intensified due to the combined effect of the gravity outflow and the easterly directed coastal tide, a corresponding increase of flow towards the front was also recorded at HW + 3:36 hours. Near surface $\bar{v}$ remained at approximately -0.25 ms^{-1} whereas negative flow which initially suggested a surface layer extending beyond a depth of 2.9 m at the front, tended towards zero some 45 m behind the front at the approximate position of where the isotherms shallow out as shown in Fig 4.16. Further into the plume body, flow at the lower levels in the water column was again directed towards the front.

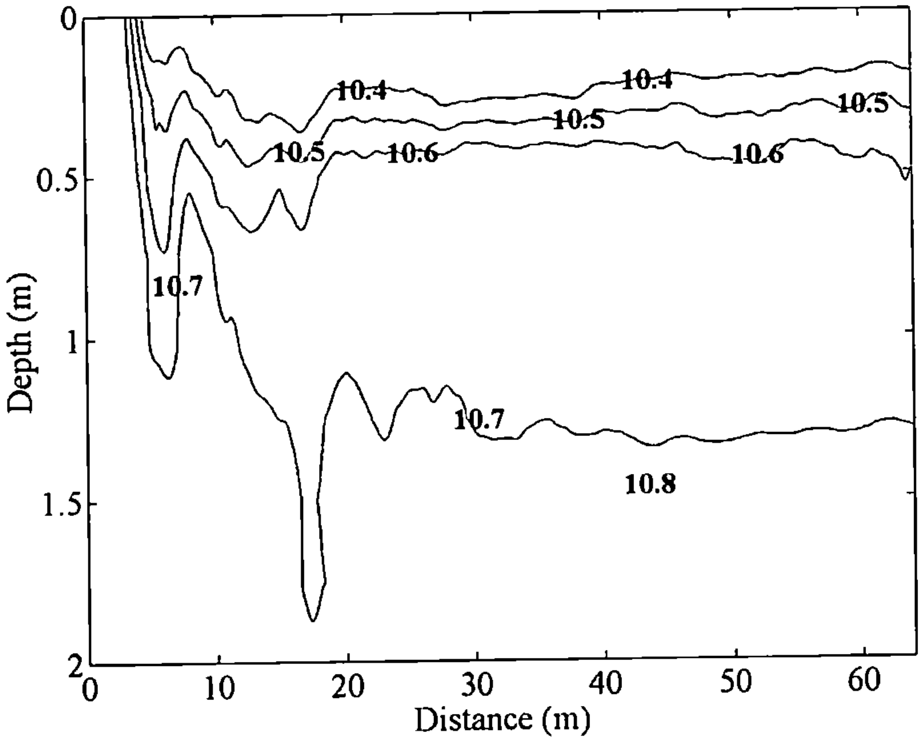

Fig 4.15: Temperature isotherm contours (°C) vs. distance (m) of Transect 3 recorded at HW + 2:40 hours (12:17 GMT) 25th November 1998.

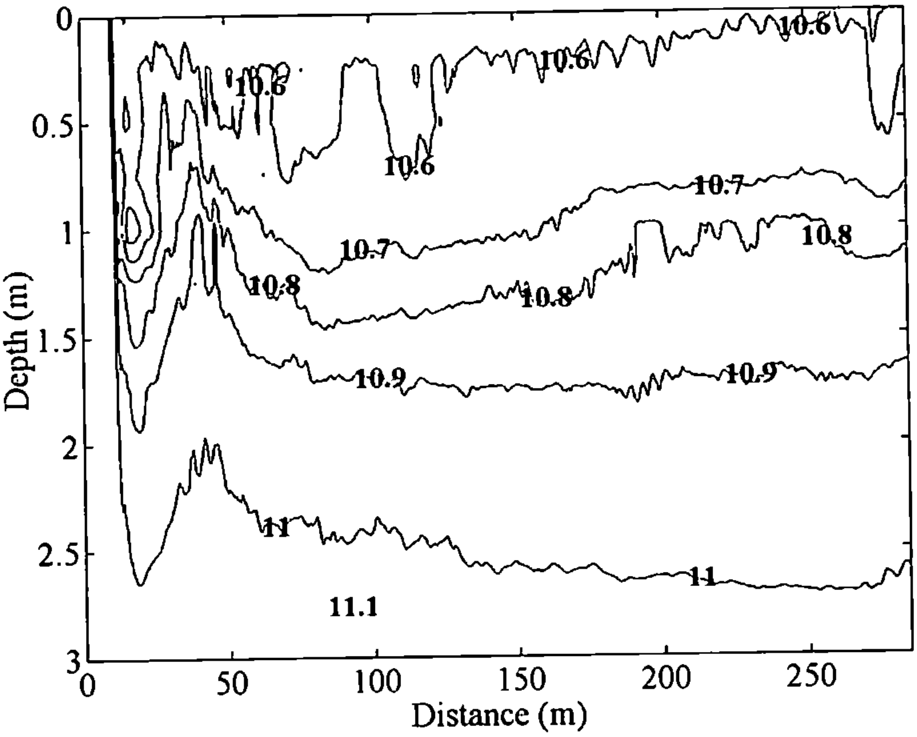

Fig 4.16: Temperature isotherm contours (°C) vs. distance (m) of Transect 10 recorded at HW + 3:42 hours (13:18 GMT) 25th November 1998.

The same deceleration of $\bar{v}$ at the 1.85 m and 2.9 m level some distance behind the front was also evident at HW + 5:12 hours. Mean velocities ($\bar{v}$) recorded at HW + 5:42 hours showed a general decrease in the intensity of the outflow. Gravity outflow appeared once more restricted to the upper 0.95 m of the water column as $\bar{v}$ below this depth had diminished towards zero.

From the isotherm records it was possible to establish that the shape of the front and the region trailing the convergence resembled the form of gravity head produced by a laboratory based physical model as described in Britter & Simpson (1978). Photographic 'shadowgrams' as illustrated in Plate 4.1 of the physical model's tank experiments showed an abrupt steepening and deepening of the gravity current at the stagnation point. This was trailed by a deeper gravity head region on the source side of the release experiment. An obvious similarity appeared between the form of gravity head wave observed in the current study's ETS temperature profiles recorded in the field to that produced in the laboratory by Britter & Simpson (1978).

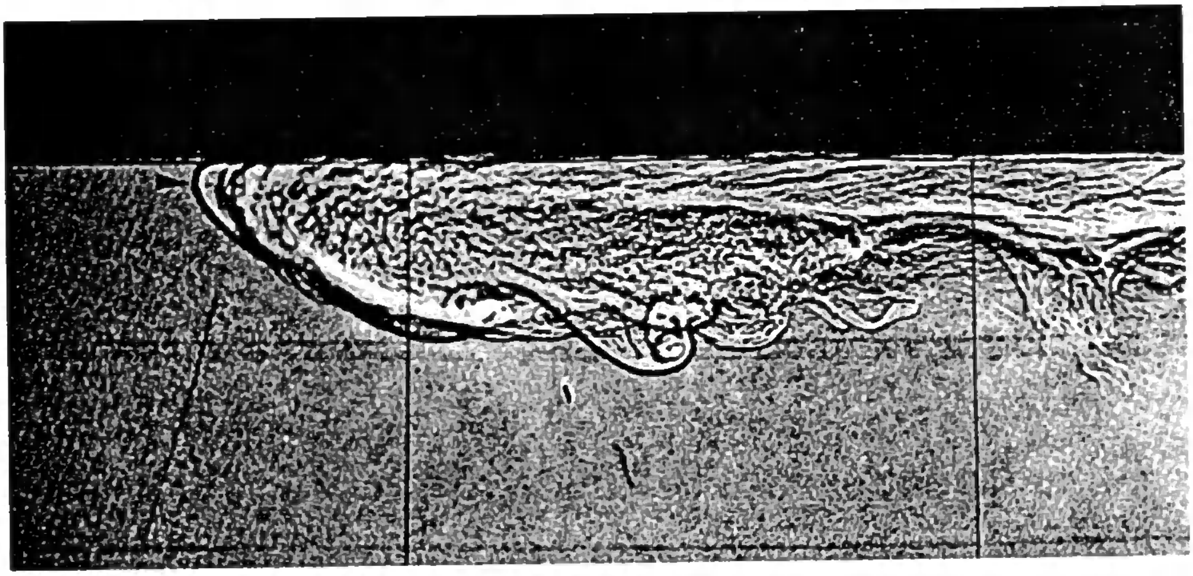

Plate 4.1: Shadowgram of a gravity current tank experiment that shows the formation of a deeper gravity head region followed by K-H billows. (From Britter & Simpson, 1978).

For further verification of the flow rates and flow structure inside the plume, replicate group averaged velocities and isotherm records were examined for frontal transects completed on the 26th November 1998. The flow velocities presented in Fig 4.17 are similar to those observed on the previous day's surveys. Unfortunately the entire survey time was restricted to only 41 minutes (HW + 3:19 to HW + 4:00 hours) due to the deterioration of sea conditions. Despite a limited data set, the three sets of group averaged velocities illustrate a similar trend in across frontal flow ($-\bar{v}$) to that observed on a full ebb tidal survey on the 25th November.

The results from the analysis of the across frontal velocity profiles suggest by their respective intensities with respect to ambient seawater the presence of a strong convergent flow at the front. A quantitative estimate of the velocity divergence or convergence can be computed through simple differentiation of each group averaged velocity record with respect to distance ($\partial\bar{v} / \partial y$). Differencing each velocity record quantitatively exaggerated the variability in each velocity profile at each level in the water column. Theoretically, the maximum peaks in the differenced velocity profiles should identify the position of convergent flow or, in the instance of a plume front, the position of downwelling. To estimate the uncertainty in each differentiated velocity value, a method applied by O'Donnell *et.al.* (1998) to a similar problem was adopted to calculate the threshold of detection around each respective estimate. This method of error estimation utilises the standard deviations ($\bar{\sigma}_v$) for each smoothed bin of the original velocity data. The uncertainty of each estimate or detection threshold is then calculated through Equation 4.14.

$$\frac{\partial \bar{v}}{\partial y} uncert = \sqrt{2}\sigma_v / y_b N_b \bullet 2 = s^{-1} \qquad [4.14]$$

$\partial \bar{v} / \partial y$ *uncert* = Uncertainty threshold of across frontal velocity divergence / convergence (s^{-1})

σ_v = Standard deviation
y_b = Length of sample increment (m)
N_b = Number of samples

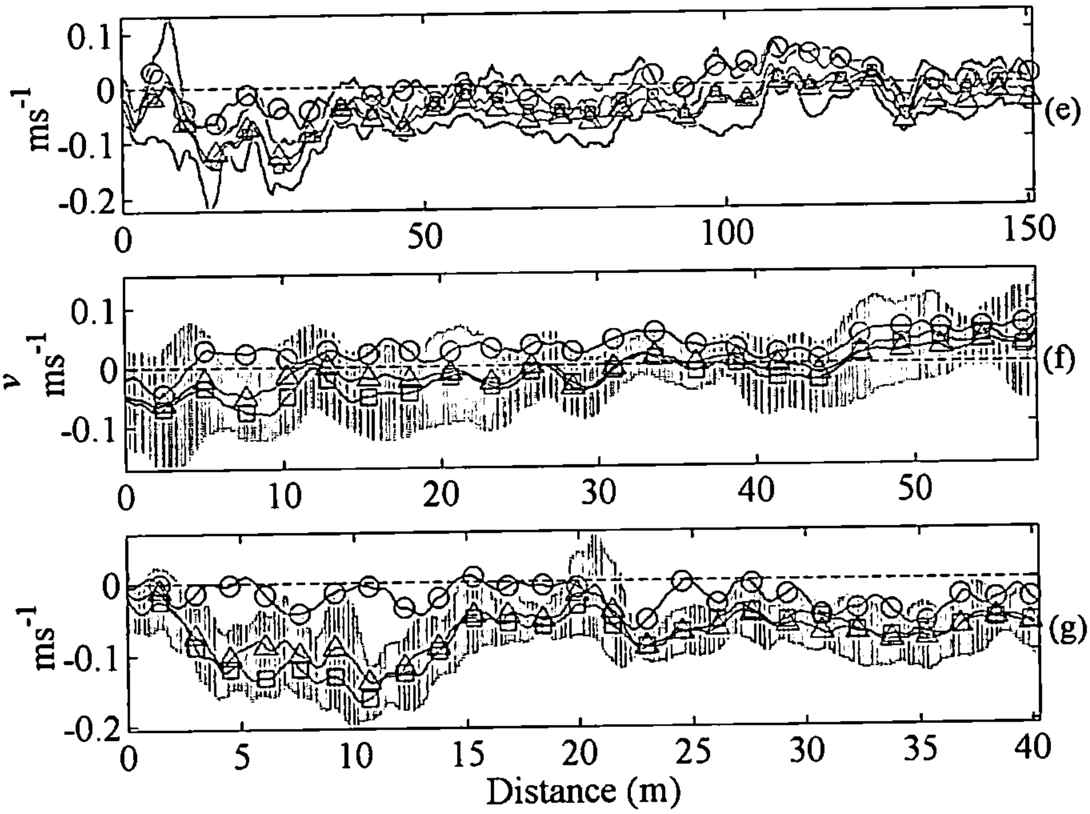

Fig 4.17: Group averaged across frontal velocity profiles, $\bar{v}$ ± 2 σ_v (ms^{-1}) versus distance (m) on the 26th November 1998. □ = 0.95 m; Δ = 1.85 m; O = 2.9 m entering the plume in the first 5 m on the left-hand side of the diagram. (e) HW + 3:23 hours; (f) HW + 3:27 hours; (g) HW + 3:59 hours.

Fig 4.18 shows the subsequent results from these computations. The values in the figure outside the grey bands are significantly different from zero. Significant convergence occurred at the 0.95 m level inside the first 5 to 10 m of the plume in each set of group averaged velocity profiles. The position of convergence indicates the proximity of the stagnation point at the foremost region of the plume front. In transect groups a, b and d the magnitude of convergence is in excess of 0.04 s^{-1} and was representative of the downwelling motion of water at the front. The plots of across frontal flow divergence also suggest a region of decelerating flow or velocity divergence some 15 to 30 m to the rear of the convergent flow. Divergent flow was thought indicative of upwelling motion behind the front. Further aspects and implications of the observed regions of convergent and divergent flow on frontal dynamics and mixing are quantified and discussed in far greater detail later in Chapter 5.

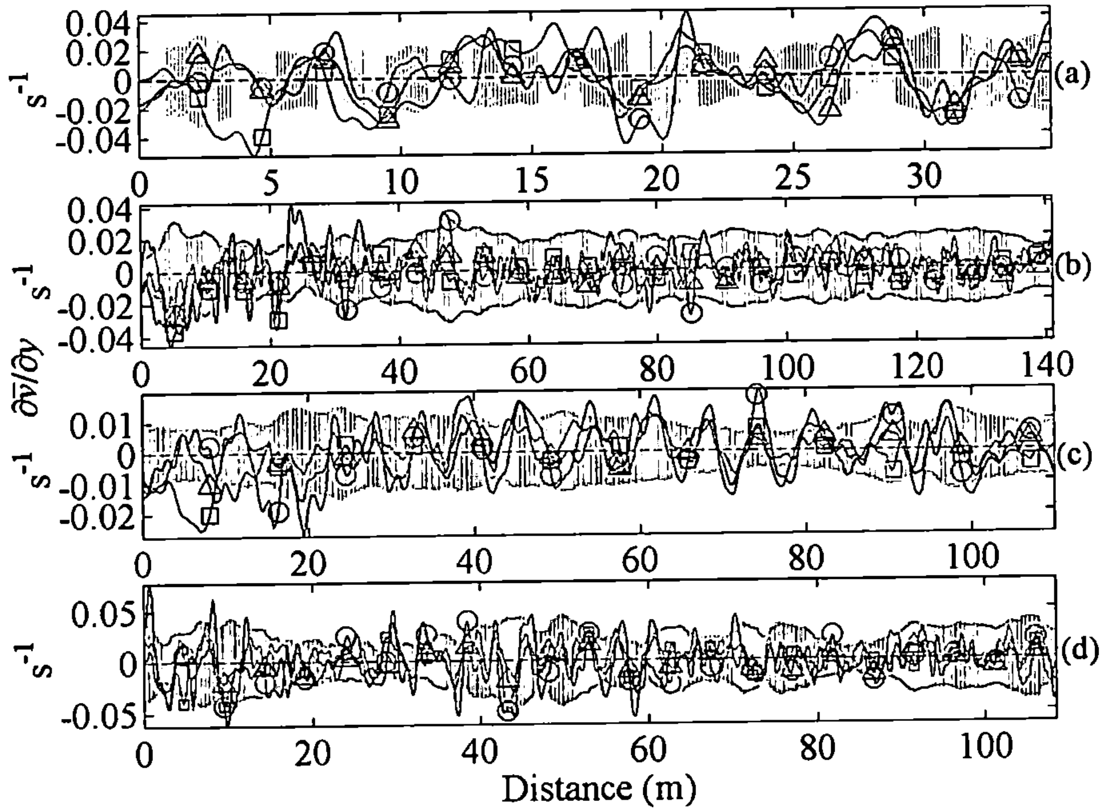

Fig 4.18: Across frontal velocity divergence ($\partial\bar{v}/\partial y$) profiles ($s^{-1}$) versus distance (m) for the 25th November 1998. □ = 0.95 m; Δ = 1.85 m; O = 2.9 m entering the plume in the first 5m on the left-hand side of the diagram. (a) HW + 2:42 hours; (b) HW + 3:36 hours; (c) HW + 5:12 hours; (d) HW + 5:42 hours. The shaded areas stipulate the uncertainty threshold.

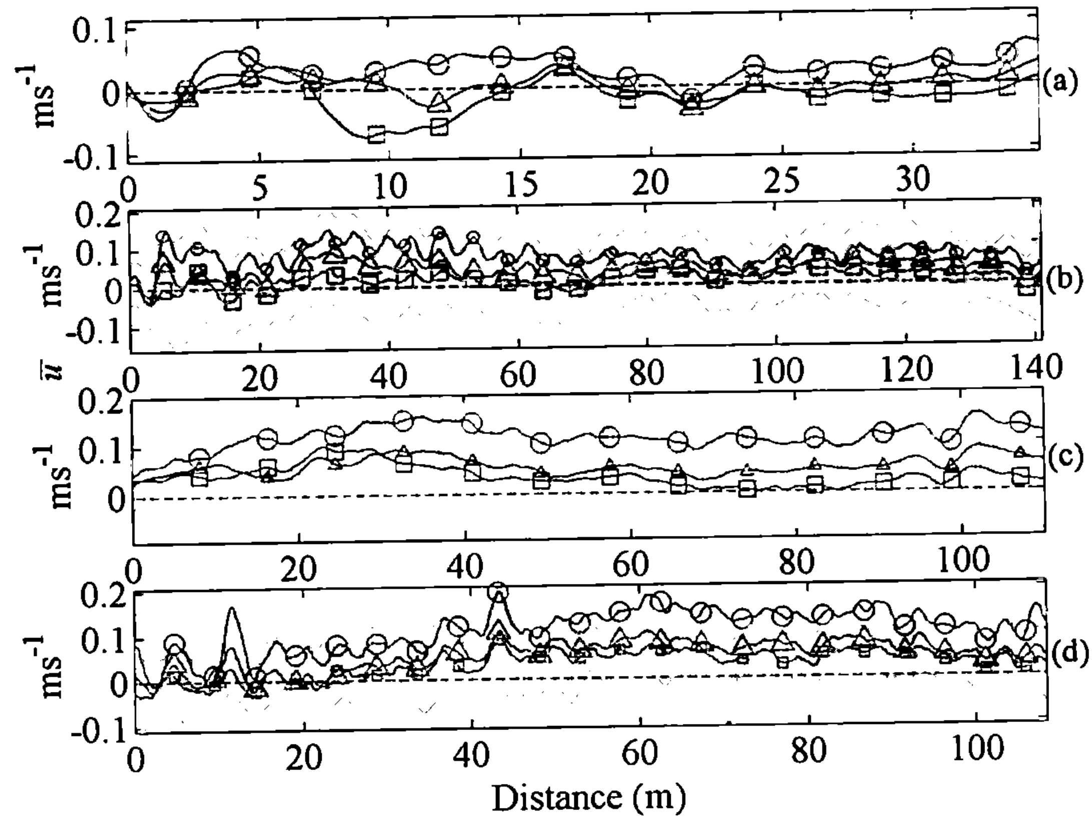

Fig 4.19: Group averaged along frontal velocity profiles, $\bar{u}$ ± 2 σ_u (ms^{-1}) versus distance (m) for the 25th November 1998. □ = 0.95 m; Δ = 1.85 m; O = 2.9 m entering the plume in the first 5 m on the left-hand side of the diagram. (a) HW + 2:42 hours; (b) HW + 3:36 hours; (c) HW + 5:12 hours; (d) HW + 5:42 hours.

Following the quantification of the across frontal component of flow during ebb discharge from the estuary, an analysis of the corresponding and simultaneous along frontal velocity profiles was conducted. The motion of the group averaged along (x - co-ordinate) frontal flow $\bar{u}$ on the 25th November is illustrated in Fig 4.19. The plots of along frontal flow velocities illustrate the presence of high variability in the group averaged values at all stages of the spreading cycle. However, observations do tentatively suggest that the along frontal motion was directed offshore away from the mouth of the estuary and flow was generally more positive at the 2.9 m level. This supports the observations made by Garvine & Munk (1974) and O'Donnell (1997) who encountered the same flow structure in the Connecticut plume front. Garvine & Munk's (1974) physical explanation of similar observations is that motion is mainly dependent on local turbulent eddy stress associated with the estuarine outflow. The current observations indicated, as did O'Donnell's (1997), large variability where the error bounds mainly indicated insignificant variations from zero in all the records. A possible alternative explanation for this inherent variability in the along frontal flow is provided by a constituent of estuarine outflow considered by Garvine & Munk (1974). At some inshore location near or inside the mouth of the estuary, both saltwater and plume water discharged from the estuary must lie adjacent to each other during the discharge on the ebb tide. This could result in the addition of some horizontal momentum transfer to the gravity outflow of the freshwater from the ebbing saltwater. The combination of this additional momentum to the vector components of a radially spreading fresher water lens could provide a mechanism that generates the higher variability present in the along frontal flow from the estuary.

4.7 Internal Features Across the Entire Plume

This penultimate section of Chapter 4 slightly diverts from the content of the previous discussions dealing with the bulk flow dynamics of the plume during the ebb discharge from the estuary. Nevertheless, the following description and quantification of internal physical features observed inside the plume during a spreading cycle provides an important context to the detailed analysis of Chapter 5 and central to the theme of the thesis.

On the 25th November one complete survey transect was completed across the entire plume (see Transect 11, Fig 4.1a). The run started to the NE of the estuary at 3° 27′35″ West, 50°32′ 30″ North and ended to the SW of estuary mouth at 3°28′31″ West, 50°31′16″ North. Assuming a constant radial spreading rate of *O*(0.2 ms^{-1}) the plume expanded laterally from 1.98 km at the start of the transect run to 2.53 km by its completion some 23 minutes later. Thus, the ETS instrument array recorded a *quasi*-static picture of internal features present across the entire radial plume at HW + 4:19 to 4:42 hours. Fig 4.20a illustrates isotherms produced from the ETS thermistors where the vertical extent of the plot is vastly exaggerated with respect to horizontal distance because of the plotting procedure. The plume was approximately 1 m deeper to the north of the estuary than to the south, but in terms of an overall lateral distance, depth was relatively consistent throughout the transect.

The horizontal density distribution through the upper plume layer and lower coastal water of the transect was calculated from the smoothed T-S data recorded by the two CT probes at depths of 0.95 m and 2.9 m. Fig 4.20b effectively illustrates the observed oscillations in the density field of the lower water column that suggested the presence of at least three distinct groups of interfacial waves on the plume-ambient seawater interface (labelled 1 to 3 in Fig 4.20b). Associated oscillations were also recorded in the isotherms at the same sites and in similar observations made on the 26th November on frontal Transect 25.

To quantify the interfacial wave observations made on the 25th November, a simple 2-layer model of stratified flow that assumes the observed oscillations inside the plume were barotropic interfacial waves was applied to the data. The upper homogenous layer was assumed to have a depth of h_1 = 2.5 m and the lower denser layer depth, according to the total depth of water at the geographical location of the waves, was h_2 = 12.5 m deep. The mean density differences between the two layers was $\Delta\rho$ = 1 kgm^{-3} with a mean upper layer density ρ_1 = 1025.1 kgm^{-3}. The interfacial wavelengths λ_i of each wave in a group was calculated by simple measurement of the length scaled density profiles through the plume. Wave numbers (k) of each respective wave in a group were then computed through, $k = 2\pi / \lambda_i$ along with the dispersion (ω_i^2) based on the simple two-layer model of long (shallow water) interfacial waves that was derived through Equation 4.15. Equation 4.15 estimates the linear dispersion (ω_i^2) relative to ambient water depth mean current, $\bar{u}$ and also ignores the effect of vertical shear (Pond & Pickard, 1991).

$$\left(\omega_i - \bar{U}k\right)^2 = \frac{g h_1 k^2 \Delta\rho}{\rho_1} \qquad [4.15]$$

ω_i^2 = Interfacial wave dispersion (s^{-2})
$\bar{U}$ = Depth mean current (ms^{-1})
k = Wave number (m^{-1})

g = gravitational acceleration (ms^{-2})
$\Delta\rho$ = Density anomaly (kgm^{-3})
ρ_1 = Density of upper layer (kgm^{-3})

Mean group ω_i^2 values shown in Table 4.3 are in close agreement. The small standard deviations of ω_i^2 in each wave packet (± 0.0003-0.0007 s^{-2}) describes the non-dispersive behaviour within each group. The values of mean λ_i and mean period, $T = 2\pi / \omega_i$ illustrates the constancy in the form and time scale of the waves observed on the interfacial region of the plume. The wave heights in each group of waves were estimated from the oscillations in the isotherms as approximately 1.5 m from peak to trough. Examples of the wave packets of groups 1 and 2 are shown in Fig 4.21 and Fig 4.22.

Group	T (s)	λ_i (m)	c_p (ms^{-1})	c_g (ms^{-1})	ω^2_i (s^{-2})
1	281.47	35.30	0.15	0.15	7.85×10^{-4}
2	278.96	34.90	0.15	0.15	8.41×10^{-4}
3	268.25	33.25	0.15	0.15	11.0×10^{-4}

Table 4.3: Mean interfacial wave properties of Transect 11 for interfacial wave groups 1, 2 and 3.

Assuming the interface is far from the bed and the free surface so that coth $kh_1 \rightarrow 1/kh_1 \gg$ coth $kh_2 \approx 1$ then the phase velocity c_p and group velocity c_g in each set of observations can then be estimated from Equations 4.16 and 4.17.

$$c_p = \frac{\omega}{k} - \overline{U} \quad \text{or} \quad \sqrt{g'h_1} \qquad [4.16]$$

$$c_g = \frac{\partial\omega}{\partial k} - \overline{U} \qquad [4.17]$$

The results from the computations displayed in Table 4.3 show that due to negligible dispersion within each group, $c_p = c_g$. However, these simple computations do not divulge any information on which direction the interfacial wave energy is travelling. Returning to the experiments of Britter & Simpson (1978) on gravity currents that suggest overturning and mixing in the frontal region, it was probable that wave groups 1 and 3 situated behind the plume's gravity head regions are propagating back into the plume interior. The physical processes responsible for interfacial wave generations are discussed in more detail later in Chapter 5. The source of wave generation inside the plume at the site of group 3 was not clear, as no obvious physical cause was evident. Probable mechanisms of interfacial wave generation are uneven bottom topography causing internal hydraulic jumps, surges in the tidal and plume outflow or they were formed behind the fronts (Farmer & Smith, 1980; New *et.al.*,1986). The first suggestion seems the most acceptable due to the considerable distance of the wave packet from either end of the plume boundary.

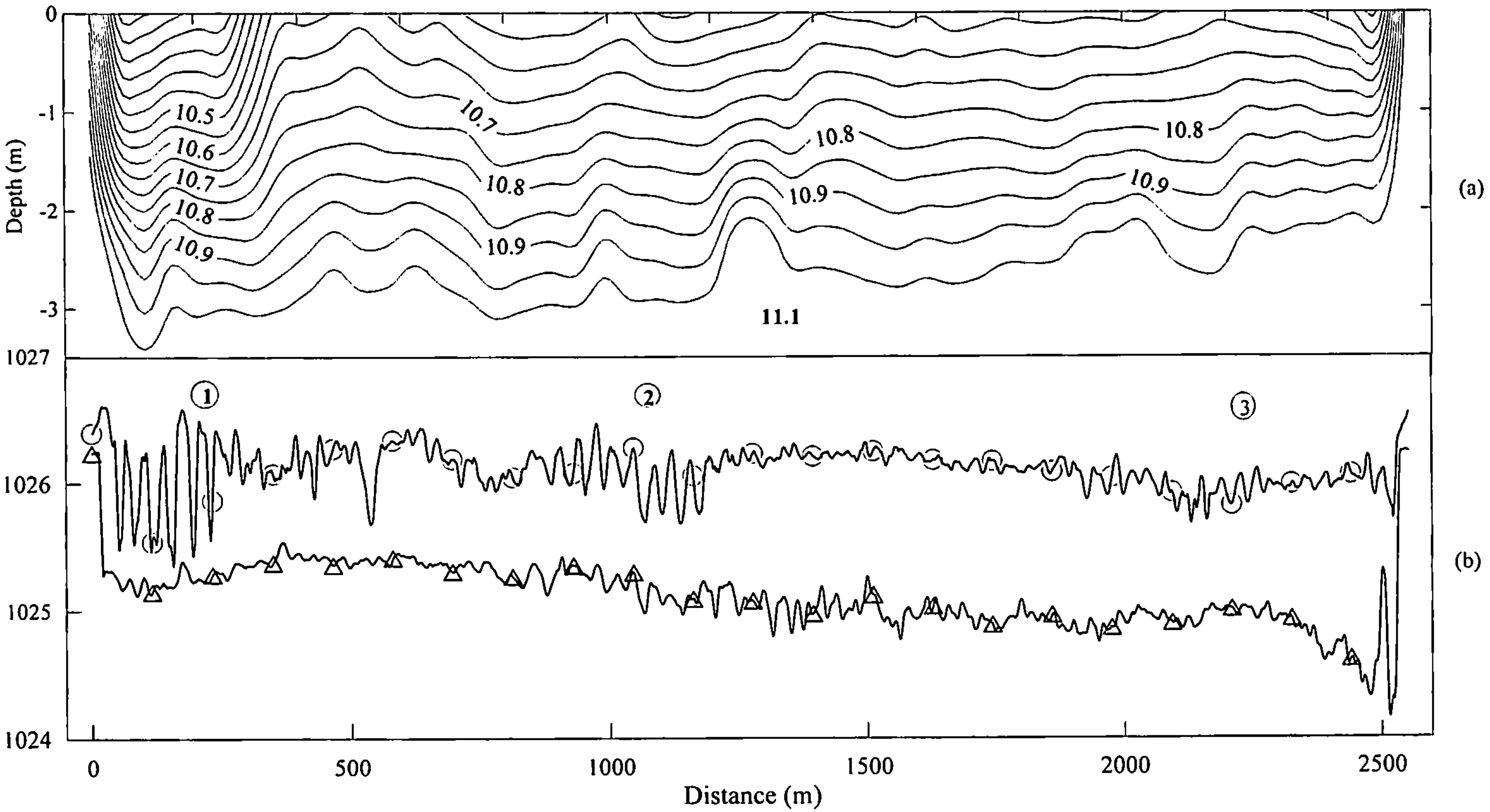

Fig 4.20: (a) Isotherm (°C) from ETS thermistors and (b) density (kgm^{-3}) from the upper and lower CT probes for Transect 11 across the entire developing plume between local HW + 4:19 to HW + 4:42 hours. Δ = Upper CT probe; O = Lower CT probe.

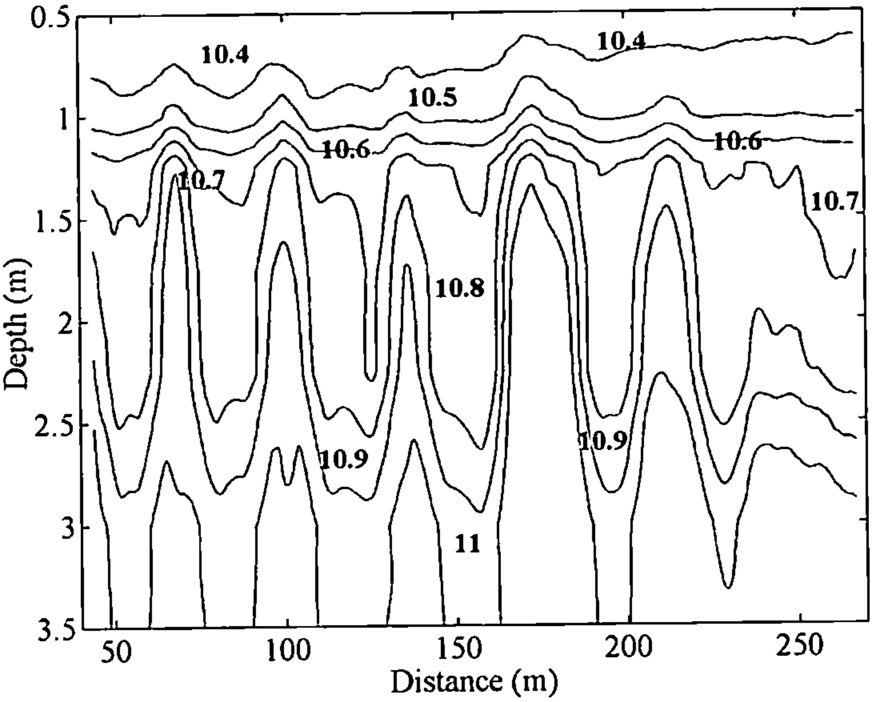

Fig 4.21: Isotherm depth profiles (°C) vs. distance (m) at the location of interfacial wave group 1.

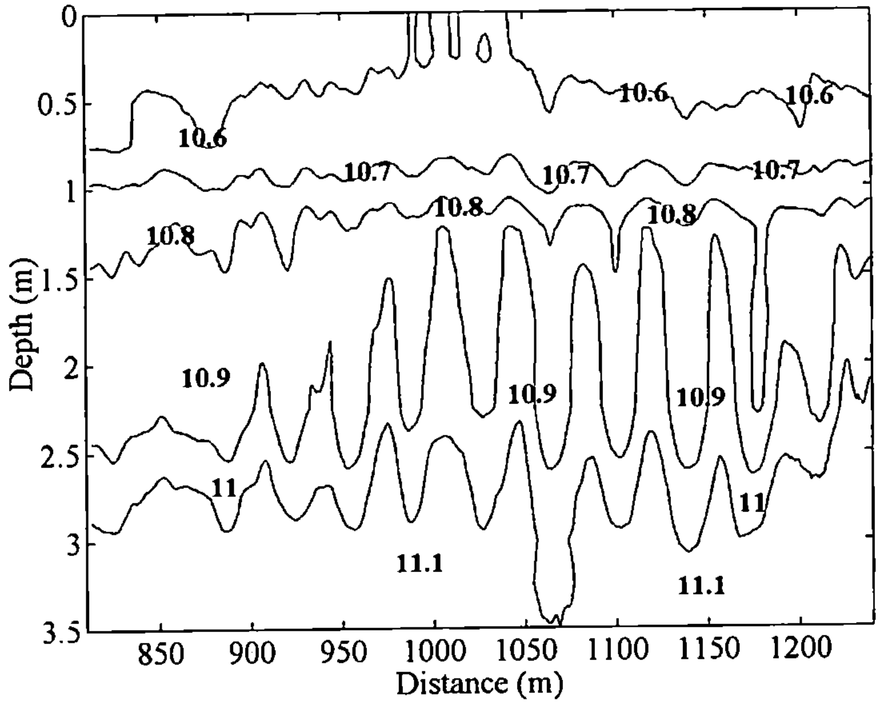

Fig 4.22: Isotherm depth profiles (°C) vs. distance (m) at the location of interfacial wave group 2.

4.8 Summary of the Observed Larger Scale Plume Dynamics

Both Section 4.5 and 4.6 have illustrated the interrelationships between the flow dynamics and physical features at the front and the local tidal regime. The influence of the barotropic ebb tidal outflow was shown to be the governing factor in the formation of the plume and the maintenance of continuity at the plume front through a discharge cycle. The actual formation of the plume and frontogenesis next to 'The Ness' is a result of the estuary's barotropic current converging with the north-easterly directed tidal stream earlier in the ebb cycle. On progression through the ebb, tidal streams are directed offshore towards the east and amalgamate with the barotropic and baroclinic components of the estuary discharge producing the observed larger flow rates towards the front. As tidal forcing begins to subside near the time of low water, flow towards the front decreases and is eventually 'cut' by the turning flood tide into the estuary. The strong convergence at the front suggests the presence of downwelling motion, as kinematically, one would expect. However, the divergence or upwelling some distance behind the front required further investigation.

The along frontal component of flow was more complex and variable in structure and it was difficult to confidently resolve the specific dynamical implications of the flow during the discharge cycle. Results suggest this component of frontal flow, although variable is mainly directed offshore from the mouth as is intuitively expected.

The last section of Chapter 4 deals with some interesting interfacial wave features and illustrated ongoing physical processes that appeared isolated from the most dynamical regions of the plume. A source or sources of interfacial wave generation at these specific sites inside the plume remain speculative. Their respective positions inside the plume could be attributed to a number of factors including wave trains propagating from the front or the generation of local instabilities by internal hydraulic jumps induced by tidal outflow over sandbars.

Chapter 5

Results: Frontal Mixing & Circulation

Having established the basic forcing mechanisms that govern the observed flow dynamics inside the Teign plume, attention was now turned to the mixing and circulation processes that disperse the brackish water discharged from the estuary.

Firstly, this chapter examines and quantifies the processes that govern mixing and circulation inside the plume in context of the results from the numerical simulations of Chapter 3. This mixing analysis is then extended and refined through use of the high resolution data set and provides a first order estimate on the level of vertical and horizontal mixing processes active inside the plume and plume front. Then through established gravity current theory, better estimates for parameters used in the initial and boundary conditions of the numerical model are derived.

The final aim of this chapter is to discuss the contributions of larger scale mixing due to the effects of tidal mixing and wind stress with the mixing at the plume front. This analysis is based on an energetic approach, as described by Blanton (1996). The plume outflow in this instance is assumed to have a closed energy budget, where potential energy from stratification provided by freshwater discharge competes with energy dissipation from tidal currents, wind stress and plume frontal dynamics.

5.1 Frontal Jump Conditions

Lewis (1997) comments that the overall mixing in a two layer flow (where $h_1 << h_2$) is usually expressed through the bulk Richardson number, Ri_b. However, for the preliminary analysis and direct model comparison, the hydraulic approach of using interfacial Froude numbers, Fr_i (see Equation 2.2) at each sampling increment throughout each plume transect was adopted. This method of quantifying mixing and instabilities present inside the plume then conforms to the model scaling arguments and frontal jump conditions stipulated in Chapter 3 (Garvine, 1984). If necessary, Ri_b could easily be produced through the inverse square of the Fr_i number from the results, as shown in Equation 5.1.

$$Ri_b = \frac{1}{Fr_i^2} \qquad [5.1]$$

T-S diagrams constructed from CTD profiles as discussed in Chapter 4 suggested that the water column in the region of the plume outflow principally comprised of 2 layers separated by a transition or interfacial region. Strictly speaking, the depth mean density of both the upper and lower layer is required to calculate Fr_i. However, based on an assumption drawn from the CTD profiles that the two CT probes were so positioned as to represent the mean temperature and salinity in the upper and lower layers, high-resolution horizontal density profiles could be calculated and used for the computation of Fr_i values through each frontal transect.

The actual interfacial depth of the plume for each respective transect was calculated from computer software developed in MATLAB that utilised the temperature isotherm contouring routines. The software selected the singular depth contour from each respective transect that represented the deepest stable temperature isotherm present in the across frontal transect temperature record. To then calculate u in the upper layer (h_1) with respect to ambient water, the lower EMCM data was subtracted from the average of the two upper EMCM's if the thermocline (pycnocline) extended beyond a depth of 1.85 m. Or, if the thermocline was shallower than 1.85 m, the lower two EMCM's were averaged and then subtracted from the upper EMCM data. Subject to a minimum depth constraint of 0.95 m, as flow velocity above this level could not be resolved with the EMCM depth configuration, Fr_i values were computed from the observed horizontal density distribution, surface layer flow velocity and interfacial depth records

The interfacial depth of the plume derived from the implementation of the interfacial depth selection software showed the plume depth to subtly vary in accordance with the time and position of the plume during the spreading cycle. However, a general trend of a gradually descending thermocline or pycnocline towards mid ebb could be observed in the temperature profiles recorded during the survey on the 25th November. As suggested in Chapter 4, the most apparent feature to appear in the plume interior behind the frontal region was a gravity head. The typical bull nose form of the head with an abruptly ascending tail region was present in some form on most transects at a consistent distance of some 30 to 60 m behind the foremost frontal interface.

Fig 5.1 shows the presence of consistent super-critical flow ($Fr_i \geq 1$) or hydraulic jump conditions when first encountering the frontal region on both surveys. This region of disturbance corresponded to the site of maximum convergence in the across frontal flow rate as shown in Chapter 4 (see Fig 4.18) and was extremely localised within 2 to 5 m of the convergence zone. Dynamically, the intense deceleration of plume outflow at the convergence or stagnation point and shallow interface was causing the outflow head wave to break and generate the unstable jump condition.

All the presented Fr_i values were derived inside the first 5 m section of the plume that started from a depth boundary of 0.95 m inside the plume. Due to the data smoothing procedure, the maximum uncertainty in the position of the initial frontal encounter is the computed position ± a horizontal distance of 1 to 1.5 m depending on the specific transect in question. Therefore, the mean Fr_i value calculated from all the Fr_i values in the first 5 m section of the plume were subject to a maximum spatial error of up to ± 1.5 m and could actually represent an 8 m section behind the front. In the context of the present study, where mixing and instability at specific sites inside the discharge were predicted to be separated by tens of metres, an error of this magnitude is inconsequential.

Behind the initial hydraulic jump at the plume front, flow conditions subdued to a sub-critical status where Fr_i values indicated mixing had apparently subsided to a relatively dynamically tranquil level. These observations agreed with those of Ingram (1976) but contravened the findings of Lukitina & Imberger (1987) and O'Donnell (1997) where they found the region of instability behind the front had a continuum of some 30 to 50 m into the plume before falling below super-critical flow conditions. However, observations did show the presence of either singular or multiple super-critical peaks in the Fr_i series to the rear of the gravity head where the interface abruptly ascended. Fig 5.2 shows an example of the super-critical flow status at the leading front and at the rear of the gravity head.

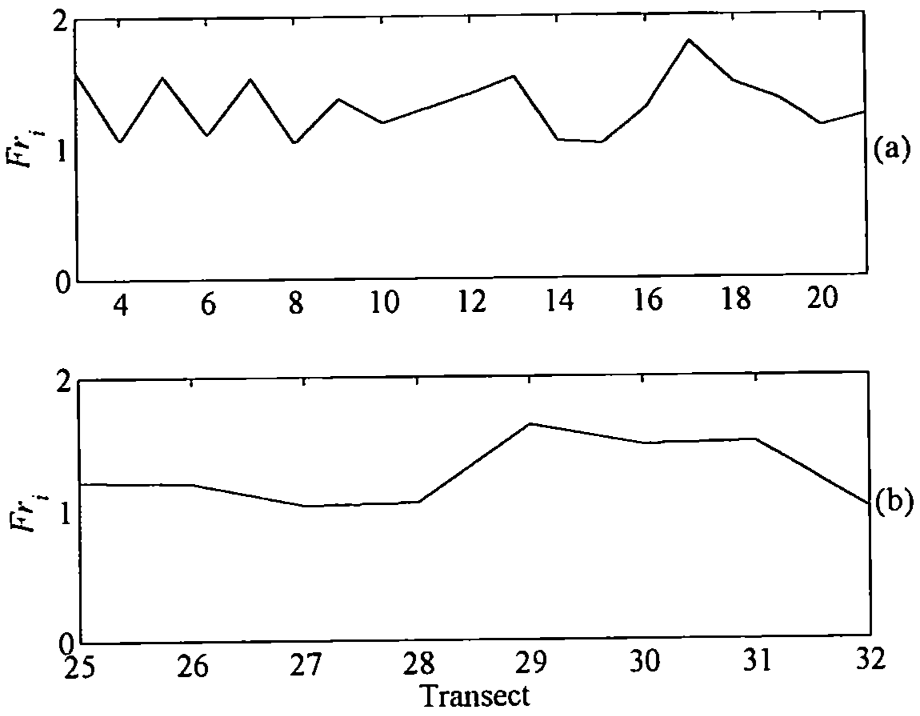

Fig 5.1: Mean Fr_i number in the first 5 m of the plume front. (a) 25th November 1998; (b) 26th November 1998.

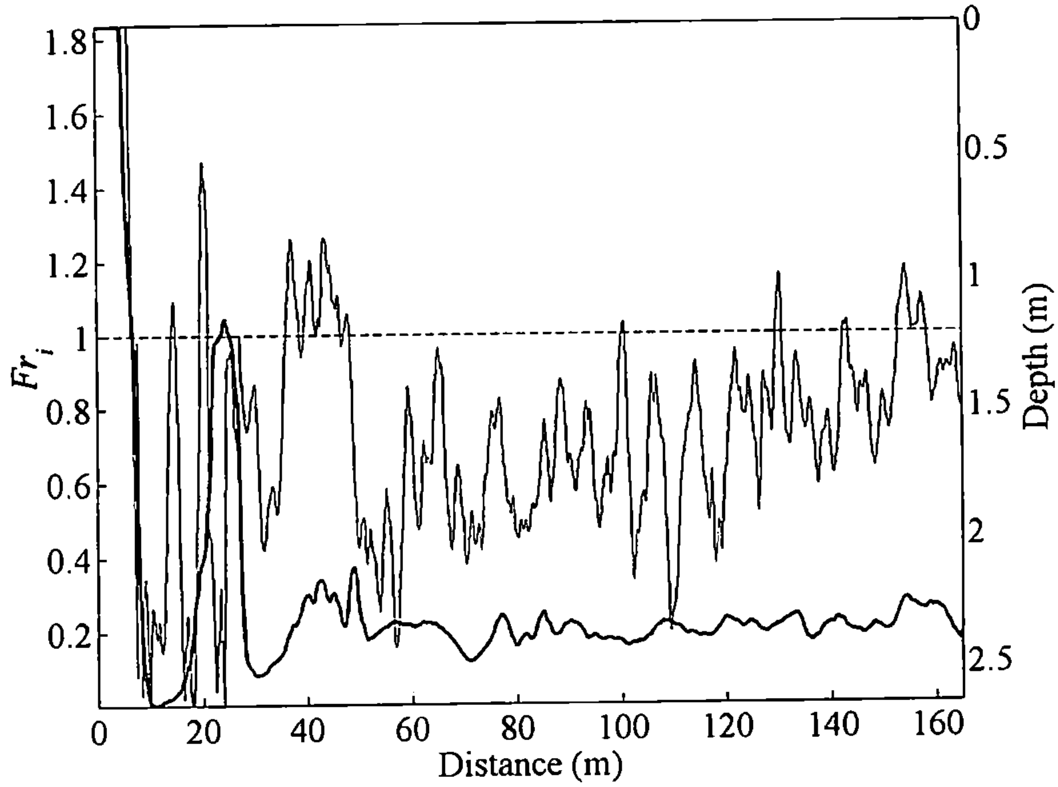

Fig 5.2: Fr_i numbers vs. horizontal distance (m) for Transect 6 (HW + 3:30 hours) recorded on the 25th November 1998. In addition, the interfacial depth (thicker line) is also plotted to indicate the position of the gravity head.

This trend of multiple jump conditions inside the plume discharge was displayed throughout the two data sets. Fig 5.3 presents a series of plots for the two separate surveys representing the percentage frequency of occurrence of super-critical flow conditions with respect to distance from the leading surface front. Individual transects from each respective day were grouped on the basis of transect length into five separate groups corresponding to length scales of 60, 120, 180, 240 and 300 m. The latter two groups were capable of resolving the internal bore feature as predicted by the model. The spatial position of super-critical Fr_i numbers were then calculated along each across frontal plume transect. This spatial length scale was determined by the limit of instrument detection i.e. the distance inside the plume from the plume fronts leading edge where the interface depth exceeded 0.95 m to the end of the transect. Then single points with a length scale of less than twice the sampling distance for each transect were discarded as anomalous perturbations in the density or velocity records. To increase confidence in the observations the position of each observation was windowed into a series of 5 m bins and then normalised by the total number of jumps.

(a) 25th November 1998

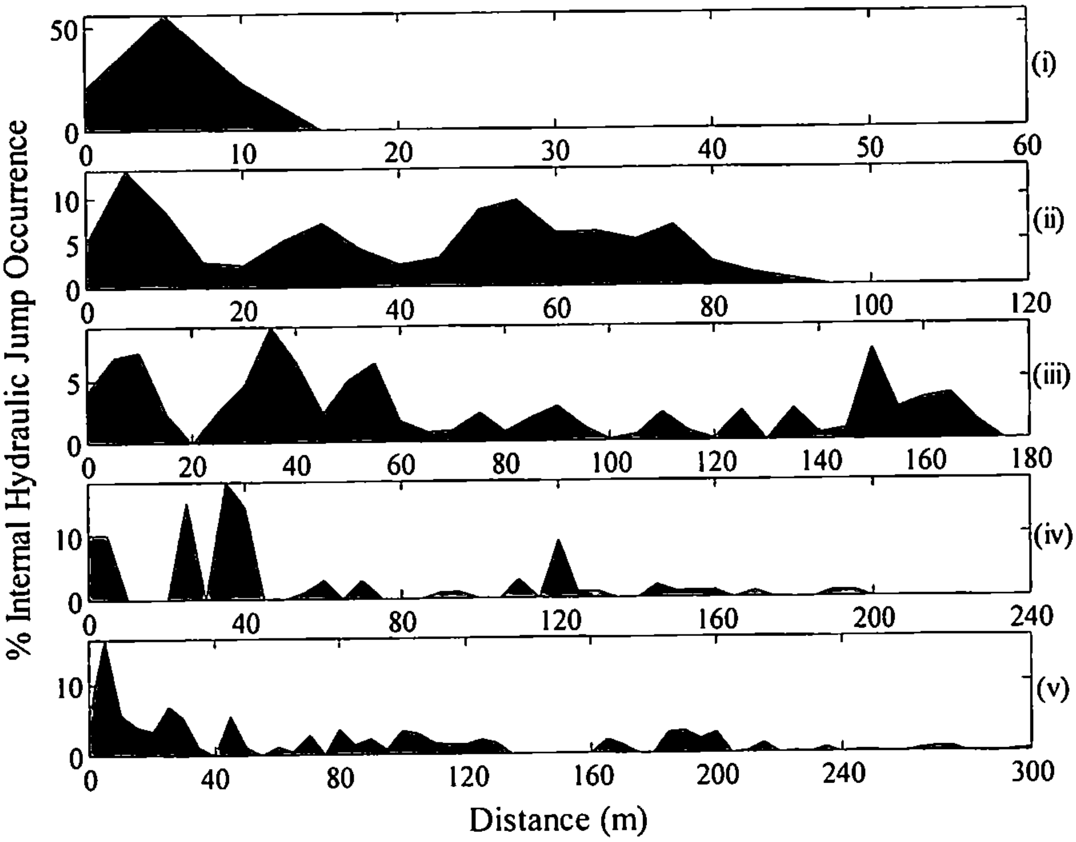

(b) 26th November 1998

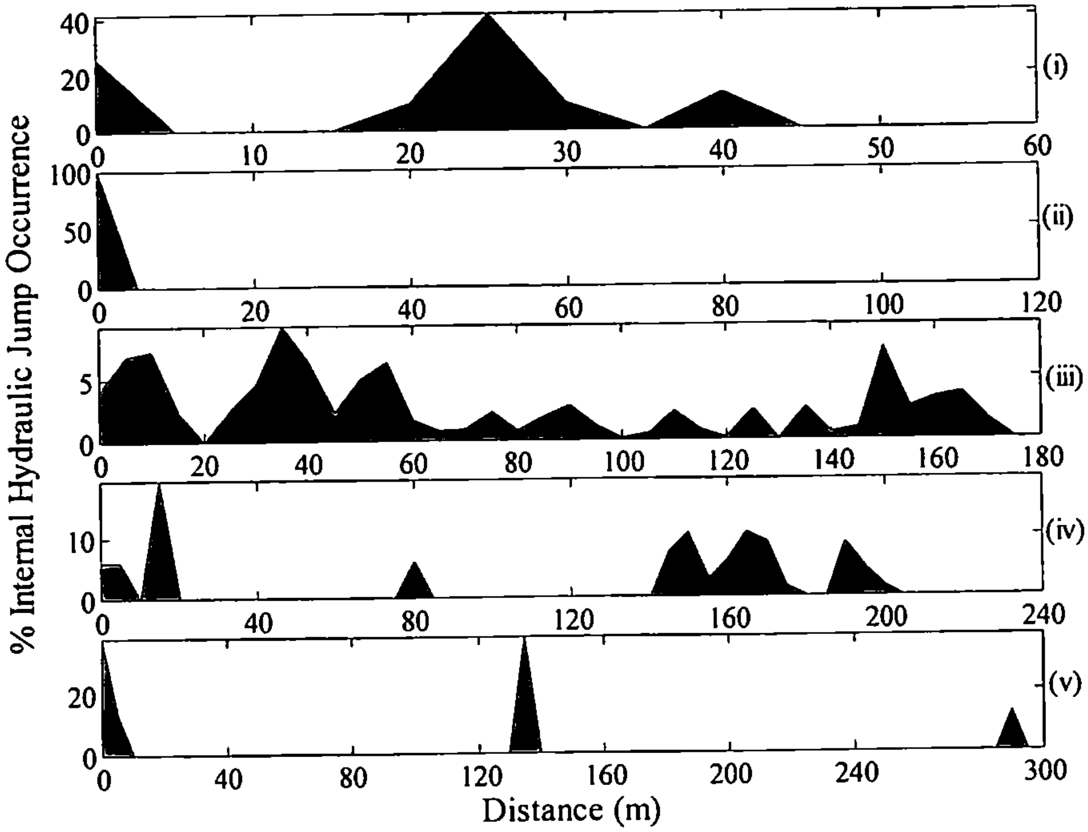

Fig 5.3: Percentage jump occurrence vs. relative distance (m) of internal hydraulic jump occurrence from the leading front for grouped Fr_i profiles from (a) 25th and (b) 26th November 1998. Group (i) = 0-60 m; Group (ii) = 0-120 m; Group (iii) = 0-180 m; Group (iv) = 0-240 m; Group (v) = 0-300 m. See Appendix 1 for specific grouping details.

As anticipated from the preliminary Fr_i computations, the majority of the groupings shown in Fig 5.3 had the highest peak in percentage jump occurrence in the first 20 m of the plume boundary symbolising the unsteady flow when entering the main plume front. On the 25th November, observations showed that on most of the longer transects', the 'primary' jump was followed by lull in the occurrence rate due to the quiescent sub-critical flow region often present behind the leading front. This was a direct resultant of the deepening thermocline or pycnocline. This reduction in depth subsequently increased the interfacial wave speed, thus, reducing the Fr_i number behind the front. The position of the 'secondary' jumps were represented by a further two peaks in Fig 5.3, approximately 30 to 50 m behind the leading front. The secondary singular jumps mostly coincided with a spatial locality either just before, just to the rear or specific to the region where the ETS data showed the isotherms to abruptly shallow at the rear of the gravity head. On other transects multiple peaks in the Fr_i records appeared as a series of multiple internal or undular type jumps as illustrated in Fig 5.4. These instabilities had wake like oscillations following the primary or leading jump as seen in undular surface bores (Massey, 1989).

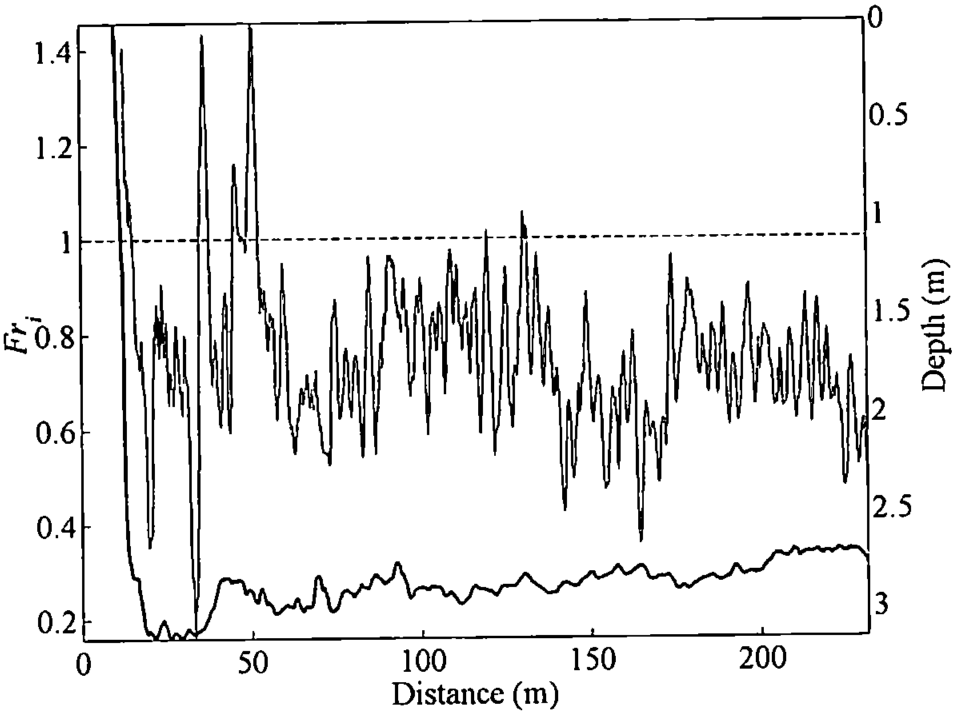

Fig 5.4: Fr_i numbers vs. horizontal distance (m) for Transect 18 at HW + 5:25 hours (Group (iv) recorded on the 25th November 1998). The plot aims to illustrate the multiple or undular oscillations in the flow. Interfacial depth (m), the thicker line is also plotted to indicate the position of the gravity head.

Super-critical flow conditions on the 26th November demonstrated subtle differences from the previous day's data. When first infiltrating the plume, the Fr_i number again showed the super-critical flow trend in the first 5 to 20 m. The secondary jumps in the flow behind the gravity head region (25 to 50 m) were only present in two of the percentage frequency plots (Fig 5.3b (i) and Fig 5.3b (iii)). Closer examination of the isotherm records suggested the gravity head on some of these transects was less defined. However, one must consider the fact that the survey time on the 26th November only covered approximately 1/8 of the total ebb cycle due to the deteriorating sea conditions. Therefore, less data was available for the analysis. In addition, the runoff rate that significantly modulates and controls the formation of a plume was close to the estimated lower threshold value for plume formation. Hence, explaining the observed decrease in gravity current flow towards the front as shown in Fig 4.17.

In the presence of low runoff conditions the passive transport of the brackish plume layer with the barotropic tidal current from the estuary would essentially flush the 'slug' of fresher water from the estuary at the same rate. Thus, the area of plume formation would be limited by the brackish water discharge volume. If the density anomaly remained relatively consistent with the previous day's observations, 'c_i' would retain a similar magnitude as on the 25th November. Thus Fr_i on the latter survey would be subject to a general decline and less instability and mixing would be present at the plume front. Less mixing would effectively cause a shallower, less pronounced head region, as the retarding baroclinic flow that arises from the steepening isopycnals would give less opposition to gravity outflow from the estuary. Consequently, the return flow and accompanying progressive interfacial wave train that the model predicts will break on coalescence with the downstream propagating interfacial waves are small and non-existent, respectively. In summary, the nature of the frontal and plume dynamics is highly sensitive to the river runoff rate.

The model predictions discussed in Chapter 3 estimated the position of a secondary internal bore some 180 m behind the leading front. The current observations did show that jumps were present in the applicable transects at approximately 150 to 200 m behind the front. However, these jumps only had a low frequency of occurrence. Further examination of the corresponding isotherm plots supplied no observable evidence of a jump condition on the plume interface as predicted by the model. Therefore, it was assumed that these sites were isolated regions of localised mixing in the plume due to inconsistencies in the plume outflow field or interfacial wave breaking. These results suggested the main internal jump(s) appeared inside the plume much closer to the surface front than predicted by the radial spreading model.

5.2 Gradient Richardson Number Analysis

To further refine the previous section's analysis and discussion on mixing in the frontal zone, the relative importance of fine scale shear and density stratification through the water column was estimated by calculation of the Gradient Richardson number (Ri_g). This analysis was aimed to try and clarify the form of mixing behind the leading front and along the plume interfacial region.

Ri_g as derived in Equation 2.4 requires prior knowledge of the vertical gradient in density and velocity. As the vertical density distribution was not directly measured from the ETS thermistors, it was necessary to derive a functional relationship between the observed vertical temperature and density distribution.

Section 4.3.1 discussed the observed linear relationship between temperature and salinity inside the plume layer. The calculation of the density of seawater is based on both salinity and temperature measurements (Millero & Poisson, 1981) and salinity is calculated from both temperature and conductivity. Thus, the only independent variable in the solutions to both density and salinity is conductivity. Therefore, it is possible to derive a functional linear relationship between the observed temperature and density measurements from the profiling CTD casts. This function, 'α' effectively represents a thermal constant of proportionality between the observed temperature and density distribution and allows the observed temperature gradients to be used in a modified form of Equation 2.4.

$$Ri_g = g\alpha \frac{\partial T}{\partial z}\left(\frac{\partial u}{\partial z}\right)^{-2} \qquad [5.2]$$

$$\text{If } \frac{\partial v}{\partial z} \neq 0 \text{ then } \frac{\partial u}{\partial z} \text{ is replaced with } \frac{\partial V_H}{\partial z} \quad V_H = \mathbf{i}u + \mathbf{j}v$$

u = horizontal velocity (ms^{-1})
T = Temperature (^{o}C)
α = Thermal constant of proportionality ($^{o}C^{-1}$)
z = Depth (m)
g = Gravitational acceleration (ms^{-2})

Values for α for each respective survey were computed from the vertical CTD casts made inside the plume during each survey period. Vertical density profiles calculated through the Millero & Poisson (1981) equation from salinity and temperature variations were then normalised by the maximum density (ρ_{max}) recorded on a specific cast. Assuming a Boussinesq approximation, α was then derived by the slope ($^{o}C^{-1}$) from simple linear regression of the vertically normalised density profile vs. the vertical temperature profile.

(a) 25th November

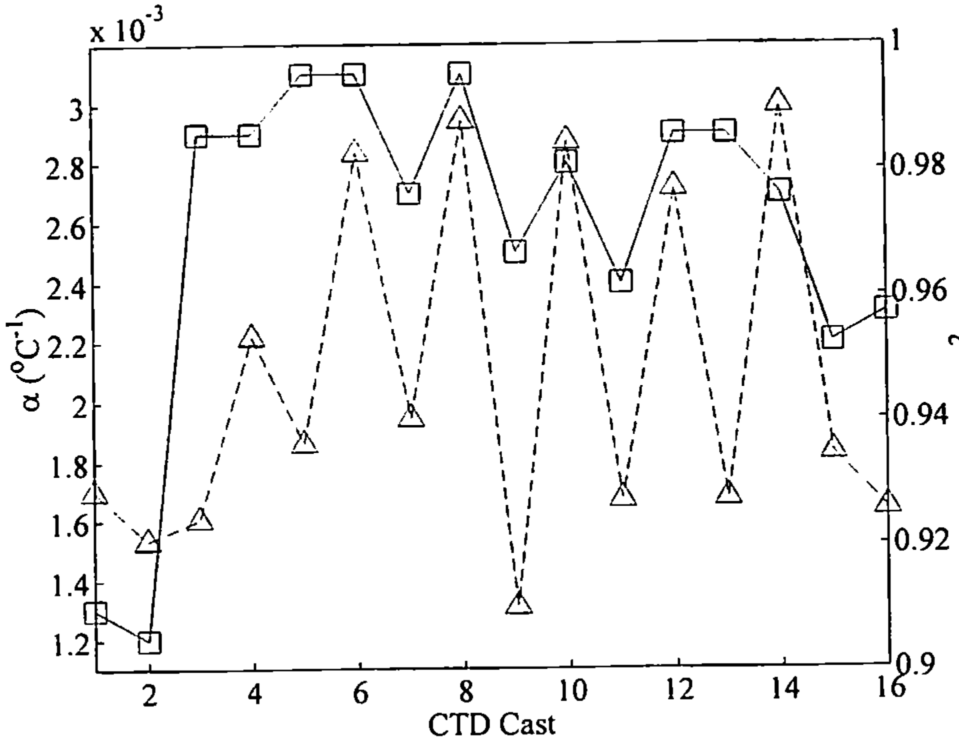

(b) 26th November

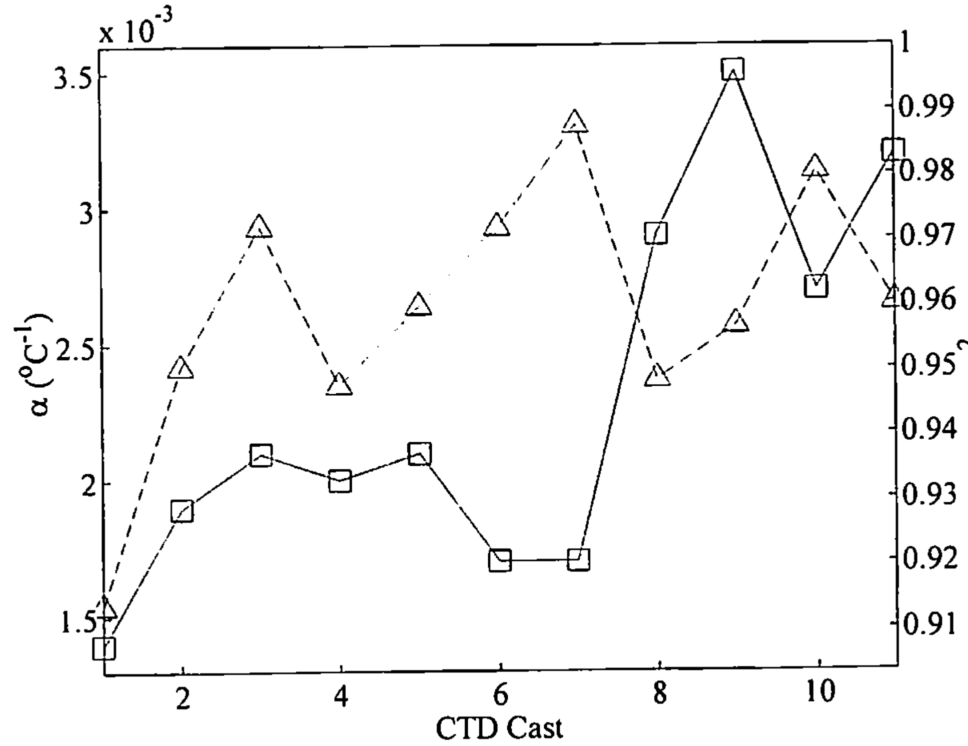

Fig 5.5: Thermal constant of proportionality α (°C^{-1}) and corresponding R^2 values derived from temperature and density profiles recorded inside the plume outflow for (a) 25th and (b) 26th November 1998. □ = α (°C^{-1}); Δ = R^2.

Fig 5.5 shows the results from the simple linear regression analysis that in addition to specific values of α for each CTD cast also illustrates the accompanying R^2 computations. The results displayed a high degree of agreement between the two variables with only minor fluctuations in the overall data set. Mean values of α were 0.0026 ± 0.0003 (95% C.I.) $^{\circ}C^{-1}$ and 0.0023 ± 0.0004 (95% C.I.) $^{\circ}C^{-1}$ for the 25th and 26th November respectively.

The corresponding vertical velocity shear profiles required to close Equation 5.2 were calculated by differentiating the vertically interpolated (3rd order polynomial fit) velocity data recorded at the three depth levels in the water column. This allowed the velocity shear to be computed at the specific depths corresponding to the ETS thermistor array. Examples of the resultant Ri_g values derived from Equation 5.2 are presented in Fig 5.6 as a series of contour plots with the corresponding Fr_i calculations from Section 5.1. Averaging was again limited to the same minimal range as in all the previous data analysis procedures. The range of Ri_g values shown in Fig 5.6 was restricted (only to increase the plot resolution) to an upper and lower threshold of 1 and -1 respectively. A negative Ri_g number as discussed in Dyer (1997) is indicative of unstable conditions i.e. where water parcels of higher and lower density are being convected and overturned forming negative vertical density gradients due to the presence of shear instability. This study was capable of capturing and quantifying such overturning events through the Ri_g numbers by using the high-resolution data collected from the ETS and the EMCM instrument array. Ri_g values outside the specified range were set to the applicable maximum or minimum limit (+1 or -1). These values encompass the criterion for a linear stability threshold in stratified flows where a breakdown of stratification due to mixing is generally accepted at $Ri_g \approx 0.25$ and a stable vertical structure at $Ri_g \geq 1$ (Miles 1961). Ri_g values outside the limits of plume stratification were classified as zero as the Ri_g in un-stratified water is meaningless.

When entering the front, the plume had a narrow turbulent ($Ri_g \leq 0.25$) band on the sloping interfacial region followed by a stable upper layer. This foremost region of the front would also be subject to shear generated by the sharp longitudinal gradients (y-direction) in both shear and density, which is not accounted for when evaluating Ri_g. Sub-critical Ri_g numbers behind the front nearer the deeper horizontal plume-coastal water interface defined a more complex series of mixed regions following the initial frontal jump. These regions appeared to extend some distance up into the water column causing some distortion and possible breakdown of the plume interface. The scale of these instabilities, judging by the Ri_g plots were in order of 2 to 10 m long and approximately 1 to 1.5 m deep.

These examples from the Ri_g analysis show good agreement with the Fr_i computations that were calculated from the density data provided by the CT probes. Regions of instability and stratification set by each of the mixing parameters critical or sub-critical threshold appeared to spatially complement each other. This suggested that both methods used to quantify mixing and instability were valid and the regions of mixing behind the plume front were unmistakable as real physical features.

The magnitude of the errors in the estimates of Fr_i and Ri_g were obtained by computing the deviation between Fr_i and Ri_g values calculated from the raw unsmoothed data and the corresponding Fr_i and Ri_g values calculated from the smoothed data. Then, by dividing through by the unsmooothed values and multiplying by 10^2, a mean percentage deviation was produced for all the smoothed Fr_i and Ri_g value on each respective frontal transect. In principle, this provided an estimate of the percentage uncertainty in the results without the added complication of considering the individual errors associated with each separately smoothed transducer record.

(a) Transect 6 (HW + 3:30 hours)

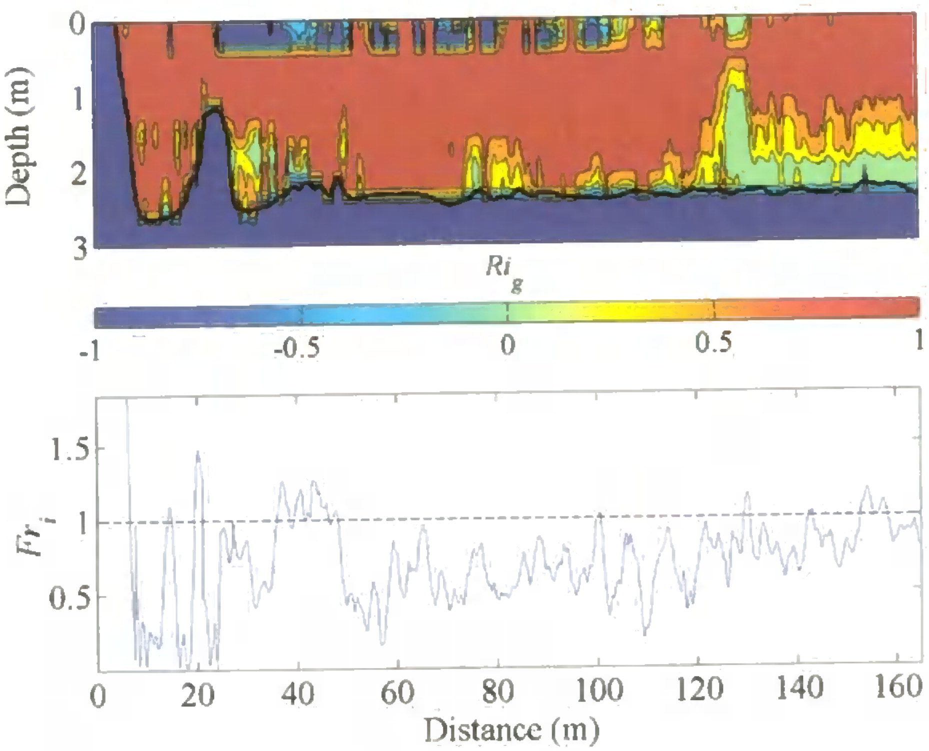

(b) Transect 9 (HW + 3:39 hours)

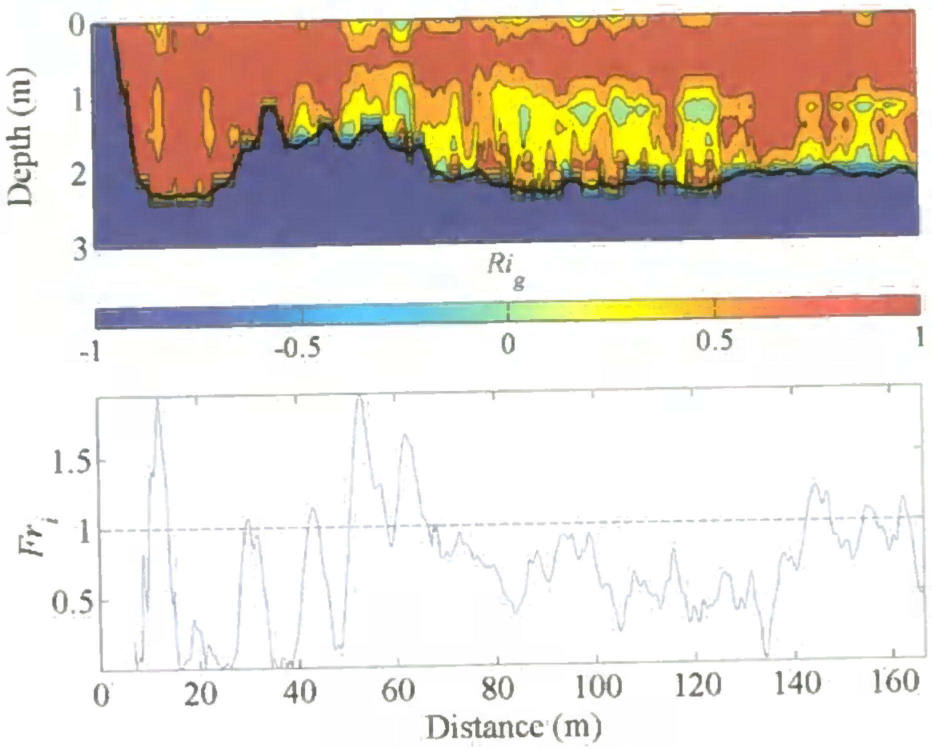

(c) Transect 16 (HW + 5:18 hours)

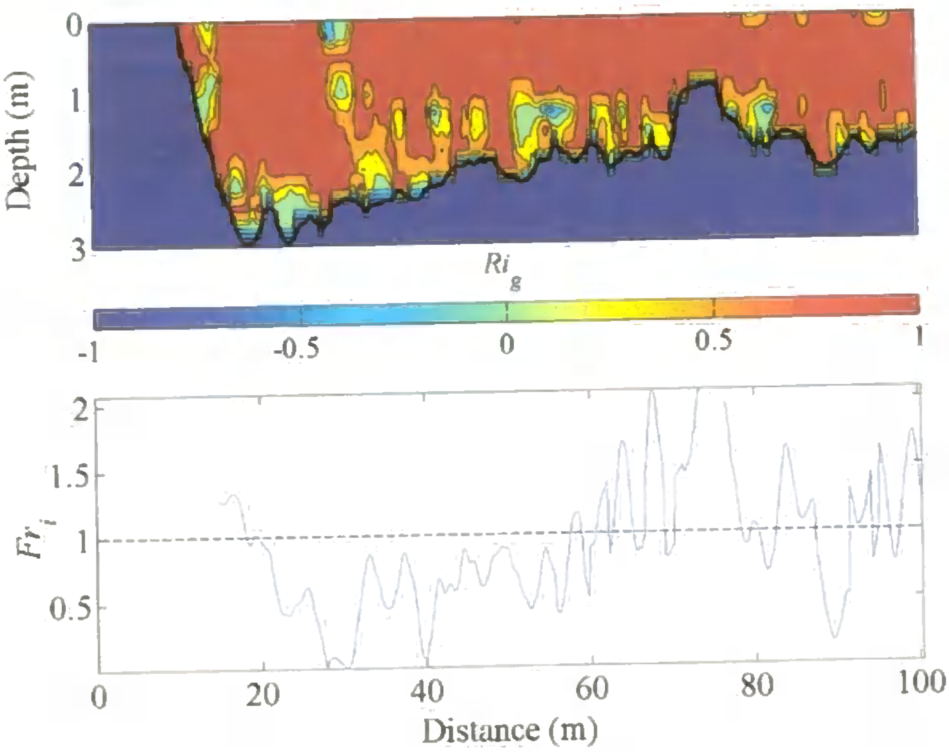

(d) Transect 20 (HW + 5:41 hours)

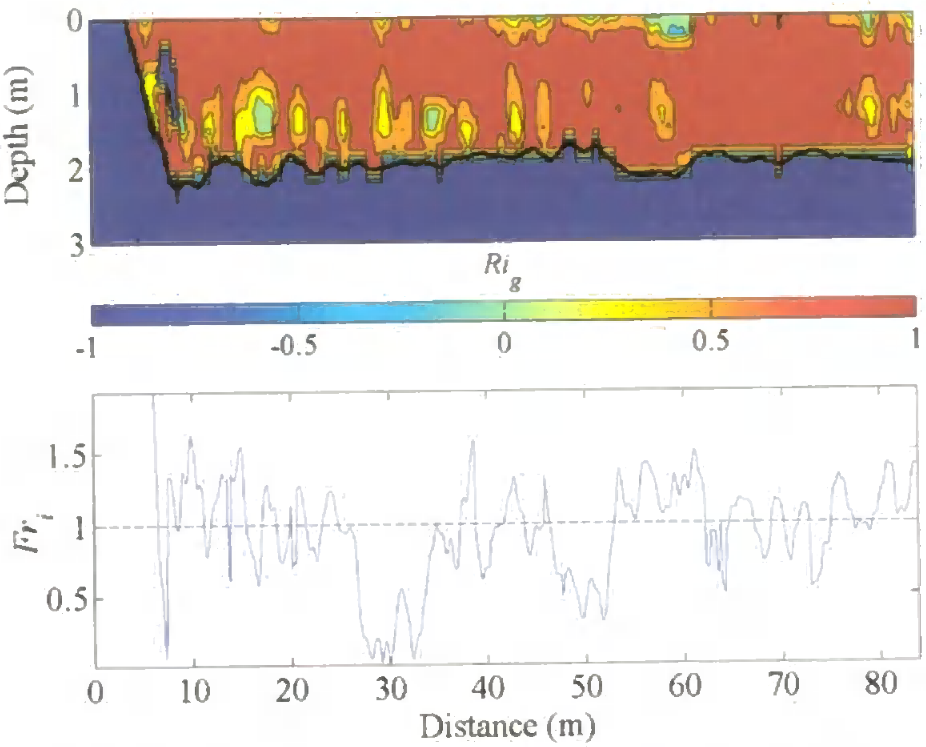

Fig 5.6: Examples of Ri_g values computed with respect to longitudinal distance (m) and depth (m) for frontal transects 6, 9, 16 and 20 on the 25th November 1998. The Fr_i values calculated from the flow velocity and density values derived from the two CT probes for each of the transects are also presented in the figures.

As in the computation of the contoured Ri_g values, spurious points that exceeded the bounds of ± 1 were set to their respective limit. This did not prove detrimental to the error analysis, as these values would effectively represent extreme stability or instability. The values of main interest to this study of instability and turbulent mixing were centred on critical threshold values of 0.25 and 1 for the Ri_g and Fr_i criterion respectively

The estimated percentage deviation of the smoothed Fr_i and Ri_g ranged from 0.5 to 36% for Fr_i and 6 to 42% for Ri_g . The mean levels of percentage uncertainty were 19% and 7.3% for Ri_g and Fr_i respectively. The generally higher level of Ri_g uncertainties reflected the higher sensitivity and lower response time of the ETS thermistor array that led to higher levels of variability in the temperature data used in the computation of Ri_g.

Generally, this analysis demonstrated that smoothing techniques significantly reduced the variability present in the smoothed data used to compute the mixing and hydraulic jump parameters' and were a good representation of the flow status present inside the spreading plume.

5.3 Frontal Circulation

The analysis presented in Sections 4.6 and 5.1 to 5.2 has examined the horizontal flow properties and discussed the associated mixing dynamics in the frontal region of the plume. Results from the respective investigations have continually suggested the presence of downwelling motion in the convergence zone, as the kinematics of the outflow plume required the less dense fluid from the discharge to be sub-ducted below the coastal water. Quantitative indication of this motion has been previously reported in the field studies of Garvine & Munk (1974), Lukitina & Imberger (1989) and O'Donnell *et.al* (1998).

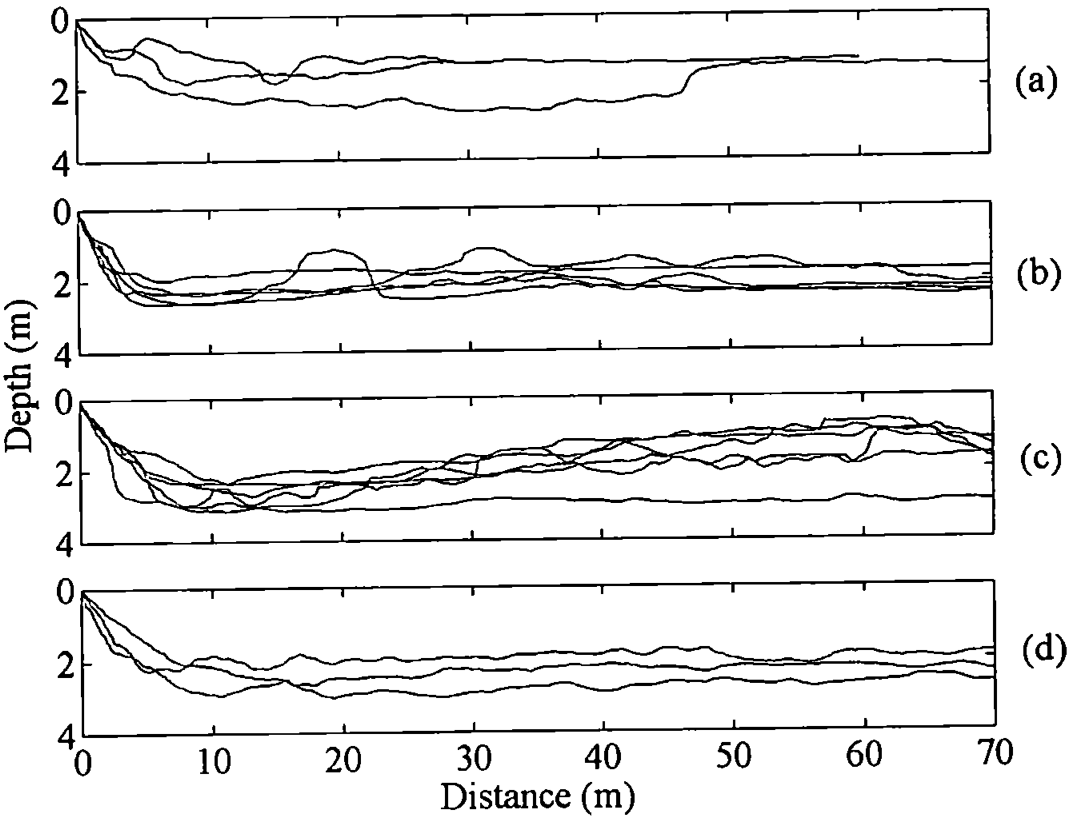
(a) 25th November

(b) 26th November

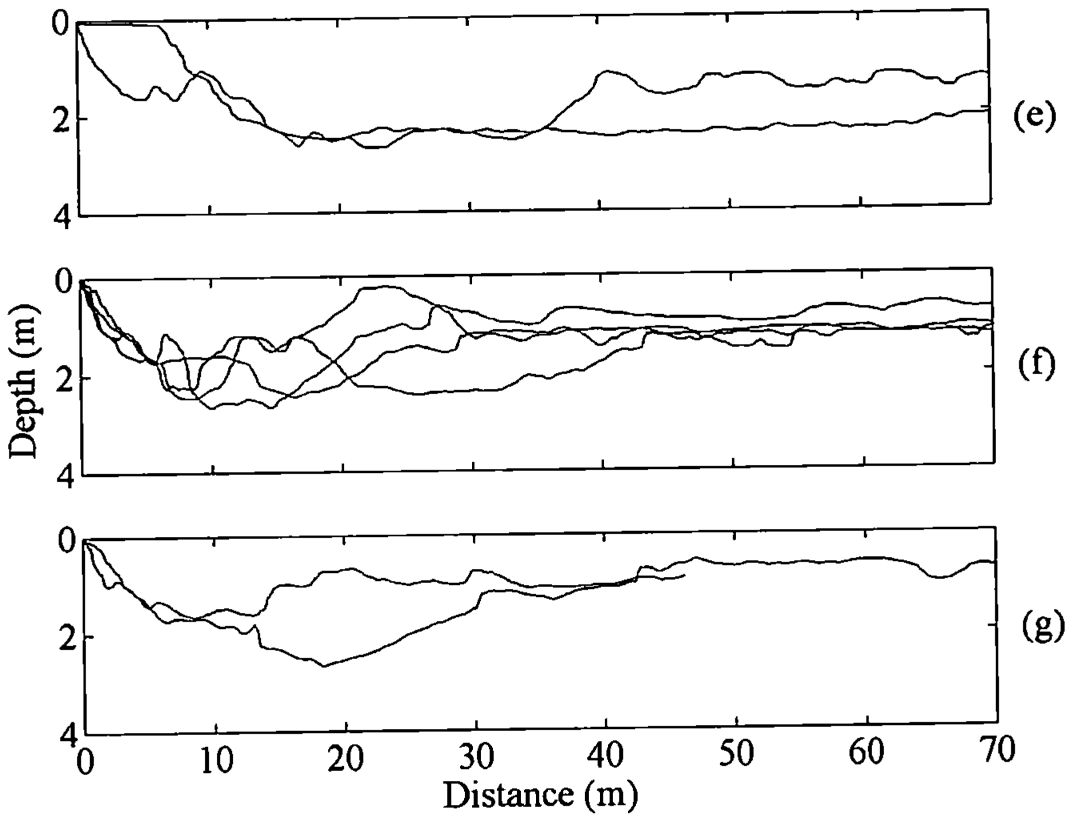

Fig 5.7: Interfacial depth (m) vs. distance (m) from convergence zone for transects grouped with respect to frontal velocity averages as described in Chapter 4 (see text) for (a) 25th and (b) 26th November 1998.

The current investigation using the X-band radar images and ETS instrument array suggests that the plume spreading rate remains relatively constant despite the intensification of surface outflow velocity towards the front through the ebb discharge cycle. The size of the depth sliced cross sectional area of the gravity head was also maintained through the ebb discharge cycle as shown in Fig 5.7. Thus, to retain a constant volume and satisfy the continuity of mass, an increase in the downward entrainment velocity and the mixing of fluid out of the front must accompany any increase in flow rate behind the front.

To quantify the vertical flux of brackish water in the frontal region of the plume the vertical entrainment velocity 'q_e' was computed in a moving reference frame (overbar) from continuity for each respective frontal transect. The same principle of calculating the velocity in the upper layer was used as in calculation of Fr_i (Section 5.1) with the exception that the mean velocity of the front was removed from the data. Then by using the plume interfacial depth computed from the isotherms derived from the ETS, q_e was estimated from Equation 5.3.

$$\frac{\partial}{\partial \bar{x}}(\bar{u}D) = q_e(\bar{x}) \qquad [5.3]$$

$\bar{x}$ = Distance from the front (m)
$\bar{u}$ = Velocity relative to the front (ms^{-1})
D = Depth of interface (m)
q_e = Entrainment velocity (ms^{-1})

Examples of applying Equation 5.3 to the velocity and isotherm depth data are shown in Fig 5.8. The figure illustrates the presence of detrainment at the front that was focused near the stagnation point or region of high across frontal convergence ($\partial v/\partial y$) in outflow velocity as shown in Fig 4.18. The horizontal length scale of detrainment was confined within a band of 1 to 3 m of the frontal convergence on any transect.

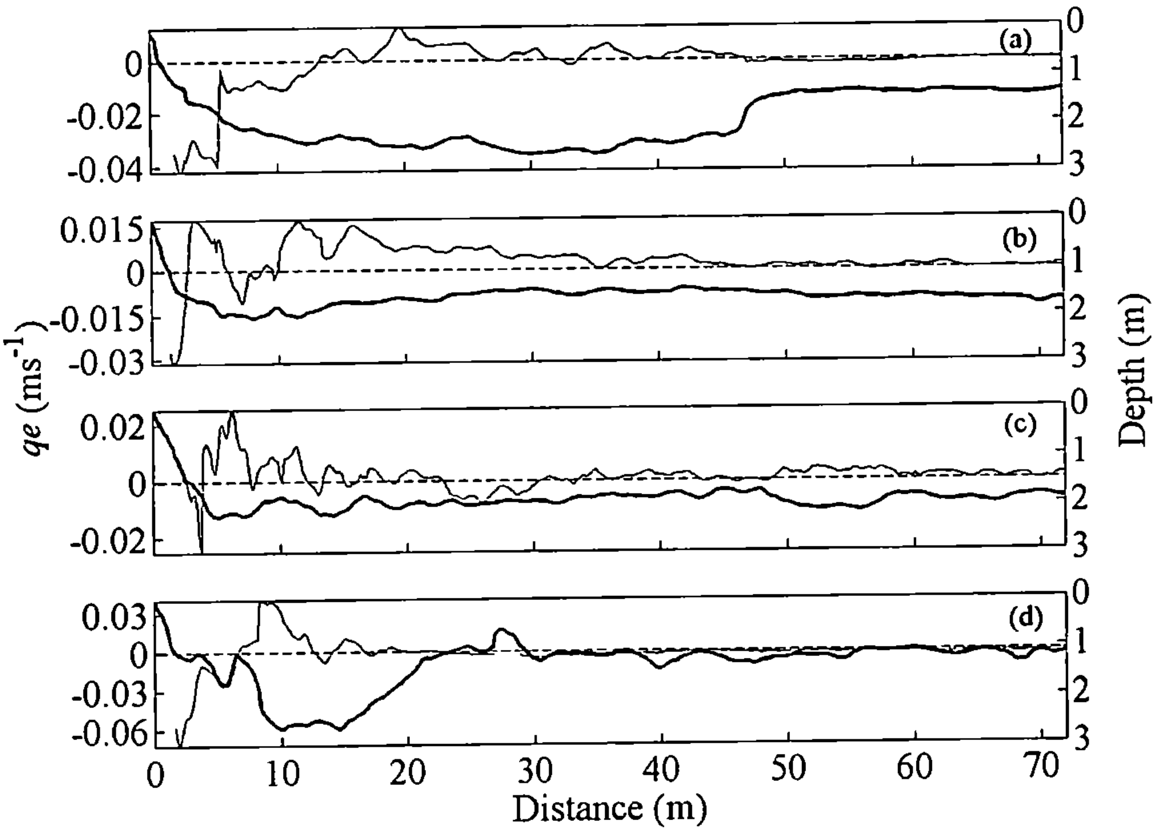

Fig 5.8: Examples of the entrainment velocity q_e (ms^{-1}) at the leading front vs. distance (m). 25th November 1998: (a) Transect 4; (b) Transect 12; (c) Transect 20. 26th November 1998: (d) Transect 29. Plume interface (m) is represented by the thicker line.

Fig 5.9 presents the maximum computed entrainment velocity, $q_{e\ max}$ in the region of maximum across frontal velocity convergence. The series of $q_{e\ max}$ values for the 25th November demonstrate a slight increase from –0.02 ms^{-1} at the start of the survey to an asymptotic value of –0.08 ms^{-1} at approximately HW + 3:42 hours (13:18 GMT) coinciding with the time of maximum across frontal velocities (see Fig 4.14). These values were in the same order of magnitude as those observed by Brubaker & Simpson (1999) in a tidal intrusion front in the James River, Norfolk, Virginia. Towards the end of the survey and spreading cycle, $q_{e\ max}$ began to decrease in conjunction with the decline in intensity of outflow velocities towards the front. The magnitude of $q_{e\ max}$ on the 26th November initially retained a reasonably constant value of –0.05 ms^{-1}, then peaked on Transect 29 and declined to a lower level in the latter three transects. The $q_{e\ max}$ record from the 26th November is probably not a fair representation of the time development in detrainment motion at the front due to the limited sampling period.

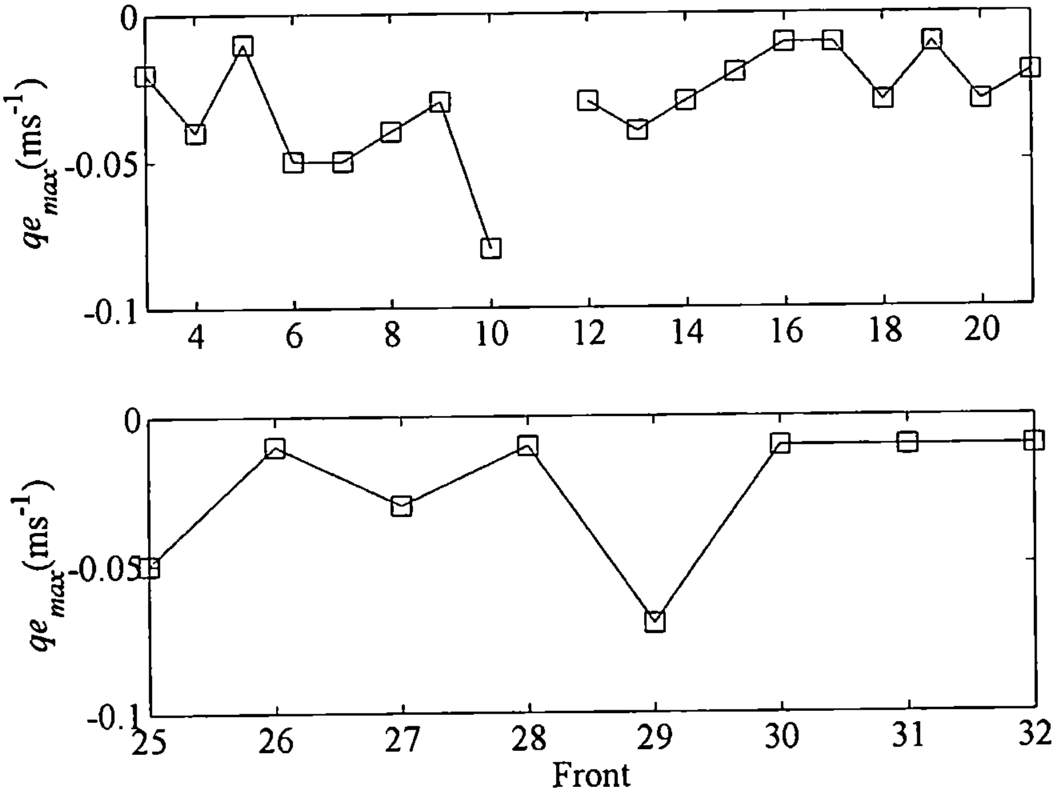

Fig 5.9: The maximum magnitude of entrainment velocity $q_{e\ max}$ (ms^{-1}) in the frontal convergence zone for across frontal transects surveyed on the 25th and 26th November 1998.

The positive (upward) flux shown in Fig 5.8 immediately behind the frontal convergence suggests water was being entrained back up into the plume's gravity head. However, these results must be interpreted with considerable caution, as in this region of the front where mixing is taking place, the interface would be undergoing rapid changes in temperature, salinity and thus density. This adds a level of uncertainty to these observations just behind the frontal region as Equation 5.3 is based on a well-defined interfacial boundary.

5.3.1 Upwelling Behind the Front

From the analysis of velocity convergence and divergence presented in Section 4.6, a suggestion of an upwelling region (see the schematic diagram in Fig 5.11) in or behind the gravity head is present in the data. Therefore, it proved necessary to test these observational results through a method based on other physical properties of the water column.

Firstly, a dynamical approach is assumed where a parcel of less dense water is downwelled at the front and retains its density anomaly (i.e. little or no mixing). Then, the spatial distance between the frontal convergence and where upwelling should occur due to the buoyancy restoring force can be estimated through the Brunt-Väisälä frequency (N^2). N^2 was computed for each across frontal transect through a combination of the vertical temperature gradient through a cross section of the plume outflow and the thermal constant of proportionality for seawater, α as derived in Section 5.2.

$$N^2 = -g\alpha\frac{\partial T}{\partial z} \qquad [5.4]$$

$$f_{B-V} = \frac{N}{2\pi} \qquad [5.5]$$

N = Brunt-Väisälä radian frequency (rad s^{-1})
∂T = Temperature gradient (°C)
$f_{B\text{-}V}$ = Frequency (s^{-1})
α = Thermal constant of proportionality for seawater ($^{o}C^{-1}$)
g = Gravitational acceleration (ms^{-2})

The actual distance taken for a parcel of water to upwell due to the buoyancy restoring force should theoretically occur at:

$$L_u = \frac{u}{2f_{B-V}} \qquad [5.6]$$

L_u = Upwelling distance (m) u = Frontal velocity (ms^{-1})

For the purpose of calculating N^2, a value of 10.4°C was assumed for the sea surface temperature which provided a good mean representation of the shallowest coherent isotherm in the plume outflows surface layer. The temperature gradient ∂T between the surface and the thermocline at a depth ∂z was then estimated by again utilising the deepest coherent isotherm as in the prior calculations of Fr_i and q_e.

Fig 5.10 presents the resultant calculations from application of Equation 5.6 to the ETS data collected on the 25th November. The figures illustrate reasonably good agreement between the expected distance of upwelling at 9 to 10 m behind the leading front based on N^2 and the regions of velocity divergence (positive vertical flow) in and behind the gravity head (see Fig 4.18).

(a) 25th November

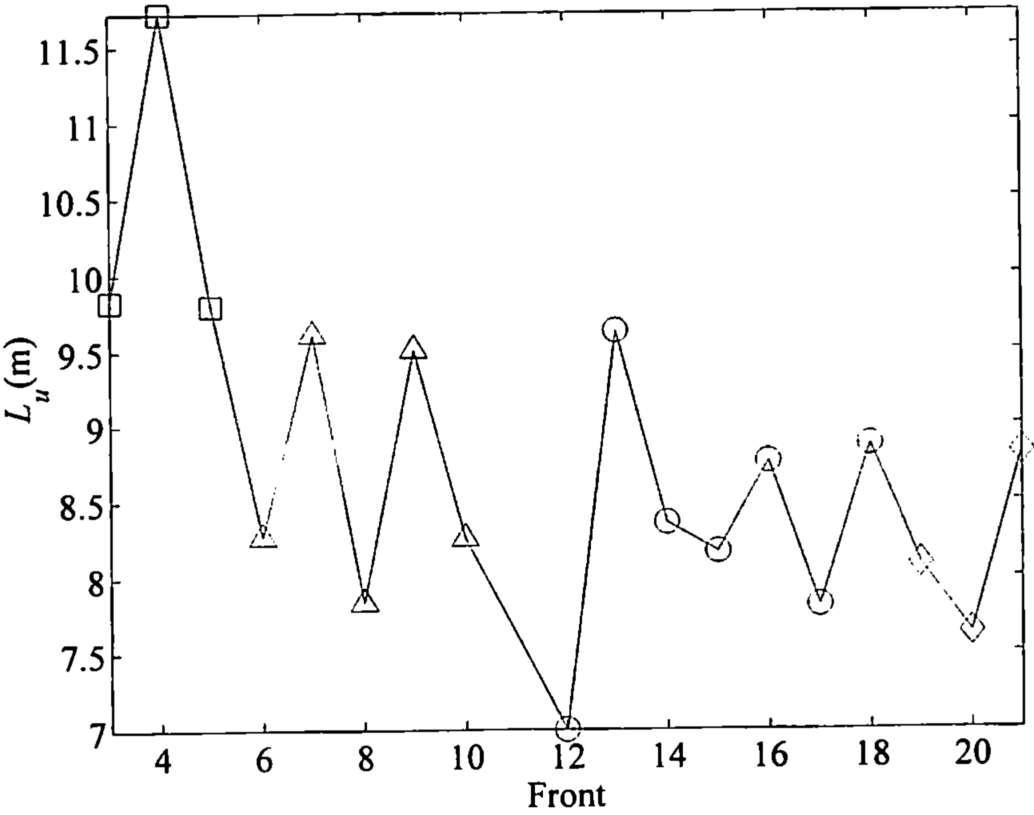

(b) 26th November

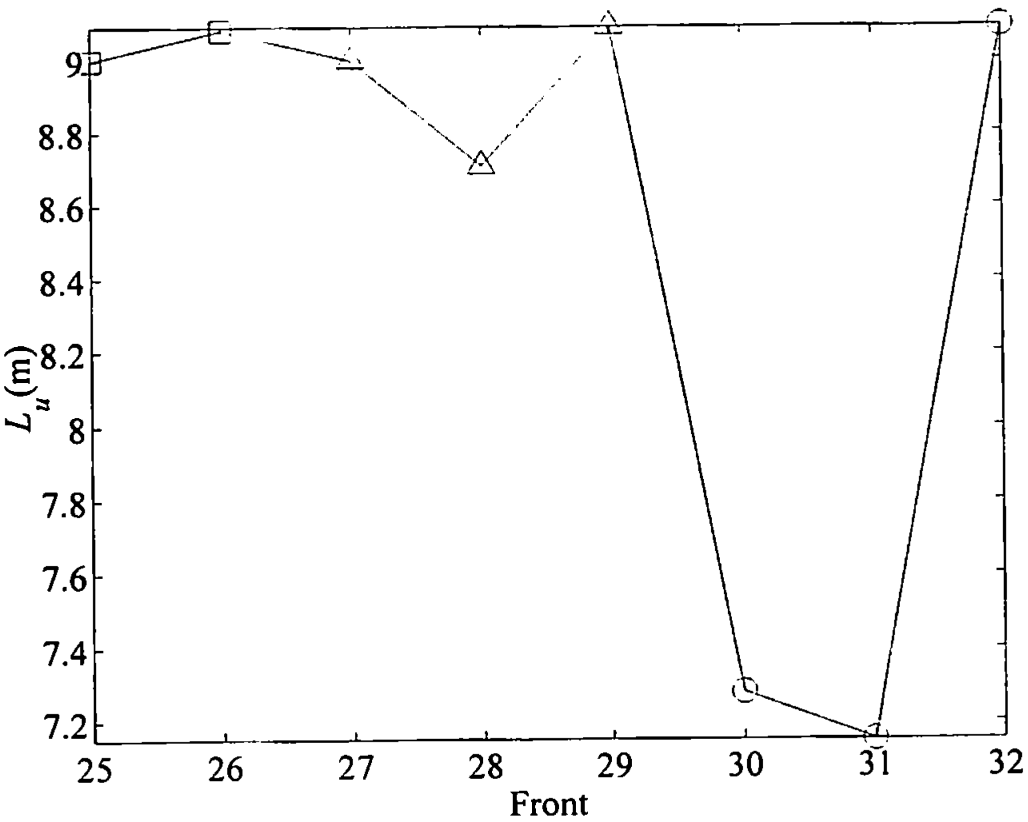

Fig 5.10: L_u (m) vs. transect number for (a) 25th November 1998. □ = group a; Δ = group b; O = group c; ◇ = group d and (b) 26th November 1998. □ = group e; Δ = group f; O = group g.

The reason for this upward flux of water in the gravity head lies in the confined and arguably inefficient mixing processes active at the front. Convergence and the associated downwelled flux of brackish and ambient seawater were shown concentrated at the foremost limit of the plume front. The accompanying interfacial shear instability that drives the mixing process between the two water types was also spatially related to the convergence as shown through the Fr_i computations. Consequently, the resultant mixing and dilution of the brackish water that is driven down into the water column at the front is limited. Thus, once the effects of downward momentum and inertia have been overcome by the buoyancy restoring force, the parcel(s) of unmixed downwelled water would begin to rise to a level of hydrostatic stability or equilibrium. Meanwhile, the front will have advanced forward so the upwelling occurs some distance to the rear of the front. This restoration process causes the velocity divergence seen behind the fronts in Fig 4.18.

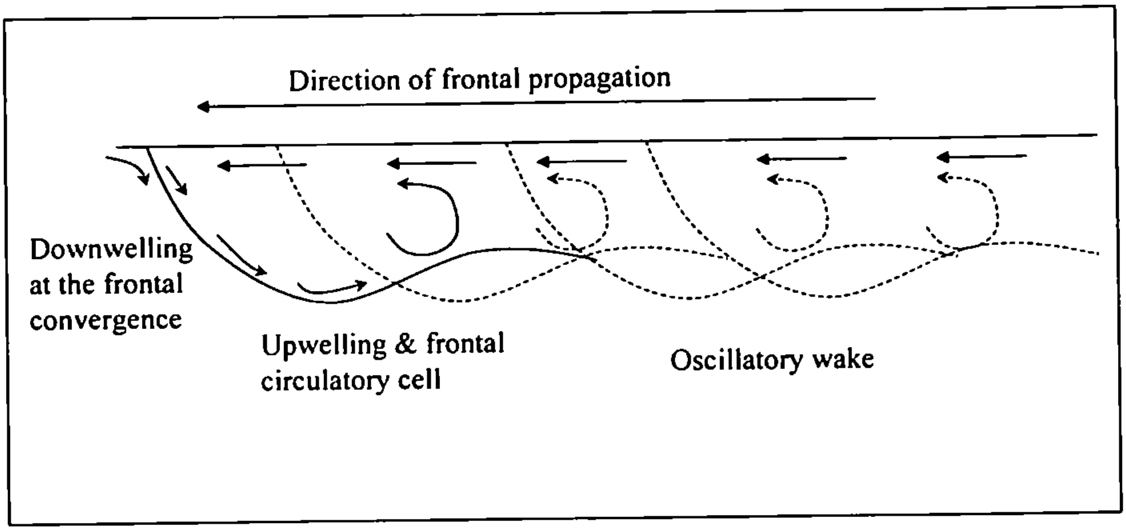

Fig 5.11: Schematic diagram of proposed 'caterpillar track' circulatory mixing inside the gravity head region of the plume outflow.

These results may indicate the presence of rotational circulation in the front and gravity head region as observed by Lukitina & Imberger (1987). As the moving head of the gravity current advanced, brackish water from the surface layer was entrained down at the relatively steep sloping interface of the convergence zone. Downwelled water is then swept back under the plume but is not fully mixed, therefore, retaining some of its buoyancy and so begins to rise to a level of hydrostatic stability. This upward flux combined with the mean lateral spreading and across frontal flow towards the front creates shear, producing instabilities and mixing as reflected in the super-critical flow and jump conditions observed in and behind the gravity head. There is a suggestion that these instabilities were Kelvin-Helmoltz billows as observed in laboratory simulations of Britter and Simpson (1978), although billow formation is caused purely by shear (see Section 5.4). The rising brackish water parcels that are not fully mixed would eventually be convected towards the front by the surface outflow current. Therefore, the mixing mechanism in the frontal region may be conceptualised as a 'tank caterpillar track' type process. The mixing zone is conveyed outwards and continually overturns the water in the front from both the source and the upwelling. This mixing 'cell' in the gravity head is followed by a diluted turbulent oscillating wake as shown in the schematic diagram of Fig 5.11 and the Fr_i data illustrated in Fig 5.3.

5.4 Entrainment & Mixing Coefficients

Sections 5.1 and 5.2 of this chapter have provided a detailed physical description of the observed mixing processes in the plume frontal region. However, the actual intensity of mixing as parameterised in the Garvine (1984) model has not yet been addressed or quantified in the present results. Therefore, the following section describes the quantification of mixing in the frontal region of the plume through a bulk mixing coefficient 'β', as specified in the model boundary conditions. Estimates of β can then be used in further numerical simulations or model validation using actual field derived β values in the frontal boundary conditions. The analysis then goes on to discuss the inter-relationship of β with entrainment coefficient, 'E' and their dependence on across frontal flow velocity.

5.4.1 β: Mixing Coefficient

β, as used to quantify mixing in the frontal region of the Garvine (1984) model, is based on the semi-empirical analysis of Britter & Simpson (1978) and Simpson & Britter (1979, 1980). They examined and quantified mixing in a gravity head current through a series of laboratory simulations and analytical models of gravity flow for inviscid fluids.

Fig 5.12 illustrates the gravity current model that was formulated in a co-ordinate system moving at a frontal velocity speed, 'u_1' relative to the ambient water and included a layer of intermediate density (h_3) and momentum between the buoyant and ambient fluid. The frontal region of the current was considered as a 'mixing box' into which, for the application to a buoyant or positive gravity current, a less dense fluid flowed from a source. The dimensionless velocity of the front Fr_i ($u_1 / (g'h_4)^{-1/2}$) was calculated through continuity and momentum equations and Bernoulli's equation applied (in the instance of this derivation) along the upper free surface of the current to the stagnation point. From the analysis, Fr_i was found to vary with the fractional depth, h_4 / h_1 and a non-dimensional mixing rate, q_m as defined in Equation 5.7. The values of q_m used in the analysis used to close Equation 5.7 were measured either experimentally or derived from billow properties behind the gravity head.

$$q_m = u_4 h_4 g' / u_1^{\,3} \qquad [5.7]$$

q_m = Non-dimensional mixing coefficient
u_1 = Frontal velocity relative to ambient water (ms^{-1})
u_4 = Inflow velocity relative to u_1 (ms^{-1})
h_4 = Interface depth (m)

The model predicted that as the dimensionless frontal propagation speed, $Fr_i = u_1 / \sqrt{g' h_4}$ increased, entrainment increased and the relative layer depth h_4 / h_1 decreased i.e. $Fr_i \approx f(h_4/h_1, q_m)$.

A further simplification of this approach to mixing is taken by Simpson & Britter (1979) where β, a modified non-dimensional mixing coefficient is estimated from a reduced version of Equation 5.7. The dimensional longitudinal inward flux $Q = u_4 h_4$ into the head is firstly combined with the velocity of advance, u_1 and the depth scale h_4 to form $Q / u_1 h_4$. Then, assuming Q / h_4 is a mean velocity of fluid arriving at the head of the gravity current, u_4 can be considered an 'overtaking velocity'. Thus, the non-dimensional mixing flux β in the head region can then be simply expressed as the ratio of u_4 / u_1 as shown in Equation 5.8.

$$\beta = \frac{u_4}{u_1} \equiv q_m Fr_i^2 \qquad [5.8]$$

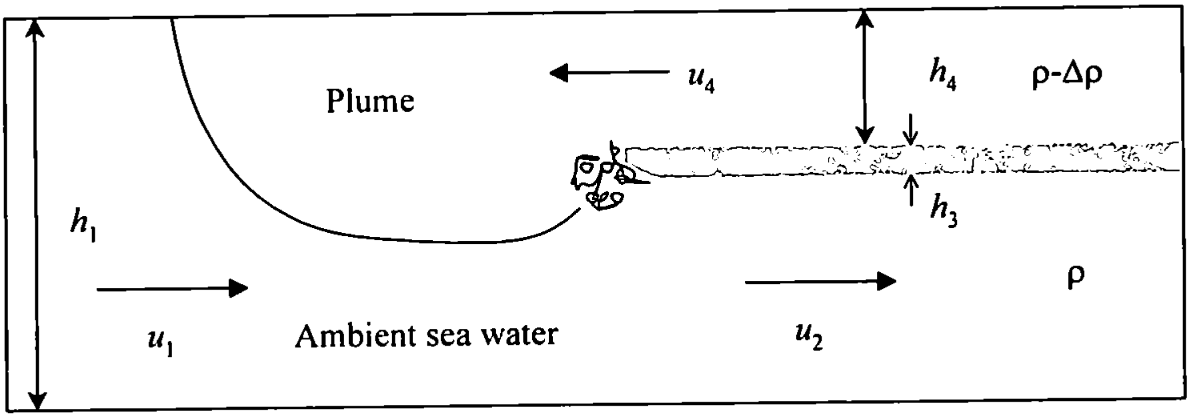

Fig 5.12: Schematic diagram illustrating the parameters used to estimate mixing coefficients (q_m and β) inside the gravity head of a positive gravity current (see text for description).

A comparison of Fr_i and relative plume depth, h_4 / h_1 between experimental data with actual field data from Lukitina & Imberger (1987) and the present study is shown in Fig 5.13 and Fig 5.14. In addition, Britter & Simpson's (1978) and Simpson & Britter's (1979) analytical solutions for the non-dimensional mixing rates, q_m and β, derived from Equation 5.7 and 5.8 respectively are displayed in the figures. Results from Britter & Simpson's (1978) experimental data suggested that an increase in frontal propagation speed increases the convergence rate at the front and decreases the relative interfacial depth i.e. how the rate of entrainment into the head increased with frontal speed.

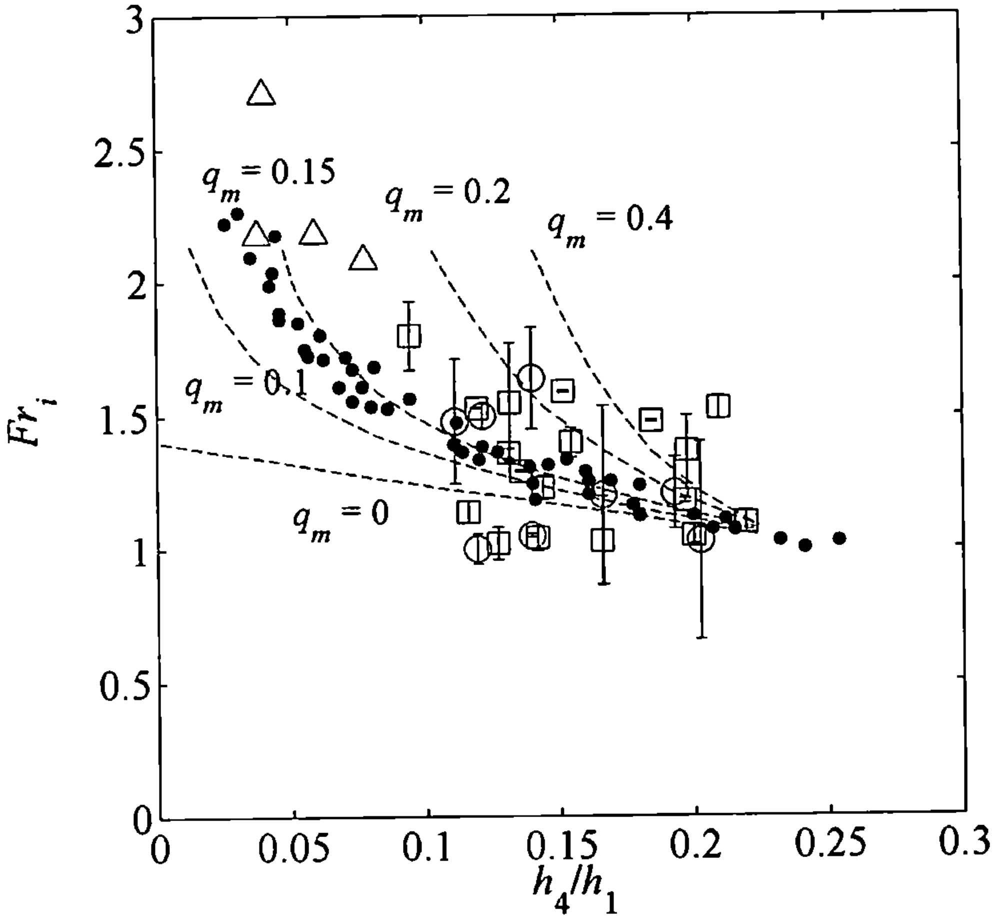

Fig 5.13: Dimensionless analysis of frontal propagation speed expressed as Fr_i Vs proportional depth of plume interface, h_4/h_1. Figure includes data from: ● = Laboratory physical models (Britter & Simpson, 1978); Δ = Field data from Lukitina & Imberger (1987); □ = Present study 25th November 1998; O = Present study 26th November 1998. Analytical solutions (bold lettering) for the dimensionless mixing rate $q_m = u_4h_4g'/u_1{}^3$ from Britter & Simpson (1978) and theoretical solution (q_m = 0) from Benjamin (1968) are shown as series of dashed lines.

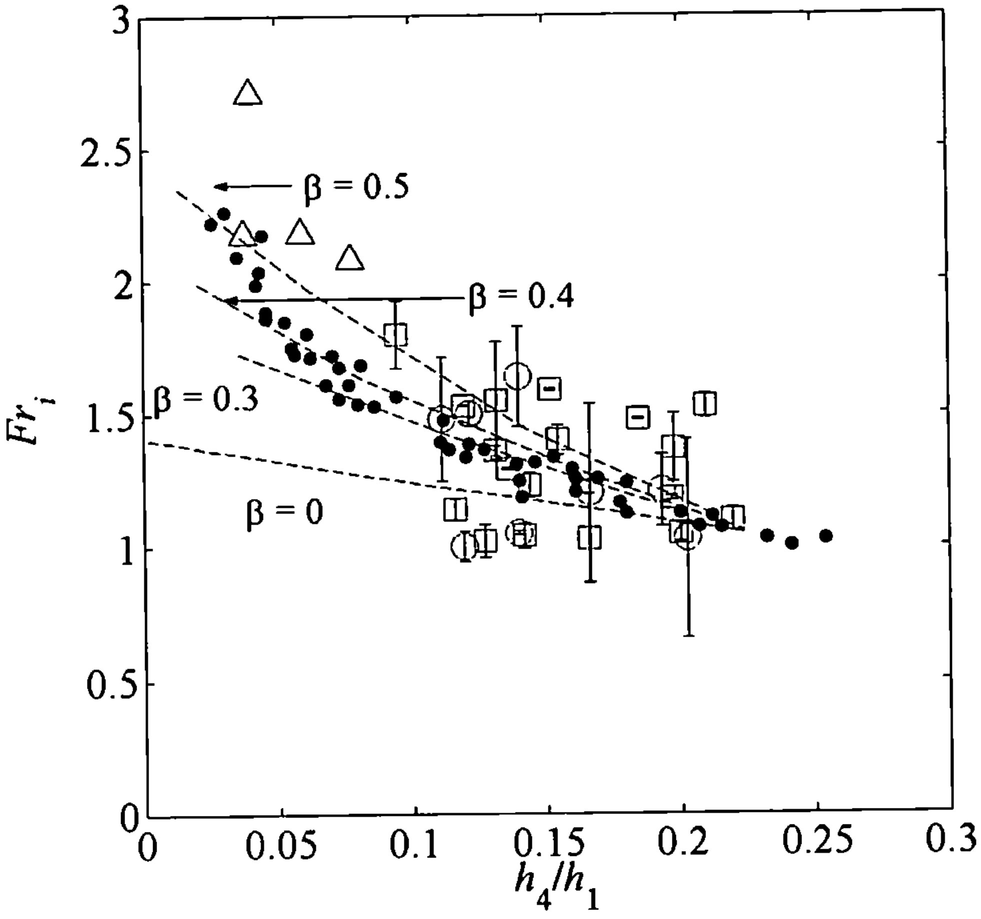

Fig 5.14: Dimensionless analysis of frontal propagation speed expressed as Fr_i Vs proportional depth of plume interface, h_4/h_1. Figure includes data from: ● = Laboratory physical models (Britter & Simpson, 1978); Δ = Field data from Lukitina & Imberger (1987); ☐ = Present study 25th November 1998; O = Present study 26th November 1998. Analytical solutions (bold lettering) for the dimensionless mixing rate $\beta = q_m Fr_i^2$ from Simpson & Britter (1979) and theoretical solution (β = 0) from Benjamin (1968) are shown as series of dashed lines.

Despite the considerable scatter shown in the present data set, the bulk of the these results fall in the lower limits of the laboratory model and the analytical solutions for gravity head mixing without friction also plotted on Fig 5.13 and Fig 5.14. However, the few outliers with error bars that fall below Benjamin's (1968) limit of zero mixing ($q_m = 0$, β = 0) that suggest mixing with friction requires explanation. The low values were representative of transect runs that had less well defined interfacial regions, especially the two outliers from the 26th November. These two runs, Transect 28 and 32 were conducted near the end of the survey period when sea conditions began to deteriorate and the plume front became more diffuse. The variability in the present data set initially made it difficult to distinguish a clear trend, which could then be used to quantify mixing in accordance with the analytical solutions.

The next stage of the analysis estimated the actual mean values of β in the frontal region of the present data set through Equation 5.8. O'Donnell's (1997) estimates of β (referred to as A) were computed from the average across-frontal velocity measurements in the upper layer. The across-frontal velocity, u_1 used in the computation of β was estimated by averaging the across-frontal velocity in a section between 10 m and 30 m behind the front. An estimate of u_4, the overtaking velocity, was calculated from the de-trended average of the across-frontal velocity record. The conditions set to estimate β, as O'Donnell (1997) mentions, were subjective.

For the present study, a more stringent criterion was chosen to compute the appropriate u_1 and u_4 values. Firstly, the same method of velocity computation based on depth averages set by the interfacial depth as in the previous Fr_i and q_e calculations was applied. Then, the spatial averaging distance used to estimate u_1 for each respective transect was specified by a longitudinal length scale computed from the 0.95 m level inside the frontal convergence to a position where the foremost interface slope was approximately zero ($\partial z \ / \ \partial y \approx 0$) behind the convergence zone. It is obvious the extent of this horizontal length scale was varied and depended on the spatial and temporal form of the interface on each individual frontal transect (see Fig 5.7). Therefore, the averaging distance used to calculate u_1 varied from between 4 m and 20 m.

The mean overtaking velocity, u_4 was then estimated from all the remaining velocity values recorded inside the plume immediately behind the u_1 'frontal section'. These values were first de-trended and then averaged to produce an arithmetic mean 'u_4' value for each respective transect. Fig 5.15 illustrates the resultant computations of β for the 25th November over the complete ebb tidal cycle. The mean value of β derived from the present calculations was 0.37 ± 0.07 (95% C.I.), approximately double the value quoted from the laboratory experiments of Britter & Simpson (1980) and slightly greater than 0.3 computed by O'Donnell (1997) for one of his survey transects.

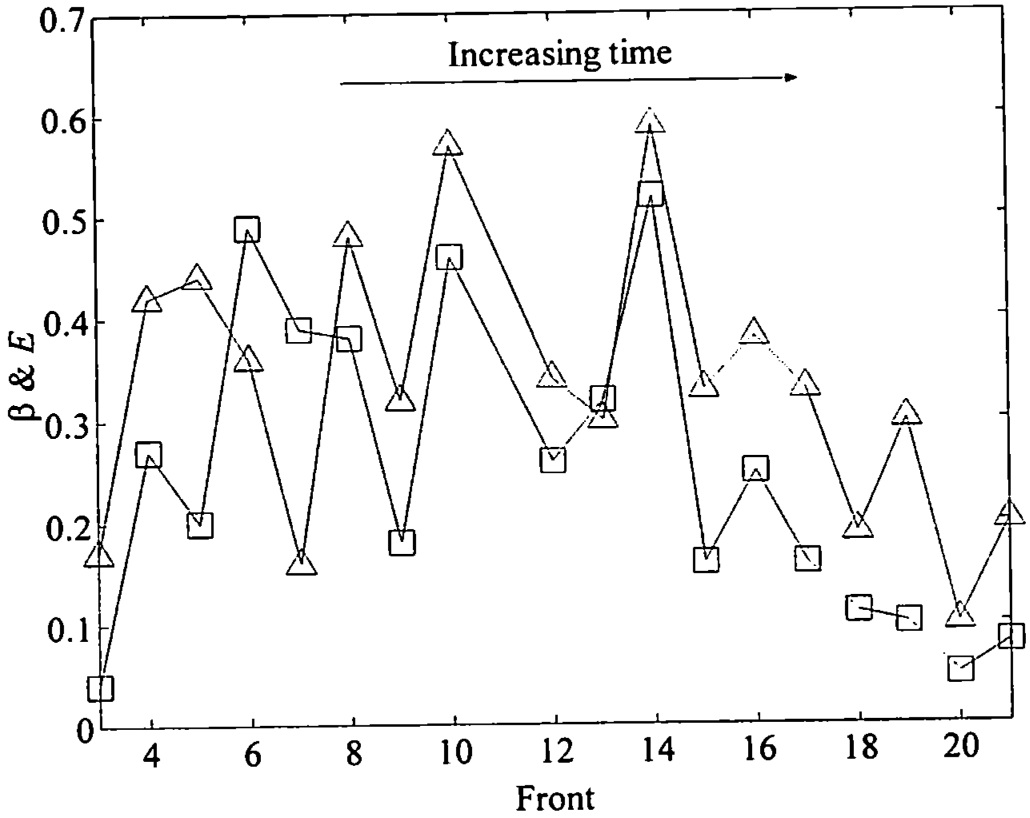

Fig 5.15: Entrainment (E) and mixing (β) coefficients computed for the 25th November plotted with respect to transect number. □ = E; Δ = β.

The figure shows how the intensity of mixing in the gravity head region increases and then declines during the ebb discharge from the estuary. However, clear discrepancies lie between the values of β computed from Equation 5.8 and the theoretical bounds for specific Fr_i, h_4 / h_1 values plotted in Fig 5.14. The discrepancy in the analytical solutions and the values derived from Equation 5.8 probably rests in the conditions in which they are estimated. The mixing coefficients derived from Equation 5.7 and Equation 5.8 by Britter & Simpson (1978) and Simpson & Britter (1979) respectively, are based upon ideal laboratory conditions where flow rates were allowed to develop into a relatively steady state before measuring the velocities in and behind the gravity head. Under the present field conditions, the flow rate behind the gravity head was modulated by the tidal outflow from the estuary and experienced periods of acceleration and deceleration during the ebb discharge cycle. This alternation of flow from the estuary added or subtracted momentum in the plume outflow over the ebb cycle. Therefore, periods of intensified mixing could exist inside the gravity current front through the Froude numbers partial functional dependence on the mixing coefficients as suggested by Equation 2.2, 5.7 and 5.8.

In the context of Equation 5.7 and 5.8, mixing coefficients and Fr_i are inextricably linked through g' and h_4. If it is assumed that the front advances at a reasonably constant velocity u_1 as anticipated from the X-band radar imagery, then both β and Fr_i will co-vary in response to any change in g' and h_4 (both $O(2)$). Therefore, the only remaining disparity independent of Fr_i in the calculation of β is u_4, the influx velocity from the estuary.

To summarise, the tidal and bulk flow properties analysis of Chapter 4 suggested a barotropic tidal modulation of the across frontal flow. This alternation in the magnitude of the ebb tidal current from the estuary with respect to a steady frontal propagation velocity gives a plausible explanation for the observed co-variance between the non-dimensional mixing coefficient and the ebb current from the estuary.

The observed difference between the analytical parameterisation of mixing through Equations 5.7 and 5.8 results in the theoretical limits of constant β values with respect to Fr_i and h_4/h_1 being approximately double those of q_m. Despite the scatter present in the field results, Fig 5.14 showed how the analytical solutions to β were in reasonable agreement with the simplified numerical solutions derived from the field data. Nevertheless, q_m was more thorough in its description of non-dimensional mixing through a larger range of Fr_i numbers as illustrated in Fig 5.13. However, in context of the present results where Fr_i and h_4/h_1 were $O(1.3)$ and $O(0.15)$ respectively, the limitation of the analytical constraints of β at higher Fr_i values and lower h_4/h_1 is inconsequential. An example of estimating both mixing coefficient for gravity currents presented in Simpson & Britter (1979) quote an approximate difference of 21% between the two methods under controlled laboratory conditions. Thus the present results that estimate a difference of $O(50\%)$ from actual field observations are not unreasonable.

5.4.2 *E*: Entrainment Coefficient

Additional calculations that estimated the magnitude of entrainment through a localised entrainment coefficient (E) were also computed over the same length scale as β using Equation 5.9 and presented in Fig 5.15. E, as defined by Ellison and Turner (1959), Turner (1973) and Garvine (1981) was applied successfully to observations made in a plume front outflow by Huzzey (1982) and describes the ratio of the vertical entrainment velocity to interfacial shear velocity. Fig 5.15 illustrates a similar trend in E on the 25th November as for the β computations where a distinct modulation of entrainment takes place over the ebb tidal cycle.

$$\frac{q_e}{\overline{u}_a} = E \qquad [5.9]$$

q_e = Vertical entrainment velocity (ms^{-1})
$\overline{u}_a$= Velocity of front relative to ambient water (ms^{-1})
E = Entrainment coefficient

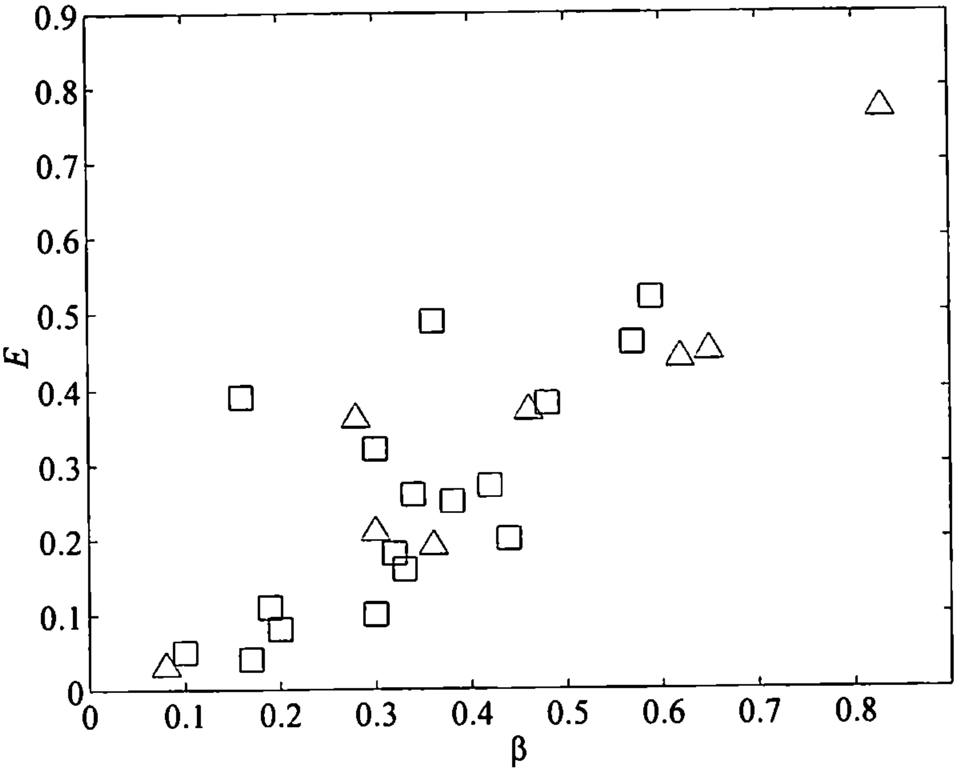

Fig 5.16: Entrainment coefficient (*E*) vs. mixing coefficient (β). □ = 25th November 1998; Δ =26th November 1998.

The magnitude of *E* as estimated by Huzzey (1982) for a plume front had a mean value of 0.18 ± 0.02 (95% C.I.) whereas in this study *E* was estimated as 0.28 ± 0.07 (95% C.I.). Fig 5.16 shows a comparison between corresponding values of *E* and β calculated from all the frontal transects conducted on the 1998 surveys. Computations showed how entrainment increased linearly with mixing through a spreading event and how both mixing and entrainment in the head region depended on the outflow velocity. These results may have been anticipated as the method and derivations used in computation of both parameters are based on properties of the across frontal flow which was shown in Chapter-4 to be tidally modulated.

5.4.3 K-H Mixing & $Ri_{b\,\Delta CR}$

To complete this section on bulk mixing and entrainment parameters, the suggestion in Section 5.3 that K-H instabilities could be responsible for mixing in the frontal region of the plume is followed up. Thorpe (1973), through a series of experiments, suggested a shear layer should eventually adjust to a level where Ri_b ($1 / Fr_i^2$) takes a critical level ($Ri_{b\Delta CR}$) and supports the observed K-H 'billow' formation. This criterion can be stated using the present nomenclature for gravity currents through Equation 5.10 (see Fig 5.12 for details of included variables).

$$Ri_{b\Delta CR} = g'h_3 / \Delta u^2 \qquad [5.10]$$

$Ri_{b\Delta CR}$ = Critical Ri_b number
g'= Reduced gravitational acceleration (ms^{-2})
h_3 = Thickness of mixed layer near the interface (m)
Δu^2 = Velocity shear across the interface (m)

Fig 5.17 illustrates the results from Britter & Simpson (1978) that replaced β with solutions to Equation 5.10 using $Ri_{b\,\Delta CR} = 0.3$ and 0.4. The results from the present study are plotted with respect to the dimensionless frontal velocity Fr_i and relative interfacial depth, h_1 / h_4 from Britter & Simpson's (1978) experimental data and Lukitina & Imberger's (1987) field data. Again, considerable scatter is present around the bounds of the specified limits of the two $Ri_{b\,\Delta CR}$ solutions and many values fall outside the limits of $Ri_{b\,\Delta CR} \approx 0.35$ as suggested by Thorpe (1973) for K-H billow formation. Section 5.4.1 discussed the source of the observed variability in the present results with those of the laboratory and analytical models. Therefore, it is not possible to confidently conclude that K-H billow formation and mixing is solely responsible for mixing processes at the plume front.

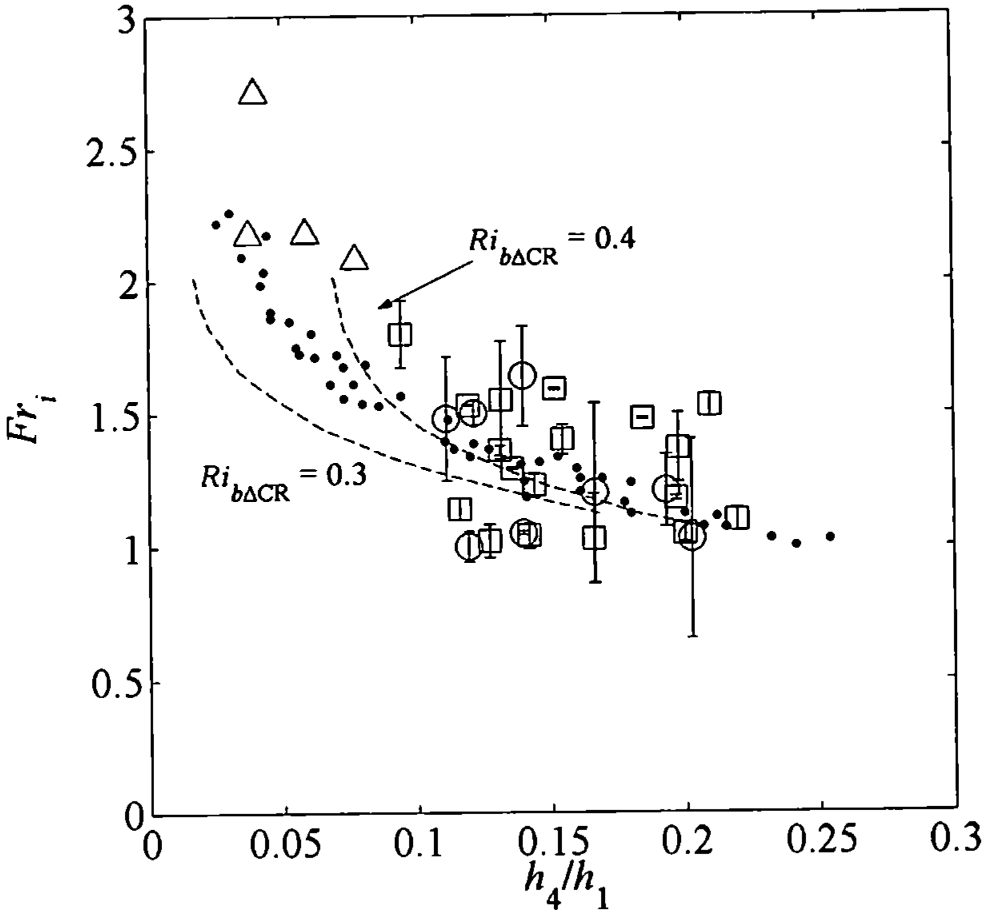

Fig 5.17: Dimensional analysis of Fr_i vs. h_4/h_1 and analytical $Ri_{b\,\Delta CR}$ solutions from Britter & Simpson (1978). Figure includes data from: o = Laboratory physical models (Britter & Simpson, 1978); Δ = Field data from Lukitina & Imberger (1987); □ = Present study 25th November 1998; O = Present study 26th November 1998. Analytical solutions (bold lettering) for the limits of $Ri_{b\,\Delta CR}$ computations from Thorpe (1973) are shown as series of dashed lines.

5.5 Energy Analysis of Tidal, Wind and Frontal Mixing

To analyse the level of work required to maintain a vertically mixed state between two fluids of different density i.e. plume and coastal water, an energetic approach as described by Blanton (1996) was adopted. The work, $\overline{P}_{vm}$ required to maintain a vertically mixed water column by mixing a density deficit, Δρ at the water surface down to a depth, $z - h_1 / 2$ may be estimated from Equation 5.11.

$$\overline{P}_{vm} = \frac{z - h_l}{2} \Delta\rho B_f \qquad [5.11]$$

$\overline{P}_{vm}$ = Energy requirement for vertical mixing (Wm^{-2})
z = Total water depth (20 m)
h_l = Depth of buoyant layer (m)
$\Delta\rho$ = Density deficit at the coast ($\approx$ 2 kgm^{-3})

Equation 5.11 neglects small losses due to sensible heat and evaporation and represents the work required to maintain a pycnocline when the upper buoyant layer receives a local buoyancy flux, B_f. B_f in this instance is directly proportional to the brackish water discharge from the Teign estuary into the Lyme Bay.

$$B_f = \frac{g}{\rho_\infty} F_{fw} \qquad [5.12]$$

F_{fw} = Freshwater flux (kgm^{2}s^{-1}) = $\rho Q_{fw} / \pi r^2$
ρ = Density of brackish water (1024.1kgm^{-3})
Q_{fw} = Brackish water discharge rate through the estuary mouth (m^{3}s^{-1})
r = Radius of plume (m)
g = Gravitational acceleration (9.81 ms^{-2})
ρ_∞ = Density of seawater (1026.1 kgm^{-3})

The power available from tidal stresses ($\overline{D}$) and wind stresses ($\overline{W}$) to work against the buoyancy forces and vertically mix B_f downwards to the specified depth (z - h_l / 2) over a tidal cycle was then estimated through Equations 5.13 and 5.14 (Simpson & Bowers, 1984; Aken, 1986).

$$\overline{D} = \frac{4}{3\pi} \gamma \rho_\infty C_D U_t^3 \qquad [5.13]$$

$\overline{D}$ = Tidal current energy dissipation (Wm^{-2}) per tidal cycle
γ = Efficiency factor for tidal stirring (0.037)
ρ_∞ = Density of seawater (1026.1 kgm^{-3})
C_D = Bottom drag coefficient (0.0025)
U_t = RMS value of the vertically averaged tidal current (0.13 ms^{-1})

$$\overline{W} = \delta \rho_a W_{10} U_w^3 \qquad [5.14]$$

$\overline{W}$ = Wind energy dissipation (Wm^{-2})
δ = Efficiency factor (0.001)
ρ_a = Density of air (1.22 kgm^{-3})
W_{10} = Wind drag coefficient (0.00145)
U_w = Average wind speed (2 ms^{-1})

Table 5.1 tabulates the results from the computation of the total energy requirement $\overline{P}_{vmT}$ to vertically mix a set buoyancy flux B_f from the estuary that is dispersed over an area of 20 km^2 on the 25th November 1998. Corresponding values of the total energy available from tidal currents $\overline{D}_T$ and wind stress $\overline{W}_T$ in the same locality are also presented. These results assume a brackish water discharge rate based on a 1m deep by 100 m cross section at the estuary mouth (1 m deep surface layer), a mean ebb flow velocity of 1 ms^{-1} and a 20 km^2 area of dispersion. This simple scaling analysis suggested that in this instance there was insufficient power supplied by the tidal currents and wind stress to fully vertically mix the surface buoyant flux down into the water column.

Area (km^2)	Q_{fw} (m^3s^{-1})	F_{fw} (kgm^2s^{-1})	B_f (m^2s^{-2})	$\overline{P}_{vmT}$ (kW)	$\overline{D}_T$ (kW)	$\overline{W}_T$ (kW)
20	100	5.1×10^{-3}	4.9×10^{-5}	16.6	-1.7	-0.28

Table 5.1: The estimated total power supplied and required to mix the Teign plume discharge over a 20 km^2 area of dispersion. $U_t = 0.13\ ms^{-1}$, $U_w = 2\ ms^{-1}$. See text for further details.

However, although these estimates were applicable to the observations on the 25th November 1998, both tidal stresses and wind stresses are very sensitive to tidal current velocity and wind speed. For example, an increase in wind speed to 8 ms^{-1} (Beaufort Scale 5) would have provided sufficient power to vertically mix the water column due to surface wave foaming. Therefore, it is acknowledged that surface layer mixing due to tidal and wind stresses can alter on temporal scales.

Energy loss across the leading frontal jump that incorporates the present results can be estimated through an argument proposed by Garvine (1984). The rate of K.E. + P.E. + mass entrainment + interfacial entrainment is estimated from the horizontal momentum multiplied by the local buoyant layer velocity relative to the front. This relationship may then be integrated both vertically and horizontally over the layer depth and width of the discontinuity to give a value for the bulk energy dissipation in the frontal zone. For a local time rate of energy dissipation i.e. $\phi = \tau_{rz}\, \partial\overline{u}/\partial z$ (τ_{rz} = vertical Reynolds stress), the bulk energy dissipation at the front is computed from Equation 5.15 (Garvine, 1984, Equation A3). The schematic physical boundaries for the calculation are shown in Fig 5.18.

Bulk energy dissipation across the front:

$$\kappa = \frac{1}{\rho_\infty}\int_0^{r_1}\int_{-d}^{0} \phi \; dz\, dr = \frac{1}{2}\left(\overline{u}_0^3 d_0 - \overline{u}_1^3 d_1\right) + g'\left(\overline{u}_0 d_0{}^2 - \overline{u}_1 d_1{}^2\right)$$

$$= \qquad \Delta \text{ K.E.} \qquad + \qquad \Delta \text{ P.E.}$$

$$+\left(\frac{\overline{u}_a^2}{2} + g'\frac{d_0 + d_1}{2}\right)\mathrm{S_e}\beta\overline{u}_a\left(d_1 - d_0\right) + \beta\tilde{\mathrm{d}}\overline{u}_a^3\left(d_1 - d_0\right) \qquad [5.15]$$

$$+ \text{ Mass Entrainment} \qquad + \text{ Interfacial Entrainment}$$

Overbar indicates velocities in a moving frontal co-ordinate system

κ = Bulk energy dissipation per unit mass, length and depth of the front (m^4s^{-3})
$\overline{u}_0$ = Velocity at d_0 (ms^{-1})
$\overline{u}_1$ = Velocity at d_1 (ms^{-1})
d_0 = Shallow boundary (m)
d_1 = Deep Boundary (m)

g' = Reduced gravity (ms^{-2})
$\overline{u}_a$ = Velocity of ambient flow (ms^{-1})
$\mathrm{S_e}$ = Entrainment direction (-1)
β = Mixing Coefficient
$\tilde{\mathrm{d}}$ = Frictional parameter
ϕ = Bulk energy dissipation (m^2s^{-3})

The instantaneous power total loss at the front, $\overline{D}_f$ (W) is then approximated by integrating along two thirds of the plume circumference (this accounts for no frontal presence and mixing near the estuary source).

$$\overline{D}_f = \rho_\infty \kappa\, L_f \qquad [5.16]$$

$\overline{D}_f$ = Total energy dissipation along the frontal boundary of the plume (kgm^2s^{-3} = W)
ρ_∞ = Density of ambient seawater (kgm^{-3})
L_f = Length of the front (m)

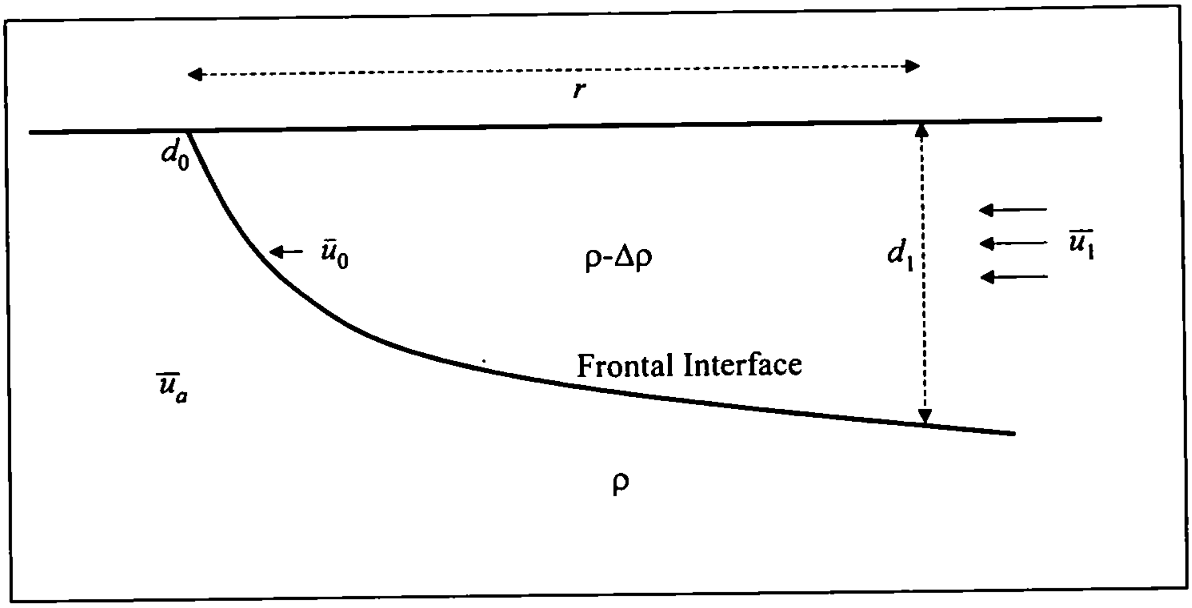

Fig 5.18: Schematic diagram to show boundary conditions and parameters used in the computation of the instantaneous frontal energy dissipation $\overline{D}_f$(W) across the entire frontal zone from Equations 5.15 and 5.16.

The variables used in computations of Equations 5.16 are based on the assumption that the front propagates at a speed of $u_0 = 0.2$ ms^{-1} and ambient water velocity is $u_a = 0.13$ ms^{-1}. Therefore, the magnitude of $\bar{u}_0$, $\bar{u}_1$ and $\bar{u}_a$ in moving co-ordinates with the front reduce to zero, $u_0(1+\beta)-u_0$(according to Equation 5.8) and $u_0 - u_a$ respectively. Depth across the frontal discontinuity is assumed as 2.5 m as shown through the plume interfacial plots (Fig 5.7), $g' = 0.02$ ms^{-2} is based on $\Delta\rho = 2$ kgm^{-3}, $\rho_\infty = 1026.1$ kgm^{-3}, $S_e = -1$ for downward entrainment and $\tilde{d}$ (described in Section 3.6) is estimated using an Fr_i value of 1.3.

Fig 5.19 shows the total and individual contribution of each energy loss term in the determination of $\overline{D}_f$ using a range of β ($f(u_1/u_0)$ in the present notation). The largest contribution to dissipation was the change in the potential energy state across the front that accounted for over 85% of the total energy loss due to the lower centre of mass outside the plume due to mixing. The results from these simple calculations based on Garvine's (1984) estimation of bulk energy dissipation at a plume front show the highly sensitive nature of $\overline{D}_f$ to β. Conceptually, this is a consequence of altering the flux of brackish water from the estuary into the front. Thus the presented argument illustrates a wide variation of $\overline{D}_f$ with only one variable (u_1) is actually, under 'real conditions', susceptible to even greater variability due to possible changes in other parameters used in the derivation of Equation 5.15 and 5.16. For example, an estimated -112 kW of power is dissipated through mixing at the front if β = 0.37 and is assumed constant through the spreading cycle whereas Section 5.4.1 showed that β depends on the surface outflow velocity from the estuary towards the front. The estimated total instantaneous energy dissipation also assumes a strongly defined frontal convergence along 2/3 of the plume perimeter and a 20 km^2 area of dispersion. In reality, the plume front was more strongly defined to the south than to the north during the ebb cycle and L_f is dependent on the area of dispersion, and is thus, subject to change in several orders of magnitude through the discharge cycle.

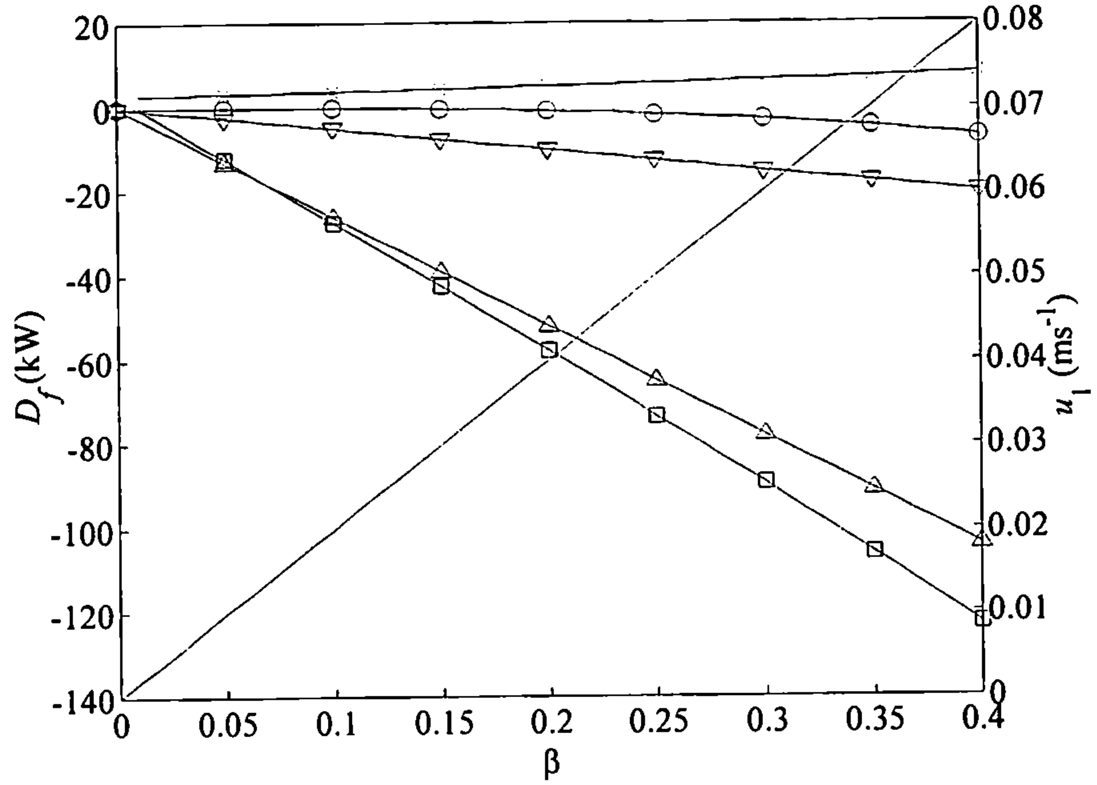

Fig 5.19: Total instantaneous frontal ($\overline{D}_f$) and component energy dissipation (kW) and overtaking velocity, $\overline{u}_l$ (ms^{-1}) vs. the non-dimensional mixing coefficient, β. — = Overtaking velocity; □ = Total energy; Δ = P.E.; O = K.E.; ∇ = Mass entrainment; × = Interfacial entrainment.

Despite the uncertainties that surround the exact value of $\overline{D}_f$, this quantified conceptual argument emphasises the comparative level of energy available to mix the buoyancy flux in the frontal zone to that available from tidal currents and wind stress in the same location. Nevertheless, the comparatively spatially narrow band (≈ 5 m wide) where frontal mixing energy is concentrated accounts for only a very small percentage of the entire plume's surface area. For example, assuming a plume area of 20 km^2, then approximately, only 0.4% of the plumes surface area is subject to frontal mixing. Hence, the spatial contribution of frontal mixing is extremely small in comparison to that available from tidal currents and wind stress.

5.6 Summary of Mixing Processes

This chapter has mainly concentrated on aspects of mixing inside the plume front and used various theoretical concepts to quantify the observations in context of the bulk mixing parameters used in the Garvine (1984) model. In addition, a more refined and rigorous mixing analysis quantified through the Fr_i and Ri_g numbers.

The conclusions drawn from the observational evidence combined with the theory suggests that entrainment and mixing in the plume front is an inherent product of a variable tidal outflow current that modulates the influx of brackish water towards the front. These observations show that both mixing and entrainment in the head region depended on the outflow velocity. Fig 5.16 and Fig 5.17 illustrated this relationship for the 25th November through co-variance in the rate of entrainment and mixing with a general increasing trend in both E and β due to an increase in outflow intensity. The magnitude of E and β eventually declines towards the end of the ebb cycle when the outflow current from the estuary begins to subside.

Mean values for β over the complete ebb tidal cycle were considerably higher than those quoted by Simpson (1982) that were used in the frontal boundary conditions of the Garvine (1984) model. García & Parsons (1996) comment that particular care should be taken on extrapolating laboratory results to field conditions as they are susceptible to the effects of scale and Reynold's number. This became apparent through the disparity between the experimental-theoretical values of β and β values estimated from field observations during the present study. These inconstancies seemed to relate to the modulation of the gravity flow into the plume as the results suggest a true steady-state inflow rate was never present through the entire tidal ebb / plume spreading cycle.

The physical investigation and analysis of the mixing processes posed questions on the source and form of the instabilities present at specific sites in the discharge plume. One possibility was the formation of K-H billows caused by the return flow and the turbulent wake from overturning inside the head and plume advance. However, K-H billow formation would require the presence and maintenance of shear driven turbidity currents that advects turbulent kinetic energy, from the front and through the entire head region of the plume. This turbulent core, as observed by Lukitina & Imberger (1987), was not evident in most of the present frontal transects. Nevertheless, this viewpoint does not take into account the concept of 'Richardson number hysteresis' where turbulence once initiated persists for Ri numbers significantly greater than 0.25 (Stull, 1998). However, the analysis from Section 5.6.3 shows considerable scatter around the required $Ri_{b\,\Delta\mathrm{CR}}$ criterion for billow formation and adds further uncertainty and conjecture to the presence of a K-H mechanism of mixing, at least through an entire plume spreading cycle.

The other potential mixing mechanism which has a sound foundation in the present results is that shear processes are predominantly concentrated at the sloping frontal interfacial region. This was shown through the narrow band of super-critical flow and unstable Ri_g values present just behind the frontal convergence. Observations went on to show that mixing was subdued just inside the gravity head where sub-critical flow conditions can then allow a return upstream flow ($Fr_i < 1$) and interfacial wave coalescence could occur some distance behind the front. The results from the Froude number analysis confirmed this through a site(s) of specific mixing and instability along the plume's bottom interface following the leading frontal jump. The percentage jump occurrences shown in Fig 5.3a displayed a distinct trend in jump formation that coincided in most instances with the rear of the gravity head region where unstable Ri_g values were also observed. Fig 5.3 also illustrated the formation of further 'multiple hydraulic jumps' that followed the main internal jump. These observations suggested that the internal hydraulic jump(s) were formed by interfacial wave coalescence and were undular. Notably, the positions of the jump(s) with respect to the surface front were on a much shorter spatial scale than predicted by the Garvine (1984) model. Chapter 6 now goes on to discuss the implications of these observations on the modelled simulations of radial plume spreading and mixing in the frontal zone.

Chapter 6

Results: Model-Data Comparison

Chapters 4 and 5 described in detail the observed dynamics in the spreading plume and concluded with a detailed physical description and quantification of mixing phenomena in the frontal region. The results from Chapter 5 through the detailed Froude number analysis indicated obvious physical differences between the internal features predicted by the modelled hydrodynamics discussed in Chapter 3 and the field data collected in the Teign plume discharge.

6.1 Model Boundary Conditions

The results from Chapters 4 and 5 suggest that there is a modulation of the 'source' outflow velocity during the Teign estuary's ebb cycle. This flow modulation from the estuary has been shown to be an important factor in the determination of mixing dynamics at the plume front. The combination of the tidal barotropic and density driven baroclinic gravity flow from the estuary with offshore directed tidal streams is not accounted for in the models 'constant' source boundary condition. Thus, the models assumption of a constant source velocity and stationary coastal water in receipt of the plume discharge is not totally true.

Probably the most important discrepancy in view of the specific aims of this study is the difference in the predicted and observed internal features inside the plume and the intensity of mixing at the front. Substantial evidence collected during the plume surveys from the ETS temperature data indicated a form of gravity head that resembled the one predicted by the scaled radial spreading model but on a smaller spatial scale. Recalling the results from Chapter 3, this head or ring region was predicted to compose of a leading frontal boundary that includes the bulk flow and mixing-frictional parameters analysed and discussed in Chapter 5 followed by an internal hydraulic jump or bore. The generic values chosen for the frontal Froude number Fr_i and non-dimensional mixing parameter β in the Garvine

(1984) model were shown through the mixing analysis presented in Chapter 5 not to be generally representative of the values measured at this particular geographical location.

Therefore, it now remained to examine the effects of implementing these field-derived values into the initial and boundary conditions of the model. This procedure discussed in the following sections was set out as a calibration or sensitivity test using the quantitative results with the model set to conditions measured from the field observations.

6.2 Froude number

The original boundary condition chosen to simulate the super-critical flow spreading of a radial plume front utilised a Froude number of $F_{al} = \sqrt{2}$. Results from the present field observations showed the leading front of the Teign plume to advance at a rate comparable to a mean Froude number (Fr_i) of $(O)1.3$, only 19% less than the estimated value. In terms of this adjustment, the minor decrease in the Froude number had very little effect on the predicted hydrodynamics. Fig 6.1 shows the results in the form of the dimensionalised characteristics plane both before and after the appropriate site-specific correction to the F_{al} (Q_a / C_f) term in the frontal boundary condition.

The leading front showed negligible shift in both time or space through radial development after decreasing $Fr_i = F_{al}$. Scrutiny of the frontal boundary condition (Equation 3.13) revealed how the speed of the leading front relative to ambient water, Q_a, remained the same as the slight decrease in F_{al} was compensated by an increase in the frontal phase speed, C_f. However, model output did show an increase in the radial distance between the leading front and trailing bore in dimensional space by some 30 m. The frontal boundary conditions outlined in Chapter 3 illustrated how any decrease in F_{al} at the front must be accompanied by a decrease in F_f resulting from an increase in C_f. Thus the higher phase speeds behind the front decrease the gradient of the Q-C characteristics slope behind the leading frontal boundary. Physically, the absolute speeds of the reflected upstream waves were now slower and travelled further upstream due to less dispersion in the leading frontal zone. Therefore, the downstream and the reflected upstream travelling waves coalesced and formed the trailing bore slightly later in R-T space.

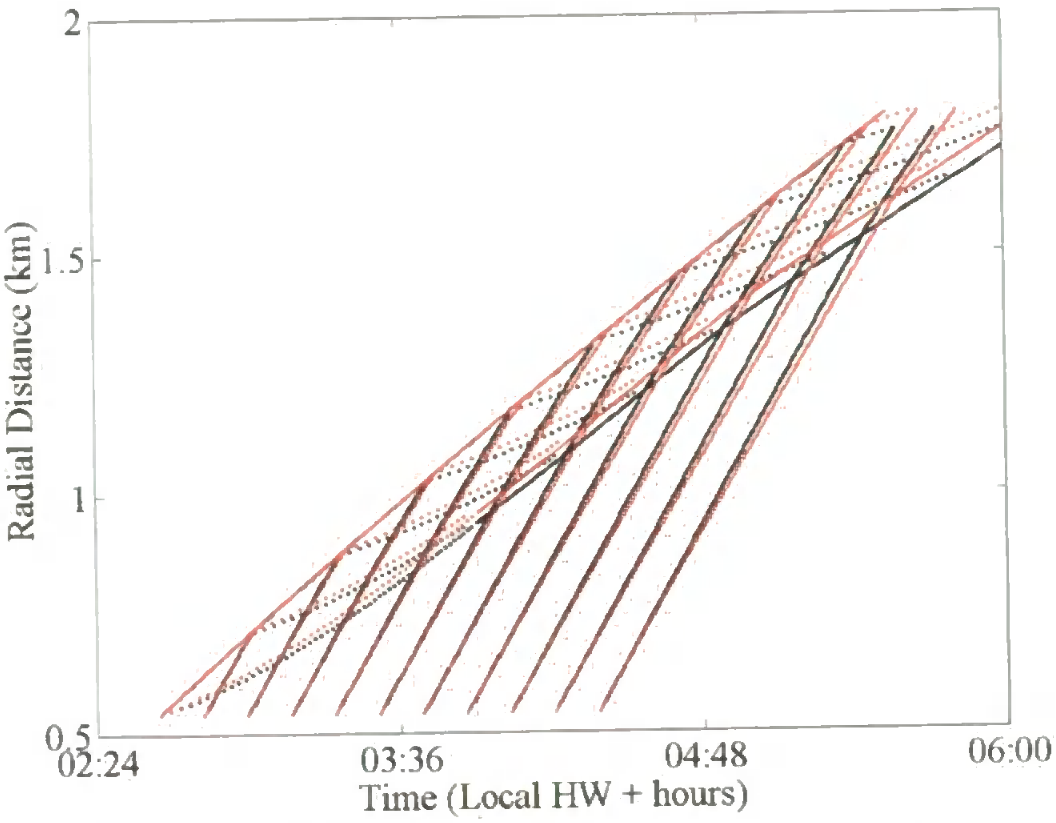

Fig 6.1: Dimensionalised plot of effective radial distance (m) vs. time (HW + hours) in the characteristics plane for model run conditions with adjusted Froude number: $F_{a1} = \sqrt{2}$; $F_{a1} = 1.3$.

Numerical experiments that increased F_{a1} above $\sqrt{2}$ showed the exact opposite to the above results. Incrementally raising the value of F_{a1} on different model runs through a range of $\sqrt{2}$ to $\sqrt{10}$ decreased the distance, in radial space (R), between the leading front and the internal bore. The lower phase speed of flow behind the front, C, positively increased the gradient of the Q-C characteristics slope meaning greater dispersion (and energy loss) at the frontal boundary. This effectively reduced the upstream distance to where upstream and downstream interfacial waves coalesce and form the internal bore.

6.3 Mixing

After decreasing the Froude number it followed to replace the bulk mixing coefficient β used to synthesise the extent turbulent exchange in the frontal region of the model. The field observations suggested β was in the order of 0.37, over twice the magnitude used by Garvine (1984) in the model and slightly higher than the maximum value recently quoted by O'Donnell (1997) for the Connecticut plume. A positive increase in β intensifies the region of turbulent exchange following the leading front. Thus, as β increases F_f increases. If Q_f remains constant then through Equation 3.14, C_f decreases. Physically, the increased turbidity and mixing decreases g' and the interfacial wave speed 'c_i'. Hence, Q_a the resultant flow velocity at the front relative to ambient water is reduced through the relationship in Equation 3.13. This reduction in propagation speed decreases the spatial scale where downstream and upstream interfacial waves coalesce. Thus, the internal jump forms nearer to the leading front as more energy is dispersed through higher wave numbers as T.K.E. This local increase in energy dissipation fuels mixing processes at the leading front and less energy is then available for upstream propagating interfacial waves that coalesce with downstream travelling interfacial waves to form the internal trailing bore.

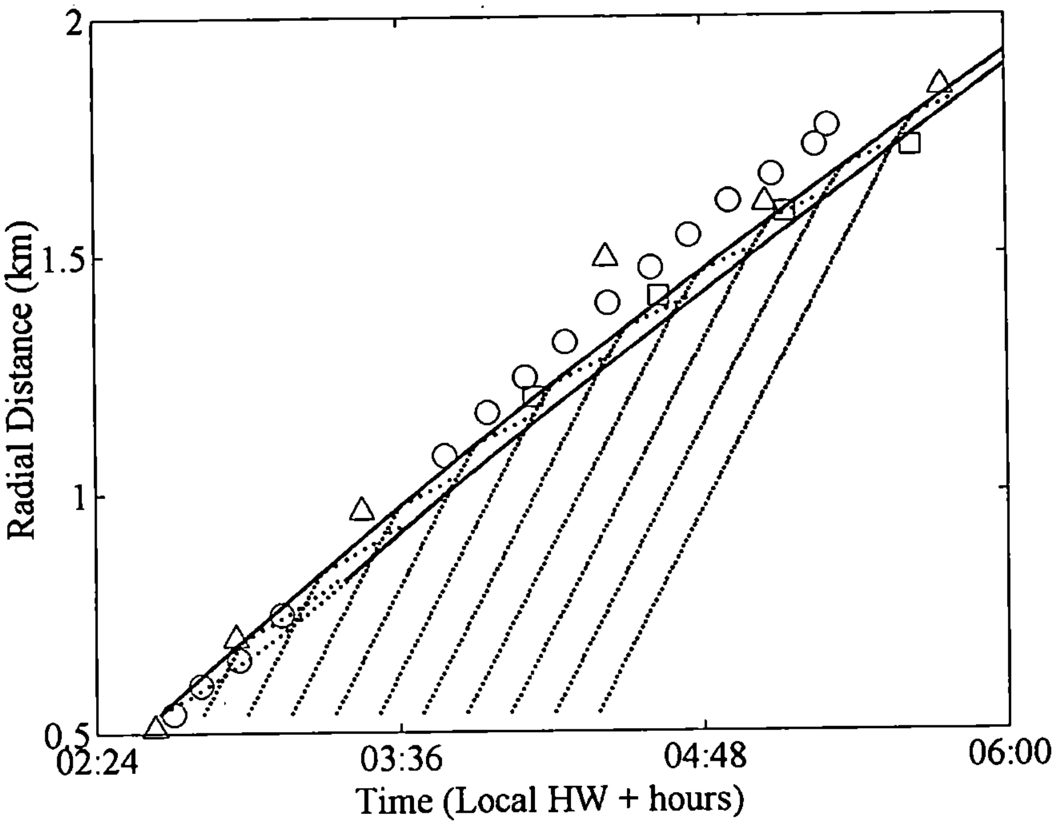

Fig 6.2: Modelled effective radial distance (m) vs. time (HW + hours) in the characteristics plane with F_{al}= 1.3, β = 0.37, Q = 1.4 and observed radial distance and time calculated from area development as captured in X-band radar imagery. Time is relative to local HW. □ = 19th November 1994; Δ = 3rd March 1995; O = 7th March 1995.

Initially, the model defaults chose a value of Q = 1.2 and scaling speed of $q^* = 0.13$ ms^{-1} giving an initial frontal velocity of 0.16 ms^{-1} at the source. To maintain a similar radial spreading rate to that observed in the X-Band radar imagery after increasing the bulk mixing coefficient β required an increase in flow speed behind the front to main continuity. The increase in source velocity effectively compensated for the extra mass lost in the front due to the elevated value of β. Fig 6.2 shows how a sequential increase in β and Q = 1.4 (frontal velocity = 0.18 ms^{-1} at the source) retains the spreading speed but reduces the lag distance of the internal jump to some 40 to 60 m behind the leading front. This distance is of the same order to that of the rear of the head region in the Teign plume where super-critical Fr_i values were observed on the 25th November 1998.

(i) 25th November

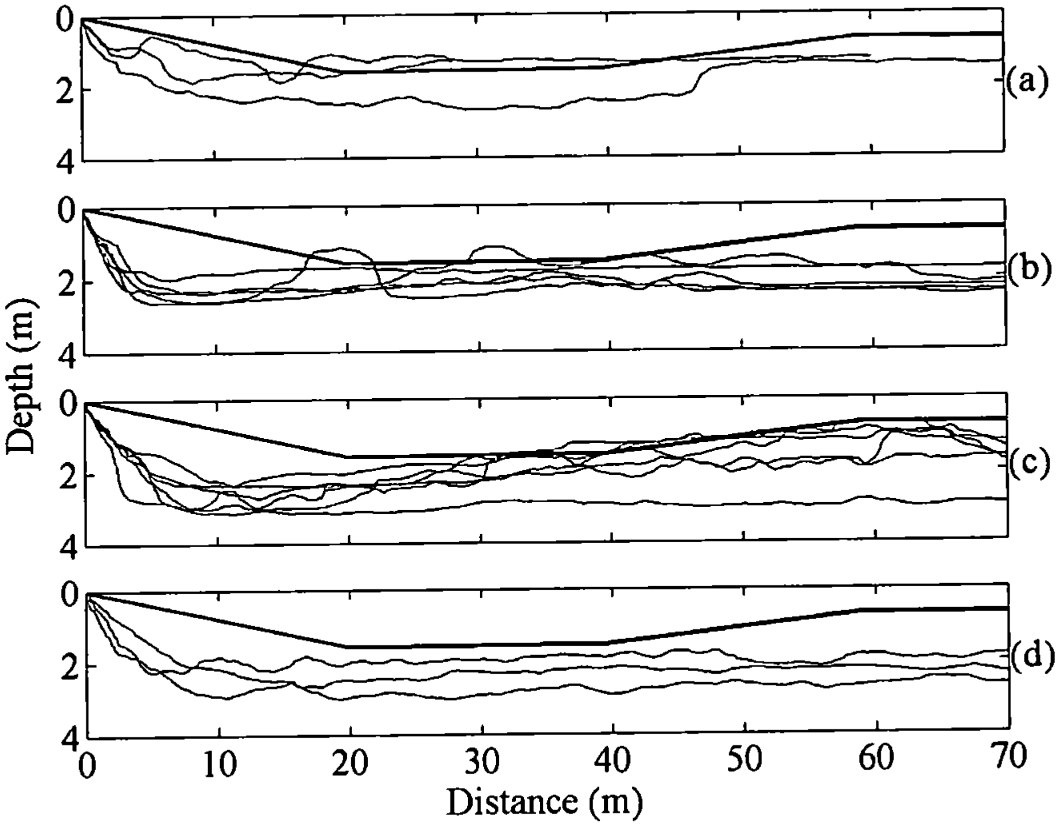

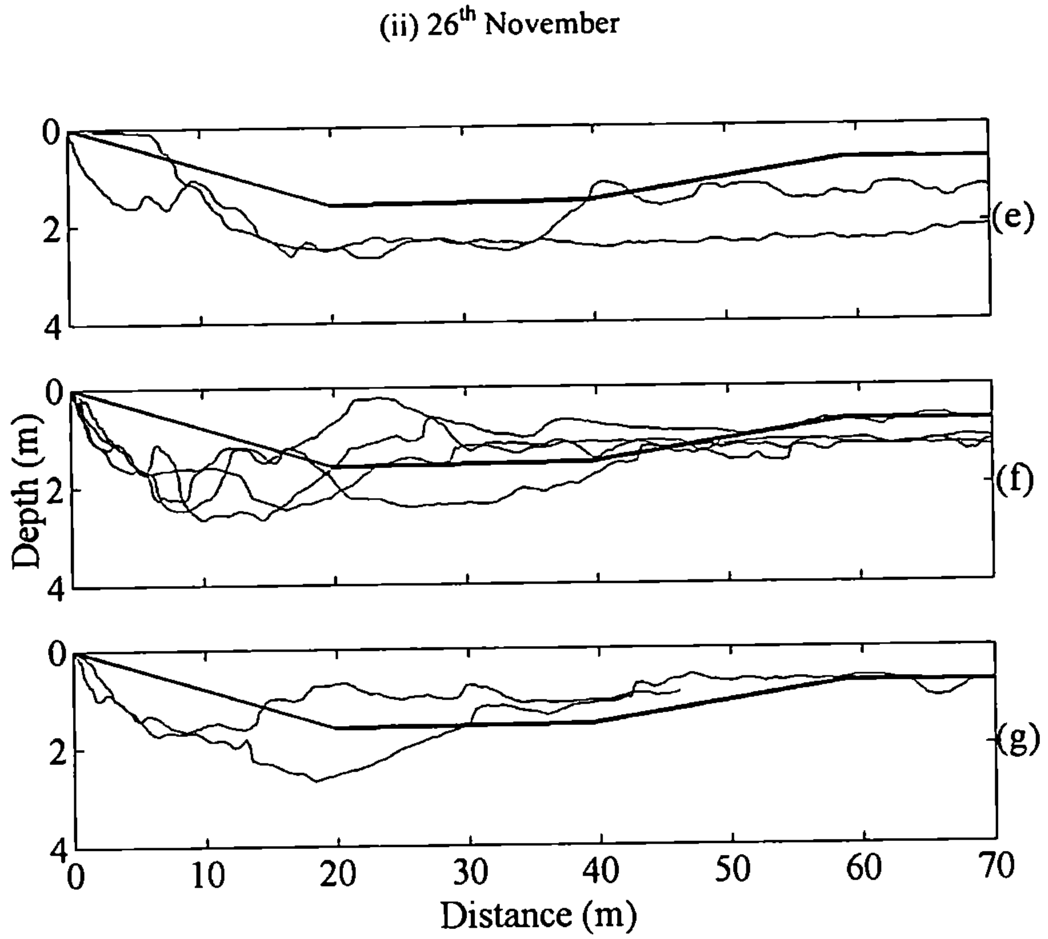
(ii) 26th November

Fig 6.3: Predicted and actual interfacial depth (m) vs. distance (m) from the convergence zone for transects grouped with respect to frontal velocity averages as described in Chapter 4. Predicted interfacial depth is represented by the thicker black line. (i) 25th November 1998: (a) HW + 2:42 hours; (b) HW + 3:36 hours; (c) HW + 5:12 hours; (d) HW + 5:42 hours. (ii) 26th November 1998: (e) HW + 3:23 hours; (f) HW + 3:27 hours; (g) HW + 3:59 hours.

Fig 6.3 shows the predicted form of the interfacial depth contour compared with actual depth as computed from ETS thermistor temperature data. The modelled interface which tends to smooth the frontal and bore discontinuities because of model grid resolution shows remarkably good agreement with the actual form of the plume interface. Both the predicted and actual interfaces ascend some 40 to 60 m behind the leading front where in most instances, a site of critical flow and instability was shown to occur through the Fr_i and Ri_g analysis presented in Chapter 5. The difference between the actual and predicted depth can be altered by increasing d_0 at the initial start condition (T=0) of model runs i.e. as d_0 increases d at the front increases. It should also be noted that for these predictions a constant value of β, q^* and F_{a1} are used throughout the modelled time development of the plume whereas, these parameters as were shown in Chapter 5 to actually vary over the tidal cycle.

6.4 Strengths & Deficiencies of the Modelled Hydrodynamics

Despite the gross simplification of the processes numerically simulated, the results from this chapter offer a feasible and quantifiable explanation of the observed phenomena in the field. Once the boundary conditions had been 'tweaked' by the introduction of the new constants, the modelled hydrodynamics showed better agreement with the observations. Frontal boundary conditions replicated the observed flow quite successfully and predicted the site of the internal bore in the same spatial location as where critical flow and jump conditions were observed on many of the across-frontal transects. Results from the numerical simulations showed that the extent of turbulent mixing in the leading front had an important effect on the lag distance of the internal bore behind the surface front. Fig 6.4 illustrates the lag distance of the bore through a range of β values (0.15 to 0.4) in a series of separate model runs. The predicted lag distance of the internal bore behind the surface front had a near linear decrease as β was incrementally increased. This result was a consequence of the reduced phase speed C_f causing interfacial wave coalescence to occur earlier in R-T space and thus formed the internal jump closer to the surface jump. Conversely, once the correct adjustment to spreading speed had been introduced to the models initial source boundary conditions, β had little effect on the form or frontal-spreading rate of the surface front through R-T space. Therefore, by introducing a site specific value for β it seemed that the modelled flow gave a reasonably good physical explanation for the observed interfacial features thought responsible for some degree of mixing in the Teign plume frontal zone.

However, the fine scale composition or physical structure of the multiple internal jumps was more complex than can be produced by the current numerical simulations. The presence of multiple jump condition requires solutions to multiple discontinuities and energy loss that is not possible through the current numerical procedure. The method of characteristics requires the fitting of a boundary or jump condition to any discontinuity to produce solutions. Hence, the numerical procedure required to solve multiple jumps or flow discontinuities using the method of characteristics would be extremely complex if not near impossible. This leads to the question of whether primitive equation models are more appropriate and emphasises that there is room for improvement in the modelling of the non-linearities present in small-scale and the near field bounds of larger scale discharge plumes as discussed in Chapter 2.

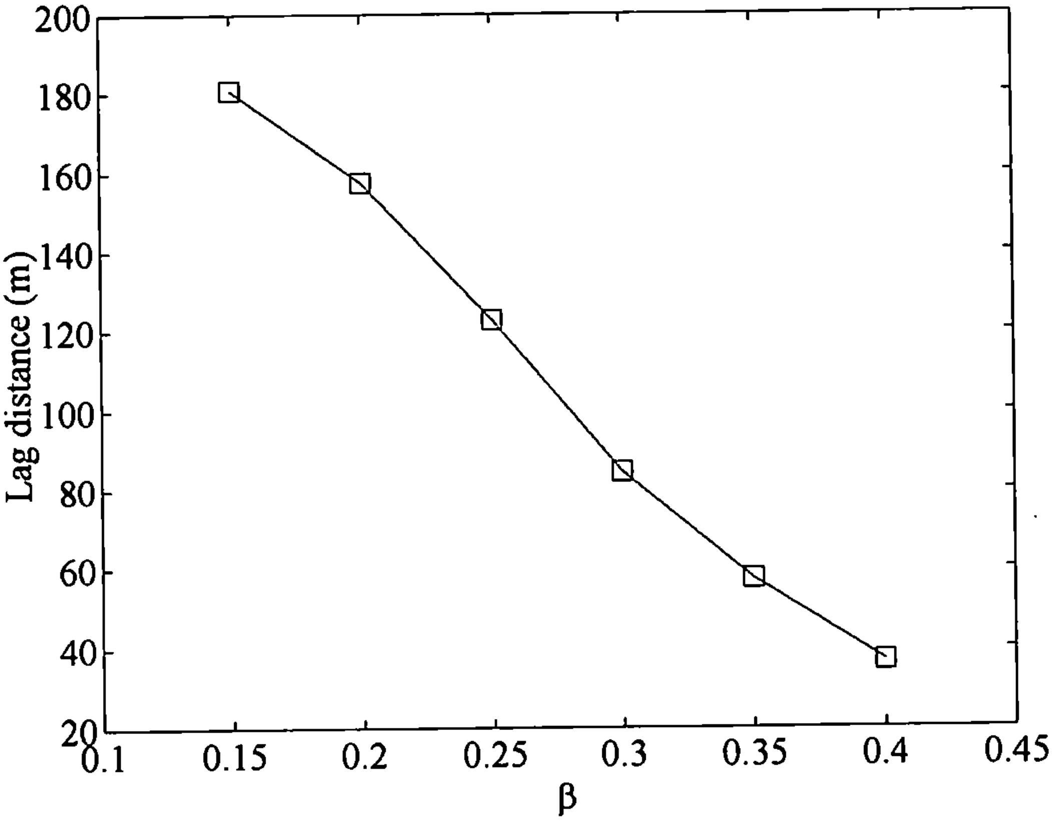

Fig 6.4: Lag distance (m) of the modelled internal bore behind the leading surface front vs. the mixing coefficient, β.

Chapter 7

Discussion & Conclusions

The comparison of observational data and numerical modelling in this study has provided an interesting insight into the physical mechanisms responsible for the temporal and spatial dispersion of the Teign river plume. This final chapter discusses the results and points the way towards future work.

7.1 Tidal Influence on Plume Spreading

Chapters 4 and 5 have shown, as would have been intuitively expected, that the estuary's ebb and coastal tidal currents dominate the dynamics in the Teign discharge. The scaling argument of Chapter 3 illustrated how the barotropic contribution to the pressure gradient force from the estuary on the ebb tide is the paramount force in plume formation, mixing and eventual dispersion of the plume. The baroclinic component that is linked to the freshwater river runoff rate essential for gravitational spreading and plume formation is subject to barotropic modulation especially when rainfall is low.

The consequence of a highly variable freshwater input and lack of data made it difficult to establish the mixing dynamics inside the estuary that significantly reduce the density anomaly at the coast. Therefore, it must be postulated that the majority of mixing inside the estuary occurs mid-estuary at the turbidity maximum some 3.5 km upstream from the estuary mouth (Wimpol, 1989). In addition, the complex circulation around 'The Salty' is likely to contribute significantly to the dispersion of the pure freshwater signal. The subsequent consequence of a variable volume of freshwater input and estuarine mixing processes is that the density anomaly varied at the coast from 1.25 to 3 kgm^{-3}. Once at the coast, the plume front forms to the south of the estuary and is attached to 'The Ness' side of the estuary. Frontogenesis next to 'The Ness' was consistent with all archived and present observational studies and is attributed to the convergence of the ebb discharge current and weak coastal tidal streams of $O(0.25\ \mathrm{ms}^{-1})$. This was shown clearly in the X-band radar image captures.

X-band radar employed to study plume radial spreading rates proved an excellent tool for temporal and spatial development studies of larger scale plume dynamics and model scaling in the coastal zone. The potential of this instrumentation to resolve frontal features and thus provide spatial mapping of a plume discharge is now realised and it proved a pity it was not available during the 1998 surveys. In hindsight, X-band radar time series captures of plume spreading could have eliminated some of the problems encountered with the EMCM's and allowed a more concise estimation of plume dynamics relative to a fixed Earth reference frame during the two current surveys. Nevertheless, the plume mapping provided by the 1995 image captures supported the current project's observations that catalogued the same frontal development by 'The Ness' and offshore spreading through the ebb tidal cycle. X-band radar imagery suggested that plume propagation speed maintained a relatively consistent radial-spreading rate throughout the ebb tide discharge. This apparently near invariant linear spreading rate as shown through the image analysis of several plume outflow events, was governed by the super-critical interfacial Froude number criterion of $O(1.3)$ in the foremost frontal region of the plume.

Once the front became established, the weak inshore tidal currents that were directed towards the NE rotated clockwise offshore and collectively with the estuary's ebb tide further accelerated the flow offshore towards the front initially through tidal forcing. In later stages of development, despite a decrease in tidal forcing, further offshore plume expansion may be present due to the outflowing estuarine gravity current as shown through the modelling study of Wheless & Valle-Levinson (1996). This caused the front and gravity head to slightly deepen and the plume to strengthen in temperature and in salinity contrast with the surrounding coastal waters. In the meantime, the plume formed its characteristic radial shape almost symmetrical around the mouth of the estuary. The radial plume formation was observed to coincide with the phase lag between the offshore and nearshore tidal currents.

Coriolis force as shown through the scaling argument of Chapter 3 proved insignificant in comparison to the effects of the pressure gradient force and no obvious geostrophic adjustment of the Teign outflow to a coastal current was evident in the present or past plume studies.

7.2 Model Application & Suitability

Application and evaluation of the Garvine (1984) radial spreading plume model to the Teign plume proved a novel and interesting exercise that answered some and raised further questions on small-scale plume dynamics and mixing. The assumptions of the modelled flow that presume a constant input of buoyant water from the source was not totally justifiable as discussed in Chapter 6. Under situations where tidal modulation of the outflow or source velocity is a prominent factor as in the Teign plume dynamics, a model would be better forced by a *sin* function (0 to π) source boundary condition. This would effectively represent ebb flow intensification after local HW and eventual decline towards LW. The reason this suggested improvement was not introduced into the model was because of the additional complication of numerically adding the multiple internal jump discontinuities as observed in field into the model scheme as discussed later in this chapter.

The most important factors to consider between the modelled and observational results in context of this study, are the agreements and discrepancies between the internal hydrodynamic features and mixing processes active in and around the plume front. As previously discussed, the frontal propagation maintained a reasonably constant Fr_i value of $O(1.3)$. This is in tentative agreement with the resent field observations made by O'Donnell (1997) in the Connecticut plume using a similar experimental protocol. The reintroduction of the field derived Fr_i value into the model's frontal boundary condition had little impact on the modelled dynamics other than to slightly increase the spatial lag of the computed position of the trailing internal bore. However, observational data gave no confident indication that the predicted internal bore formed in this region of the plume but did identify a similar feature much closer to the leading front than the model predictions suggested. The proposed reason for the model-data discrepancy is again related to the estuarine outflow dynamics that ultimately controlled the mixing processes active in the Teign plume front.

Computation of the mixing-frictional coefficient β or the parameter that represents the extent of turbulent exchange in the frontal region of the model was not constant throughout the ebb spreading cycle and was modulated by the estuary's discharge current. This result could have been anticipated from the findings of Chapter 4 and Chapter 5 through its method of derivation from the across frontal flow velocity. Under laboratory conditions, flow as in the experiments of Britter & Simpson (1978) and Simpson & Britter (1979) is in steady state. In the present field study, the influx of brackish water from the estuary undergoes a period of intensification shortly after the peak ebb flow and retardation towards local LW. The results from these observations were not accounted for in the Garvine (1984) model boundary conditions that assumes a constant β value. Chapter 5 suggests this variability in context of the analytical solutions provided by the Britter & Simpson (1978) and Simpson & Britter (1979) experiments was attributed to the non-steady state flow conditions from the estuary.

Further examination of mixing parameters in context of the Britter & Simpson (1978) and Simpson & Britter (1979) experiments showed variability around the specific $Ri_{b\ \Delta CR}$ criterion of 0.35 for the formation of shear generated K-H billows and thus attached uncertainty on whether this process of mixing was present behind the front at all times during a spreading cycle. The present results suggested the method of brackish water dispersion in the frontal region was more passive in comparison to larger scale billow mixing. Mixing behind the plume front appeared to be confined to smaller scale instabilities in the form of internal hydraulic jumps rather than larger scale turbulent billows.

Repeated survey transects into the plume front indicated a gravity head region with a steep leading front where longitudinal and vertical gradients in temperature and velocity were great and mixing and turbulence levels high. This frontal region was accompanied by downwelling motion and downward entrainment in the convergence zone as observed by Garvine & Munk (1974) and O'Donnell (1998). The front was then followed by a region of stability that contravened the findings of Lukitina and Imberger (1987) who suggested the presence of a turbulent rotor following the gravity head on a length scale of 10's of metres. Results from the Fr_i and Ri_g number analysis within the plume front indicated that rather than one concentrated region of mixing, overturning through instability was in the form of an ensemble of multiple internal hydraulic jumps following the main frontal region. The majority of these jumps were located at what the isotherms suggest as the rear of the gravity head where isotherms were observed to ascend. The concentration of hydraulic jumps behind the gravity head some 40 to 60 m behind the leading front was high and consistent through consecutive frontal transects.

This leads to the question on the suitability of a model based on the methods of characteristics as this method of solving the non-linear long wave dynamics cannot provide solutions to multiple discontinuities. Despite the presence of subtle physical inconstancies between the modelled jump and those detected through observations, a flow discontinuity or hydraulic jump(s) was present in the region behind the gravity head. After an appropriate 'tweaking' of model boundary conditions through the improved mean value of the mixing parameter β, the observational data and modelled interfacial depth profiles showed excellent agreement. Also, near the site of the main rear internal jump, a region of upwelling seems evident where it is thought a 'caterpillar' type circulatory cell in the head region of the plume re-circulates previously downwelled water from the leading front.

At the end of Chapter 5 a simple scaling analysis was proposed between the level of energy dissipation at the plume front and the corresponding values due to the effects of the wind stress and the tidal currents. The level of mixing due to tidal currents and wind stress inside the plume was shown insufficient to vertically mix the buoyancy flux during the majority of the ebb tidal cycle. However, scaling showed higher wind speeds $O(8\ \mathrm{ms}^{-1})$ are quite capable of mixing the buoyancy flux from the estuary although this is also subject to high seasonal variability.

A specific value for a comparative level of energy loss due to mixing at the plume front holds uncertainties in the proposed argument that sums specific losses in the front due to different contributory losses of P.E, K.E., mass and interfacial entrainment, frontal definition and length of the frontal perimeter. The results showed that this argument is highly sensitive to scalars (interfacial depth, length) and vector (reduced gravity, velocities) properties and the specific value of β used in the solution. Despite the uncertainty on the exact value of total energy dissipation along the plume front i.e. $\overline{D}_f\, O(1.5 - 7) > \overline{P}_{vmT}$, the energy argument helps to illustrate the intensity of vertical mixing around the frontal perimeter in comparison to the power available for mixing inside the plume from the wind and tide.

The points to be drawn from the energy analysis of mixing is the tendency of the buoyancy flux to overcome the ability of tidal power and under relatively calm conditions, local wind stress to mix the brackish water discharge. This results in the maintenance of a plume where mixing is predominately confined to the narrow, strongly defined frontal region that either fully or in part encompasses the plume. The energetic arguments highlight the inherent variably and non-linearity of small scale plumes and helps to explain the inshore lower salinity and temperature residuals sometimes present outside the Teign estuary and similar tidally modulated buoyant discharges.

7.3 Instrumentation & Sampling Protocol

The sampling protocol used to detect and measure the Teign plume frontal dynamics that was ultimately based on the seasonal temperature contrasts in river and coastal waters proved an excellent method for small-scale river plume studies.

Instrumentation employed to examine the frontal region of the Teign plume through detection of the river-seawater temperature anomaly was the greatest asset to the current project's high-resolution examination and quantification of plume frontal structure and mixing dynamics. Although not novel (see Sturley (1990) & Sarabun (1993)) in using thermistor arrays for estuarine water column structural studies, the ETS's use in the quantification of vertical and horizontal mixing dynamics has been proved through the current project. Without the simultaneous horizontal and vertical temperature, salinity and velocity profiles through the water column, plus the accurate geographical positioning and corrections provided by the DGPS, the study would not have been possible. In addition, the spectral methods used to filter survey vessel pitch and roll and surface wave activity was shown as a useful technique that could be easily employed and applied to other similar problems where data is contaminated by periodic signals.

Some of the difficulties experienced with the EMCM's during the study were foreseen before any surveys commenced. However, despite the precautions taken through recording voltage offsets before and after deployment, offset problems still arose and velocity records still required considerable attention before any further analysis could commence. Nevertheless, with the assumptions discussed in Chapter 4, the velocity data still provided the required measurements and detail for the subsequent parameterisation of mixing and model comparisons of Chapters 5 and 6.

7.4 Conclusions

The current project has proved the advantage and highlighted some of the difficulties encountered when measuring and quantifying the dynamics of river discharge plumes in a moving reference frame. The results and conclusions from the study of plume and plume mixing dynamics has proved the ability to solve small scale river plume dynamics through careful planning and the use of 'state of the art' instrumentation. Model validation through the field study has shown the tentative ability of a simple numerical simulation of radial plume spreading to replicate real geophysical discharges although there is still room for improvement in the modelling schemes of such small-scale features. The discrepancies identified in model-data comparisons require a more rigorous theoretical approach to solving the observed mixing dynamics in the non-linear phase of plume development. The numerical methods used to explore the non-linear plume dynamics in this study was at best a very simplistic representation of a complex system that developed in time and space. Entrainment and mixing in the front was more intense than anticipated from laboratory experiments and remained proportional to estuarine outflow/brackish water inflow velocity into the plume. The distance that the predicted internal jump(s) formed behind the leading front was considerably less when the fractional extent of turbulent mixing (β) was increased in the leading frontal boundary and its form was actually a series of undular disturbances on the plume interface.

7.5 Future work

For future studies of larger and smaller scale mixing processes, the author recommends, where possible, a combination of modelling, remote sensing and field observations. Their ability to aid and complement each other could provide high quality data sets and predictions enabling a more concise overview of a plume study and help overcome some of the difficulties encountered during the current project when in the field.

This study's account of plume formation and local tidal effects are based on the available results from tidal current meter data, X-band radar and observational evidence. To help fully understand the local tidal regime, a fine scale grid numerical model that simulates and predicts local inshore tidal streams and circulation is required. Such a model would add a significant contribution to the knowledge of the effect of the estuarine discharge jet and coastal tidal currents on plume spatial development. At present, such models are being developed by HR Wallingford as part of the COAST 3-D project and are yet unavailable.

As previously mentioned in Chapter 3, the complex sand bar system present outside the estuary mouth must have an effect on the initial spreading dynamics of the plume. Current research within IMS, University of Plymouth is studying this inshore region through ARGUS video imaging and as part of the COAST 3-D project. Results from these longer term experiments may reveal greater information on local inshore hydrodynamics that affect the earlier stages of plume development. Also a meteorological station and tide gauge has been set up on the Teignmouth pier to complement and aid the interpretation of the ARGUS video data. The data provided by the station on wind speed and direction could be used to study the effect of local wind forcing on larger scale plume dynamics and mixing. This could remove some of the speculation on the level and role of wind stirring and mixing of the buoyancy flux discussed in this thesis.

As a possible continuance of the present work, other studies could resolve fine-scale mixing down to turbulent eddy length scales by utilising the ETS to examine small-scale turbulence in and around the frontal regions of the plume, and perhaps help determine turbulence levels in the internal jump(s). The current project did consider such an analysis using the methods described by Osborn & Cox (1972) and with hindsight could have logged data at the higher frequencies required to resolve molecular and turbulent length scales.

To try to resolve the uncertainties that still surround the along frontal components of flow, new high frequency broad band ADCP's are becoming available. ADCP's are capable of resolving, 3-dimensionally, the near surface velocity bins that are of the greatest interest to the investigator of shallow plume discharges (Brubaker & Simpson, 1999). Alternatively, the newer models of EMCM's have vastly improved and suffer less from offset wandering than the problematic models used in the current study. Thus EMCM's could still prove useful in the quantification of near surface (≤ 0.3 m) flows towards and along the plume front. In addition undulating towfish CTD profiling would complement the ETS thermistor arrangement and provide further supportive evidence of ETS results in the small-scale outflows.

References

Benjamin, T.B., 1968. Gravity currents and related phenomena. *J.Fluid Mech.*, **31**, 209-248.

Blanton, J., 1996. Reinforcement of Gravitational Circulation by Wind. In: D.G. Aubrey & C.T. Friedrichs (Eds.). Coastal & Estuarine Studies: *Buoyancy Effects on Coastal & Estuarine Dynamics*, Vol.53. American Geophysical Union, Washington. DC, USA. 359 pages.

Bomford, G., 1980. *Geodesy* (4th Edition). Clarenden Press, Oxford University Press Inc., New York, USA. 855 pages.

Bowden, K.F., 1983. *Physical Oceanography of Coastal Waters*. Ellis Horwood Limited, Chichester, UK. 302 pages.

Bowman, M.J., 1988. Estuarine Fronts In: B. Kjerfve (Ed.). *Hydrodynamics of Estuaries Vol.1 Estuarine Physics*. CRC Press, Boca Raton, Florida, USA. 163 pages.

Bowman, M.J. & R.L. Iverson, 1978. Estuarine and Plume Fronts. In: M.J. Bowman & W.E. Esaias (Eds.). *Oceanic Fronts in Coastal Processes*. Proceedings of a workshop held at the Marine Sciences Research Centre, May 25-27, 1977. Springer-Verlag, New York, USA. 114 pages.

Britter, R.E. & J.E. Simpson, 1978. Experiments on the dynamics of small gravity current heads. *J.Fluid Mech.*, **88**, 223-240.

Brubaker, J.M. & J.H. Simpson, 1999. Flow convergence and stability at a tidal estuarine front: Doppler current observations. *J.Geophs.Res.*, **104**, 18,257-18,268.

Campbell, A.R., J.H. Simpson & G.L. Allen, 1998. The Dynamical Balance of flow in the Menai Strait. *Estuarine Coastal Shelf Sci.*, **46**, 449-455.

Chao, S.-Y. & W.C. Boicourt, 1986. Onset of estuarine plumes. *J.Phys.Oceanogr.*, **16**, 2137-2149.

Chao, S.-Y., 1988a. Wind-driven motions of estuarine plumes. *J.Phys.Oceanogr.*, **18**, 1144-1166.

Chao, S.-Y., 1988b. River forced estuarine plumes. *J.Phys.Oceanogr.*, **18**, 72-88.

Chao, S.-Y., 1990. Tidal modulation by estuarine plumes. *J.Phys.Oceanogr.*, **20**, 1115-1123.

Chereskin, T.K., 1983. Generation of Internal Waves in Massachusetts Bay. *J.Geophs.Res.*, **88**, 2649-2661.

Csanady, G.T., 1979. A developing turbulent surface shear layer model. *J.Geophs.Res.*, **84**, 4944-4948.

Cunningham, P.M., R.T. Guza & R.L. Lowe, 1979. Dynamic calibration of electromagnetic flow meters. Proceedings of Oceans '79. IEEE, New York, USA.

Davies, A.M & J. Xing, 1999. Sensitivity of plume dynamics to the parameterisation of vertical mixing. *Int. J.Numer.Meth.Fluids*, **30**, 357-405.

Dyer, K.R., 1988. Tidally Generated Estuarine Mixing Processes In: Kjerfve B. (Ed.). *Hydrodynamics of Estuaries Vol.1 Estuarine Physics*. CRC Press, Boca Raton, Florida, USA.163 pages.

Dyer, K.R., 1997. *Estuaries A Physical Introduction* (2nd Edition). John Wiley & Sons Ltd. Chichester, UK. 195 pages

Ellison, T.H. & J.S. Turner, 1959. Turbulent Entrainment in Stratified Flows. *J.Fluid Mech.*, **6**, 423-448.

Environmental Resources Ltd., 1990. Teign Estuary Regional Sewage Disposal Scheme: Environmental Statement. Final Report to SWWS Ltd.

Farmer, D.M. & J.D. Smith, 1980. Tidal interaction of stratified flow with a sill in Knight Inlet. *Deep-Sea Res.*, **27**, 239-254.

García, M.H. & J.D.Parsons, 1996. Mixing at the front of gravity currents. *Dyn.Atmos.Oceans*, **24**, 197-205.

Garvine, R.W., 1974a. Dynamics of small-scale oceanic fronts. *J.Phys.Oceanogr.*, **4**, 557-569.

Garvine, R.W., 1974b. Physical Features of the Connecticut River Outflow During High Discharge. *J.Geophys.Res.*, **79**, 831-846.

Garvine, R.W. & J.D. Monk, 1974. Frontal structure of a river plume. *J.Geophys.Res.*, **79**, 2251-2257.

Garvine, R.W., 1981. Frontal jump conditions for models of shallow, buoyant surface layer dynamics. *Tellus*, **33**, 301-312.

Garvine, R.W., 1982. A steady state model for buoyant surface plume hydrodynamics in coastal waters. *Tellus*, **34**, 393-306.

Garvine, R.W., 1984. Radial Spreading of Buoyant, Surface Plumes in Coastal Waters. *J.Geophys.Res.*, **89**, 1989-1996.

Garvine, R.W., 1987. Estuary plumes and fronts in shelf waters: A layer model. *J.Phys.Oceanogr.*, **17**, 1877-1896.

Garvine, R.W., 1994. A dynamical system for classifying buoyant coastal discharges. *Cont.Shelf Res.*, **15**, 1585-1596.

Garvine, R.W., 1996. Buoyant discharge on the continental shelf: A frontal model. *J.Mar.Res.*, **54**, 1-33.

George, K.J. & J. Buxton, 1983. Amphidromic movement and tidal distortion in the English Channel. *Hydrog. J.*, **29**, 41-46.

George, K.J., 1995. *Tides for Marine Studies* (2nd Provisional Ed.). University of Plymouth. 178 pages.

Gill, A.E., 1977. The hydraulics of rotating channel flow. *J.Fluid Mech.*, **80**, 641-671.

Gill, A.E., 1982. *Atmosphere-Ocean Dynamics*. Academic Press, Inc. (London) Ltd. UK. 662 pages.

Gmitrowicz, E.M. & J. Brown, 1993. The variability and forcing of currents within a frontal region off the Northeast coast of England. *Cont.Shelf.Res.*, **13**, 863-890.

Gregg, M.C., 1987. Diapycnal mixing in the thermocline: A Review. *J.Geophys.Res.*, **92**, 5249-5286.

Griffiths, R.W. & P.F. Linden, 1982. Laboratory experiments on fronts. *Geophys. Astophys. Fluid Dyn.*, **19**, 159-187.

Hickey, B.M., 2000. Transport Due to Freshwater Discharge into the Coastal Ocean In: University of Maryland Centre for Environmental Science Technical Report TS-237-00.

Hill, A.E., 1998. Buoyancy effects in coastal seas. In: K. Brink & A. Robinson (Eds.). *The Sea: The Global Coastal Ocean Processes and Methods*, Vol.10, John Wiley & Sons Inc., New York, USA. 604 pages.

Huang, N.E., 1979. On surface currents in the ocean. *J.Fluid Mech.*, **91**, 191-208.

Huang, W.G., A.P. Cracknell & R.A. Vaughan, 1993. Satellite Thermal Observations of the River Shannon Plume. *Estuarine Coastal Shelf Sci.*, **36**, 207-219.

Huntley, D.A., 1980. The North-West European Shelf Seas. In F.T.Banner, M.B.Collins and K.S. Massie (Eds.). *The Sea Bed and the Sea in Motion II. Physical and Chemical Oceanography, and Physical Resources*. Elsevier Scientific Publishing Company. Amsterdam, Netherlands. 638 Pages.

Huntley, D.A. & D.M. Hanes, 1987. Direct measurements of suspended sediment transport. In: N.C. Kraus (Ed.). Coastal sediments. ASCE, New Orleans, USA. page 723-737.

Huzzey, L.M., 1982.The Dynamics of a Bathymetrically Arrested Estuarine Front. *Estuarine Coastal Shelf Sci.*, **15**, 537-552.

Ingram, R.G., 1976. Characteristics of a Tide-Induced Estuarine Front. *J.Geophys.Res.*, **81**, 1951-1959.

Jaeger, J., 2000. Freshwater Input In: University of Maryland Centre for Environmental Science Technical Report TS-237-00.

Jenkins, G.M. & D.G. Watts, 1968. *Spectral Analysis and its Applications*. Holden Day, San Francisco, CA, USA. 525 pages.

Johannesen, J.A., R.A. Schuchmann, O.M. Johannesen, K.L. Davidson, & D.R. Lyzenga, 1991. Synthetic aperture radar images of upper ocean circulation features and wind fronts. *J.Geophys.Res.*, **96**, 10,411-10,422.

Johannesen, J.A., R.A. Schuchmann, G. Digranes, D.R. Lyzenga, C. Wackermann & O.M. Johannesen, 1996. Coastal Ocean fronts and eddies imaged with ERS 1 synthetic aperture radar. *J.Geophys.Res.*, **101**, 6651-6667.

Johnson, D.R. & A.D. Weidemann, 1998. A tidal plume front and internal solitons. *Cont.Shelf.Res.*, **18**, 923-928.

Kourafalou, V.H., T.N. Lee, L. Oey & J. Wang, 1996a. The fate of river discharge on the continental shelf, Part II: Transport of coastal low-salinity waters under realistic wind and tidal forcing. *J.Geophys.Res.*, **101**, 3415-3434.

Kourafalou, V.H., L. Oey, J. Wang & T.N. Lee, 1996b. The fate of river discharge on the continental shelf, Part I: Transport of coastal low-salinity waters under realistic wind and tidal forcing. *J.Geophys.Res.*, **101**, 3435-3456.

Largier, J.L., 1993. Estuarine Fronts: How Important Are They ?
Estuaries, **16**, 1-11.

Lewis, R.E., 1984. Circulation and Mixing in Estuary Outflows.
Cont.Shelf.Res., **3**, 201-214.

Lewis, R.E., 1997. *Dispersion in Estuaries and Coastal Waters*. John Wiley & Sons Ltd., Chichester, U.K. 312 pages.

Linden, P.F., 1979. Mixing in Stratified Fluids. *Geophys.Astrophys.Fluid.Dyn.*, **13**, 3-23.

Linden, P.F. & J.E. Simpson, 1988. Modulated mixing and frontogenesis in shallow seas and estuaries. *Cont.Shelf.Res.*, **8**, 1107-1127.

Luketina, D.A & J. Imberger, 1987. Characteristics of a Surface Buoyant Jet. *J.Geophys.Res.*, **92**, 5435-5447.

Luketina, D.A. & J. Imberger, 1989. Turbulence and Entrainment in a buoyant surface plume. *J.Geophys.Res.*, **94**, 12,619-12,636.

Lyzenga, D.R., 1991. Interaction of short surface and electromagnetic waves with ocean fronts. *J.Geophys.Res.*, **96**, 10,765-10,772.

Marmorino, G.O. & C.L. Trump, 1996. High-resolution measurements made across a tidal intrusion front. *J.Geophys.Res.*, **101**, 25,661-25,674.

Marmorino, G.O., T.F. Donato, M.A. Sletten & C.L. Trump, 2000. Observations of an inshore front associated with the Chesapeake Bay outflow plume. *Cont.Shelf.Res.*, **20**, 665-684.

Masse, A.K. & C.R. Murthy, 1990. Observations of the Niagara River thermal plume (Lake Ontario, North America). *J.Geophs.Res.*, **95**, 16,097-16,110.

Masse, A.K. & C.R. Murthy, 1992. Analysis of the Niagara River plume dynamics. *J.Geophs.Res.*, **97**, 2403-2420.

Massey, B.S., 1989. *Mechanics in Fluids* (6th Edition), Chapman & Hall, London, UK. 599 pages.

Matthews, R.C., 1997. Dynamics of the Teignmouth Estuarine Plume. M.Phil. Thesis, University of Plymouth. 192 pages.

Maxworthy, T., 1979. A note on the internal solitary waves produced by tidal flow over a three dimensional ridge. *J.Geophs.Res.*, **84**, 338-346.

McClimans, T.A., 1988. Estuarine Fronts and River Plumes: In: J. Dronkers, W. van Leussen (Eds.) *Physical Processes In Estuaries*. Springer-Verlag, Berlin, Germany. 560 pages.

Miles, J.W., 1961. On the stability of heterogeneous shear flows. *J.Fluid Mech.*, **10**, 496-508.

Miles, J.R., 1997. Enhanced Sediment Transport near Sea Walls and Reflective Beaches. Ph.D. Thesis, University of Plymouth. 192 pages.

Millero, F.J. & A. Poisson, 1981. International one-atmosphere equation of state of seawater. *Deep-Sea Res.*, **28**A, 625-629.

Morris, A.W., J.I. Allen, R.J.M. Howland & R.G. Wood, 1995. The estuary plume zone: Source or sink for land-derived nutrient discharges? *Estuarine Coast. Shelf Sci.*, **40**, 387-402.

Munchow, A. & R.W. Garvine, 1993a. Buoyancy and wind forcing of a coastal current. *J.Mar.Res.*, **51**, 293-322.

Munchow, A. & R.W. Garvine, 1993b. Dynamical properties of a buoyancy driven coastal current. *J.Geophs.Res.*, **98**, 20,063-20,078.

New, A.L., K.R. Dyer & R.E. Lewis, 1986. Predictions of the Generation and Propagation of Internal Waves and Mixing in a Partially Stratified Estuary. *Estuarine Coastal and Shelf Sci.*, **22**, 199-214.

New, A.L. & K.R. Dyer, 1988. Internal Waves and Mixing in Stratified Estuarine Flows. In: J. Dronkers, W. van Leussen (Eds.) *Physical Processes In Estuaries*. Springer- Verlag, Berlin, Germany. 560 pages.

Nilsson, C.S. & P.C. Tildesley, 1995. Imaging of oceanic features by ERS 1 synthetic aperture radar. *J.Geophs.Res.*, **100**, 953-967.

Nittrouer, C.A., D.J. DeMaster, A.G. Figueiredo & J.M. Rine, 1991. AMASSEDS: An interdisciplinary investigation of a complex coastal environment. Oceanography, **4**, 3-7.

O'Donnell, J.,1988. A numerical technique to incorporate frontal boundaries in layer models of ocean dynamics. *J.Phys.Oceanogr.*, **20**, 551-559.

O'Donnell, J.,1990. The Formation and Fate of a River Plume: A Numerical Model. *J.Phys.Oceanogr.*, **20**, 551-569.

O'Donnell, J., 1993. Surface Fronts in Estuaries: A Review. *Estuaries.* **16**, 12-39.

O'Donnell, J., 1997. Observations of near-surface currents and hydrography in the Connecticut River plume with the surface current and density array. *J.Geophys.Res.*, **102**, 25,021-25,033.

O'Donnell, J., G.O. Marmorino & C.L. Trump, 1998. Convergence and Downwelling at a River Plume Front. *J.Phys.Oceanogr.*, **28**, 1481-1495.

Osborn, T.R. & C.S. Cox, 1972. Oceanic fine structure. *Geophys.Fluid Dyn.*, **3**, 321-345.

Pelegri, J.L., 1988. Tidal Fronts in Estuaries. *Estuarine Coastal and Shelf Sci.*, **27**, 45-60.

Pond, S. & G.L. Pickard, 1991. Introductory Dynamical Oceanography (2nd Edition). Pergamon Press, Oxford, UK. 329 pages.

Pugh, D.T. 1987. *Tides, Surges and Mean Sea Level.* John Wiley & Sons, Chichester, UK. 472 pages.

Robinson, A.H.W., 1975. Cyclic Changes in Shoreline Development at the Entrance to Teignmouth Harbour, Devon, England. In: J.Hails & A.Carr (Eds.). *Nearshore Sediment Dynamics and Sedimentation: An Interdisciplinary Review.* John Wiley & Sons Ltd., London, UK. 316 pages

Sarabun, C.C.,Jr., 1993. Observations of a Chesapeake Bay Tidal Front. *Estuaries*, **16**, 68-73.

Simpson, J.E. & R.E. Britter, 1979. The dynamics of the head of a gravity current advancing over a horizontal surface., *J.Fluid Mech.*, **94**, 447-495.

Simpson, J.E. & R.E. Britter, 1980. A laboratory model of an atmospheric meso-front. *Q.J.R. Meterol.Soc.*, 106, 485-500.

Simpson, J.E., 1982. Gravity Currents in the Laboratory, Atmosphere and Ocean. *Annu. Rev. Fluid Mech.*, **14**, 213-234.

Simpson, J.E. & P.F. Linden, 1989. Frontogenesis in a fluid with horizontal gradients. *J.Fluid Mech.*, **202**, 1-16.

Simpson, J.H. & R.A. Nunes, 1981. The Tidal Intrusion Front: An Estuarine Convergence Zone. *Estuarine Coastal and Shelf Sci.*, **13**, 257-266.

Simpson, J.H. & D.G. Bowers, 1984. The role of tidal stirring in controlling the seasonal heat cycle in shelf seas. *Annales Geophysicae*, **2**, 4, 411-416.

Simpson, J.H. & I.D. James, 1986. Coastal and estuarine fronts. In: C.N.K. Mooers (Ed.) *Baroclinic Processes on the Continental Shelf.* American Geophysical Union, Washington, D.C., USA.

Simpson, J.H., W.G. Bos, F. Schirmer, A.J. Souza, T.P. Rippeth, S.E. Jones, D. Hydes, 1993. Periodic stratification in the Rhine ROFI in the North Sea. *Oceanologica Acta*, **16**, 23-32.

Soulsby, R.L., 1997. *Dynamics of marine sands*. Thomas Telford Serivces Ltd. London, UK. 249 pages.

Souza, A.J. & J.H. Simpson, 1996. The modification of tidal ellipses by stratification in the Rhine ROFI. *Cont.Shelf Res.*, **16**, 997-1007.

Stoker, J.J., 1958. *Water Waves: The Mathematical Theory with Applications*. John Wiley & Sons Inc.,New York, USA. 567 pages.

Stronach, J.A., 1981. The Fraser River Plume, Strait of Georgia. *Ocean Management*, **6**, 201-221.

Stull, R.B., 1988. An Introduction to Boundary Layer Meteorology. Klumer Academic Publishers.

Stumpf, R.P., G. Gelfenbaum & J.R. Pennock, 1993. Wind and tidal forcing of a buoyant plume, Mobile Bay, Alabama. *Cont.Shelf Res.*, **13**, 1281-1301.

Sturley, D.R.M., K.R. Dyer, 1990. The Estuarine Thermistor Spar: an instrument for making thermal profiles in shallow water. *The Hydrographic Journal*, **55**, 13-21.

Sturley, D.R.M., 1990. Topograhically Induced Internal Waves and Enhanced Vertical Mixing in an Estuary. Ph.D. Thesis, University of Plymouth. 209 pages.

Thompson, R.O.R.Y., 1980. Efficiency of conversion of kinetic energy to potential energy by a breaking internal wave. *J.Geophys.Res.*, **85**, 6631-6635.

Thorpe, S.A., 1973. Experiments on instability and turbulence in a stratified shear flow. *J.Fluid Mech.*, **61**, 731-751.

Turner, J.S., 1973. *Buoyancy Effects in Fluids*. Cambridge University Press. Cambridge, UK. 367 pages.

Van Aken, H.M., 1986. The onset of stratification in shelf seas due to differential advection in the presence of a salinity gradient. *Cont.Shelf Res.*, **5**, 475-485.

Vogelzang, J., K.G. Ruddick & J.B. Moens, 1997. On signatures of river outflow fronts in radar imagery. *Int. J. Remote Sensing*, **18**, 3479-3505.

Waever, A.J. & W.W. Hsieh, 1987. The influence of buoyancy flux from estuaries on continental shelf circulation. *J.Phys.Oceanogr.*, **17**, 2127-2140.

Wheless, G.H. & A. Valle-Levinson, 1996. A modeling study of tidally driven exchange through a narrow inlet onto a sloping shelf. *J.Geophys.Res.*, **101**, 25,675-25,687.

Wimpol, 1989. Summary Fieldwork Report. South West Water: Environmental Survey and Mathematical Modelling of the River Teign Estuary and Coastal Region. Contract No. W25 0001 5170.

Wiseman, W.J. & R.W. Garvine, 1995. Plumes and coastal currents near large river mouths. *Estuaries*, **18**, 509-517.

Wu, Y., L. Washburn & B.H. Jones, 1994. Buoyant plume dispersion in a coastal environment: evolving plume structure and dynamics. *Cont.Shelf Res.*, **14**, 1001-1023.

Yankovsky, A.E. & D.C. Chapman, 1997. A Simple Theory for the Fate of Buoyant Coastal Discharges. *J.Phys.Oceanogr.*, **27**, 1386-1401.

Zhang, S.Y., G. Janowitz & L. Pietrafesa, 1987. The interaction of estuarine and shelf waters: A model and applications. *J.Phys.Oceanogr.*, **17**, 455-467.

Appendix 1

Mooring	Instrument Type	Dates of deployment	Duration (days)	Epoch time	Geographical position (WGS84)	Water depth (m)	Height above seabed (m)
RCM 1	Aanderaa RCM 3	2/8/88 – 30/8/88	28	00:00 GMT 2/8/88	50°32.19′ N – 3°28.70′W	8.0	3.5
RCM 2	Aanderaa RCM 3	2/8/88 – 30/8/88	28	00:00 GMT 2/8/88	50°35.02′ N – 3°24.80′W	12.0	4.0
RCM 3	Aanderaa RCM 3	2/8/88 – 30/8/88	28	00:00 GMT 2/8/88	50°31.81′ N – 3°25.04′W	20.0	8.5
RCM 4	Aanderaa RCM 7	3/10/97 – 0/10/97	27	17:00 GMT 3/10/97	50°31.80′ N – 3°27.60′W	18.0	2.4
TG0	NBA DNT8	1/8/88 - 1/9/88	38	00:00 GMT 2/8/88	50°32.81′ N – 3°25.04′W	20.0	0.5
TG1	NBA DNT8	1/8/88 - 1/9/88	32	00:00 GMT 2/8/88	50°32.73 N – 3°30.54 W	2.5	0.0

Table 1: Summary of RCM and tidal gauge moorings geographical location, duration of deployment and position in the water column.

Front	Mean bearing (°N)	Alignment (° N) of axis normal to front	Correction (± °)
3	56.2	27.0	29.2
4	299.6	297.0	2.6
5	302.1	297.0	5.1
6	289.0	297.0	8.0
7	348.8	333.0	15.8
8	295.6	318.6	23.0
9	371.1	326.9	44.2
10	309.0	330.3	21.3
11	-	-	-
12	326.0	331.6	5.6
13	319.8	12.9	53.1
14	49.5	16.5	33.0
15	319.3	356.8	37.5
16	48.3	2.4	45.9
17	293.5	255.1	38.4
18	313.7	255.0	58.7
19	310.0	345.0	35.0
20	300.0	297.3	2.7
21	304.0	348.9	44.9
25	299.7	297.0	2.7
26	346.8	10.0	23.2
27	4.4	3.9	0.5
28	297.6	351.8	54.2
29	303.2	359.2	56.0
30	317.9	355.5	37.6
31	321.0	15.8	54.8
32	301.3	350.3	49.0

Table 2: Summary of transect bearing, alignment axis and angle of rotation of EMCM data recorded on the 25th and 26th November 1998.

Group number	Distance (m)	Transect numbers 25th November	Transect numbers 26th November
i	60	3 5	31
ii	120	8, 16, 17, 20	27
iii	180	4, 6, 7, 9, 14, 19	26, 32
vi	240	15, 18	25, 28
v	300	10, 12, 13, 21	29, 30

Table 3: Grouping details for Fr_i percentage occurrence analysis in Chapter 5.

Appendix 2

Pritchard, M. & Huntley, D.A. & O'Hare, T.J., 2000. Mixing in a Small Tidal Estuarine Plume. In: Estuarine and Coastal Modelling: Proceedings of the Sixth International Conference. November 3rd - 5th 1999, New Orleans, Louisiana., USA / edited by Malcolm L. Spaulding, H. Lee Butler. Pages 931-946 ISBN 0-7844-0504-2. 1299 pages.

Mixing in a Small Tidal Estuarine Plume

M. Pritchard [1], D.A. Huntley [1] & T.J. O'Hare[1]

Abstract

Features inside a radially spreading river plume discharge in the English Channel are compared to those predicted by a simple generic model that simulates radial spreading from a constant source. X-band radar imagery used to scale model output predicted the presence of an internal bore lagging the surface front of the plume by approximately 200m. High-resolution measurements of temperature, salinity and velocity recorded inside the plume outflow found no evidence of the internal bore in its predicted position. However, temperature contours showed an abrupt shallowing of the interfacial region some 40m behind the surface front. Super-critical Froude numbers present in this region of the plume suggest the bore may form closer to the leading front than predicted by the model. Field measurements show the initial value chosen for the mixing parameter (β) included in the frontal boundary condition is underestimated by about a factor of 2. The required increase in β reduced the lag length scale of bore formation to one where critical Froude numbers were detected inside the plume. Further estimates of entrainment velocity in the frontal region showed convergence and downwelling at the surface front that is followed by a region of upwelling. A 'caterpillar track' type circulation is thought to be responsible for mixing and entrainment in the head region of the plume. This head remains a reasonably constant size due to any increase in across frontal velocity over the ebb tidal cycle being matched by increased entrainment and mixing.

Introduction

River plume dynamics have been studied in the past through extensive modelling exercises (see O'Donnell, 1993). However, as yet, few observational campaigns have provided the high-resolution data necessary to resolve the internal features and mixing hypothesised by their output. Recent field experiments made by O'Donnell *et.al.* (1998) observed convergence and downwelling in the frontal zone of a plume outflow. Field results are compared with a model proposed by Garvine (1974) which examined small-scale frontal dynamics. The results presented by O'Donnell *et.al.* (1998), although interesting, failed to quantify mixing parameters in the frontal region.

---

[1] Institute of Marine Studies, University of Plymouth, Drake Circus, Plymouth, Devon, PL4 8AA, UK.

However, mixing is thought to be intense and site specific to the plume front. Lukitina & Imberger (1989) using a high- resolution data set identified a highly turbulent regime within the frontal region, but their instrumentation was static and could not follow frontal development and mixing over a tidal cycle.

To fully understand mixing and dispersion of freshwater plumes and thereby aid model development, detailed spatial and temporal field measurements are required to quantify boundary conditions and parameterise mixing. This will hopefully encourage improvements in plume model boundary conditions used to forecast the dispersion of conservative pollutants and sediment in the coastal zone. The aim of this paper is to present some results from recent field measurements and a modelling exercise that examined the sensitivity of a radial spreading river plume model to *in situ* derived mixing parameters.

Theoretical Background

The model chosen for this exercise was one developed by Garvine (1984). This effectively simulated a radial spreading river plume unbound by coastal features. After an initial start up, the source flow was assumed constant at all times, Coriolis force and wind-stress were ignored and the receiving coastal water was assumed stationary. The method of characteristics was employed to solve the non-linear wave dynamics of the unsteady flow. Full model derivation and methods of finding solutions may be found in Garvine (1981, 1984).

The model basically sets two regimes, one of steady non-critical flow, where the Froude number, *Fr* is <1 and the second as a front boundary where *Fr* >1 as shown in classical hydraulic theory on hydraulic jumps and bores (Stoker, 1957). The governing equations of the model are:

mass:

$$\frac{\partial c^2}{\partial t} + \frac{1}{r}\frac{\partial}{\partial r}\left(rc^2 q\right) = 0$$

(1)

momentum:

$$\frac{\partial q}{\partial t} + \frac{\partial}{\partial r}\left(\frac{q^2}{2} + c^2\right) = 0$$

(2)

r = Radial distance from spreading source (m)
t = Time From release (s)
c = Phase speed of internal wave on the interface = $\sqrt{g'd}$ (ms^{-1})
g' = Reduced gravity ($\Delta\rho/\rho$)g (ms^{-2})
d = Buoyant layer depth (m)
q = Fluid velocity (ms^{-1})

The mass continuity and momentum equations (1&2) are hyperbolic with a pair of characteristic lines given locally by:

$$\frac{dr}{dt} = q \pm c \qquad (3)$$

where a change in radius with change in time is equal to radial water velocity ± long internal wave speed. The corresponding characteristic equations along the lines given by (3) are:

$$dq \pm 2dc = \mp \frac{cq}{r} dt \qquad (4)$$

The ± families represent non-linear internal gravity waves that propagate upstream and downstream respectively, at phase speed c relative to the buoyant layer and at an absolute wave speed $q \pm c$ relative to fixed co-ordinates. The model is non-dimensionalised by introducing scaled variables using q^*, d^* and r_0 as a reference velocity, depth and length scale (schematic diagram is shown in Fig 1):

$$R \equiv r/r_0 \qquad T \equiv q^* t / r_0$$

$$Q \equiv q / q_0 \qquad C \equiv c / q^*$$

$$D \equiv d / d^* = C^2 \qquad F = Q / C$$

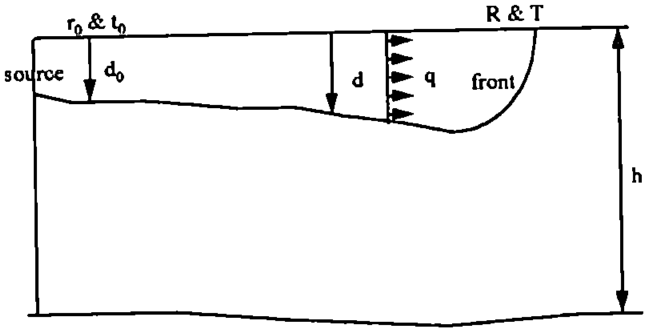

Fig 1: A schematic diagram of the radial spreading plume model (adapted From Garvine. 1984).

The frontal boundary conditions are derived in Garvine (1981). He assumes that the magnitude of the vertical entrainment velocity, q_e (see equation 8) is linearly proportional to the relative velocity of the lower layer, Q_a and decays exponentially away from the front towards the source. The vertical direction of entrainment may be selected as positive (upward), zero or negative (downward). For the limit of a surface front where the buoyant layer depth tends to zero, the frontal 'jump' boundary conditions are:

$$Q_a = F_{al}\, C_f \qquad (5)$$

$$Q_f = F_{al}\,(1 - S_e\beta)C_f \qquad (6)$$

Where:

Q_f = Fluid speed behind the front
C_f = Phase speed behind the front
Q_a = The speed of the front relative to the ambient water.

$F_{al} = [2\beta(\tilde{d} + S_e^2\beta)]^{-1/2}$ = The Froude number based on Q_a and C_f
β = Positive dimensionless constant that indicates the decay scale or fraction of the front where significant turbulent mass exchange (entrainment) and momentum exchange (interfacial friction and entrainment of momentum) occurs.

$\tilde{d}$ = Positive constant that specifies the ratio of interfacial friction and entrainment coefficients.
S_e = Entrainment factor i.e. 0 = No entrainment; 1= upward entrainment: -1= downward entrainment.

The Froude number that describes the state of flow behind the front, $F_f = Q_f / C_f = F_{al}\,(1 - S_e\beta)$ is held constant. Equations (5) and (6) are the two jump conditions of Garvine (1981) adapted to describe the mass continuity and horizontal momentum balance in the frontal region of a radially spreading plume. These are combined with the plus family branch of (4). This relates, Q_f and C_f to the interior flow state Q and C, at the point where the plus or downstream propagating wave of (3) passes through the front and intersects the previous R step. Stoker (1957), Garvine (1981, 1984) and O'Donnell (1993) provide full discussions of the derivation of boundary conditions.

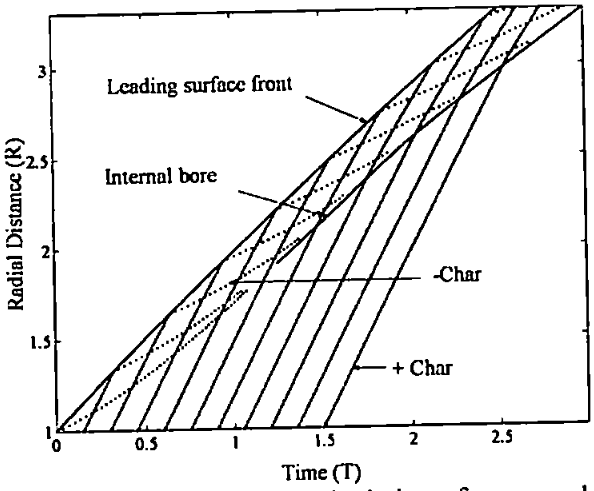

Fig 2: Plot of sample calculation from model in dimensionless form. Leading surface front and internal bore are shown with respect to R-T space and time.
$\beta = 0.15$; $F_{al} = 2^{1/2}$ $S_e = -1$.

Results from model runs showed the formation of an internal bore behind the leading front. As the method of characteristics cannot solve discontinuities in a variable properly, Garvine (1984) fitted a second jump condition. Garvine (1984) suggests the internal bore forms as a result of internal waves that propagate downstream from the source coalescing with upstream propagating waves that are reflected from the leading front. A plot of the characteristics plane as shown in Fig 2, describes a steady-state radial spreading regime that is preceded by a radial ring where the leading edge forms the front and the trailing edge an internal hydraulic jump or bore.

Our field experiments discussed in the following section were designed to test the hypothesis of a trailing internal bore that forms behind a leading surface front in a small radially spreading river plume. In addition, the mixing in the plume is quantified, as previous model sensitivity tests showed the magnitude of the mixing parameter is an important factor in determining the existence and / or position of the internal bore.

Field Site

Fig 3 shows the site chosen to compare observational data to the radial spreading model was the Teign Estuary, Teignmouth, Devon, U.K. The most physically pronounced plumes are discharged from the estuary into Lyme Bay between October and March in response to high precipitation. A minimum threshold runoff rate of approximately 12 m^3s^{-1} seems to be the lower limit for a definable plume to form. When runoff is sufficient, a radial shaped brackish water plume, roughly symmetrical about the mouth develops on the ebb tide. Plume formation and spreading was captured in a series of X-band radar images recorded in 1995. A radar station located on the shoreline effectively mapped the developing plumes frontal boundaries and produced a time series of the developing plume on 2 ebb tidal cycles. Thus, by comparing time stack images of plume area development through an ebb tidal cycle it was possible to estimate the rate of radial spreading. This speed was then used to 'seed' the radial spreading model through the scaling arguments. Spatial maps of the plume development through time are shown in Fig 3. Colour contrast due to sediment load and damped sea surface roughness were present inside the confines of the plume front.

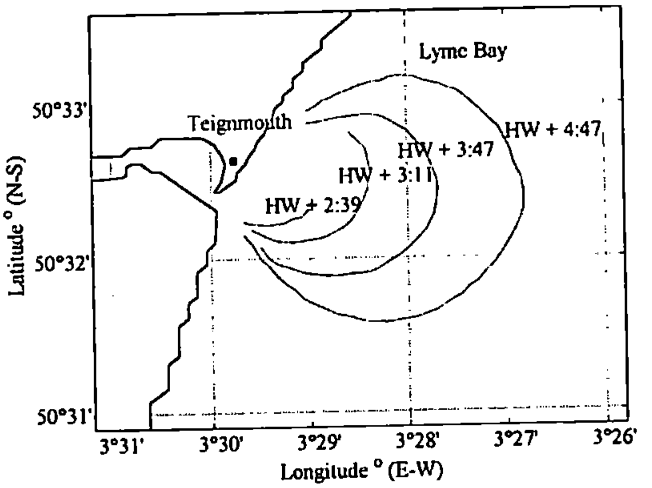

Fig 3: Map of study area including projections of plume development as estimated from X-band radar imagery. Imagery was made available courtesy of M. Tenorio and N. Ward, SOC.

The tidal regime at Teignmouth is semidiurnal with a mean range at the mouth of the estuary of 3.5 m. The local coastal waters receiving the discharge have low amplitude recti-linear (NE-SW) tidal currents rarely exceeding 0.25 ms^{-1}

and 0.12 ms^{-1} on Spring and Neap tides respectively. Initial formation of the front appears due to a converging coastal tidal current and outflow from the estuary. Radial spreading between the 2nd and 4th quarter of the estuary's ebb cycle is relatively unaffected by the coastal tidal currents. Small residual currents have little impact on plume development and spreading dynamics. Estimates of the Kelvin number as defined by O'Donnell (1993) showed that Earth's rotation is unimportant near to the estuary mouth.

Initial model conditions were scaled to radial spreading rates calculated from the X-band radar imagery, CTD casts and velocity measurements recorded in 1995. Regression analysis of incremental increases in area calculations made from X-band radar imagery gave a steady state critical radial flow velocity of $q*$ =0.13ms^{-1} and we set Q_0 = 1.2 and F_{al} = $2^{1/2}$ as in Garvine (1984). S_e = -1 was chosen from field observations made by O'Donnell *et.al.* (1998). Simpson's (1982) estimate of β = 0.15 the dimensionless mixing coefficient, is derived from laboratory experiments. β describes the ratio of the mean speed of gravity current propagation to the overtaking speed of fluid into the head. In context of the model any increase in β intensifies and spatially lengthens the mixing scale in the frontal zone.

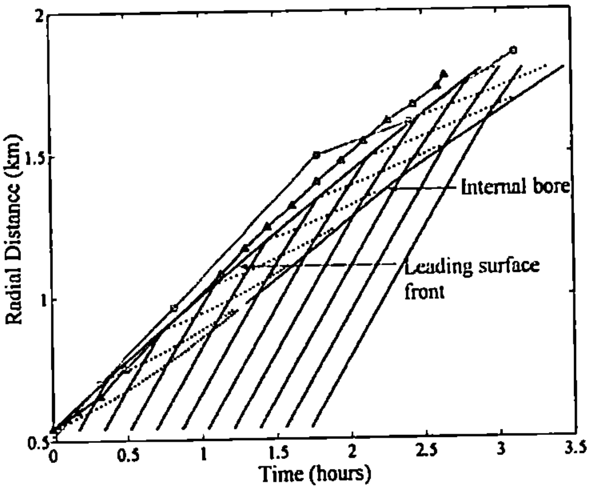

Fig 4: A comparison between modelled characteristics plane and observed radial spreading rates from the 3rd and 7th March 95. □ = Spreading rate 3rd March 95; Δ= Spreading rate 7thMarch. β = 0.15; F_{al}= $2^{1/2}$ S_e = -1.

Fig 4 illustrates the numerical output as a characteristics plane plot scaled to plume spreading rates calculated from X-band radar imagery. For the two-recorded spreading events on the 3rd March 1995 and the 7th March 1995, good agreement is shown between the observed and modelled rate of spreading. The scaled model output predicts the formation of an internal jump or bore lagging the leading front by a distance of some 200 m.

Fig 5 illustrates the predicted interfacial depth scaled by CTD profiles recorded in the plume near the source (d^*=2.5 m). The abrupt shallowing of the interface from the deeper head region to the sub-critical plume layer behind the internal jump has a predicted length scale of approximately 30 m.

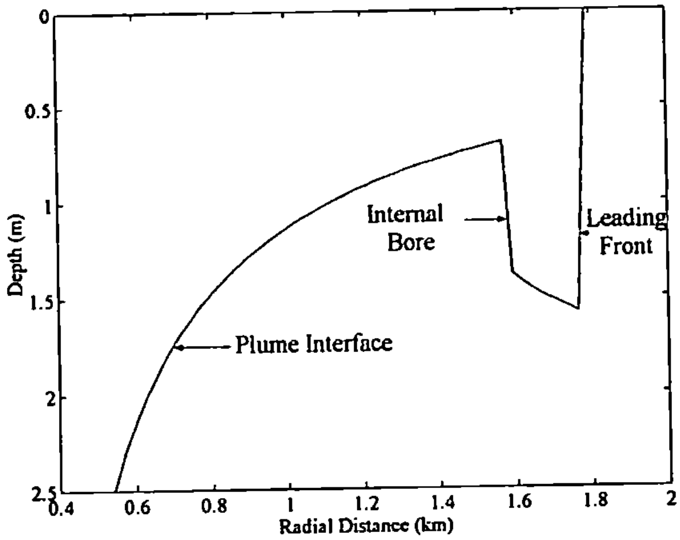

Fig 5: Modelled output of the internal interfacial features that show the formation of an internal hydraulic jump 200m behind the leading surface front. $\beta = 0.15$; $F_{01} = 2^{1/2}$ $S_c = -1$.

Field Study & Results

To test the model hypothesis of internal bore formation and the magnitude of mixing in the frontal zone we carried out multiple survey transects on several tidal ebb spreading cycles of the Teign plume. We used a high frequency (8Hz) logging instrument package consisting of the Estuarine Thermistor Spar (ETS), a vertical array of 15 Fastip thermoprobe thermistors fitted to a 4m aluminium tube (Sturley & Dyer, 1990). On the ETS we mounted 2 Valeport CT probes, 3 Valeport electro-magnetic current meters and Druck pressure transducers. The ETS was deployed from a small boat and used to survey the plume in the autumn of 1997 and 1998 during which a Trimble DGPS with local correction was used to calculate position. All instrument records were subject to 1 Hz low-pass filtering. Spectral coherence filtering between pressure tranducers and all the deployed instruments was used to remove the signals due to surface waves and boat movement. Seasonal temperature contrast between coastal water and the cooler river outflow water was used as the predominant tracer of water type (temperature/salinity correlation: $R^2 = 0.95$). Contoured water column temperature from several across frontal transects recorded through temporal and spatial development of the plume is presented in Fig 6a to 6c. The temperature profiles through the plume outflow reveal the abrupt contrast in the temperature signal of the plume and ambient seawater. Spatially, temperature and salinity changes were detected within a few metres when entering the plume. This abrupt frontal convergence was followed by a steeply descending isotherm layer that extended to a depth of 2 –3m. Fig 6b and 6c show no evidence of an internal bore 200 metres behind the leading front, as was the case in all the longer frontal transects. However, the contoured isotherms did appear to ascend to a shallower depth approximately 40m behind the leading front. This appeared to conform to the form of gravity head feature as observed in the experiments of Britter & Simpson (1978). This head feature was evident in nearly all our observations.

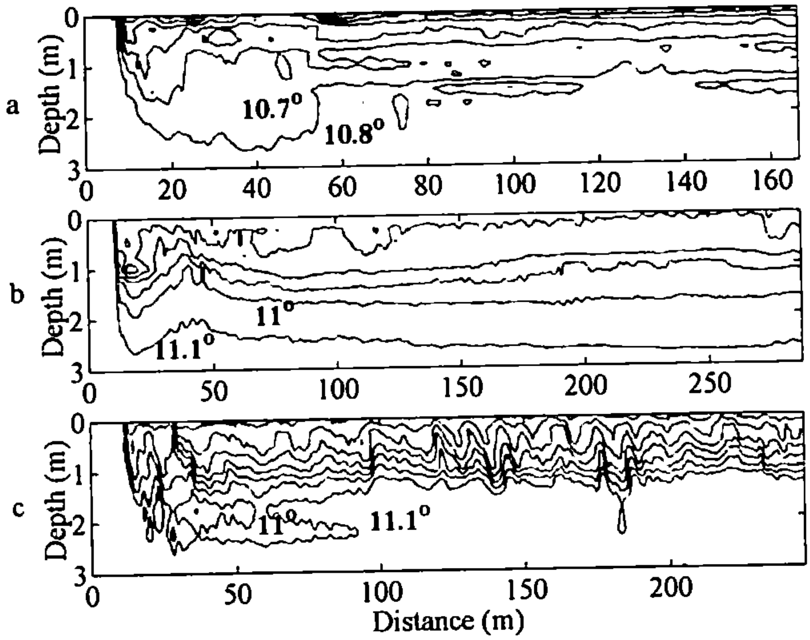

Fig 6a-Fig 6c: Temperature (°C) versus spatial distance (m) contour plots from thermistor outputs of 3 plume front transects. Plots show the deepening of the interface behind the leading front and formation of the gravity head.

Development of flow dynamics inside the plume is illustrated through four sets of across frontal velocity profiles in Fig 7a to Fig 7d. Velocity measurements recorded along each transect at 3 levels (0.95m, 1.85m, 2.9m) in the water column were grouped specific to a time and spatial locality after local high water. The individual transects in a group were then spatially aligned with respect to each other and averaged together. This produced a mean flow for each level in the water column at a progressive distance from the source and time after local high water.

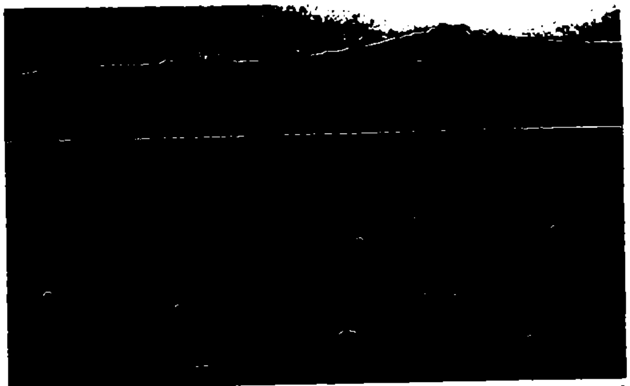

Plate 1. Photograph of spreading plume and convergence line of the Teign plume outflow on the 25th November 1998.

Negative flow (-ve) represents flow towards the front with respect to ambient seawater (non-plume water). The velocity data shows significant flows ranging from 0.1ms^{-1} to 0.25 ms^{-1} towards the front at the 1m level. Below this level flow is less intense but still forced towards the front. In the instance where flow is towards the front at all depths, the observations suggest a deeper surface layer extending beyond the depth of the lower current meter.

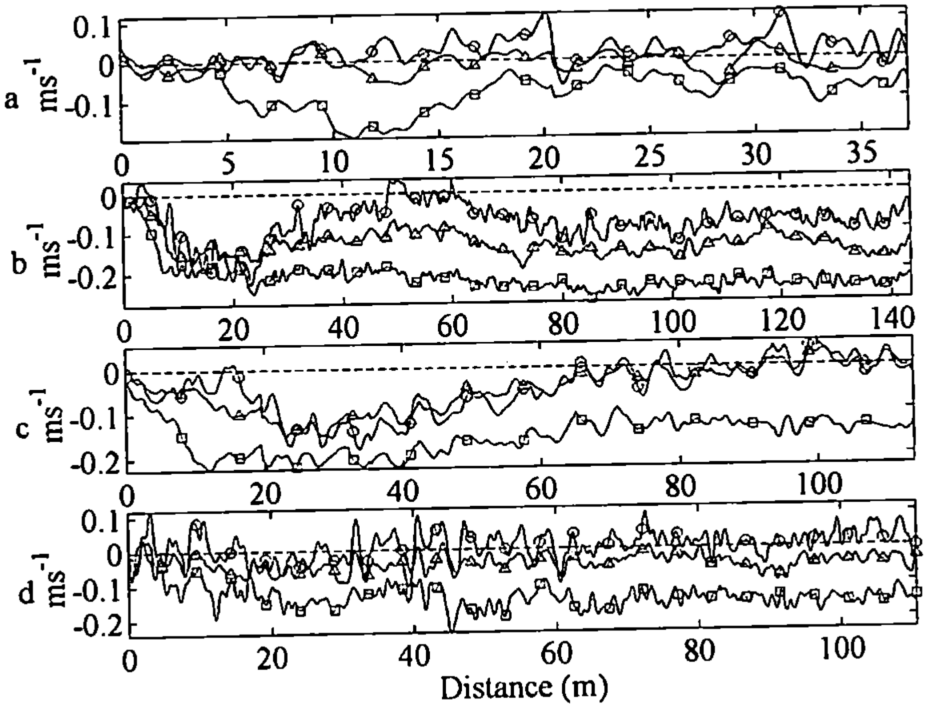

Fig 7a-Fig 7d: Group averaged frontal velocity profiles (ms^{-1}) versus distance (m) of time developing flow at □ = 0.95m; Δ = 1.85m O = 2.9m entering the plume in the first 5m on the left-hand side of the diagram. Fig 7a –HW + 2:42; Fig 7b-HW + 3:36; Fig 7c-HW + 5:12; Fig 7d-HW + 5:42.

The most intensive flow recorded in these observations is mid ebb corresponding to maximum outflow from the estuary and then slightly subsides towards the end of the plume spreading cycle. The across frontal flow was convergent with a distinct foam line present at the boundary as shown in Plate 1. Steeply sloping isotherms indicated the abruptness of the convergence with frontal slopes ranging from 0.13 - 0.47.

To quantify hydraulic jump conditions for model comparisons we calculated the densimetric Froude number, *Fr*:

$$Fr = \frac{u}{\sqrt{g'h}} \tag{7}$$

u = Surface layer velocity relative to ambient water (ms^{-1})
g'= Reduced gravity ($\Delta\rho/\rho$)g (ms^{-2})
h = Depth of surface layer (m)

Critical flow ($Fr \geq 1$) was evident on immediate encounter with the frontal region, symbolic of a typical hydraulic jump. Interestingly, the sites of critical flow were very localised as shown in Fig 8a – Fig 8c.

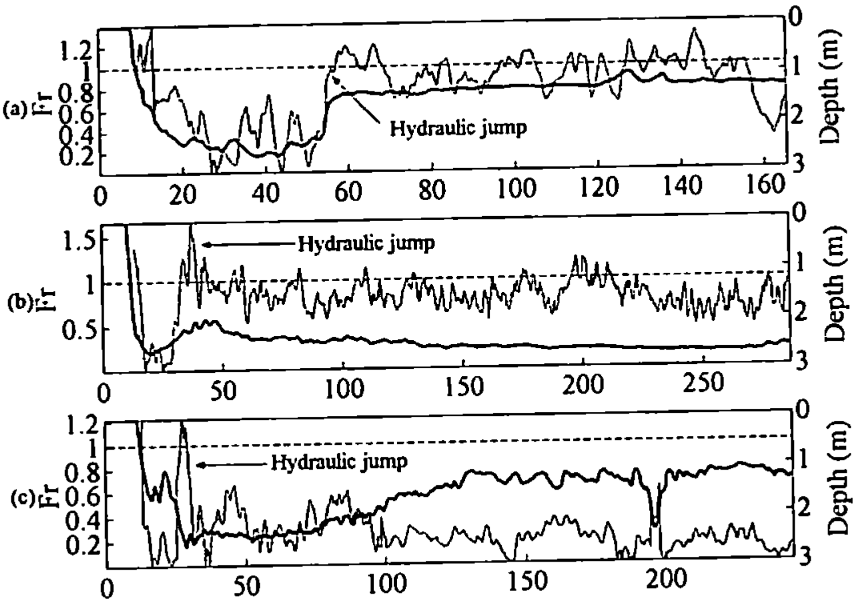

Fig 8a–Fig 8c: Froude number versus spatial distance for the 3 temperature contour plots shown in Fig 6a to Fig 6c. Interface depth (thick line) is plotted to indicate the position of the gravity head.

A running average smoothing of the data gives a spatial resolution of the critical flow sites as approximately 2-3m wide at the leading front. The quiescent sub-critical flow region often present behind the leading front was considered a result of the deepening of the pycnocline that subsequently increased the interfacial wave speed thus reducing the *Fr* number in the head.

Sharp peaks appeared in the *Fr* spatial series inside the plume. The position of the peaks and suggestion of jump conditions corresponded to the region behind the apparent gravity head illustrated in Fig 6. Also, the fluctuating critical / sub-critical *Fr* numbers seen inside the plume in Fig 8a and Fig 8b suggest the presence of multiple hydraulic jumps inside the plume. The main internal jump appeared inside the plume much closer to the surface front than predicted by the model.

To quantify the downwelled flux of brackish water at the front we calculated the vertical entrainment velocity, q_e, for each respective frontal transect. Fig 9 illustrates an example of the observed vertical entrainment velocity, q_e, calculated in a moving reference frame (overbar) from continuity.

$$\frac{\partial}{\partial x}(\bar{u}D) = q_e(\bar{x}) \qquad (8)$$

$\bar{x}$ = Distance from the front (m)
D = Depth of interface (m)
$\bar{u}$ = Velocity relative to the front (ms^{-1})
q_e = Entrainment velocity (ms^{-1})

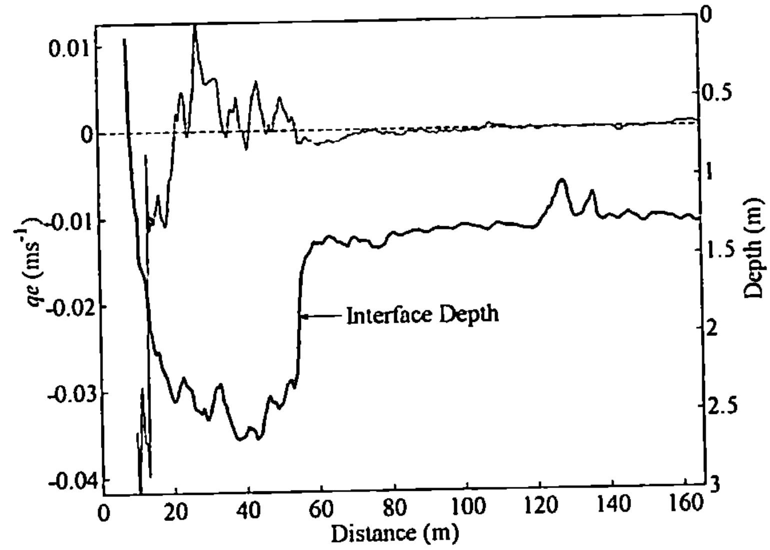

Fig 9: Entrainment velocity (ms^{-1}) versus distance (m) for the temperature transect shown in Fig 6a. Interfacial depth is plotted to indicate regions of down and upwelling.

When encountering the front, brackish surface water is initially forced down at a rate of up to 0.05 ms^{-1} emphasising the dynamic nature of the foremost convergent zone. Immediately behind the convergence observations indicated a smaller upwelled flux of water inside the gravity head. This suggested the previously downwelled water at the front was being entrained back into the plume in and behind the gravity head.

Localised entrainment coefficients, *E* and mixing coefficient, β were estimated within the realm of the leading front. The results presented are mean values calculated in the region of the vertically sloping interface i.e. from the surface to maximum horizontal depth of the head. *E*, as defined by Ellison and Turner (1959), Garvine (1981) and Huzzey (1982) describes the ratio of entrainment velocity to interfacial shear velocity.

$$\frac{q_e}{\bar{u}_a} = E \qquad (9)$$

$\bar{u}_a$= Velocity of front relative to ambient water (ms^{-1})
E = Entrainment coefficient

Further quantification of mixing and influx of fresher water into the frontal region was estimated through the β parameter as described in the experiments of Britter & Simpson (1978) and Simpson & Britter (1979). β provides a bulk estimate of mixing in the gravity head region of a gravity flow current through

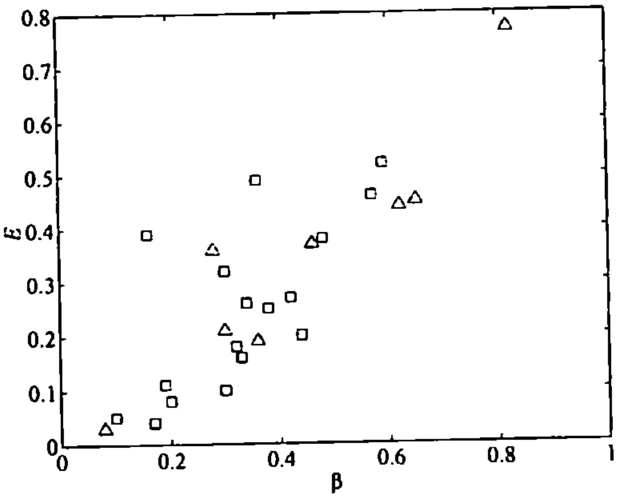

Fig 10: Entrainment coefficient (E) versus mixing coefficient (β). □ = 25th Nov 98; Δ =26th Nov 98.

the ratio of overtaking speed to frontal propagation speed. Estimates of β were calculated for each cross frontal transect from the cross frontal velocity profiles. Values derived from calculations centred around the head region ranged from 0.08 to 0.83 with a mean of 0.37 ± 0.07 (95% C.I.) This value is approximately double that quoted from the laboratory experiments of Simpson & Britter (1979).

Fig 10 shows a comparison between corresponding values of E and β calculated for survey transects from 2 separate spreading cycles. Entrainment increased linearly with mixing through a spreading event. These observations suggest mixing and entrainment in the head region remained proportional to the outflow velocity.

Fig 10 shows a comparison between corresponding values of E and β calculated for survey transects from 2 separate spreading cycles. Entrainment increased linearly with mixing through a spreading event. These observations suggest mixing and entrainment in the head region remained proportional to the outflow velocity.

Thus in context of a constant Fr, if g' decreases and $h \approx$ constant, then u the surface layer velocity must increase. So to maintain volume continuity in the head of the plume outflow velocity must increase, as our observations suggest.

Discussion

The results from the observational data presented in this paper show discrepancies between the theoretical and observed internal features of radially spreading river plumes. Temperature and velocity records failed to identify an internal hydraulic jump in or around the predicted site. However, consecutive temperature profiles made inside the plume outflows did suggest the presence of the gravity head as observed in laboratory simulations (Britter & Simpson, 1978).

Group averaged velocity profiles near to the front illustrate the development of flow inside the plume thorough a spreading cycle. Flow towards the front increased as the ebb tide from the estuary intensified. This eventually subsided towards local low water. The convergence zone at the front was the site of persistent downwelling where surface water was subducted down in to the water column. The mean estimated entrainment coefficient in the frontal zone for the 2 surveys discussed was 0.28, slightly greater than those found by Huzzey (1982). This region was marked by a narrow vertical band of super-critical flow followed by a region of deeper sub-critical flow. Repeated observations showed super-critical Fr numbers behind the head region as well as an upward component of velocity. Super-critical flow and upwelling possibly correspond to a jump as predicted in the Garvine (1984) model. Putting results into context of the modelled flow, we found that the leading front advanced with a Fr number $(O)1.3$, the same order of magnitude as selected for the modelled runs. However, the initial mixing coefficient β = 0.15, or the extent of turbulent exchange used in the frontal region of the model, was under estimated. Our field observations showed β to be of order 0.37, which is slightly higher than the maximum value recently calculated by O'Donnell (1997) in the Connecticut plume. A positive increase in β basically intensifies and lengthens the region of turbulent exchange following the leading front. Thus as β increases F_f increases. If Q_f remains constant then through Equation 6, C_f decreases. Physically, the increased turbidity and mixing decreases g' and interfacial wave speed 'c'. Hence, Q_a the resultant flow velocity at the front relative to ambient water is reduced through the relationship in Equation 5. The reduction in propagation speed reduces the spatial scale where downstream and upstream interfacial waves coalesce and the internal jump thus forms nearer to the leading front as energy is dispersed through turbulent kinetic energy which fuels local mixing rather than interfacial wave generation. To maintain the same spreading rates as observed in the X-Band radar imagery requires an increase in flow speed behind the front to main continuity. This would compensate for the extra loss in mass due to the elevated value of β. Fig 11 shows how a sequential increase in β and Q retains the speed but reduces the lag distance of the internal jump to some 50 m behind the leading front. This distance is the same order to that of the rear of the head region in the Teign plume where we observed super-critical Fr values.

These results may indicate the presence of rotational circulation in the front /head region as observed by Lukitina & Imberger (1987). As the moving head of the gravity current advanced, brackish water from the surface layer was entrained down at the relatively steep sloping interface of the convergence zone. Down-welled water is then swept back under the plume but is not fully mixed thus retaining some of its buoyancy and thus begins to rise. This upward flux combined with the mean forward motion of the plume creates shear, producing instabilities possibly akin to the Kelvin-Helmoltz billows observed in the laboratory by Britter and Simpson (1978). Brackish water that is not fully mixed then begins to rise finding stability at some equilibrium level. This component or parcel of water would eventually be convected towards the front by the surface outflow current. Thus mixing in the frontal region may be conceptualised as a 'caterpillar track' type process where the mixing zone is conveyed outwards from the source leaving a diluted oscillating wake in the general body of the plume. At the end of the ebb cycle the source flow is terminated and effectively cuts off the mixing mechanism.

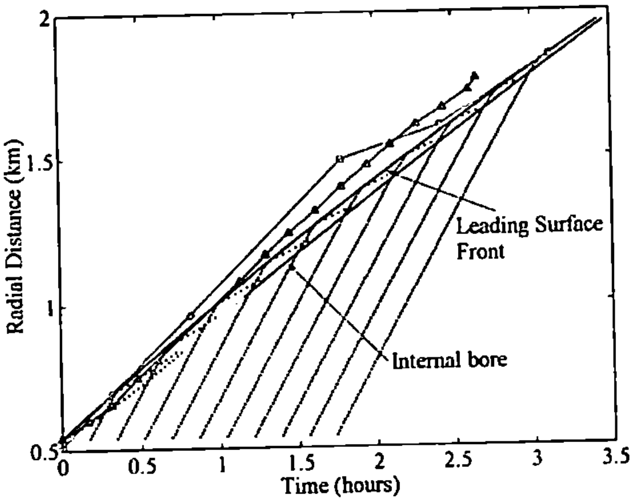

Fig 11: Characteristics plot of plume spreading with modified mixing coefficient (β) and an increase in the initial release speed Q_0. O = Spreading rate 3rd March 95; Δ= Spreading rate 7th March 95.

To conclude, the current study has presented a comparison between theoretical concepts and observational data of river plume dynamics. The numerical methods employed to explore internal mixing take a very simplistic approach to a complex system that develops in time and space. Entrainment and mixing in the front appears more intense than anticipated from laboratory experiments and remains proportional to outflow velocity. The distance that the predicted internal jump forms behind the leading front is considerably less when mixing (β) is increased in the leading frontal boundary. An increase in initial outflow velocity is thus required to maintain a similar spreading rate to that predicted from the X-band radar.

The physical description of mixing in the front proposed from our results requires further verification from field studies and the possibility of multiple jumps created by this mixing mechanism is not modelled by the method of characteristics and would require a different modelling approach.

Acknowledgements

The presented work was supported by a Plymouth University and PERC studentship. The authors would like to thank Miguel Tenorio and Nick Ward of Southampton Oceanographic Centre for the use of their X-band radar imagery.

References

Britter, R.E. & J.E. Simpson, 1978. Experiments on the dynamics of a gravity current head. *J. Fluid Mech.* **88**, 223-240.

Ellison, T.H. & J.S. Turner, 1959. Turbulent Entrainment in Stratified Flows. *J. Fluid Mech.* **6**, 423-448.

Garvine, R.W. 1974. Dynamics of Small Scale Oceanic Fronts. *J. Phys. Oceanogr.*, **4**, 557-569.

Garvine, R.W. 1981. Frontal jump conditions for models of shallow, buoyant surface layer dynamics. *Tellus.* **33**, 301-312.

Garvine, R.W. 1984. Radial Spreading of Buoyant, Surface Plumes in Coastal Waters. *J. Geophys. Res.*, **89**, 2, 1989-1996.

Huzzey, L.M. 1982. The Dynamics of a Bathymetrically Arrested Estuarine Front. *Estuarine, Coastal and Shelf Science.* **15**, 537-552.

Luketina, D.A. & J. Imberger, 1987. Characteristics of a Surface Buoyant Jet. *J. Geophys. Res.*, **92**, 5435-5447.

Luketina, D.A. & J. Imberger, 1989. Turbulence and Entrainment in a buoyant surface plume. *J. Geophys. Res.*, **95**, 12,619-12636.

O'Donnell J., 1993. Surface Fronts in Estuaries: A Review *Estuaries*, **16**, 12-39.

O'Donnell J., 1997. Observations of near-surface currents and hydrography in the Connecticut River plume with the surface current and density array. *J. Geophys. Res.*, **102**, 25,021-25,033.

O'Donnell, J., G.O. Marmorino & C.L. Trump, 1998. Convergence and Downwelling at a River Plume Front. *J. Phys. Oceanogr.*, **28**, 1481-1495.

Simpson, J.E & R.E. Britter, 1979. The dynamics of the head of a gravity current advancing over a horizontal surface. *J. Fluid Mech.*, **94**, 477-495.

Simpson J.E, 1982. Gravity currents in the laboratory, atmosphere and ocean. *Ann. Rev. Fluid Mech.* **14**, 213-234.

References continued

Stoker J.J. 1957. Water Waves. Interscience, New York, USA.

Sturley D.R.M., Dyer K.R., 1990. The Estuarine Thermistor Spar: an instrument for making thermal profiles in shallow water. *The Hydrographic Journal*, 55, 13-21.